FACULDADE DE ENGENHARIA DA UNIVERSIDADE DO PORTO

Study and development of optical fiber structures based on graphene

Catarina da Silva Monteiro

Programa Doutoral em Engenharia Física

Supervisor: Orlando José dos Reis Frazão

Co-Supervisor: Susana Ferreira de Oliveira Silva

June 2, 2023

Study and development of optical fiber structures based on graphene

Catarina da Silva Monteiro

Programa Doutoral em Engenharia Física

Approved in oral examination by the committee:

Chair: Prof. Joana Cassilda Rodrigues Espain de Oliveira
External Examiner: Prof. Paulo Sérgio de Brito André
External Examiner: Prof. António Barbosa Lobo Ribeiro
Local Examiner: Prof. José Luís Campos de Oliveira Santos
Supervisor: Prof. Orlando José dos Reis Frazão
Co-Supervisor: Dr. Susana Ferreira de Oliveira Silva

June 2, 2023

Bolsa de doutoramento da Fundação para a Ciência e a Tecnologia com a referência SFRH/BD/135820/2018, financiada por fundos nacionais do MCTES e pelo Fundo Social Europeu através do Programa Operacional Regional do Norte.

Abstract

With the advent of graphene in 2004, new solutions to scientific and technological challenges emerged. The discovery of graphene sparked intense scientific interest, resulting in extensive research on the matter. Graphene oxide (GO) has been closely associated with graphene, mainly considered its precursor and low-grade graphene due to its poorer electrical properties. This point of view changed with the discovery of the valuable properties of GO for scientifical and practical applications. Contrary to graphene, GO presents solubility and processability in water and in several organic solvents. Moreover, the properties of GO can be adapted through chemical modifications and the ability of mass production makes it particularly appealing for technological applications when compared to graphene. In this dissertation, graphene oxide is the main focus, presenting solutions for deposition, sensing applications, and laser fabrication in optical fibers.

First, an overview of graphene, GO, and reduced GO (rGO) is presented, focused on material properties, synthesis methods, and characterization techniques. This overview is followed by a study on thin film assembly on optical fibers. Contrary to planar substrates, optical fibers present a complex geometry that hinders the use of many well-developed techniques for thin film deposition. The layer-by-layer technique surpasses some limitations posed by optical fibers, allowing the deposition of multilayered structures using intermolecular interactions. The technique was studied in terms of adsorption kinetics and layer growth with the aim of being optimized and applied for optical sensing.

Afterwards, graphene and GO are examined for their use in optical sensing, beginning with a brief overview of the current state of the art. Two new sensors based on Fabry-Perot interferometry with GO are presented. The first sensor comprises a multi-mirror Fabry-Perot coated with a multilayered film of a dielectric material and GO using the layer-by-layer technique. The proposed sensor was theoretically and experimentally studied, exhibiting reflection phase shift with the external refractive index dependent on the number of layers. The second sensor is based on a Fabry-Perot interferometer with a GO membrane, fabricated through dip coating, showing a capability of deflecting with external pressure enabling acoustic sensing. The sensor was capable of detecting acoustic waves with a high-frequency bandwidth and of withstanding temperatures up to 45 °C.

The following chapter discusses the remarkable properties of GO in combination with micro and nanofibers. Micro and nanofibers are fibers with a waist diameter in the order of the wavelength of the traveling light and exhibit interesting optical properties. These properties, along with fabrication methods and applications of micro and nanofibers are presented. Afterwards, the fabrication method of micro and nanofibers was explored and optimized, allowing analysis in real-time. The integration of GO on the tapered fibers was studied using spray-coating, a technique that enables the deposition of a thin film on a highly fragilized structure such as a nanofiber. The nonlinear properties of GO were also studied for the generation of ultrashort pulses. The inclusion of a GO film, deposited using spray-coating, allowed the observation of saturable absorbance. This, in turn, resulted in the generation of short pulses (*ns*) through Q-switching and ultra-short pulses

(*ps*) through mode-locking.

The methodology and results reported convey novel practical developments to the applications of GO in photonics. In particular, they also established solid ground for further research and improvement on the development of thin films of GO to be applied in optical fibers and the combination of GO and nanofibers for the generation of ultrashort pulses.

Keywords: graphene oxide, optical fibers, fiber sensors, Fabry-Perot interferometry, Q-switching, mode locking, microfibers

Resumo

Com o advento do grafeno em 2004, surgiram novas soluções para desafios científicos e tecnológicos. A descoberta do grafeno despertou um intenso interesse científico, que resultou numa extensa investigação sobre esta temática. O óxido de grafeno (GO) tem sido estreitamente associado ao grafeno, considerado seu precursor e como um grafeno de baixo nível devido às suas propriedades eléctricas inferiores. Este ponto de vista mudou com a descoberta das valiosas propriedades do GO para aplicações científicas e práticas. Ao contrário do grafeno, o GO apresenta solubilidade e processabilidade em água e em vários solventes orgânicos. Além disso, as propriedades do GO podem ser adaptadas através de modificações químicas e a capacidade de produção em massa torna o GO particularmente apelativo para aplicações tecnológicas quando comparado com o grafeno. Nesta dissertação, o óxido de grafeno é o foco principal, apresentando soluções para a sua deposição, aplicações de detecção, e fabricação de laser em fibras ópticas.

Inicialmente é apresentada uma visão geral do grafeno, GO, e GO reduzido (rGO), centrada nas propriedades dos materiais, métodos de síntese e técnicas de caracterização. Esta análise é seguida por um estudo sobre a produção de filmes finos em fibras ópticas. Ao contrário dos substratos planares, as fibras ópticas apresentam uma geometria complexa que dificulta a utilização de muitas técnicas bem desenvolvidas para a deposição de filmes finos. A técnica layer-by-layer ultrapassa algumas limitações impostas pelas fibras ópticas, permitindo a deposição de estruturas multicamadas utilizando interacções intermoleculares. A técnica foi estudada em termos da sua cinética de adsorção e crescimento de camadas, com o objectivo de ser optimizada e aplicada para detecção óptica.

Posteriormente, o grafeno e o GO são examinados para a sua utilização em sensores óticos, começando com uma breve revisão do actual estado da arte. São apresentados dois novos sensores baseados em interferometria Fabry-Perot com GO. O primeiro sensor consiste num Fabry-Perot multiespelho revestido com um filme multicamada de um material dieléctrico e GO usando a técnica *layer-by-layer*. O sensor proposto foi estudado teórica e experimentalmente, exibindo uma variação de fase no sinal de reflexão com o índice de refracção externo dependente do número de camadas. O segundo sensor é baseado num interferómetro Fabry-Perot com uma membrana de GO. A membrana de GO foi fabricada através de revestimento por imersão, mostrando uma capacidade de deflexão com pressão externa permitindo a detecção acústica. O sensor é capaz de detectar ondas acústicas com uma alta gama de frequências de funcionamento e de resistir a temperaturas até 45 $^{\circ}$ C.

O capítulo seguinte aborda as notáveis propriedades do GO em combinação com micro e nanofibras. As micro e nanofibras são fibras óticas com um diâmetro mínimo na ordem do comprimento de onda da luz guiada e exibem propriedades óticas interessantes. Estas propriedades são apresentadas, juntamente com os métodos de fabrico e aplicações de micro e nanofibras. Posteriormente, o método de fabrico de micro e nanofibras foi explorado e optimizado, permitindo uma análise em tempo real. A integração de GO nas fibras afiladas foi estudada utilizando o revestimento por pulverização, uma técnica que permite a deposição de um filme fino sobre uma

estrutura altamente fragilizada, como uma nanofibra. As propriedades não lineares do GO foram também estudadas para a geração de impulsos ulta-curtos. A inclusão do filme de GO, depositado por revestimento por pulverização, permitiu a observação de absorção saturável. O que, por sua vez, resultou na geração de pulsos curtos (*ns*) através de Q-switching e pulsos ultra-curtos (*ps*) através de mode-locking.

A metodologia e os resultados relatados veiculam novos desenvolvimentos práticos para as aplicações de GO na fotónica. Em particular, estabeleceram também fundamentos sólidos para a investigação e melhoria do desenvolvimento de filmes finos de GO a serem aplicados em fibras ópticas e a combinação de GO e nanofibras para a geração de impulsos ultra-curtos.

Keywords: óxido de grafeno, fibras óticas, sensores em fibra, interferometria de Fabry-Perot, Q-switching, mode locking, microfibras

Acknowledgements

I would like to express my deepest gratitude to my supervisors Dr. Orlando Frazão and Dr. Susana Silva for all the challenges, inspiration, opportunities, and support over the years. Thank you for all of the insightful conversations and for allowing me to follow my own ideas, removing all barriers to my progress.

Thanks to the Centre for Applied Photonics at INESC TEC, my host institution, particularly to Professor Paulo Marques and Dr. Ireneu Dias. Thank you for giving me the opportunity to pursue my PhD journey by providing the facilities and financial support. I would also like to thank all senior researchers at INESC for their constant support.

Thanks to Prof. Manuel Marques for all the support with lab equipment and valuable discussions. I would also like to show gratitude to Filipe Silva for his important help in the chemistry lab, particularly in the preparation and handling of the "piranha" solution. Thank you so much! During my PhD journey, I was also fortunate to collaborate with Prof. Maria Raposo and Prof. Paulo Ribeiro. Thank you for the insightful ideas and discussions.

I would like to thank Prof. António Pereira Leite and Prof. José Luís dos Santos for their inspirational and wise words.

I would also like to acknowledge Carlos Gaspar for all his help with the technical side of this journey and Luísa Mendonça for all the help with administrative aspects and all the talks and laughs!

I would also like to acknowledge my colleagues and friends from INESC TEC. From earlier times: André, Vítor, João Maia, and Helena. For the ones that arrived later: Tiago, Pedro, João Mendes, Paulo Robalinho, and Susana Novais. And the ones that stuck during the whole time: Luís Coelho, Nuno, António, and Paulo Santos. Thank you all for the laughs, support, and very meaningful discussions during this time. They were all very valuable during this endeavor. Special thanks to the participants in the ongoing round table discussions during the coffee break: Miguel, António, Tiago, Dr. Luís Coelho, Dr. Nuno Silva, Dr. Ireneu Dias, Prof. José Manuel Almeida, and Prof. Ariel Guerreiro. These were invaluable discussions, that helped me grow as a person and researcher.

Thank you Diana Guimarães Guedes. You are an inspiration as a researcher, friend, and mother. Thank you for helping me grow, and for all the advice during the last few years. Filipa Barbosa, thank you for helping me navigate through the life's challenges that this journey brought.

A special thanks to my mother, father, and sister. Thank you for making me believe that I can achieve what I set out to do and that the challenges that life poses are not obstacles but rather opportunities to grow and learn. Thank you, Margarida, for always compelling me to be better and to do better.

Lastly, I would like to thank Miguel, my partner in life. Thank you for showing me new perspectives in both the lab and life. Thank you for making this journey together with me. To my beloved Rita, who, without knowing, was a fundamental part of this journey. She was my companion in the lab while growing up and my writing partner for this dissertation. You are my ultimate inspiration. Thank you.

"There must be no barriers for freedom of inquiry. There is no place for dogma in science. The scientist is free, and must be free to ask any question, to doubt any assertion, to seek for any evidence, to correct any errors."

J. Robert Oppenheimer

Contents

1 Introduction **1**
- 1.1 Motivation and objectives . . . 2
- 1.2 Dissertation overview . . . 2
- 1.3 Main contributions . . . 3
- 1.4 List of publications . . . 3

2 Graphene and graphene-based materials **5**
- 2.1 Material Properties . . . 5
  - 2.1.1 Mechanical Properties . . . 5
  - 2.1.2 Electrical Properties . . . 5
  - 2.1.3 Optical Properties . . . 6
- 2.2 Synthesis methods . . . 6
  - 2.2.1 Graphene . . . 6
  - 2.2.2 Graphene Oxide . . . 9
  - 2.2.3 Reduced Graphene Oxide . . . 9
  - 2.2.4 Comparison . . . 10
- 2.3 Characterization Techniques . . . 10
- 2.4 Concluding remarks . . . 12

3 Graphene oxide coated optical fibers using layer-by-layer technique **13**
- 3.1 Layer-by-layer technique . . . 14
  - 3.1.1 Graphene oxide adsorption kinetics . . . 14
  - 3.1.2 Bilayer growth . . . 16
  - 3.1.3 Coating characterization with Raman spectroscopy . . . 16
- 3.2 Graphene oxide coated hollow microspheres . . . 18
  - 3.2.1 Microsphere fabrication . . . 19
  - 3.2.2 Experimental Results . . . 19
- 3.3 Concluding Remarks . . . 23

4 Sensing applications of optical fibers coated with graphene-based materials **25**
- 4.1 A brief review on optical fiber sensors enabled by graphene and graphene-based materials . . . 25
  - 4.1.1 Evanescent Field . . . 25
  - 4.1.2 Surface Plasmon Resonance . . . 28
  - 4.1.3 Lossy mode resonance . . . 30
  - 4.1.4 Fiber gratings . . . 30
  - 4.1.5 Interferometric sensors . . . 31

4.2 Fabry-Perot microcavities with layered graphene-dielectric hybrid coatings for RI sensing . . . 35
4.2.1 Principle of operation . . . 35
4.2.2 Materials and Methods . . . 37
4.2.3 Experimental Results . . . 38
4.2.4 Results and Discussion . . . 41
4.3 Acoustic sensor based on graphene oxide membrane . . . 43
4.3.1 Working principle . . . 44
4.3.2 Experimental Results . . . 47
4.3.3 Results and discussion . . . 54
4.4 Concluding Remarks . . . 55

5 Optical micro and nanofibers 57
5.1 Introduction . . . 57
5.1.1 Fabrication Techniques . . . 58
5.1.2 Electrospinning . . . 61
5.1.3 Comparison . . . 62
5.1.4 Optical Properties . . . 62
5.1.5 Applications . . . 66
5.2 Experimental Results . . . 72
5.2.1 Laser-heated taper drawing . . . 72
5.2.2 Electrically-heated taper drawing . . . 73
5.2.3 Results . . . 78
5.3 Concluding Remarks . . . 86

6 Conclusions and future work 89

A Piranha solution: experimental protocol 93
A.1 Piranha solution preparation . . . 93
A.2 Piranha solution disposal . . . 93

B Software for the acoustic characterization of the sensor based on graphene oxide membrane 95
B.1 Software block diagram . . . 95
B.1.1 OSA Mode . . . 95
B.1.2 Acquisition Mode . . . 96
B.1.3 Recalibration Mode . . . 97
B.2 Graphical user interface . . . 98

C Constants 101

D Fiber drawing monitoring software 103

E Fiber profile monitoring software 105

List of Figures

2.1 Optical microscope image of graphene with a varying number of layers. 6
2.2 Cost and quality assessment for different graphene production techniques. 7
2.3 Micromechanical exfoliation process. First, the adhesive tape is pressed on the highly oriented pyrolytic graphite sample. Then, the tape is peeled away, with a graphite layer attached. To form a graphene sample on a Si/SiO_2 substrate, the adhesive tape is pressed softly into the substrate releasing some graphene layers. . 7
2.4 Synthesis of graphene in a copper substrate through CVD. 8
2.5 Transference of CVD-grown graphene film to optical fibers. 8
2.6 An example of AFM (a) topographic image and (b) respective profiles of a graphene sample. Images adapted from [48]. 11
2.7 (a) Typical Raman spectrum of graphene, image adapted from [49]; (b) Variation of Raman spectrum with the different number of layers, image adapted from [50]. 11
2.8 (a) SEM and (b) TEM image of a graphene sample. Adapted from [51]. 12

3.1 Layer-by-layer deposition technique. 14
3.2 GO adsorption kinetics experimental setup for the reflected spectrum acquisition composed by a broadband source, an optical circulator, an optical switch that allows attaining multiple spectra almost simultaneously, and an OSA. 15
3.3 In-situ adsorption kinetics of a layer of graphene oxide onto (a) an optical fiber coated with PEI and (b) $(PEI/GO)_{10}$/PEI LbL film already adsorbed on the optical fiber. 15
3.4 Reflectivity variation with the number of PEI/GO bilayers. 16
3.5 Raman spectrum of an uncoated single mode fiber, using an excitation wavelength of 532 nm, with 10-second integration time. 17
3.6 Raman spectra of (a) a 6-layer PEI/GO coated fiber with corresponding peak bands annotated, for an excitation wavelength of 532 nm. The D band is located at 1345 cm^{-1} and the G band at 1600 cm^{-1}, approximately. A microscope photograph of the fiber surface and corresponding regions of interest are presented in the inset; (b) samples with different numbers of PEI/GO layers and a GO-coated fiber. . . . 18
3.7 Schematic image of a hollow microsphere at the tip of an optical fiber. The dominant reflected waves are defined as $I_{1,2,3}$. 18
3.8 (a) Microsphere fabrication process; (b) Microscope image of the fabricated hollow microsphere. 19
3.9 (a) Experimental setup for spectrum acquisition in a reflection scheme; (b) Reflected spectrum of the hollow microsphere. 20
3.10 (a) Experimental reflected spectrum (in dots) and theoretical curve fitting (line); (b) FFT of the reflected spectrum. 20
3.11 FFT of the reflected spectrum at each bilayer number. 21

3.12 (a) The signal from the reflected spectra resultant from filtering the component associated with the second peak of the FFT and (b) the corresponding wavelength shift. . . . 21
3.13 Reflected spectrum before and after deposition of the PEI layer after (a) 1 and (b) 29 PEI/GO layers, respectively. . . . 22
3.14 Reflected spectrum of a microsphere coated with 30 PEI/GO layers, immediately after the coating process and after 24 hours of being exposed to normal environmental conditions. . . . 22

4.1 Scheme of an evanescent field-based fiber sensor with an evanescent field penetrating the external medium. . . . 26
4.2 Graphene coated taper-based sensors: (a) scheme of a tapered optical fiber and (b) tapered structure proposed by Zhao *et al*. Adapted from [74]. . . . 26
4.3 Scheme of the Mach-Zehnder configuration . . . 27
4.4 Basic scheme of an SPR sensor in an optical fiber. . . . 28
4.5 SPR sensors enhanced by graphene presented in the literature: (a) cross-section of the sensor proposed by Patnaik *et al.*, image adapted from [82]; (b) schematic diagram of the D-shaped PCF coated with graphene over gold for RI sensing, adapted from [83]; (c) SPR-based biosensor with an exposed core, image adapted from [84]; (d) fabrication process of the biosensor, image adapted from [85]. . . . 29
4.6 Fiber sensors based on FBGs enhanced by graphene: (a) humidity sensor based on a tilted FBG, adapted from [94], and (b) schematics of the D-shaped PCF coated with graphene over gold, image adapted from [96]. . . . 31
4.7 Biosensor based on an LPG. . . . 31
4.8 Interferometry-based sensors with graphene oxide: (a) RI sensor proposed by Dash *et al.*, image adapted from [99]; (b) gas sensor proposed by Yu *et al.*, image adapted from [100]; (c) gas sensor proposed by Yu *et al.*, image adapted from [101]. 32
4.9 Schematic diagram of a Fabry-Perot interferometer with graphene diaphragm. . . 33
4.10 Fabry-Perot interferometer with a Pd and multilayered graphene film for hydrogen detection, image adapted from [110]. . . . 34
4.11 Fabry-Perot interferometry based sensors with GO: (a) acoustic sensor proposed by Wu *et al.*, image adapted from [111]; (b) humidity sensor proposed by Li *et al.*, image adapted from [12]. . . . 34
4.12 Scheme of the sensor using a three-wave Fabry-Perot cavity with an outside multilayered hybrid surface coating (shown in green). The dimensions of the Fabry-Perot microcavities (D and d) and the three primary waves reflected off the cavity interfaces (of intensity I_1, I_2, and I_3), are also defined. . . . 35
4.13 Calculated reflected spectrum of a three-mirror Fabry-Perot interferometer, considering an air cavity of 250 μm and a silica cavity of 50 μm. . . . 37
4.14 (a) Sensor fabrication process; (b) microscope image of the fabricated sensor with an air cavity length of 258 µm and a silica slab length of 64 µm. . . . 37
4.15 Experimental setup for the acoustic characterization of the fiber sensor. . . . 38
4.16 Reflected spectrum before and after the deposition of (a) PEI and (b) 10 layers of PEI/GO. . . . 39
4.17 Reflected spectrum measured with the cavity immersed in liquid environments having different refractive indices ($n_{out} = 1.3327 - 1.3830$) for (a) uncoated fiber; (b) PEI coated fiber; (c) fiber coated with 10 PEI/GO layers; (d) fiber coated with 40 PEI/GO layers. . . . 39

4.18 Fast Fourier transform (FFT) of the reflected spectrum calculated for a RI equal to 1 for the different external RI for the sensor coated with (a) 10 and (b) 40 layers of PEI/GO. In Figure (a), a zoomed section of the peak corresponding to the component of the external interface is presented as an inset. 40
4.19 Band-pass filtered signal reconstructed by an inverse FFT for the sensor coated with (a) 10 and (b) 40 layers of PEI/GO. 41
4.20 Fit of the spectral shifts in the shortest period (Λ_2) measured from the filtered FFT of the reflected spectra to the theoretical model. Two data sets are shown for identical sensors coated with 10 (blue points) and 40 GO/PEI bilayers (orange points). The solid lines represent the corresponding theoretical curves, obtained for reasonable values of the free parameters in the model — $\xi = 0.0188$, $n_{pol} = 1.617$ — and a distance between consecutive GO monolayers of $\delta = 95.8$ nm and $\delta = 95.6$ nm, respectively. For comparison, the corresponding curves in the absence of GO membranes (i.e. $\xi = 0$) are shown as dashed lines. 42
4.21 Optical microscopy images of a PEI/GO thin film, with 10 layers, deposited on glass. 42
4.22 Schematic diagram of the Fabry-Perot interferometer with the GO membrane. The main reflections are annotated in the image. 44
4.23 Simulated reflected spectrum for an optical cavity of approximately 250 μm, with the tunable laser wavelength set to the quasi-linear region around the quadrature point. In the inset, the variation of optical power for different applied acoustic pressure is demonstrated. 45
4.24 First eigenfrequency and eigenmode calculated using COMSOL Multiphysics, attaining a value of 283.71 Hz. 46
4.25 Calculated maximum displacement caused by the applied static acoustic pressure. 47
4.26 (a) Sensor fabrication process: silica capillary fusion spliced to the SMF and cleaved to the desired length; dip coating of the capillary with graphene oxide; the sensor is, then, placed on a furnace for 1 hour at 60 °C; (b) Photograph image of the dip coating process with the graphene oxide placed on a microscope slide; the fiber is placed on a motorized translation stage and is constantly monitored until the capillary reaches the GO dispersion; at this point, the fiber is pulled out at a constant speed; (c) microscope photograph of the final structure of the sensor. 48
4.27 SEM image of (a) the GO membrane assembled at the top of the capillary and (b) the ruptured membrane with annotated thickness measurement of approximately 40 nm. 48
4.28 Interrogation system for the Fabry-Perot interferometer characterization. 49
4.29 Experimental reflected spectrum for the fabricated Fabry-Perot cavity in (a) a range between 1520 and 1620 nm and (b) in the nearest region around the wavelength of interest exhibiting the pure sinusoidal behavior as expected. 49
4.30 Experimental setup for the acoustic characterization of the fiber sensor. 50
4.31 Time domain response of the electrical microphone and optical fiber sensor to an applied acoustic wave with a frequency of 25 kHz and an SPL of 2.4 Pa. 51
4.32 Response of the sensor for different applied acoustic frequency, with fixed SPL (a) in the frequency domain and (b) corresponding SNR. 51
4.33 Output voltage for the applied acoustic pressure showing a linear response and, thus, no non-linearities were observed. 52
4.34 (a) Schematic diagram of the directivity characterization setup; (b) SNR directional response of the sensor for an applied frequency of 30 kHz. 53

4.35 Response of the sensor to temperature for temperatures between 16 and 90 °C: (a) initial and final reflected spectrum and (b) wavelength shift with temperature. . . 54

5.1 (a) SEM image of a coiled fiber with a 260 nm diameter; (b) TEM image of the surface of a 330 nm silica wire, in the inset the electron diffraction pattern is shown, demonstrating that the wire is amorphous. Images adapted from [147]. . . 57
5.2 Scheme of the taper-drawing technique. 58
5.3 Scheme of flame-heated taper drawing setup. 59
5.4 Scheme of the CO_2 laser-heated taper drawing setup. 59
5.5 Scheme of the electrically-heated laser-heated taper drawing setup. 60
5.6 Scheme of the "self-modulated" taper drawing setup. 60
5.7 Scheme of the setup for taper drawing from bulk glasses. 61
5.8 Scheme of the setup for electrospun MNFs. 61
5.9 Profile of the Poynting vector in the z-direction for a fiber composed of silica at a wavelength of 633 nm with a diameter of (a) 400 and (b) 200 nm. Image adapted from [175]. 64
5.10 Applications of MNFs. 66
5.11 Schematic diagram of typical configurations of MNF-based optical resonators: loop, knot, and coil. Image adapted from [208]. 67
5.12 Schematic diagram of typical microcavity configurations on MNF: (a) Fabry-Perot, (b) Mach-Zehnder, and (c) Sagnac. 68
5.13 Gratings inscribed on an MNF (a) an FBG inscribed by FIB milling, image adapted from [259], and (b) LPG fabricated through point-by-point dip coating method, image adapted from [265]. 69
5.14 (a) Microscope photograph of the double knot laser proposed by [271]; (b) Microscope photograph of a 450 μm diameter knot immersed in a 5 mM/L rhodamine 6G dye solution, that is evanescently pumped by 532 nm wavelength light guided along the knot that exhibits yellow photoluminescence, image adapted from [273]; (c) image of the hybrid structure presented by Ding *et al.* pumped at 355 nm, image adapted from [274]. 70
5.15 SEM image of the twisted section of the coupler proposed by Shao *et al.* [277]. . 70
5.16 (a) Concept of the particle manipulation device, trapping 100-600 nm liposomes near a nanofiber, image adapted from [182]; (b) Time-lapse image compilation of polystyrene orbiting around an optical nanofiber due to the azimuthal force caused by the guidance of an elliptically polarized field, image adapted from [183]. . . . 72
5.17 Schematic diagram of the laser-heated taper drawing setup composed of a cw CO_2 laser, a set of two silver-coated mirrors to redirect the laser beam to the fiber. The optical fiber is clamped on a motorized translation stage with two motors controlled simultaneously. A concave mirror was added to the setup to reflect the light back to the fiber, to increase the symmetry of the tapered region. 72
5.18 (a) Photograph of the fabricated taper using the CO_2 laser system; (b) Corresponding transmission spectra before and after taper drawing. 73
5.19 Schematic diagram of the electrically-heated taper drawing setup composed of a microheater with temperature controller, two linear stages, and the optical monitoring system composed of an optical source and a spectrometer. 74
5.20 (a) Close-up photograph of the fiber slot microheater, heated to approximately 1200° C.; (b) Fiber clamps, mounted on the motorized linear stages, placed at the same distance from the heater. 74

5.21 Structure of the fiber taper composed of three different regions: unstretched fiber where the diameter is r_0, taper waist where the diameter is minimum and constant, and the taper transition region. 75
5.22 The radius of the waist of the taper with respect to the total travel distance. 76
5.23 Schematic diagram of (a) the diffraction method, (b) resultant diffraction pattern, and (c) geometrical analysis. 77
5.24 Experimental setup for the taper diameter measurement composed by a He-Ne laser that is focused on the tapered fiber, creating an interference pattern on the target. 78
5.25 Transmission spectra of the taper during the pulling process, for wavelengths between 1520 and 1620 nm. 78
5.26 Transmitted spectrum of the taper (a) at a wavelength of 976 nm, and (b) for several different wavelengths. 79
5.27 Microscope photograph of the fabricated MNF using the electrically-heated taper drawing technique, with a waist diameter lower than 900 nm. 79
5.28 The packaging system for the MNFs was composed of a transparent plastic box and two silica slabs that prevented the MNF from touching the plastic box walls. 80
5.29 Illustration of the spray coating process, showing the basic components and vertical arrangement of the nozzle and the tapered fiber. 80
5.30 Experimental setup for the optical characterization of the GO-coated MNFs using a cw laser with a central wavelength of 976 nm. 81
5.31 Output power with input laser current for (a) MMF and (b) MMF+SMF. 81
5.32 Transmission spectrum of the tapered fiber with a waist diameter of approximately $3\mu m$ using the cw laser with a central wavelength of 976 nm. 82
5.33 Temporal behavior of the intensity of the electric field for five oscillating modes with equal amplitude and locked phases. 83
5.34 (a) Experimental setup composed of an EDFL ring laser, a polarization controller, an output 99:1 coupler connected to the OSA, and the fabricated MNF; (b) Output spectrum of the ring laser with the taper for a pump power of 300 mW. 84
5.35 Experimental setup composed of an EDFL ring laser, a polarization controller, an output 95:5 coupler, and the GO film positioned between two connectorized fibers. 84
5.36 (a) Output spectrum of the ring laser without and with GO film for different pump power values; (b) Output pulse train in mode-locking operation. 85
5.37 The experimental setup composed of an EDFL ring laser, a polarization controller, an output 90:10 coupler, and the GO film positioned between two connectorized fibers, for Q-switching operation. 86
5.38 (a) Output pulse train in mode-locking operation; (b) Evolution of the repetition rate with the increase of pump current. 86

B.1 Diagram of the main system blocks. 95
B.2 Block diagram of OSA mode. 96
B.3 Block diagram of acquisition mode. 97
B.4 Block diagram of recalibration mode. 98
B.5 Front panel of the program. 99

D.1 Graphical user interface developed for the ULS2048CL-EVO spectrometer. . . . 103
D.2 Block diagram of the software developed for the ULS2048CL-EVO spectrometer. 104

E.1 Graphical interface of the program. 105

List of Tables

2.1 Young's modulus for graphene, GO and rGO. 5
2.2 Comparison between different preparation methods of graphene. 10
2.3 Characterization techniques for graphene and graphene-based materials. 12

3.1 Fitting parameters of GO adsorption kinetics. R is the correlation coefficient. . . 16

4.1 FFT peaks and corresponding calculated cavity lengths for the two sensors. . . . 41
4.3 Parameters of the properties of the sensor for the calculation of the first resonant frequency. 46
4.4 Characteristics and performance of previously reported sensors. 52
4.5 Review of the main results. 54

5.1 Main advantages and disadvantages between the principal MNFs fabrication methods. 62
5.2 Effective hot-zone dimension calculated at three different vertical positions of the heater. 76
5.3 Taper waist diameter for the different traveling velocities, for a constant traveling distance of 15 mm. 77

Abbreviations

AFM	Atomic force microscopy
ATPC	Atomically thin planar conductors
BSA	Bovine serum albumin
CVD	Chemical vapor deposition
CW	Continuous wave
DMF	Dimethylformamide
EDFA	Erbium-doped fiber amplifier
EDFL	Er-doped fiber laser
FET	Field effect transistor
FBG	Fiber Bragg grating
FEM	Finite element method
FFT	Fast Fourier transform
FIB	Focused ion beam
FP	Fabry-Perot
FSR	Free spectral range
FTIR	Fourier transform infrared spectroscopy
FWM	Four-wave mixing
GO	Graphene oxide
GVD	Group velocity dispersion
ICP-MS	Inductively coupled plasma mass spectroscopy
IR	Infrared
ITO	Indium Tin Oxide
LbL	Layer-by-layer
LMR	Lossy mode resonance
LPG	Long period grating

LRSEP Longe-range surface exciton-polaritons

MDP Minimum detectable pressure

MMF Multimode fiber

MNFs Micro and nanofibers

NMP N-Methyl-2-pyrrolidone

OSA Optical spectrum analyzer

PCF Photonic crystal fiber

PEI Polyethylenimine

PWM Pulse width modulation

rGO Reduced graphene oxide

RI Refractive index

SEM Scanning electron microscopy

SLG Single layer graphene

SMF Single mode fiber

SNR Signal to noise ratio

SPL Sound pressure level

SPM Self-phase modulation

SPR Surface plasmon resonance

SRS Stimulated Raman scattering

TEM Transmission electron microscopy

TMM Transfer matrix method

UV-vis Ultraviolet-visible spectroscopy

WDM Wavelength division multiplexer

XANES X-ray absorption near edge spectroscopy

XFR X-ray fluorescence

XPM Cross-phase modulation

XPS X-ray photoelectron spectroscopy

XRD X-ray diffraction

Chapter 1

Introduction

Graphene is a material composed of carbon atoms packed in a honeycomb monolayer lattice. It has been studied for sixty years and has served as a thriving theoretical toy model [1]. Before its discovery, graphene was presumed not to exist and considered thermodynamically unstable [1]. The discovery of graphene in 2004 by Novoselov and Geim [2] propelled it to the spotlight of science and technology due to its outstanding electronic, optical, and mechanical properties. Graphene was first isolated through micromechanical exfoliation where a graphite sample was peeled using adhesive tape. This technique allows the attainment of high-quality graphene but is incapable of producing large-scale samples. Ever since different synthesis methods have emerged to overcome some limitations of micromechanical exfoliation. The various fabrication processes show different advantages and yield graphene samples with different characteristics and purity, but they also come with their own limitations. For some applications, graphene-based materials present themselves as a remarkable trade-off achieving similar properties to graphene, but with synthesis methods capable of being employed in mass production systems. Besides the less time-consuming and lower production cost, graphene-based materials such as graphene oxide (GO) exhibit strong hydrophilicity, allowing it to be exfoliated in different solvents including water. Moreover, it allows graphene oxide to be deposited in substrates with complex geometry using, for example, the layer-by-layer technique.

Photonics concerns the generation, transmission, manipulation, and sensing of light. The development of optical fibers, which played a critical role in the emergence of some photonic systems in the 1970s, revolutionized communication systems [3]. In addition to their lightweight and compact characteristics, optical fibers are also extremely flexible, resistant to harsh environments, and immune to electromagnetic interference, making them an interesting alternative to well-established technologies. The use of optical fibers not only allows for optical communication, but they can also be used for sensing applications in many fields, including biomedicine [4], [5], military [6], engineering [7], and fundamental sciences [8], among others. The combination of the outstanding properties of graphene with optical fiber sensors has been a matter of research since the discovery of graphene. This is a scientifically rich field, with vast multidisciplinary application opportunities. Recent years have seen the development of multiple photonic elements made possible by graphene and graphene-based materials [9], [10]. These elements are used in sensing [11], [12], light detection [13], and for the creation of new optical light sources [14].

This chapter provides an overview of the motivation and objectives of this work, followed by a description of the structure of the dissertation. A list of publications resulting from this PhD is also included after the main contributions to the field.

1.1 Motivation and objectives

The research activities developed in the context of the PhD program were motivated by the vast research opportunities offered by graphene-based materials for photonic applications using fiber optics. In particular, the pursuit of a deposition method of graphene-based materials compatible with the complex geometry of optical fibers and the subsequent study and development of new sensing elements. Furthermore, the integration and combination of optical properties of graphene based-materials with advanced fiber structures such as nanofibers is also a scientifically rich area that is currently being explored. Over the course of the PhD program, the main objectives of research activities were:

- Development and optimization of graphene oxide coating techniques for application in optical fibers.
- Study sensing applications of graphene oxide-coated fiber sensors.
- Fabrication and characterization of nanofibers and tapers using a CO2 laser system and an electrical microheater.
- Development of optical sources exploiting nonlinear properties of nanofibers and tapers, and optical properties of GO (e.g., saturable absorption).

1.2 Dissertation overview

This dissertation is organized into six chapters. A summary of the contents of each chapter of the dissertation is provided below.

Chapter 1 outlines the scope, goals, and structure of this thesis. The main publications that resulted from this thesis are also presented.

Chapter 2 provides an overview of graphene and graphene-based materials with a particular focus on their optical, mechanical, and electrical properties, synthesis methods, and characterization methods.

Chapter 3 introduces the concept of the layer-by-layer technique applied to GO thin film deposition on optical fibers. The adsorption kinetics of the film growth was studied in two conditions. Afterward, this technique was applied to an optical fiber structure based on Fabry-Perot interferometry. The spectral changes and structure with film growth were studied. The stability of the film to real-life environmental conditions was also studied.

Chapter 4 presents the state-of-the-art of optical fiber sensors that take advantage of the properties provided by graphene and graphene-based materials. Two new optical fiber sensors based on Fabry-Perot interferometry coated with graphene oxide are also presented theoretically and experimentally.

Chapter 5 is dedicated to micro and nanofibers. An introduction to their properties, fabrication methods, and applications is presented. The experimental results are presented, where two different fabrication techniques were explored to fabricate microfibers. The most well-suitable technique, the electrically-heated taper drawing, is studied and optimized. The application of micro and nanofibers for developing short and ultrashort light pulse generation is finally presented.

Chapter 6 summarizes the main findings of the work developed in this thesis and the opportunities for future work are presented.

1.3 Main contributions

The research conducted in the framework of this thesis resulted in the following scientific contributions:

- The deposition of GO on complex geometries with the layer-by-layer technique was studied and optimized using *in-situ* and real-time monitoring of adsorption kinetics, allowing to fully characterize GO coatings for sensing applications in optical fibers.

- The development of two new sensing structures. The first sensor developed exhibited a tunable behavior to the environmental refractive index according to the number of layers of PEI, a dielectric material, and GO here considered a two-dimensional material. This behavior allows the production of fully adaptable sensors for the specified application. The second sensor consisted of a Fabry-Perot interferometer with a GO membrane for acoustic sensing using the dip coating technique. As compared to similar structures presented in the literature, this sensor achieved the same level of performance but with a fabrication method that does not contain any hazardous materials.

- The study of the combined properties of GO and microfibers to generate short and ultrashort pulses through Q-switching and mode-locking techniques, respectively. Although the properties of graphene have been thoroughly studied in this regard, Q-switching and mode-locking using GO are still underdeveloped despite the fact that they could offer a significant benefit for mass production.

1.4 List of publications

International Journals

- **C. S. Monteiro**, M. Ferreira, J. P. Mendes, L. C. C. Coelho, S. O. Silva, and O. Frazão, "Optical Fiber Flowmeter Based on Graphene Oxide Coated Michelson Interferometer," IEEE Sensors Journal, **(submitted)**.

- A. V. Rodrigues, J. Reis, A. J. M. Martins, **C. S. Monteiro**, S. O. Silva, C. M. R. Caridade, S. O. Tavares, and O. Frazão, "Cavity length dependence on strain sensitivity for Fabry–Perot sensors," Microw. Opt. Technol. Lett., vol. 64, no. 11, pp. 1951–1957, 2022, doi: 10.1002/mop.33405.

- D. Silva, **C. S. Monteiro**, S. O. Silva, O. Frazão, J. V. Pinto, M. Raposo, P. A. Ribeiro, and S. Sério, "Sputtering Deposition of TiO2 Thin Film Coatings for Fiber Optic Sensors," Photonics, vol. 9, no. 5, 2022, DOI: 10.3390/photonics9050342.

- R. Peixoto, J. P. S. Pires, **C. S. Monteiro**, M. Raposo, P. A. Ribeiro, S. O. Silva, O. Frazão, and J. M. V. P. Lopes, "Environmental Sensitivity of Fabry-Perot Microcavities Induced by Layered Graphene-Dielectric Hybrid Coatings," Physical Review Applied, vol. 16, no. 4, p. 44041, 2021, DOI: 10.1103/PhysRevApplied.16.044041.

- **C. S. Monteiro**, A. V. Rodrigues, D. Viveiros, C. Linhares, H. Mendes, S. O. Silva, P. V. S. Marques, S. M. O. Tavares, and O. Frazão, "Optical Fiber Sensors for Structural Monitoring in Power Transformers," Sensors, vol. 21, no. 18, p. 6127, 2021, DOI: 10.3390/s21186127.

- **C. S. Monteiro**, M. Raposo, P. A. Ribeiro, S. O. Silva, and O. Frazão, "Acoustic Optical Fiber Sensor Based on Graphene Oxide Membrane," Sensors, vol. 21, no. 7, p. 2336, 2021, DOI: 10.3390/s21072336.

- M. Raposo, C. Xavier, **C. Monteiro**, S. Silva, O. Frazão, P. Zagalo, and P. A. Ribeiro, "Thermally Stimulated Desorption Optical Fiber-Based Interrogation System: An Analysis of Graphene Oxide Layers' Stability," Photonics, vol. 8, no. 3, p. 70, 2021, DOI: 10.3390/photonics8030070.

- C. Linhares, J. Santo, R. Teixeira, C. Coutinho, S. Tavares, M. Pinto, J. Costa, H. Mendes, **C. Monteiro**, A. Rodrigues, and O. Frazão, "Magnetostriction Assessment with Strain Gauges and Fiber Bragg Gratings," EAI Endorsed Trans. Energy Web, vol. 7, no. 25, p. 161420, 2020, DOI: 10.4108/eai.13-7-2018.161420.

- **C. S. Monteiro**, M. Raposo, P. A. Ribeiro, S. O. Silva, and O. Frazão, "Tuning of Fiber Optic Surface Reflectivity through Graphene Oxide-Based Layer-by-Layer Film Coatings," Photonics, vol. 7, no. 1, p. 11, 2020, DOI: 10.3390/photonics7010011.

International and National Conferences

- **C. S. Monteiro**, M. Ferreira, J. P. Mendes, Luís C. C. Coelho, S. O. Silva, and O. Frazão, "Optical Fiber Flowmeter Based on a Michelson Interferometer,", in 11th European Optical Society Annual Meeting (EOSAM 2023), 2023, Dijon, France **(submitted)**.

- **C. S. Monteiro**, R. P. Herrera, S. O. Silva, and O. Frazão, "Short Pulse Generation in Erbium-Doped Fiber Lasers Using Graphene Oxide as a Saturable Absorber," in 11th International Conference on Photonics, Optics and Laser Technology (Photoptics), 2023, Lisbon, Portugal.

- **C. S. Monteiro**, S. O. Silva, and O. Frazão, "Microheater optical nanofibers: fabrication and optimization," in 4th Doctoral Congress in Engineering (DCE2021), 2021, Porto, Portugal.

- **C. S. Monteiro**, S. O. Silva, J. L. Santos, and O. Frazão, "Graphene oxide diaphragm for acoustic fiber sensing," in Optical Fiber Sensors Conference 2020 Special Edition, paper W4.45, DOI: 10.1364/OFS.2020.W4.45.

- **C. S. Monteiro**, D. Viveiros, C. Linhares, S. M. Tavares, H. Mendes, S. O. Silva, P. V. Marques, and O. Frazão, "3D prototyping of a fiber Bragg grating vibration sensor for power transformers," in Fourth International Conference on Applications of Optics and Photonics (AOP 2019), Oct. 2019, Vol. 11207, pp. 484-487, Lisbon, Portugal. DOI: 10.1117/12.2530084 (**"Best Student Poster Award"**)

- **C. S. Monteiro**, M. Raposo, P. Ribeiro, S. O. Silva, and O. Frazão, "Graphene oxide as a tunable platform for microsphere-based optical fiber sensors," in Fourth International Conference on Applications of Optics and Photonics (AOP 2019), Oct. 2019, Vol. 11207, pp. 199-203, Lisbon, Portugal. DOI: 10.1117/12.2527267.

- **C. S. Monteiro**, A. Vaz, D. Viveiros, C. C. Linhares, S. M. Tavares, H. Mendes, S. O. Silva, P. V. Marques, and O. Frazão, "FBG two-dimensional vibration sensor for power transformers," in Seventh European Workshop on Optical Fibre Sensors (EWOFS'2019), Aug. 2019, Vol. 11199, pp. 105-108, Limassol, Cyprus. DOI: 10.1117/12.2541132.

Chapter 2

Graphene and graphene-based materials

Graphene is a remarkable material composed of a flat monolayer of carbon atoms, packed in a two-dimensional honeycomb lattice [1]. Graphene was extensively studied at a theoretical level, but it was regarded as an 'academic' material since it was presumed to not exist. The experimental discovery of graphene triggered tremendous scientific and technological interest. Graphene presents exceptional properties making it attractive to a very wide number of applications. This chapter presents the general properties of graphene and graphene-based materials, followed by the most common production and characterization techniques.

2.1 Material Properties

2.1.1 Mechanical Properties

Mechanical properties of pristine graphene have been studied and experimentally verified [15]–[19]. Extensive work has been done to achieve similar properties using graphene oxide (GO) and reduced graphene oxide (rGO). The mechanical properties of GO and rGO samples vary due to the number of surface groups and defects resulting from the oxidation of other treatment processes [15]. The Young's modulus values are summarized in table 2.1.

Table 2.1: Young's modulus for graphene, GO and rGO.

Sample	Young's Modulus (GPa)	Reference
Graphene	1000.0 ± 100.0	[16]
Graphene oxide	207.6 ± 23.4	[17]
Reduced graphene oxide	250.0 ± 150.0	[18]

Other mechanical properties of graphene have been studied such as intrinsic tensile strength (130.5 GPa) and break strength (42 Nm^{-1}). A recent study also confirmed the low fracture on graphene sheets, with an attained fracture toughness of 4 ± 0.6 MPa $m^{1/2}$ [19].

2.1.2 Electrical Properties

Graphene is an electrically conductive material with ultrahigh electron mobility, weakly dependent on temperature. This implies that high mobility can be achieved at room temperature [20]. Carrier mobility of 2000 $cm^2/V{\cdot}s$ has been achieved for micromechanically deposited graphene

[21]. Further improved mobility values can be achieved by improving sample preparation, attaining mobilities of more than 25000 $cm^2/V{\cdot}s$. The substrate material and quality affect charge mobility. In reality, suspended and annealed graphene mobility can exceed 200000 $cm^2/V{\cdot}s$, the largest ever reported value for a semiconductor or a semimetal [22].

The fabrication of GO results in the disruption of the sp^2 bonding orbitals of graphene and in the addition of surface groups, inhibiting electrical conductivity and making GO an electrical insulator. Studies found that reducing GO can lead to an increase in conductivity with insulator-semiconductor-semimetal transitions [23]. Voiry *et al.* [24] achieved an increase of mobility up to 1000 $cm^2/V{\cdot}s$. Electrical properties of GO can also be tuned using different reduction techniques [25].

2.1.3 Optical Properties

Graphene is a transparent material in the visible range. For normal incident light, graphene transmittance and reflectance depend only on the fine-structure constant α. This constant, given by $\alpha = 2\pi e^2/hc \approx 1/137$, describes the coupling between light and relativistic electrons. In fact, for few-layer graphene, the transmittance is linearly dependent on the film thickness (for up to 5 layers) [21]. This property enables quality assessment using optical microscopy, as presented in figure 2.1.

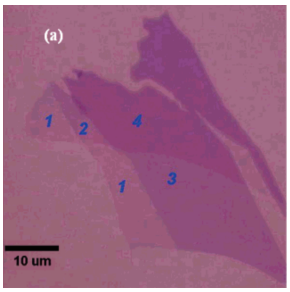

Figure 2.1: Optical microscope image of graphene with 1 to 4 layers. Image adapted from [26].

In the near- to the mid-infrared range, properties of graphene offer the possibility of studying the connection between the electrons, holes, and plasmons energy dispersion relation [21]. Additionally, studies suggest the possibility of attaining large gain in stimulation-emission phenomena in optical and infrared (IR) regions, allowing the fabrication of THz emitters based on graphene [27], [28].

2.2 Synthesis methods

2.2.1 Graphene

Graphene was first fabricated by micromechanical exfoliation of graphite [2]. This synthesis method still, to this day, gives higher purity samples. However, it is not feasible for large-scale production. Several different approaches have been developed to overcome this issue. Among them, the most common synthesis methods applied nowadays for graphene production are epitaxial growth, chemical vapor deposition, and liquid-phase exfoliation. The different production methods yield graphene samples with different levels of purity, size, and properties [29], as presented in figure 2.2.

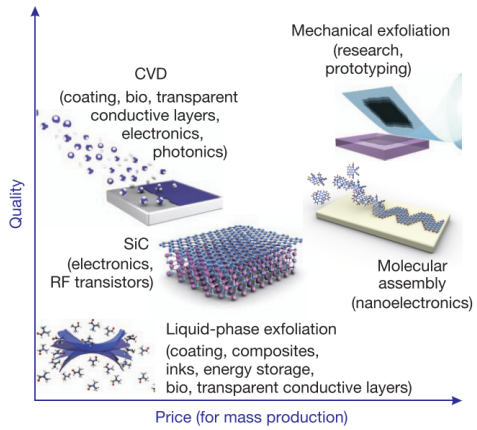

Figure 2.2: Cost and quality assessment for different graphene production techniques. Image adapted from [30].

Micromechanical Exfoliation

The first proposal of using this method for the production of graphene was introduced by Geim and Novoselov in 2004 [2]. In this method, a common adhesive tape is applied on a graphite sample, and, by peeling the adhesive tape a force is applied to the graphite, overcoming the inter-layer Van der Waals interactions, removing a sample of graphene [31]. To this day, micromechanical exfoliation yields better-quality graphene samples, with high structural and electronic quality. For that reason, this is the method of choice for fundamental research but is not feasible for large-scale applications due to the low throughput. The fabrication process is demonstrated in Figure 2.3.

Figure 2.3: Micromechanical exfoliation process. First, the adhesive tape is pressed on the highly oriented pyrolytic graphite sample. Then, the tape is peeled away, with a graphite layer attached. To form a graphene sample on a Si/SiO_2 substrate, the adhesive tape is pressed softly into the substrate releasing some graphene layers.

Epitaxial Growth on silicon carbide

This method involves the thermal treatment of silicon carbide (SiC), which results in the sublimation of the silicon atoms, reorganization, and graphitization of the carbon-enriched surface to form layers of graphene [31]. This method results in a lower quality graphene sample, with many defects and non-uniformities, and is not capable of producing single-layer graphene resulting in a quasi-2D structure. Another obstacle of this production method is the difficulty of transferring graphene samples to other substrates due to strong binding between the graphene layer and the SiC substrate [32].

Chemical Vapor Deposition

Chemical vapor deposition (CVD) is a process in which a material in the vapor phase is deposited on a substrate surface by thermal decomposition of chemicals [33]. For graphene synthesis, the most widely used substrate materials are transition metals such as copper (Cu) or nickel (Ni) [34]. In the CVD process, a hydrocarbon is fed into the reactor and passes through the hot zone, where the substrate is located. In this area, the hydrocarbon precursors decompose to carbon radicals at the metallic substrate, forming single-layer and few-layer graphene. The graphene synthesis process in a Cu substrate is demonstrated in figure 2.4.

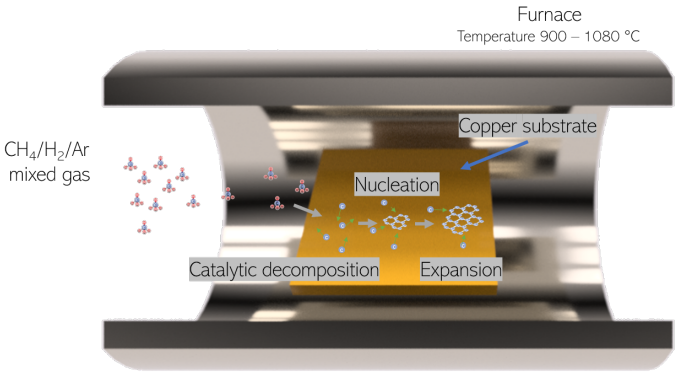

Figure 2.4: Synthesis of graphene in a copper substrate through CVD.

The substrate material works as a catalyst, lowering the reaction energy barrier, and determines the deposition mechanism, influencing the quality of the resultant graphene sample [35]. This method can achieve high throughput, with the advantage of enabling the transference to other substrates.

Graphene produced by CVD in Cu substrates has been successfully transferred into optical fibers. The transfer process is shown in figure 3.1. A multi- or few-layered graphene in a Cu substrate is immersed in ferric chloride ($FeCl_3$) solution. This solution will etch the copper foil, detaching the graphene film. After chemical etching the Cu foil, the graphene film is moved to deionized water to remove residual ions. After rinsing, the graphene film is deposited on the optical fiber surface through the Van der Waals force.

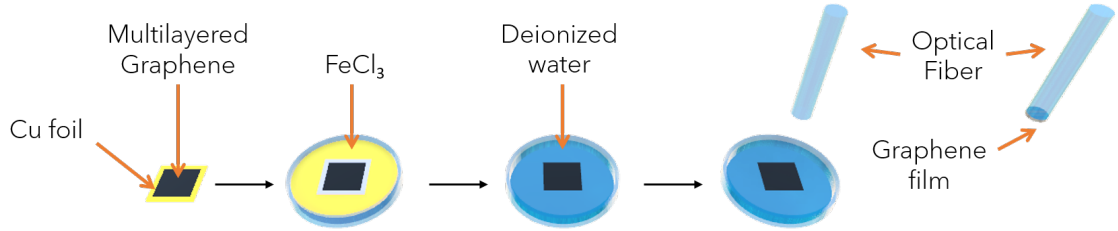

Figure 2.5: Transference of CVD-grown graphene film to optical fibers.

Liquid-phase exfoliation

This technique involves ultrasonication of a dispersion of graphite flakes in an organic solvent - typically dimethylformamide (DMF) or N-Methyl-2-pyrrolidone (NMP). The exposure of the

dispersion to high-intensity ultrasounds leads to the separation of graphitic layers, creating single, multi, and few-layer graphene. The single-layer graphene can be identified using microscopic or spectroscopic techniques [32]. Even though this is a fast production technique, the throughput is relatively low.

2.2.2 Graphene Oxide

The first synthesis methods of graphene oxide were proposed by Brodie [36] and Staudenmaier [37], and later improved by Hummers and Offeman [38]. Each synthesis method relies on the oxidation of graphite to produce graphene oxide [15]. In order to make the technique safer, Hummers and Offeman made several improvements to the original two techniques. Due to the safer and more scalable nature of Hummer's method, this is generally used for GO synthesis nowadays. Several methods have been proposed in the literature in the last few years to improve or modify this method.

In general, a carbon source is placed on a protonated solvent (sulfuric acid, phosphoric acid, or a combination of the two) and, then, a strong oxidizing agent is added. After a dilution process, the resulting mixture is commonly treated with hydrogen peroxide (H_2O_2) to remove metal ions from the oxidizer. After separating the resulting solids, they are treated with a diluted solution of hydrochloric acid (HCl). This treatment helps to further remove any metal species. After, the solution is washed and centrifuged. This step is repeated until the pH of the solution is neutral.

Recently, an improved Hummer's method has been proposed by Marcano et al. [39]. The proposed method does not generate toxic gases and the temperature of the reactions are easily controlled and results in GO powders with a higher degree of oxidation.

2.2.3 Reduced Graphene Oxide

The presence of oxygen functional groups on GO significantly reduces electric conductivity in comparison to pristine graphene. For some applications, it is needed to reduce some oxygen-containing functional groups. The resultant material is called partially reduced graphene oxide (rGO). Reduced GO can be synthesized using thermal, chemical, or electrochemical reduction of exfoliated graphene oxide [40]. The different methods result in rGO with different morphology, electrical properties, etc, and have different advantages in scalability, produced chemical waste, and energy usage.

Thermal reduction of GO can be achieved by thermal annealing GO in an oxygen-free environment at high temperatures (around 1000 °C). This method leads to the decomposition of the GO oxygen groups into CO and CO_2 gases. The fast evolution of the gases exfoliates individual GO nanosheets [15]. This method results in no chemical hazards but is very energy intensive. Due to the high temperatures, this method cannot be applied in rGO deposition in polymeric substrates.

Reduction of GO can also be achieved via chemical processes. The chemical reduction can be accomplished by adding reducing agents - typically hydrazine (N_2H_4) or derivatives - to GO. This method results in rGO with higher hydrophobicity [32]. This is a highly hazardous process due to the chemical products, toxicity, and explosive nature. Extensive work has been done to reduce production risks and to introduce "green" reduction agents [41]. Photocatalyzed reactions can also be used for rGO production, using UV light in the presence of a TiO_2 catalyst.

2.2.4 Comparison

The comparison between graphene synthesized using the different techniques is presented in table 2.2.

Table 2.2: Comparison between different preparation methods of graphene.

	Mechanical Exfoliation	Epitaxial Growth	CVD	GO	rGO
Quality of synthesized graphene	Very high	Very high	High	NA	NA
Maximum electron mobility ($cm^2/V{\cdot}s$)	200 000 [42]	11 000 [43]	350 000 [44]	>∼1 [24]	1 000 [24]
Scalability	Not scalable	Scalable	Scalable	Scalable	Scalable
Feasibility of SLG production	Yes	Yes [45]	Yes	No	No
Advantages	High crystallinity with great uniformity	High quality	Suitable for low-cost and large-area production; easy to transfer to other substrates	Suitable for bulk applications	Suitable for bulk applications
Disadvantages	Small sample size; shape and layer number not uniform	Expensive substrate; difficult to transfer to different substrates	Metal catalysts and high temperature needed	Poorer material properties	Reduction methods can be chemically hazardous; not possible to totally reduce GO

2.3 Characterization Techniques

The quality and properties of graphene and graphene-based materials are highly dependent on the quality of the fabrication method. In order to locate, recognize and characterize samples several techniques have been proposed [21]. In this section, the most relevant techniques will be discussed for graphene and GO characterization.

Optical Microscopy

Single to few-layered graphene is a transparent material in the visible range, with linearly dependent transmittance for normal incident light. This property allows graphene to be located and characterized in terms of the number of layers using optical microscopy, as shown in figure 2.1. Several techniques have been pursued to enhance optical contrast [46].

Atomic Force Microscopy

In atomic force microscopy (AFM), a cantilever is scanned across a sample surface and, due to changes in the heterogeneity of the surface, it will change vibration amplitude and frequency [47]. This technique is capable of measuring film thickness and surface roughness and can be used for both graphene and graphene-based samples. An example of topography and surface roughness is presented in figure 2.6.

Raman Spectroscopy

Raman spectroscopy is a widely used technique that involves the absorption (Stokes process) and emission (anti-Stokes process) of phonons [47]. This is a non-destructive technique, sensitive and fast, that enables the investigation of the structure and quality of carbon-based materials. Typically, the Raman spectrum of graphene (see figure 2.7a) presents three major peaks: the D peak (at 1320–1350 cm^{-1}), G peak (at 1580–1605 cm^{-1}), and 2D or sometimes labeled G' peak (at 2640–2680 cm^{-1}). By understanding the nature of each peak, is possible to determine the

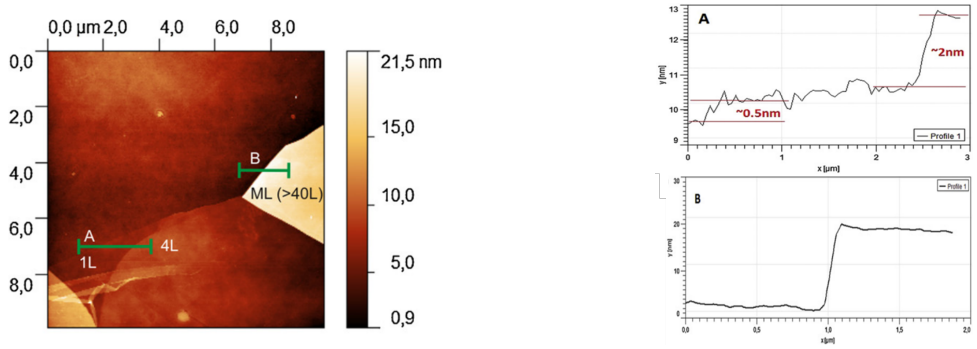

(a) (b)

Figure 2.6: An example of AFM (a) topographic image and (b) respective profiles of a graphene sample. Images adapted from [48].

presence of defects and impurities, and the number of layers. The presence of defects can be assessed by the presence and relative intensity of the D peak. By analyzing the position and width of the 2D peak it is possible to determine the number of layers present in the sample, as can be seen in figure 2.7b.

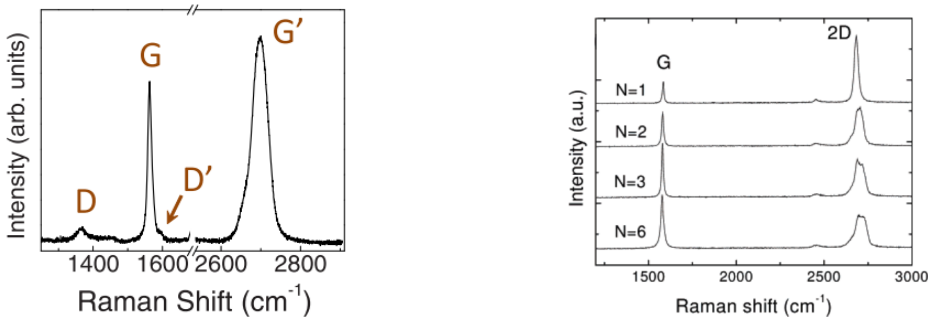

(a) (b)

Figure 2.7: (a) Typical Raman spectrum of graphene, image adapted from [49]; (b) Variation of Raman spectrum with the different number of layers, image adapted from [50].

SEM and TEM

Electron microscopy can be used for investigating morphology, structure, and layer information about carbon-based samples [47]. Scanning electron microscopy (SEM) and transmission electron microscopy (TEM) are the most explored techniques. Sample images of SEM and TEM of graphene are presented in figure 2.8.

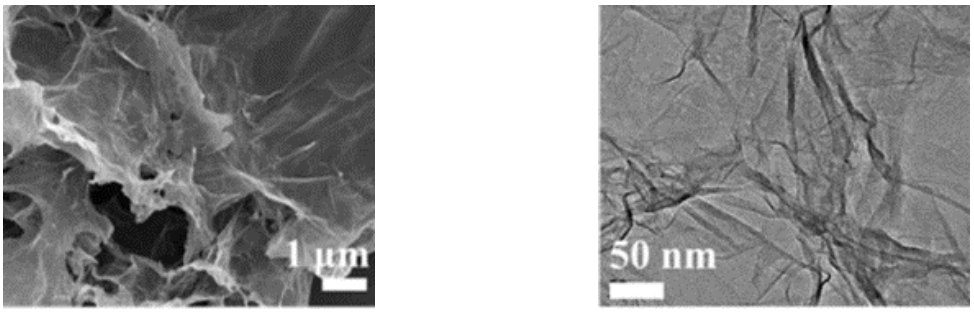

(a) (b)

Figure 2.8: (a) SEM and (b) TEM image of a graphene sample. Adapted from [51].

Other Techniques

Apart from the aforementioned characterization techniques, different graphene and graphene-based material properties can be assessed using other techniques. Maocong Hu *et al.* [47], summarized possible characterization techniques presented in table 2.3.

Table 2.3: Characterization techniques for graphene and graphene-based materials.

Technique	Characterization
X-ray Photoelectron Spectroscopy (XPS)	elemental composition, chemical state, and electronic state of the elements on the surface
Fourier Transform Infrared Spectroscopy (FTIR)	residual functional groups of oxidized samples
X-ray diffraction (XRD) and X-ray absorption near edge spectroscopy (XANES)	structure, oxidation state, and local symmetry
Ultraviolet-visible spectroscopy (UV-vis)	reduction of GO
X-ray fluorescence (XRF) and inductively coupled plasma mass spectroscopy (ICP-MS)	residual metal concentration

2.4 Concluding remarks

This chapter provides an overview of the properties of graphene and graphene-based materials, including GO and rGO. A comparison between the mechanical and electrical properties of these materials is presented. Additionally, the main synthesis methods for graphene, GO and rGO are described and compared based on sample quality, electrical properties, scalability, and advantages and disadvantages posed by each method. Furthermore, a brief overview is provided of the main techniques used for material characterization.

Chapter 3

Graphene oxide coated optical fibers using layer-by-layer technique

Optical fiber has revolutionized the telecommunication industry, outperforming well-established technologies due to the low propagation loss and attenuation, higher bandwidth, multiplexing capabilities, and lower cost. Adding to the aforementioned properties, the optical fiber is also compact and lightweight, flexible, resistant to harsh environments, and immune to electromagnetic interference [52]. These unique characteristics can be explored in different sensing applications, originating much research interest in the development of optical fiber sensors [53].

Optical fiber sensitivity to chemical, biological, or physical parameters can be promoted or enhanced by the use of different coating materials [54], [55]. In particular, graphene and graphene-based materials have attracted much attention in the last years in optical fiber sensing. Graphene synthesis methods have been extensively researched in the last years, and it is now possible to produce high-quality graphene sheets, with relatively large dimensions. The main synthesis methods are optimized for planar substrates. However, optical fiber poses some challenges due to its cylindrical shape and compact dimensions. One procedure to overcome this restriction is by using an important property of graphene: the ultrastrong adhesion [56]. This property allows a graphene sheet produced by chemical vapor deposition to be easily transferred to the optical fiber surface through the Van der Waals force. Due to the outstanding properties of graphene, several sensing methods have surfaced in the last few years.

High-purity pristine graphene can be produced by several synthesis methods as previously mentioned, but these are all time-consuming, expensive, and not suitable for mass production. Graphene-based materials can be a good compromise between the great properties exhibited by pristine graphene, with production methods that allow higher throughput. Reduced GO exhibits great properties, with a higher resemblance to pristine graphene when compared to GO. The main advantage of using rGO is the high throughput production methods, which allow production at a lower cost. Graphene oxide demonstrates poorer electrical, mechanical, and optical properties, but introduces an interesting property: strong hydrophilicity. This feature is due to the presence of hydroxyl and epoxide functional in basal planes as well as carbonyl and carboxyl groups at the GO sheet edges [57]. The higher solubility warrants the possibility of exfoliating GO in many organic solvents including water. Another feature enabled by the polar oxygen functional groups of GO is the functionalization of the surface. In the following chapter, graphene oxide deposition in optical fibers using the layer-by-layer technique is studied and optimized.

3.1 Layer-by-layer technique

Layer-by-layer (LbL) technique is a thin-film fabrication technique that relies on the existence of multiple intermolecular interactions between polyelectrolytes with positive (polycations) and negative (polyanions) charge to assemble a multilayered structure. Electrostatic interaction between the oppositely charged polyelectrolytes is the main driven force of the LbL technique, but other intermolecular interactions (e.g. Van der Waals, hydrogen bonding and covalent bonding) may occur [58], [59]. It is worth noting that the LbL technique offers a significant advantage over other deposition methods, as it enables the deposition of thin films onto substrates with highly complex geometries, making it a particularly useful technique for coating optical fibers.

The deposition process starts by removing biological residues using a solution composed of sulfuric acid (H_2SO_4) and hydrogen peroxide (H_2O_2). Further information concerning the experimental procedure can be found in Appendix A. This procedure also hydroxylates the surface of the fiber, promoting the adsorption of positively charged polyelectrolytes. Afterward, the air-dried substrates are immersed in polyethylenimine (PEI, Sigma-Aldrich P3143) a polycationic solution, with a concentration of 2×10^{-4} M, for around 60 seconds. The excess of polyelectrolytes that were not adsorbed by the fiber surface is removed by rinsing the optical fibers in Milli-Q water for around 20 seconds. After drying, the substrates are immersed in the polyanionic solution of GO (Sigma-Aldrich, 777676), of the same concentration as the PEI solution. This process was repeated to build the required PEI/GO bilayers. The drying procedure can be accomplished by air-drying the substrates for a period of 2 minutes or using a nitrogen (N) flow. The LbL procedure is presented in Figure 3.1.

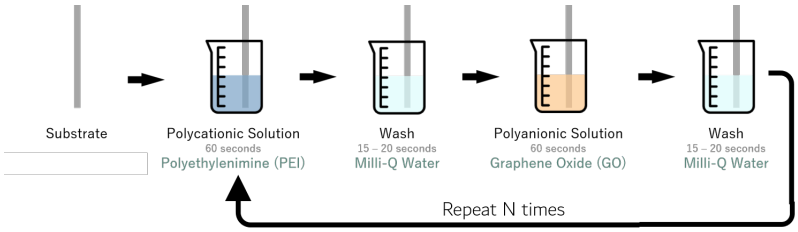

Figure 3.1: Layer-by-layer deposition technique.

3.1.1 Graphene oxide adsorption kinetics

Adsorption kinetics is related to the rate of retention or release of a water-dispersed solute in an adsorbent [60]. Adsorption kinetics can be described by the Langmuir kinetics, widely used for the description of the quantity of adsorbed substance on a substrate (or adsorbent) and its equilibrium concentration in an aqueous solution. The Langmuir kinetics can be approximated by a pseudo-first-order rate equation, commonly called the Lagergren equation [61]. This equation relates the amount of adsorbate at a given time and the rate of adsorption by the following expression:

$$\frac{dq}{dt} = k_1(q_e - q) \tag{3.1}$$

where q and q_e are respectively the amounts of adsorbed adsorbate at time t and at equilibrium with units g/kg, and k_1 is the first-order rate constant with units min^{-1}. By solving the first-order linear differential equation, the total adsorbed amount can be calculated by:

$$q(t) = q_e\left(1 - exp\left(-\frac{t}{\tau}\right)\right) \tag{3.2}$$

where τ is the characteristic time of adsorption.

In order to study adsorption kinetics in optical fibers, 5 cleaved optical fibers coated with PEI were placed for 15 hours in a GO solution. The reflectivity of the cleaved fibers, which is directly related to the total amount of adsorbed adsorbate at a given time, was measured in intervals of 5 minutes. The reflectivity of the surfaces of the fibers was measured using an experimental setup comprised of a broadband source - with a central wavelength of 1550 nm and a 100 nm bandwidth - an optical circulator, an optical switch, and an optical spectrum analyzer (OSA - Advantest Q384) with a resolution of 0.05 nm. Apart from the set of fibers tested, a reference fiber was added to eliminate the influence of optical power fluctuations at the source. The experimental setup is presented in Figure 3.2.

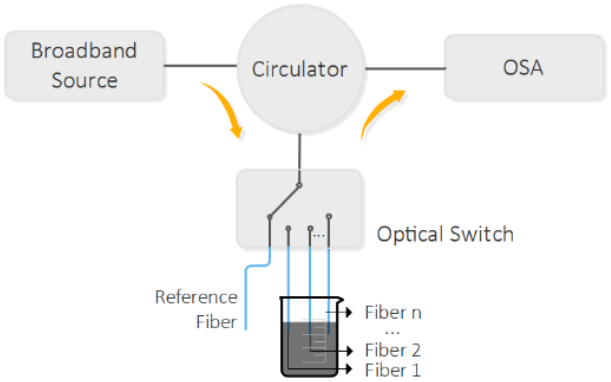

Figure 3.2: GO adsorption kinetics experimental setup for the reflected spectrum acquisition composed by a broadband source, an optical circulator, an optical switch that allows attaining multiple spectra almost simultaneously, and an OSA.

Adsorption kinetics was studied under two different conditions: without previous GO layers, meaning that the fibers had only a layer of PEI, and with 10 PEI/GO layers. In the two situations, the reflectivity curve is in accordance with the adsorption kinetics given by the equation 3.2. The experimental averaged results are presented in Figure 3.3.

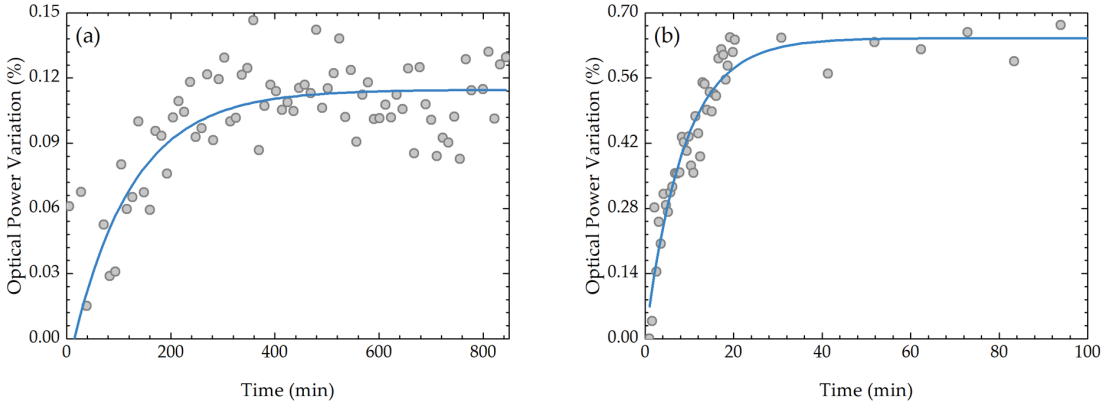

Figure 3.3: In-situ adsorption kinetics of a layer of graphene oxide onto (a) an optical fiber coated with PEI and (b) $(PEI/GO)_{10}$/PEI LbL film already adsorbed on the optical fiber.

The fitting parameters are summarized in table 3.1. The attained values reveal that the adsorption characteristic times of the GO layer is 120 ± 20 minutes for the first layer and 10 ± 3 minutes for the tenth layer. This result is in accordance with the literature, namely, for the case of kinetics

curves of polyaniline, a conducting polyelectrolyte, whose adsorption characteristic time decreases strongly as the number of bilayers already adsorbed increases [62]. The adsorbed amount is seen to increase with the number of adsorbed bilayers due to an increase of surface roughness of the LbL film as demonstrated by Ferreira *et al* [63] and, therefore, also demonstrating that one cannot expect uniformity of LbL mounted GO films.

Table 3.1: Fitting parameters of GO adsorption kinetics. R is the correlation coefficient.

Parameter	1^{st} GO layer	10^{th} GO layer
q_e (%)	0.0013±0.0005	0.0055±0.0005
τ (min)	120±20	10± 3
R	0.87	0.93

3.1.2 Bilayer growth

The PEI/GO bilayer growth study in optical fibers was accomplished by following the above-mentioned LbL method, with an immersion time on each dispersion of 5 minutes. The coating process was carried out in all five samples simultaneously to minimize experimental errors. The reflected light from the cleaved fibers was measured using the experimental setup presented in Figure 3.2. The mean variation of surface reflectivity with the increased number of bilayers is presented in Figure 3.4, where a consistent increase of the reflected optical power with bilayer number can be observed. The increase in surface reflectivity presented some dispersion due to surface roughness variations that resulted from the cleaving process and the variability of film roughness. These results also corroborate the applicability of the LbL technique to provide controlled thickness GO coatings onto an optical fiber cross-section.

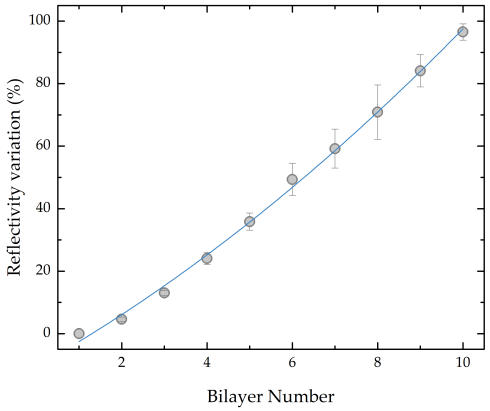

Figure 3.4: Reflectivity variation with the number of PEI/GO bilayers.

3.1.3 Coating characterization with Raman spectroscopy

Raman spectroscopy is a characterization technique that allows probing the chemical composition of materials. This is a common characterization technique used on graphene or graphene-based samples, as it is fast, non-destructible, and easy to interpret. In this work, the Raman spectrum was

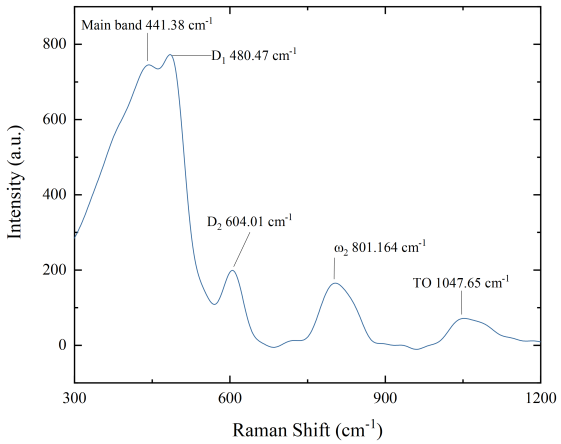

Figure 3.5: Raman spectrum of an uncoated single mode fiber, using an excitation wavelength of 532 nm, with 10-second integration time.

attained using a confocal spectrometer Raman InViaTM Qontor®, with a cooled CCD at -70 °C, with a spectral resolution better than 2 cm^{-1} for the different possible excitation wavelengths at the visible range at 532 and 633 nm and in the NIR region at 785 nm.

In order to eliminate the influence of the fused silica in the Raman spectra, the spectrum of an uncoated fiber was first attained as can be observed in Figure 3.5. The attained spectrum was smoothed using an FFT filter to remove high-frequency noise and, afterward, the baseline was calculated and removed. The results are in accordance with the literature for fused silica.

The Raman spectra of four different regions of a sample with 6 PEI/GO layers are presented in Figure 3.6a. The spectra contain four peaks corresponding to the D, G, 2D, and G+D bands. The D band, that is located at 1320 - 1350 cm^{-1}, is attributed to defects and structural disorder, and the G band, located at 1580 - 1605 cm^{-1}, is associated with the first order scattering of the E_{2g} phonon of sp^2 carbon atoms [47]. The additional bands - D', 2D, and D+G - appear due to defects on the graphitic structure [64]. Additionally, the ratio of the intensity of the D and G bands gives qualitative information about structural defects, attributed to the presence of many functional groups formed during the oxidation of graphite.

It can be observed that the intensity of the Raman spectra varies with the location of the sample. This can be attributed to the film roughness observed on the surface of the fiber, leading to a variation in the efficiency of the light collection by the spectrometer. Another aspect that can cause this effect is the presence of multilayered GO with a variable number of layers in different positions of the fiber.

Additional samples with a number of PEI/GO layers between 10 and 40 and a sample containing only GO were also evaluated through Raman spectroscopy, shown in Figure 3.6b. Considering the dispersion of the intensity on different fiber positions, the Raman spectra were attained in five positions for each sample. It can be observed that the peak corresponding to the D band changes only in intensity, meaning that no significant variations in the defects and structural disorder were observed between the samples. However, the peak corresponding to the G band exhibits a slight shift suggesting a variation in the crystallinity of the sample [65].

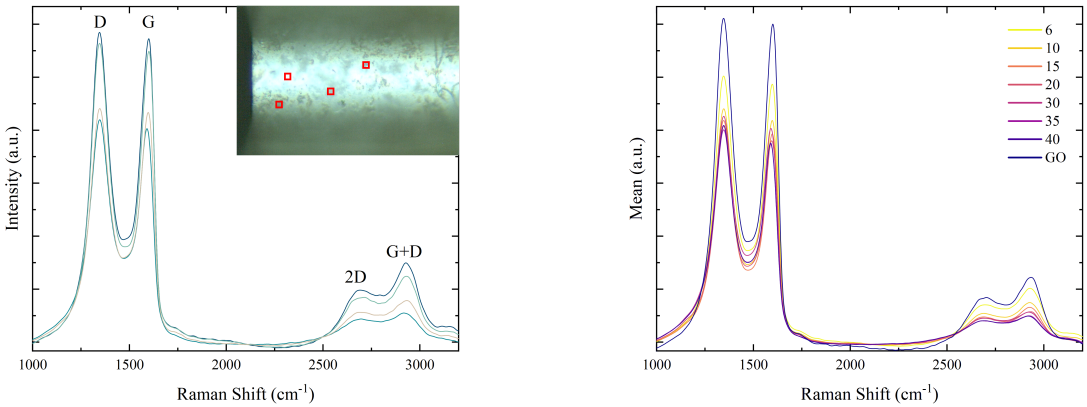

Figure 3.6: Raman spectra of (a) a 6-layer PEI/GO coated fiber with corresponding peak bands annotated, for an excitation wavelength of 532 nm. The D band is located at 1345 cm^{-1} and the G band at 1600 cm^{-1}, approximately. A microscope photograph of the fiber surface and corresponding regions of interest are presented in the inset; (b) samples with different numbers of PEI/GO layers and a GO-coated fiber.

3.2 Graphene oxide coated hollow microspheres

Hollow core microspheres are small spherical structures that can be placed at the tip of optical fibers. The working principle can be explained by the Fabry-Perot interferometry. In recent years, these interferometric configurations have been proposed in the literature for several sensing applications such as strain, lateral load or temperature [66]–[68]. Hollow microspheres can be fabricated at the tip of an optical fiber forming a structure that can be approximated to a three-wave or cascaded Fabry-Perot interferometer as presented in Figure 3.7.

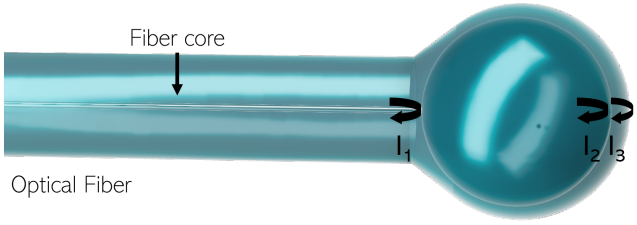

Figure 3.7: Schematic image of a hollow microsphere at the tip of an optical fiber. The dominant reflected waves are defined as $I_{1,2,3}$.

Considering that the reflectivity at each air/silica interface is very low (less than 4%), the hollow microsphere can be approximated to a three-mirror Fabry-Perot interferometer as higher-order interference can be neglected. The reflected intensity signal can be approximated by [69]:

$$I_r(\lambda) = I_1 + I_2 + I_3 - 2\sqrt{I_1 I_2}cos(\phi_1) - 2\sqrt{I_2 I_3}cos(\phi_2) + 2\sqrt{I_1 I_3}cos(\phi_1 + \phi_2) \tag{3.3}$$

where

$$\phi_1 = \frac{4\pi}{\lambda} n_{air} d \quad \text{and} \quad \phi_2 = \frac{4\pi}{\lambda} n_{microsphere} \delta \tag{3.4}$$

with λ is the light's wavelength, n_{air} and $n_{microsphere}$ are the refractive index of air and fused silica respectively, d is the air cavity length, δ is the microsphere thickness, and I_n is the total reflected intensity at each interface.

3.2.1 Microsphere fabrication

Hollow microsphere fabrication was achieved using fusion splicing technique as previously demonstrated in literature [67] and is schematized in Figure 3.8a. In the first step, a cleaved optical fiber is fusion spliced with a fused silica capillary. The electric arc must be applied with care to avoid the capillary's collapse, which leads to higher optical losses at the interface between the capillary and the optical fiber. To avoid this, the fusion splicer is set to a manual mode, and the electric arc is performed far from the capillary with lower power. Afterward, the capillary is cleaved to a determined length, controlled by a stereo microscope, and two consecutive electric arcs with higher power are performed at the tip of the capillary forming a microsphere. The final result is presented in Figure 3.8b.

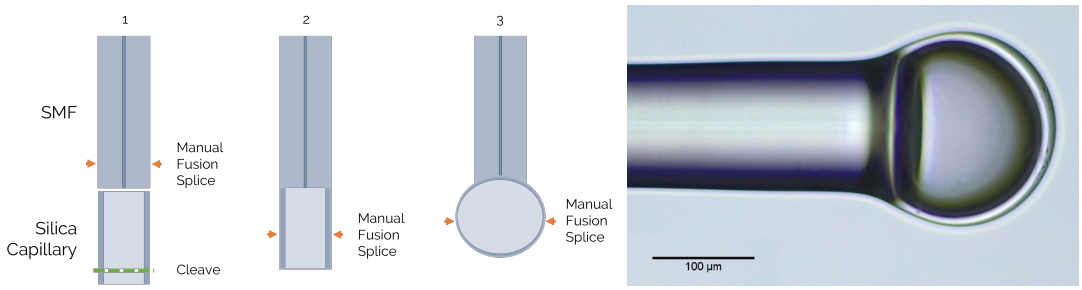

Figure 3.8: (a) Microsphere fabrication process; (b) Microscope image of the fabricated hollow microsphere.

3.2.2 Experimental Results

The hollow microsphere's reflected spectrum, shown in Figure 3.9b, was acquired using a broadband optical source, an optical circulator, and an optical spectrum analyzer (Advantest Q8384) with 0.1 nm resolution, as presented in Figure 3.9a.

The reflected spectrum was fitted to equation 3.3, to determine the length of the two optical cavities assuming a refractive index of 1 in the first cavity and a refractive index of 1.4446 in the fused silica cavity. The fitted equation achieved an R^2 = 0.982, indicating good accordance between the theoretical model and the experimental results as presented in Figure 3.10a. From the curve fitting an air cavity length of 125 μm and a silica thickness of 36 μm were determined. Cavity length can also be estimated by calculating the fast Fourier transform (FFT) of the reflected spectrum. Considering that the spatial frequency is related to the cavity length [70], the FFT magnitude signal can be plotted with respect to the cavity length calculated for a refractive index equal to 1 as presented in Figure 3.10b. The two major peaks presented in the FFT signal are related to the lengths of the air and air+silica cavities. The first peak is related to the air cavity (d) at approximately 120 μm and the second peak is related to the cavity formed by air and silica (d_{total}), at approximately 180 µm. From the two values, it is possible to estimate silica wall thickness (δ) considering that $d_{total} \approx n_{silica}\delta + n_{air}d$ and assuming that the refractive index of the silica cavity is 1.4446, then $\delta \approx 41.5\mu$m, a difference of 15% comparing to the curve fitting

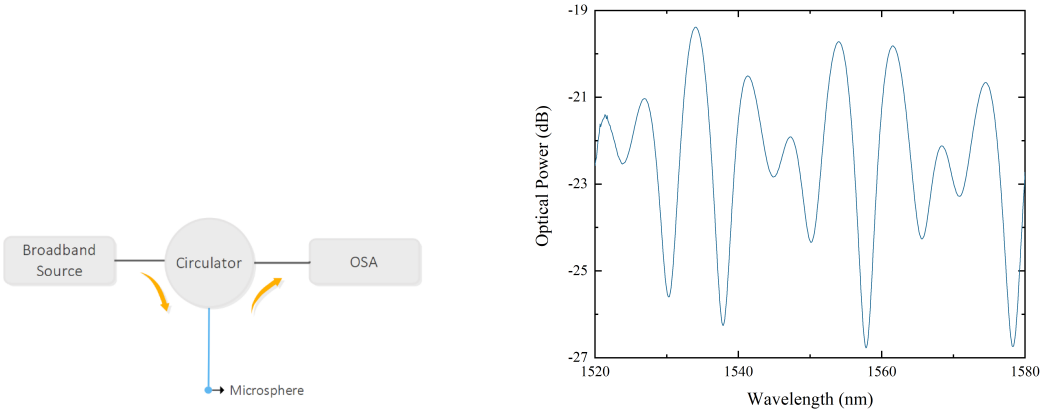

(a) (b)

Figure 3.9: (a) Experimental setup for spectrum acquisition in a reflection scheme; (b) Reflected spectrum of the hollow microsphere.

method. The peak corresponding to the cavity composed only of silica is not visible in the FFT signal due to the low resolution, provided by the short bandwidth of the optical source.

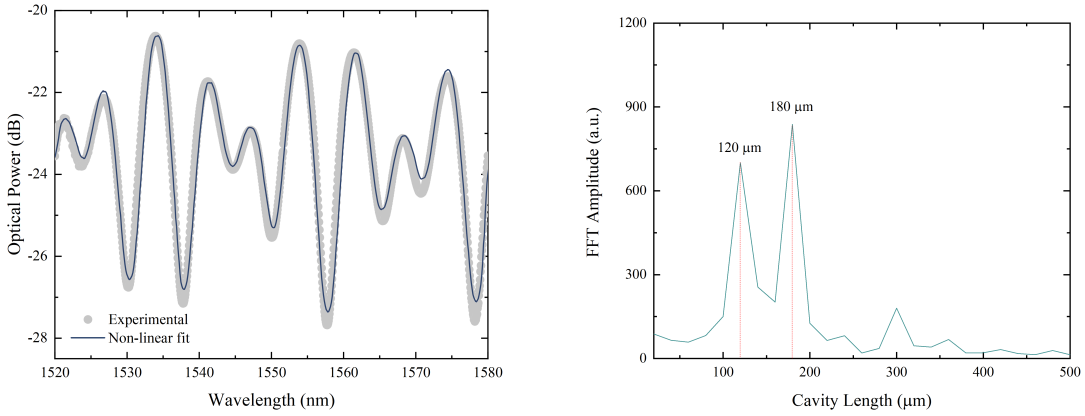

(a) (b)

Figure 3.10: (a) Experimental reflected spectrum (in dots) and theoretical curve fitting (line); (b) FFT of the reflected spectrum.

3.2.2.1 Bilayer Growth

Bilayer deposition of PEI/GO was carried out in the hollow microsphere replicating the LbL method as previously mentioned. Considering the complexity of the reflected spectra, the influence of the PEI/GO coating was studied using the FFT of the reflected signal. As shown in Figure 3.10b, two dominant peaks are present in the FFT signal. The first peak corresponds to the air cavity and is expected to remain constant during the coating process as no modifications are being applied in this cavity. The second peak, corresponding to the air plus silica cavity, can vary in amplitude due to variations in the outer surface reflectivity. In Figure 3.11, the FFT signal for the different bilayer number is presented. As expected, the magnitude of peak 1 remains constant during the process and the amplitude of peak 2 varies during the coating process.

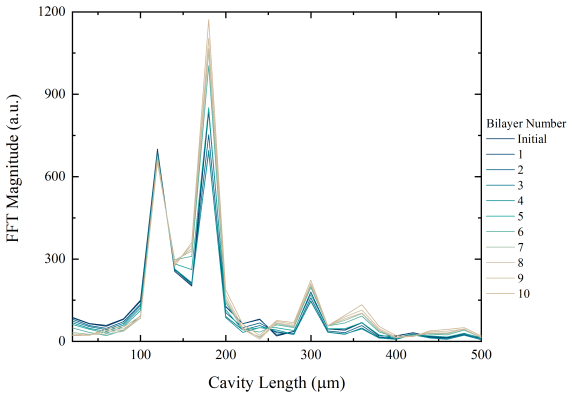

Figure 3.11: FFT of the reflected spectrum at each bilayer number.

The signal component that corresponds to the air plus silica cavity can be filtered from the total reflected spectrum by applying band-pass filters centered at the corresponding frequency peak. Analyzing the filtered signal, the influence of PEI/GO coating on the reflectivity of the outer surface can be attained. In Figure 3.12a, the filtered signal associated with the second peak from the FFT signal at each bilayer number is presented. The PEI/GO coating leads to a linear wavelength shift of 254 ± 7 pm/bilayer number, as shown in Figure 3.12b. An amplitude variation on the filtered signal following a similar trend as the FFT peak value, was also attained presenting a maximum increase of around 4 dB when compared to the filtered signal from the uncoated fiber.

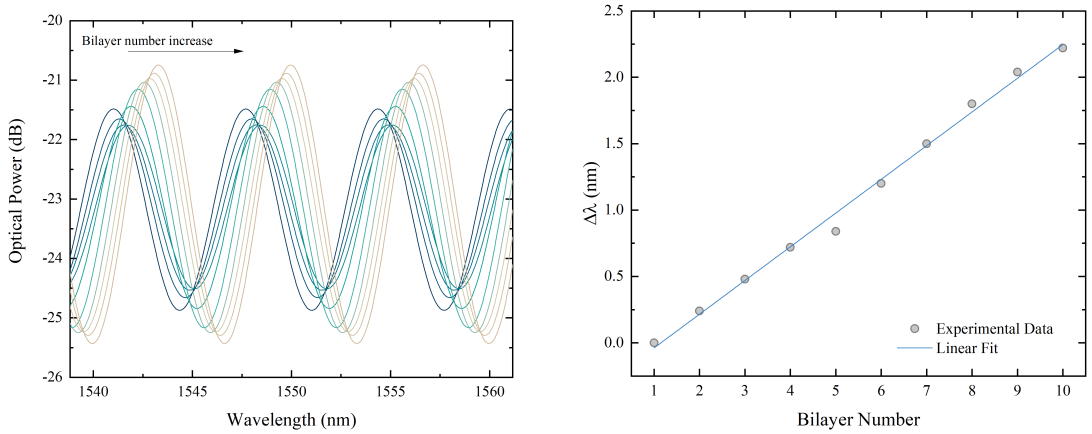

Figure 3.12: (a) The signal from the reflected spectra resultant from filtering the component associated with the second peak of the FFT and (b) the corresponding wavelength shift.

From equation 3.3, one has $I(\lambda) \propto cos(\frac{4\pi}{\lambda}(n_{air}d + n_{microsphere}\delta))$. Assuming that the component $n_{air}d$ is constant during the coating process and that thickness variations of δ can be neglected, the signal is only dependent on refractive index variations of the outer surface. Therefore, the wavelength shift is caused by a variation of the effective refractive index due to PEI/GO coating.

3.2.2.2 PEI Influence

The influence of the polycation in the reflected signal was studied by comparing the spectrum before and after adding the PEI polycationic layer. The reflected spectra, presented in Figures 3.13a

and 3.13b, show no significant variations between before and after the deposition of the additional PEI layer.

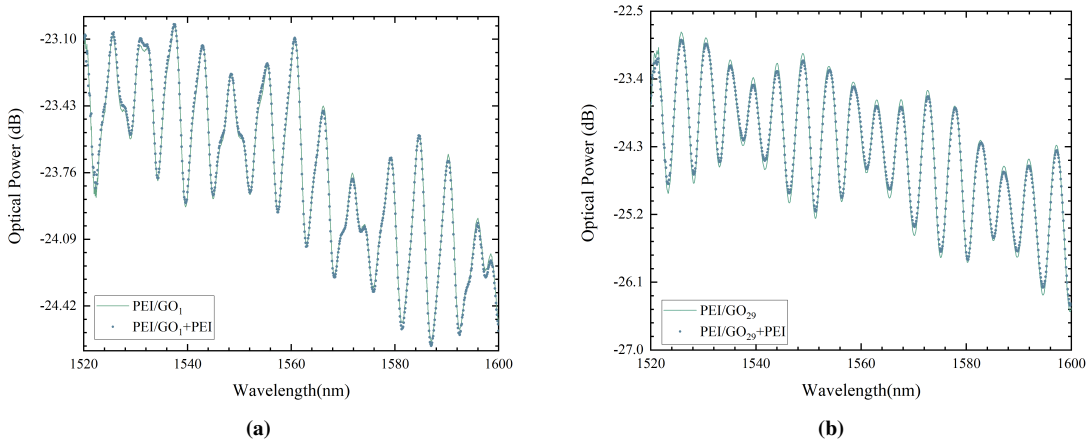

Figure 3.13: Reflected spectrum before and after deposition of the PEI layer after (a) 1 and (b) 29 PEI/GO layers, respectively.

3.2.2.3 Coating stability

To study the stability of the coating, a microsphere was coated with 30 PEI/GO layers, and the reflected spectrum immediately after the coating process and after 24 hours were compared as shown in Figure 3.14. The sensor was maintained in a real-world setting, with variable and not controlled temperature and humidity conditions. It was observed that the main characteristics of the reflected spectrum, such as visibility and phase, were not altered but a decrease of 2.3 dB on the mean optical power and a decrease of SNR in the signal was observed.

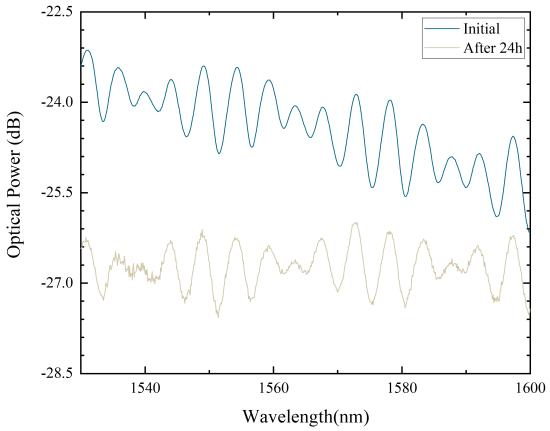

Figure 3.14: Reflected spectrum of a microsphere coated with 30 PEI/GO layers, immediately after the coating process and after 24 hours of being exposed to normal environmental conditions.

3.3 Concluding Remarks

In this chapter, the study of the deposition of PEI/GO layers using the LbL technique on optical fibers was presented. It was observed an increase in reflectivity with the number of layers, for up to ten PEI/GO bilayers. The deposition technique was subsequently applied in a fiber interferometric structure based on Fabry-Perot interferometry, which allowed the study of wavelength-dependent properties. It was observed a wavelength shift of the spectral component that interacts with the film linearly dependent on the number of PEI/GO layers. This indicates that it is possible to fine-tune the spectral properties of interferometric sensors with the PEI/GO film deposition, particularly in complex geometries, by using the LbL technique.

The adsorption kinetics of GO was also studied using an *in-situ* scheme by measuring the reflectivity of five cleaved optical fibers in real-time. The cleaved fibers were coated with PEI and were placed on a GO solution for 15 hours. Afterward, the fibers were coated with 10 PEI/GO layers and were, again, placed on the GO solution for an additional 15-hour period. The evolution of the reflectivity followed the typical Langmuir kinetics, demonstrating that this method can be applied as an *in-situ* adsorption kinetics monitoring system, capable of being applied to other molecules.

Chapter 4

Sensing applications of optical fibers coated with graphene-based materials

A number of studies have been conducted since the discovery of graphene in order to explore its outstanding mechanical, electrical, and optical properties. In the last few years, these attributes have become increasingly useful for a variety of practical applications. There are a number of remarkable features associated with graphene, which could prove beneficial or even lead to the creation of new solutions in the field of photonics and optoelectronics.

This chapter presents a brief review of the graphene-, GO- and, rGO-based optical fiber sensors with a description of the main sensing mechanisms and different applications. Afterwards, two new optical sensors based on GO are presented. The first sensor is an all-silica Fabry-Perot (FP) with a cavity coated with PEI/GO layers for refractive index (RI) sensing. The influence of the number of PEI/GO layers on the performance of the sensor was studied both theoretically and experimentally. It was observed that the sensitivity of the sensor can be tuned by changing the number of layers, creating a tunable platform for RI sensing. The second developed sensor is based on a GO thin film capable of deflecting due to the pressure variations caused by acoustic waves. The interferometric sensor was studied for frequencies between 20 and 100 kHz and fully characterized in this frequency range. Moreover, the stability of the membrane to temperature was studied.

4.1 A brief review on optical fiber sensors enabled by graphene and graphene-based materials

4.1.1 Evanescent Field

The principle of light propagation in optical fibers is the total internal reflection at the interface of two media with different refractive indices. This means that incident light that reaches an interface between an optically dense medium and a sparse medium with an angle superior to the critical angle will be totally reflected back to the incident medium [71]. In fact, due to the continuity of the tangential components of the electric and magnetic field imposed by Maxwell's equations, the electromagnetic field penetrates in the adjacent sparse medium. The established electric field, called the evanescent field, presents an exponentially decreasing intensity with the distance normal to the interface. A diagram of this mechanism is presented in Figure 4.1.

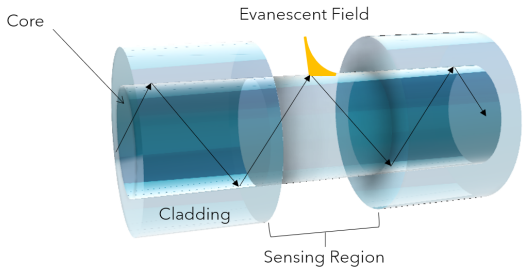

Figure 4.1: Scheme of an evanescent field-based fiber sensor with an evanescent field penetrating the external medium.

In order to enhance optical sensitivity to a specific analyte, a material with good affinity can be coated on the sensing region. In particular, graphene and graphene-based materials have attracted much attention in recent years due to their high adsorption capacity. Several sensing structures that rely on this mechanism have been proposed in the literature in the last few years, with different applications.

4.1.1.1 Graphene

The ability of graphene to adsorb molecules has been explored for the detection of hemoglobin in human blood [72]. In this work, it was proposed a sensor based on an evanescent field, composed of a sensing region, with an exposed core, coated with an adhered 3-layer graphene sheet. The effective RI varied with the hemoglobin concentration, due to the graphene adsorption capacity. The proposed sensor lowered the detection limit of hemoglobin when compared to conventional sensors.

The interaction between light and the external medium can also be achieved using tapered fibers or micro/nanofibers. The structure of a tapered fiber is presented in Figure 4.2a. Similarly to an optical fiber with a section of the cladding removed, tapered fibers present a region in which the light interacts with the external medium. The combination of this structure with the properties of graphene has been proposed by Qiu *et al.* [73] for glucose detection. The proposed sensor was composed of a tapered polymer optical fiber coated with graphene, that was fabricated through the CVD technique. Due to the high molecule adsorption and atom-thickness nature of graphene, the authors were able to attain a linear response in a broad range of glucose concentrations. A different approach was presented by Zhao *et al.* [74]. The proposed sensor was composed of a graphene-coated down-taper and up-taper, forming an interferometric structure, as shown in Figure 4.2b. The proposed sensor was capable of determining ammonia concentration with a sensitivity of 15 pm/ppm, representing a 2-fold increase of sensitivity when compared to the uncoated structure.

(a) **(b)**

Figure 4.2: Graphene coated taper-based sensors: (a) scheme of a tapered optical fiber and (b) tapered structure proposed by Zhao *et al*. Adapted from [74].

The use of micro/nanofibers was also reported in the literature. Yao *et al.* [75] proposed an ammonia (NH_3) gas sensor based on a Mach-Zehnder interferometer as shown in Figure 4.3. The Mach-Zehnder interferometer was composed of two arms: a reference path, and a sensing path. The sensing path consisted of a microfiber attached to a magnesium fluoride (MgF_2) substrate coated with graphene. The adsorption of NH_3 caused a variation of the graphene RI, altering the effective index of the medium surrounding the microfiber, and modifying the optical path. Using this sensing structure, high concentration sensitivity was achieved for concentrations lower than 240 ppm, with a maximum resolution of ~ 0.3 *pm*. Gas sensing was also achieved by Wu *et al.* [76] using a similar structure. In the presented work, graphene was deposited on a micro fiber Bragg grating (FBG). The FBG was fabricated using an excimer laser followed by a chemical etch, reducing the fiber diameter to $\sim 11\mu m$. As in the previously presented work, the working principle is based on RI variations due to gas adsorption on the graphene layer. In this case, the variation of the effective RI of the FBG results in a variation of the resonance peak, λ_{Bragg}. The proposed sensor achieved a detection limit of $\sim 0.2ppm$ for NH_3 gas, representing a 10-fold increase when compared with similar structures without graphene.

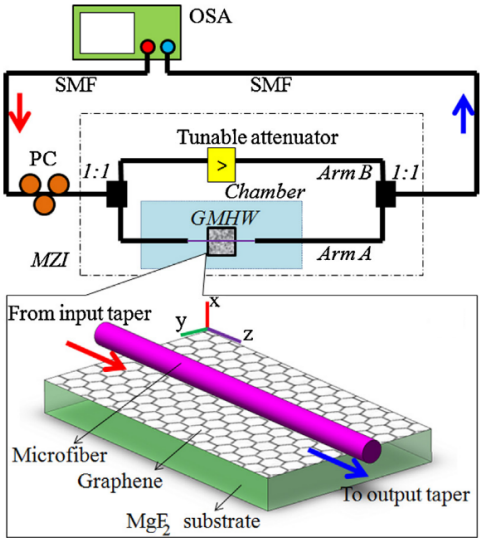

Figure 4.3: Scheme of the Mach-Zehnder configuration proposed by Yao *et al.*, image adapted from [75].

4.1.1.2 Graphene-based materials

Evanescent field fiber sensors can also be performed using graphene-based materials. In 2016, Yi Xiao *et al.* [77], proposed a toluene gas sensing in a side polished fiber coated with an rGO thin film. The presence of toluene molecules near the film leads to adsorption by the rGO film. This molecule adsorption induced a modification of the film conductivity that translated into a variation of the film's RI. The proposed sensor achieved a detection limit of 79 ppm, with a recovery time of 256 seconds. The use of a side polished fiber coated with rGO was also proposed for temperature sensing [78]. Temperature variations induced changes in the rGO conductivity, leading to a variation in light absorption. The proposed sensor achieved a sensitivity of 0.134 $dB°C^{-1}$, and a precision of 0.03 °C, for temperatures between -7.8 and 77 °C.

4.1.2 Surface Plasmon Resonance

Surface plasmon polaritons are surface electromagnetic waves that propagate along an interface between a dielectric and a metal [79]. This electromagnetic wave arises from the oscillation of free electrons that are excited by a traveling p-polarized wave reflected at the boundary between metal and dielectric, generating an evanescently-decaying field that penetrates the metal and can reach the upper boundary between the metal layer and the outer medium [79]. When the oscillation frequency of the surface electrons is matched to the wave vector of the incident wave, the light will be absorbed by the metal, inducing an absorbance band and achieving surface plasmon resonance (SPR). The principle of SPR is presented in Figure 4.4.

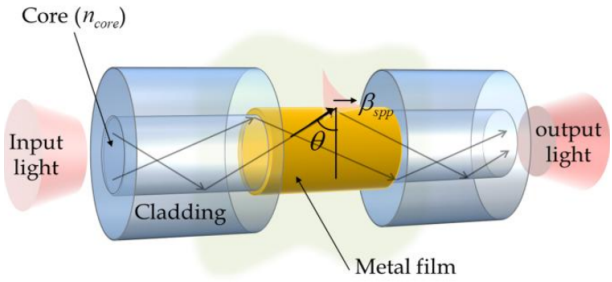

Figure 4.4: Basic scheme of an SPR sensor in an optical fiber. Image adapted from [80].

This physical phenomenon has been applied in optical fiber sensors for molecule detection, in biomedical applications. SPR in optical fibers can be achieved by coating regions near the core of the fiber with highly reflective metals (typically silver or gold). This can be achieved by removing the cladding of the fiber and exposing the core, as shown in Figure 4.4, or by using tapers or D-shaped fibers.

4.1.2.1 Graphene

Recently, it has been observed that when graphene is deposited over a metal layer, the electric field is enhanced [81]. Moreover, due to the $\pi - \pi$ stacking, graphene presents high biomolecule adsorption, meaning that graphene can be used to functionalize SPR-based sensors to these molecules. Based on these properties, Patnaik *et al.* [82] proposed a D-shaped SPR fiber sensor, coated with graphene for RI sensing. The proposed sensor, presented in Figure 4.5a, is an SPR sensor based on a D-shaped fiber coated with Indium Tin Oxide (ITO). This material allows the plasma frequency to be tuned to the infrared region, by changing its doping concentration. Nevertheless, ITO is not capable of molecule adsorption having the need to add a functionalization material: graphene. The proposed sensor presented a maximum resolution of 1.754×10^{-5} RIU. It can also be applied for layer thickness monitoring, with a maximum resolution of 62.5 pm.

D-shaped fibers coated with graphene for SPR sensing have also been proposed by An *et al.* [83]. The sensing structure was studied for RI detection using a D-shaped photonic crystal fiber (PCF) coated with graphene over gold using finite element method (FEM) analysis as shown in Figure 4.5b. The theoretical analysis found that the proposed structure can achieve a maximum wavelength interrogation sensitivity of 4391 nm/RIU with a dynamic range of 1.33 to 1.39 RIU.

Numerical analysis for a graphene-coated SPR biosensor for DNA hybridization was presented by Rahaman *et al.* [84]. The studied structure consisted of an optical fiber with an exposed core, coated with silver, tungsten disulfide (WS_2), and graphene, constituting a hybrid design (see Figure

4.5c). Due to the high carrier mobility of WS_2, the SPR effect is enhanced. The proposed structure presented an increased sensitivity when compared to similar work.

A biosensor based on a D-shaped polymer fiber coated with graphene over gold was presented by Xi *et al.* [85]. To increase contact between the gold and the graphene layer, a gold nanofilm was directly sputtered on the graphene layer. The Au-graphene film was, then, transferred to the D-type region of the fiber. The tighter connection between the layers is translated into an enhancement of the SPR effect. The fabrication process is presented in Figure 4.5d. The sensor was studied as a RI sensor using an ethanol solution with RI values between 1.3330 and 1.3657 RIU, achieving a sensitivity of 1223 nm/RIU. The proposed sensor is also capable of detecting nucleotide bonding between the double-stranded DNA helix structures.

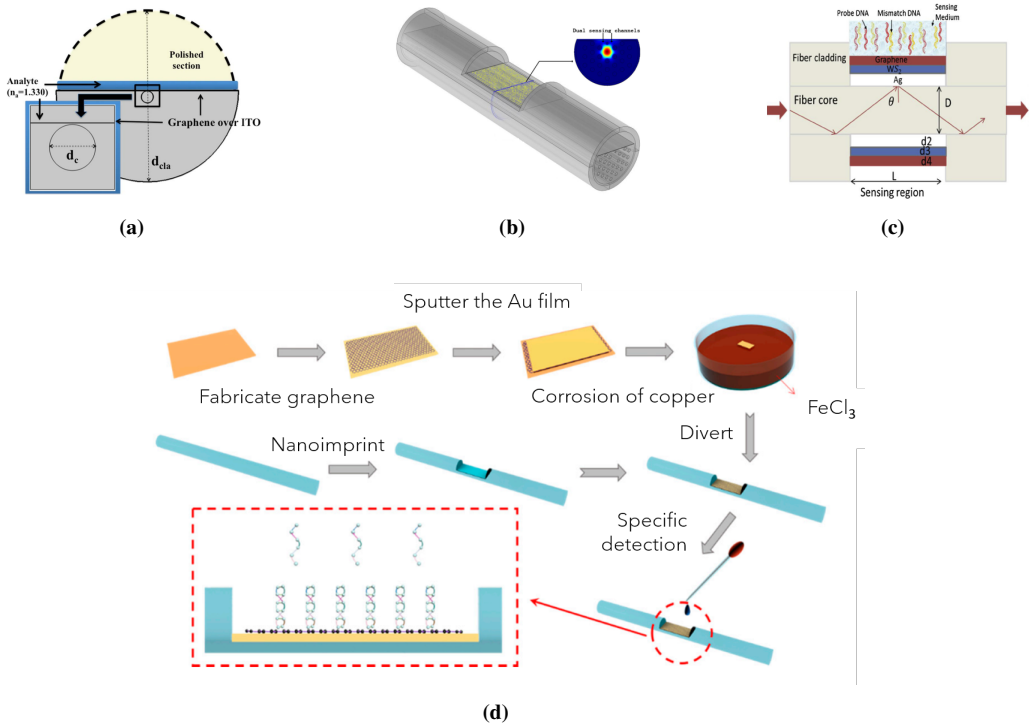

Figure 4.5: SPR sensors enhanced by graphene presented in the literature: (a) cross-section of the sensor proposed by Patnaik *et al.*, image adapted from [82]; (b) schematic diagram of the D-shaped PCF coated with graphene over gold for RI sensing, adapted from [83]; (c) SPR-based biosensor with an exposed core, image adapted from [84]; (d) fabrication process of the biosensor, image adapted from [85].

4.1.2.2 Graphene-based materials

The SPR effect can be enhanced using graphene-based materials. Moreover, these structures can be functionalized for biomolecule selectivity, for example. Mishra *et al.* [86] proposed an ammonia gas sensor based on SPR, using rGO. The proposed sensor was composed of an unclad region of a standard optical fiber, coated with copper through thermal evaporation. Afterwards, a PMMA/rGO film was deposited on the copper region using the dip coating technique. The proposed sensor was tested for the detection of different gases at room temperature, achieving higher selectivity to ammonia. The sensor also presented high reproducibility of results and stability.

4.1.3 Lossy mode resonance

Similarly to SPR, lossy mode resonance (LMR) occurs when an electromagnetic wave interacts with a thin film. When an electromagnetic wave interacts with a thin film with a RI whose imaginary part is different from zero, the introduced losses can generate electromagnetic resonances [87]. Besides SPR and LMR, also long-range surface exciton-polaritons (LRSEP) can be produced. For LMR to occur, the thin film material must present a positive real part permittivity and higher in magnitude than the imaginary part ($\varepsilon' > 0$ and $|\varepsilon'| > |\varepsilon''|$) [87]. Contrarily to SPR, LMR is independent of the electromagnetic wave polarization increasing the possible materials to be used [88]. Although SPR has attracted much attention in the literature, LMR is still not much explored, with only a few works published on LMR using graphene-based materials. Two works based on graphene oxide in LMR sensors were proposed by Hernaez *et al.*[88], [89]. The first sensor was proposed for ethanol detection. The sensor was fabricated by thermally removing the cladding from a section of a multimode fiber. Afterward, a Tin(IV) oxide (SnO_2) thin film was deposited using sputtering. The GO was deposited on the surface using the layer-by-layer (LbL) technique, combined with PEI. Different numbers of PEI/GO bilayers were studied, using ethanol solutions with concentrations varying between 0% and 100% v/v. The highest sensitivity was achieved for the sensor with 4 PEI/GO bilayers, achieving a response time of 1 second, with a recovery time of 2.75 s. The later proposed sensor was based purely on PEI/GO films, with a variable number of bilayers, deposited on a cladding-free fiber region. The proposed sensor was used for RI sensing.

4.1.4 Fiber gratings

Fiber gratings can be defined as a periodic perturbation of a property of the fiber, typically the RI of the fiber core [90]. Fiber gratings can be divided into two categories based on the periodicity of these perturbations: for short-period perturbations in the sub-micron scale, the grating is called fiber Bragg grating (FBG), and for long periodicity typically between 100 μm to 1 mm are called long period gratings (LPGs). Besides the periodicity of the RI modulation, the working principle is also different. While FBGs result in the coupling between the forward and a backward-propagating mode of the fiber that occurs at a well-defined wavelength, in LPGs a portion of the light is coupled to the fiber cladding resulting in a series of attenuation bands due to the high attenuation of cladding modes [91]. FBGs and LPGs can be inscribed on optical fibers by exposing the fiber core to an UV beam using two different techniques: using phase masks that create the periodic pattern on the fiber or through point-by-point direct writing [92].

An etched FBG was proposed for strain and temperature sensing, using an rGO coating [93]. The proposed sensor exhibits a temperature sensitivity of 33 pm/°C for temperatures ranging from -100 to 300 °C, and a strain sensitivity of 5.5 pm/$\mu\varepsilon$ for a maximum strain value of 1000 $\mu\varepsilon$. Compared to a bear FBG, the proposed structure exhibited an increase of more than 4 times the strain sensitivity, and more than doubled the temperature sensitivity.

Interaction between light and the external medium can also be achieved by using tilted FBGs. Youqing Wang *et al.* [94] proposed a GO-coated tilted FBG for humidity sensing. The proposed sensor, presented in Figure 4.6a, relied on the variation of intensity due to water adsorption in the GO film to determine humidity variations. The authors attained a sensitivity of 0.129 dB/%RH for humidity ranging from 10% up to 80%. Due to the characteristics of the tilted FBG, the sensor can be used as temperature and power references by using the peaks corresponding to the Bragg mode and the ghost mode.

The incidence of photons in graphene induces the generation of electron-hole pairs due to the strong light-matter interactions in graphene. Because of the strong electron-electron interactions,

the photoexcited electron-hole pair will lead to ultra-fast heating of the carriers in graphene [95]. Strong phonon-electron coupling leads to conversion into Joule heating due to the zero bandgap in graphene [96]. This property, called photothermic effect, was used for the fabrication of an ultra-broadband photodetector, for light tracking [96]. The proposed sensor, presented in Figure 4.6b, consists of an FBG coated with graphene. The proposed sensor was capable of detecting light from the visible (400 nm) to the far infrared (10.768 μm). The combination of graphene with bismuth telluride (Bi_2Te_3) resulted in an 87% increase in the photoresponse. The proposed sensor presented high stability even under atmosphere conditions after 100 days.

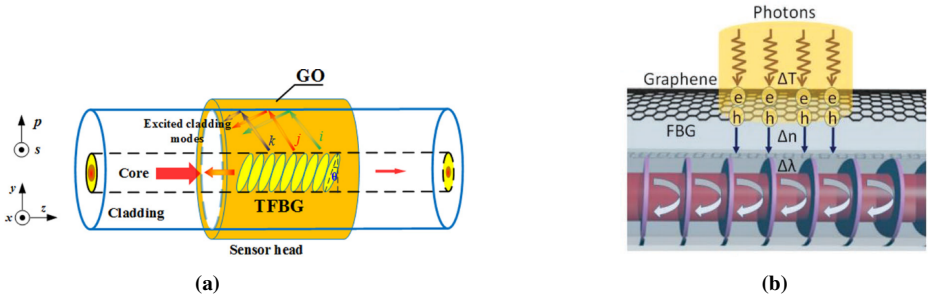

Figure 4.6: Fiber sensors based on FBGs enhanced by graphene: (a) humidity sensor based on a tilted FBG, adapted from [94], and (b) schematics of the D-shaped PCF coated with graphene over gold, image adapted from [96].

The combination of fiber gratings with the properties of graphene-based materials has also been proposed by Flavio Esposito *et al.* [97]. The sensor consisted of an LPG coated with a polycarbonate-graphene oxide multilayer for the detection of biomolecules. The sensor attained a sensitivity of 2000 nm/RIU (2 μm/RIU), 30-fold than the uncoated fiber. Biotinylated bovine serum albumin (BSA) was detected for concentrations between 0.1 and 1000 aM (attomolar), with a limit of detection lower than 0.2 aM. More recently, LPG coated with GO was proposed as a biosensor [98]. The sensor, whose surface biofunctionalization is presented in Figure 4.7, achieved a linear response for concentrations up to 1.2 mg/mL, with a sensitivity of around 0.77nm/(mg/L). The sensor exhibited a response time of 2.16 s and great selectivity. This last property allowed the sensor to be used for label-free bio-sensing.

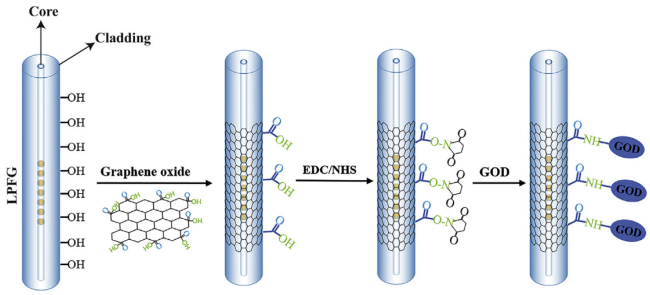

Figure 4.7: Biosensor based on an LPG, adapted from [98].

4.1.5 Interferometric sensors

Interferometry can be achieved by dividing an incoming incident light beam into different optical paths with different lengths or refractive indices. Optical fiber sensors based on interferometry have been extensively studied in the last decades and have found many applications in physical and chemical sensing. The most prevalent configurations presented in the literature are based on

Sagnac, Mach-Zehnder, or on FP interferometers. In this section, other interferometric configurations enhanced by graphene-based materials will be addressed.

Dash *et al.* [99] proposed a Mach-Zehnder interferometer based on a photonic crystal fiber (PCF) with collapsed limits. The PCF allows the light to be guided in different optical paths, creating the interferometer as presented in Figure 4.8a. The optical fiber was chemically functionalized with GO for RI sensing. The proposed sensor can work as an intensity or wavelength-shift sensor, attaining sensitivities of 130 dB/RIU and 212 nm/RIU, respectively.

Interferometry can also be achieved by using a knot resonator in a microfiber. By coating the knot resonator with GO, it is possible to detect gas, as proposed by Yu *et al.* [100]. The developed structure, shown in Figure 4.8b, results in the interference between the light that travels across the taper and the light that goes through the knot structure. Due to the small dimensions, the light that goes through the knot resonator is highly affected by the external medium. So, any change in the RI will affect the interference pattern. By coating the knot resonator with graphene oxide, it was possible to attain a gas sensor due to the high adsorption capacity of GO. The proposed structure was tested as NH_3 and carbon monoxide (CO) sensor, achieving different sensitivities due to the different adsorption energy and charge transfer ability. A maximum sensitivity of 0.35 pm/ppm for NH_3 was achieved, for concentrations below 150 ppm. An NH_3 sensor based on a simple microfiber that combined an interferometric structure with the properties of GO - Figure 4.8c - was also proposed by Caibin Yu *et al.* [101]. The microfiber was coated with platinum and GO (Pt/GO) and the result was compared with a GO-coated microfiber. The Pt/GO coated microfiber exhibited higher sensitivity, with a value of 10.2 pm/ppm.

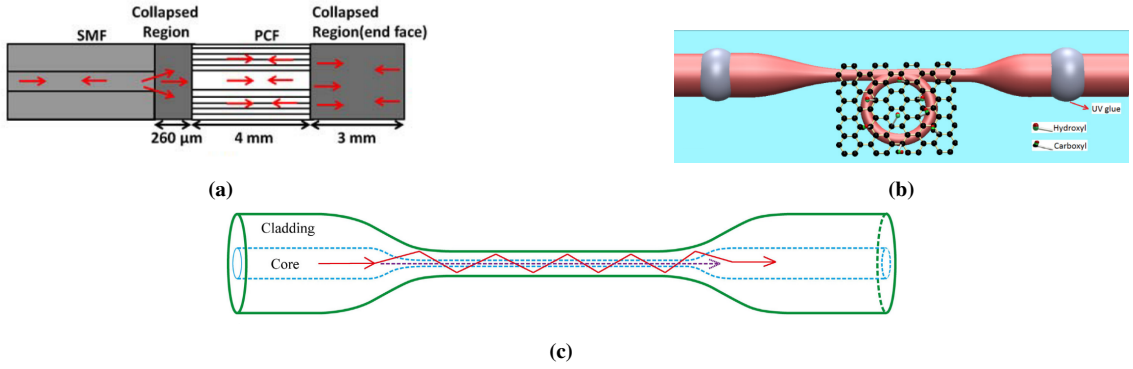

Figure 4.8: Interferometry-based sensors with graphene oxide: (a) RI sensor proposed by Dash *et al.*, image adapted from [99]; (b) gas sensor proposed by Yu *et al.*, image adapted from [100]; (c) gas sensor proposed by Yu *et al.*, image adapted from [101].

FP interferometers gained popularity due to their compactness and simple fabrication procedures [102]. FP interferometers can be fabricated in optical fibers by creating a silica cavity using FBGs as mirrors [103], or by creating an air cavity through chemical etching [104] or micromachining [70], for example. Air cavities can also be achieved by using a reflective surface separated from the fiber end face. FP interferometers can be easily enhanced by taking advantage of different material properties. In particular, graphene and graphene-based materials have been widely studied in the last few years as a material for FP-based sensors.

4.1.5.1 Graphene

Pressure sensing using an FP cavity can be achieved by creating a diaphragm reasonably flexible and capable of deflecting when pressure is induced. Jun Ma *et al.* [105] presented a highly sen-

sitive pressure sensing based on a graphene diaphragm attached to a silica capillary. The silica capillary served as a spacer to create an air cavity. Several fiber-tip microcavities were fabricated achieving different pressure sensitivities in a pressure range of 0 to 5 kPa. The different sensitivity values were linked to the non-constant pre-stress and thickness of the graphene layers in the different microcavities. Cheng Li *et al.* [106] reported multilayer graphene suspended on a zirconium dioxide (ZrO_2) ferrule with a 125 μm diameter for pressure sensing. The effects of gas pressure-induced damping and pre-tension in the diaphragm and resonance characteristics were experimentally investigated for pressure values between 101 and 300 kPa at room temperature. A pressure sensor fabricated through focused-ion beam (FIB) micromachining was recently proposed by Cui *et al.* [107]. An extensive theoretical study was presented to analyze the behavior of the diaphragm under pressure. The presented work revealed that air leakage was negligible, attaining a pressure sensitivity of 1.28 nm/mmHg (corresponding to 9.6 pm/Pa) at a 1300 nm wavelength.

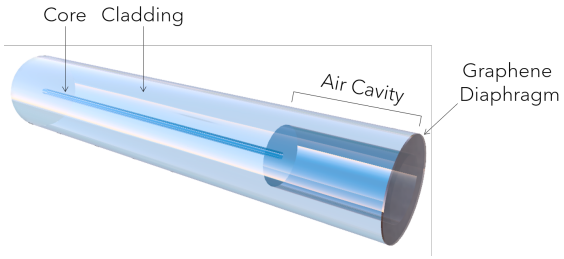

Figure 4.9: Schematic diagram of a Fabry-Perot interferometer with graphene diaphragm.

Pressure variations can be induced by the propagation of acoustic waves. The induced pressure variation is dynamic, meaning that the pressure sensed on a surface is time-variable. Similarly to pressure sensing, acoustic sensing can be achieved by determining the deflection of a thin diaphragm to the applied pressure. Cheng Li *et al.* [108] proposed a structure composed of a graphene diaphragm suspended on a ZrO_2 ferrule. The graphene used in said work was prepared from commercially available Trivial Transfer Graphene samples. The graphene samples were fabricated using CVD and were deposited on a PMMA layer. The proposed sensor achieved a dynamic pressure sensitivity of 2380 nm/kPa (2.38 nm/Pa), and a minimum detectable pressure level of $\sim$2.7mPa/$\sqrt{Hz}$ at the center frequency of 15 kHz. A similar sensing structure was proposed by Wenjun Ni *et al.* [102], achieving a dynamic response range between 5 Hz and 0.8 MHz. The proposed sensor was also tested for underwater acoustic sensing using ultrasonic sound.

FP interferometers can also be used for temperature sensing. Temperature variations can induce two different effects: thermal expansion/contraction and thermo-optic effect. The thermo-optic effect consists in the variation of the RI of a material with the temperature under constant pressure conditions, and its rate is given by the thermo-optic coefficient that is characteristic of the material. This leads to a change in the diaphragm reflectivity, resulting in a variation of visibility on the reflected spectrum. Thermal variations also lead to mechanical variations on the material resulting in their contraction or expansion. Considering an air cavity between an optical fiber and a graphene diaphragm several effects can be experienced due to thermal variations. On one hand, the graphene RI can change due to the thermo-optic effect. On the other hand, the air contained in the cavity can expand or contract, resulting in a pressure variation inside the cavity. This induced pressure variation can result in a diaphragm deflection. This was the main mechanism exploited by Cheng Li *et al.* [108]. The proposed sensor achieved a sensitivity of 352 nm/°C in the tested range of 20 to 60 °C, where the reflectivity of the graphene diaphragm was essentially constant.

Ling Li *et al.* [109] proposed an all-silica FP interferometer with a graphene diaphragm for high-temperature sensing. The proposed sensor was tested in three different temperature ranges between 40 and 1008 °C. The sensor demonstrated linear response in the three temperature ranges: between 40 and 60 °C, 500 and 510 °C, and 1000 and 1008 °C. A maximum sensitivity of 1.87 nm/°C was attained for the higher temperature range, with a resolution of ±0.32 °C.

The combination of graphene properties with FP interferometry was also used for hydrogen detection [110]. The proposed sensor, presented in Figure 4.10, consisted of a palladium (Pd) and multilayered graphene film deposited on a silica capillary. The incorporation of graphene into the structure resulted in a lower response time of ∼18 s and a detection limit of ∼ 20 ppm.

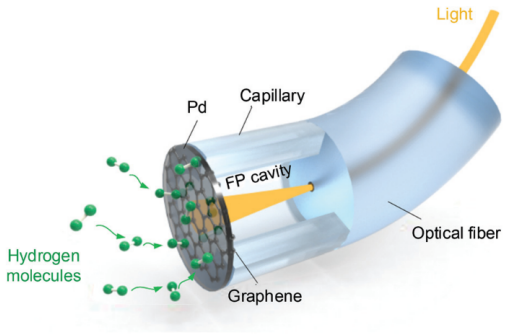

Figure 4.10: Fabry-Perot interferometer with a Pd and multilayered graphene film for hydrogen detection, image adapted from [110].

4.1.5.2 Graphene-based materials

Similarly to graphene, GO can also be used as a diaphragm material. This structure has been proposed in the literature for acoustic [111] and humidity [12] sensing, for example. Acoustic sensing was achieved by Yu Wu *et al.* [111], by depositing a GO membrane on a horn-shaped glass tube. The proposed sensor, presented in Figure 4.11a, attained an acoustic sensitivity of 10.2 μPa/Hz$^{1/2}$ over the entire audible frequency range. The results suggest that this structure can also be applied for ultrasonic wave detection.

A GO membrane deposited on a capillary for humidity sensing was presented by Li *et al.* [12]. The proposed sensor, depicted in Figure 4.11b, achieved a sensitivity of around 0.2 nm/%RH, for relative humidity between 10 and 90% RH, with a response time of 60 ms.

(a) (b)

Figure 4.11: Fabry-Perot interferometry based sensors with GO: (a) acoustic sensor proposed by Wu *et al.*, image adapted from [111]; (b) humidity sensor proposed by Li *et al.*, image adapted from [12].

4.2 Fabry-Perot microcavities with layered graphene-dielectric hybrid coatings for RI sensing

Interferometric sensors have been extensively studied in the last decades since it was first proposed in optical fibers by Sirkis *et al.* [112], in 1993. Several applications have been found for sensors based on FP interferometry from temperature, curvature, or humidity sensing [113]–[115], for different fields of expertise such as medicine [116], [117] and engineering [118], [119], for example.

The periodicity of the interference pattern of a fiber FP interferometer can be engineered to be dependent on the physical or chemical properties of the surrounding environment. This can be accomplished by coating the external interface with a material or a layered structure that can induce a reflection phase shift on the interference pattern. Over the years, several materials have been proposed such as metallic coatings [5], plasmonic nanostructures [120], or dielectric multilayered structures [121]. Recently, Choi *et al.* [122] reported nontrivial internal interference effects in hybrid coatings made of lossy dielectrics deposited on thin conducting films, which enables the control of the reflection coefficient of the surface at sub-wavelength scales. This effect can also be achieved using atomically thin planar conductors (ATPC) to produce hybrid dielectric-ATPC multilayered structures. In particular, this can be achieved by employing graphene or a two-dimensional graphene precursor.

In this section, the tunability of the reflection phase shift in coatings composed of layered dielectric/conducting materials is used to fabricate a fiber-based RI sensor. The nontrivial interference effects in these hybrid coatings are theoretically studied and experimentally demonstrated. The feasibility of using hybrid coatings for RI sensing was studied using cascaded FP interferometers, also known as three-mirror FP interferometers, coated with polyethyleneimine (PEI), a dielectric, and GO, a two-dimensional graphene precursor. The polyethyleneimine/graphene oxide (PEI/GO) layers were coated through the layer-by-layer technique, which takes advantage of intermolecular interactions between oppositely charged electrolytes to self-assemble a multilayered structure.

4.2.1 Principle of operation

4.2.1.1 Reflection Interference Pattern in a Three-Wave Fabry-Perot Cavity with a nanostructured coating

The reflection spectrum of the uncoated sensor can be approximated as the sum of the three primary reflections at each material interface, represented in Figure 4.12. This approximation is valid due to the low reflectivity of the surfaces of the sensor.

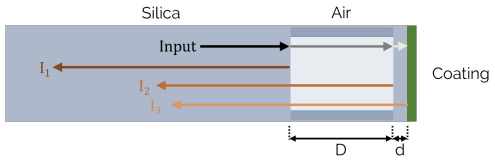

Figure 4.12: Scheme of the sensor using a three-wave Fabry-Perot cavity with an outside multilayered hybrid surface coating (shown in green). The dimensions of the Fabry-Perot microcavities (D and d) and the three primary waves reflected off the cavity interfaces (of intensity I_1, I_2, and I_3), are also defined.

The intensity of the reflected spectrum, under the three-wave approximation, is given by the following:

$$\begin{aligned} I_r(\lambda) = I_1 + I_2 + I_3 - 2\sqrt{I_1 I_2}\cos\left(\frac{4\pi D}{\lambda}\right) \\ - 2\sqrt{I_2 I_3}\cos\left(\frac{4\pi n_s d}{\lambda} + \theta_c\right) + 2\sqrt{I_1 I_3}\cos\left(\frac{4\pi(D+n_s d)}{\lambda} + \theta_c\right) \end{aligned} \tag{4.1}$$

where $I_{1,2,3}$ are the reflected intensity at each interface as defined in Figure 4.12, D and d are the air and silica cavity lengths, respectively, n_s is the effective RI of the silica cavity, and λ is the light's wavelength. The reflected intensities can be calculated from the Fresnel laws at normal incidence, resulting in:

$$\sqrt{I_1} = \left|\frac{n_s - 1}{n_s + 1}\right|; \qquad \sqrt{I_2} = \frac{4n_s|n_s - 1|}{(n_s+1)^3}; \qquad \sqrt{I_3} = \frac{16{n_s}^2 R_c}{(n_s+1)^4} \tag{4.2}$$

The effects of the coating in the interference pattern are encapsulated in its complex reflection coefficient, specified by the corresponding reflectivity (R_c) and reflection phase shift θ_c, which are wavelength-dependent and can be calculated from the complex reflection coefficient, r_c, that is attained using a transfer matrix method (TMM) described in [123]:

$$r_c^{\lambda} = \frac{\left(\frac{n_s}{n_{pol}} - 1\right)\left(\frac{n_{out}}{n_{pol}} + 1\right) + \left(1 - \frac{n_{out}}{n_{pol}}\right)\left(1 + \frac{n_s}{n_{pol}}\right) e^{\frac{4i\pi n_{pol}\Delta}{\lambda}}}{\left(\frac{n_s}{n_{pol}} + 1\right)\left(\frac{n_{out}}{n_{pol}} + 1\right) - \left(1 - \frac{n_{out}}{n_{pol}}\right)\left(1 - \frac{n_s}{n_{pol}}\right) e^{\frac{4i\pi n_{pol}\Delta}{\lambda}}} \tag{4.3}$$

where n_{pol} and Δ are the RI and thickness of the dielectric coating, respectively. Considering a small neighborhood near a central wavelength λ_c, equation 4.1 can be approximated to the lowest-order expansion near λ_c, arising a periodic pattern:

$$\begin{aligned} I_r^{\lambda_c+\Delta\lambda} \approx I_1 + I_2 + I_3 - 2\sqrt{I_1 I_2}\, cos\left(\frac{2\pi\Delta\lambda}{\Lambda_1} - \frac{4\pi D}{\lambda_c^2}\right) \\ - 2\sqrt{I_2 I_3}\, cos\left(\frac{2\pi\Delta\lambda}{\Lambda_2} - \frac{4\pi n_s d}{\lambda_c^2} - \theta_c^{\lambda_c}\right) \\ + 2\sqrt{I_1 I_3}\, cos\left(\frac{2\pi\Delta\lambda}{\Lambda_3} - \frac{4\pi(D+n_s d)}{\lambda_c^2} - \theta_c^{\lambda_c}\right) \end{aligned} \tag{4.4}$$

The periodic pattern that appeared has three effective periods $\Lambda_{1,2,3}$, resultant from the interference of the combination of the three partial waves as schematized in Figure 4.12, and are given by:

$$\Lambda_1 = \frac{\lambda_c^2}{2D}; \qquad \Lambda_2 = \frac{2\pi\lambda_c^2}{4\pi n_s d + \lambda_c^2\, {}^{d\theta_c^{\lambda}}/_{d\lambda}\big|_{\lambda_c}}; \qquad \Lambda_3 = \frac{2\pi\lambda_c^2}{4\pi(D+n_s d) + \lambda_c^2\, {}^{d\theta_c^{\lambda}}/_{d\lambda}\big|_{\lambda_c}}; \tag{4.5}$$

The components resulting from the reflection of the output interface, Λ_2 and Λ_3, suffer a variation due to the coating. Additionally, they also show a phase shift, that is dependent on wavelength. This is a feature that is absent in a dielectric-dielectric interface. The shifts caused in Λ_2 and Λ_3 arise from the sign and magnitude of ${}^{d\theta_c^{\lambda}}/_{d\lambda}\big|_{\lambda_c}$, which can be tuned by changing the RI of the output medium. This is the main mechanism for the operation of this sensor. In Figure 4.13, the expected reflected spectrum for a three-wave FP sensor with an air cavity (D) equal to 250 μm and a silica length of 50 μm is presented.

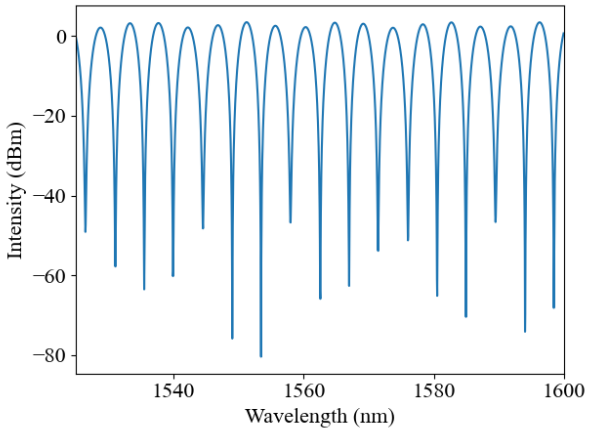

Figure 4.13: Calculated reflected spectrum of a three-mirror Fabry-Perot interferometer, considering an air cavity of 250 μm and a silica cavity of 50 μm.

4.2.2 Materials and Methods

To study the previous theoretical proposal, two similar three-wave FP microcavities were fabricated at the tip of an SMF. One microcavity was coated with a purely dielectric thin film composed of PEI while the other was coated with a multilayered PEI/GO hybrid coating.

4.2.2.1 Fabrication and coating of the sensor

The sensor was composed of an air cavity, formed using a silica capillary with an internal diameter of 75 μm, and by a silica slab fusion spliced at the end face of the capillary. The fabrication of the sensor is initiated by fusing the silica capillary to an SMF, as presented in Figure 4.14a, using a fusion splicer (Sumitomo Type-71C). The silica capillary was, then, cleaved to the appropriate length, attaining an air cavity. Afterward, the capillary was spliced to another SMF, which was subsequently cleaved to a small dimension. It is noteworthy that the electric arc must be applied directly on the SMF, distanced from the silica capillary, to avoid its collapse minimizing optical losses at the interfaces. A microscope image of the resultant sensor is presented in Figure 4.14b.

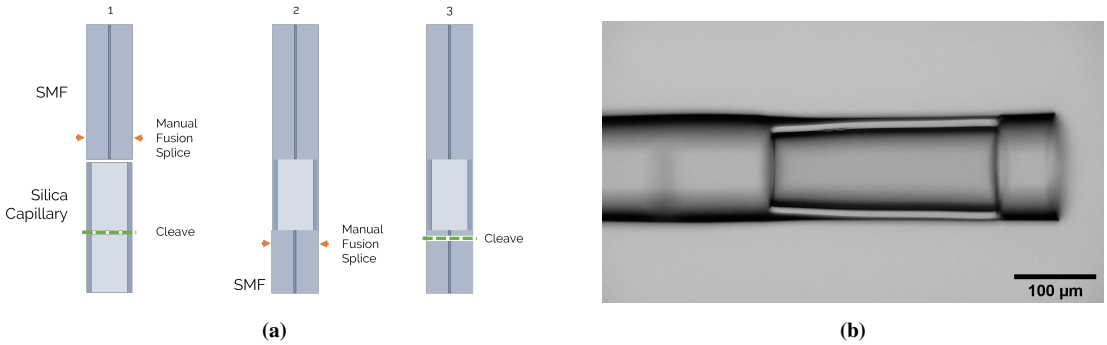

Figure 4.14: (a) Sensor fabrication process; (b) microscope image of the fabricated sensor with an air cavity length of 258 µm and a silica slab length of 64 µm.

The deposition of the multilayered structure of PEI/GO was achieved using PEI (Sigma-Aldrich P3143) acquired in a water solution with a concentration of 50% (w/v), that was further diluted to a concentration of 2×10^{-2}M using ultrapure water (Milli-Q water), and GO (Sigma-Aldrich 777676) that was also diluted using ultrapure water to match the PEI solution, to a concentration of 2×10^{-2}M. The coating of the fiber was attained by using the layer-by-layer (LbL) technique and followed the same procedure as presented in section 3.1. For the purely dielectric coatings, where only PEI was coated to the sensor, the fiber was immersed in the diluted PEI for 1 minute, followed by a brief rinse in the ultrapure water. The rinse process allows the removal of all non-adsorbed residues from the surface of the fiber. This process was repeated 10 times, in order to reach a significant PEI film thickness on the surface of the fiber.

4.2.2.2 Experimental setup

The experimental setup used for the characterization of the sensors is composed of an amplified spontaneous emission (ASE) source, an optical circulator, and an OSA (AQ6370C, Yokogawa Electric), as presented in Figure 4.15. The ASE source had a central operation wavelength of 1550 nm and a bandwidth of approximately 100 nm, and the optical circulator allowed it to guide the light reflected in the sensor to the OSA.

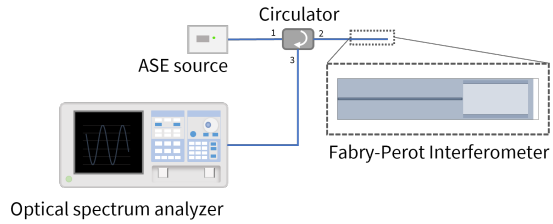

Figure 4.15: Experimental setup for the acoustic characterization of the fiber sensor.

4.2.3 Experimental Results

4.2.3.1 Influence of PEI and hybrid PEI/GO coating

The influence of the deposition of the thin film on the output surface was studied by comparing the reflected spectrum before and after coating the FP interferometers. In the case of the sensor coated with PEI, no significant variations were observed in terms of wavelength shift or intensity, as can be observed in Figure 4.16a. In the case of the sensor coated with the PEI/GO film, visible variations in the interference pattern were attained in terms of phase, intensity, and fringe visibility. In Figure 4.16b, the reflected spectrum before and after coating with 10 PEI/GO layers is presented, and the phase shift is marked. The coating resulted in a small decrease in the average reflected optical power, however with increased fringe visibility.

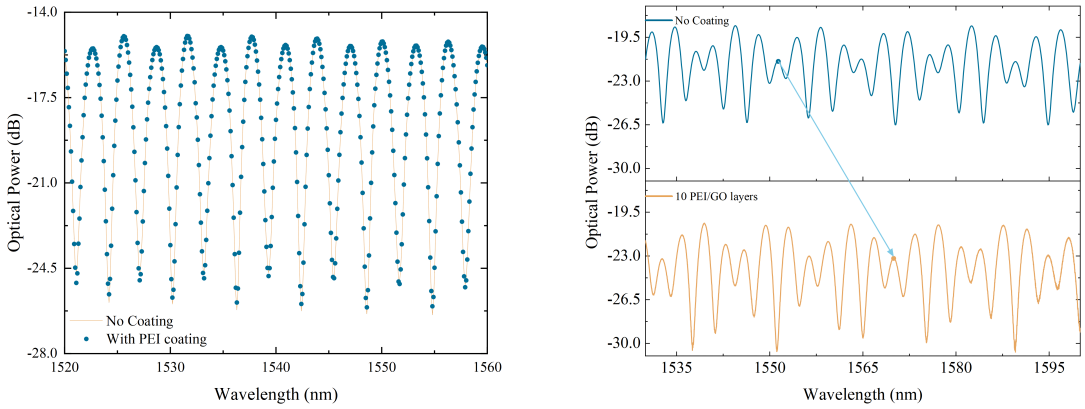

Figure 4.16: Reflected spectrum before and after the deposition of (a) PEI and (b) 10 layers of PEI/GO.

4.2.3.2 Refractive index sensitivity

The influence of GO on the sensitivity of the FP interferometer sensor to external RI variations was studied using four different conditions: one uncoated sensor, one sensor coated with only PEI, one sensor coated with 10 PEI/GO layers, and one sensor coated with 40 PEI/GO layers. The four sensors were immersed in liquid samples with refractive indices ranging from 1.3327 and 1.3830. The RI values were evaluated using a digital Abbe refractometer (Atago DR-A1-Plus), with an LED light source approximated to the wavelength of D-Line (589.3 nm).

The reflected spectra for the different output indices of the four sensors are presented in Figure 4.17. It can be observed that for the uncoated fiber, in Figure 4.17a, and in the dielectric-only coated fiber, in Figure 4.17b, no significant variations were attained considering the different RI of the external medium. On the other hand, for the hybrid PEI/GO coated fibers evident variations on the reflected spectra were observed (Figures 4.17c and d). This indicates an increase in the sensitivity of the sensor to variations in the external RI in the presence of a hybrid PEI/GO coating.

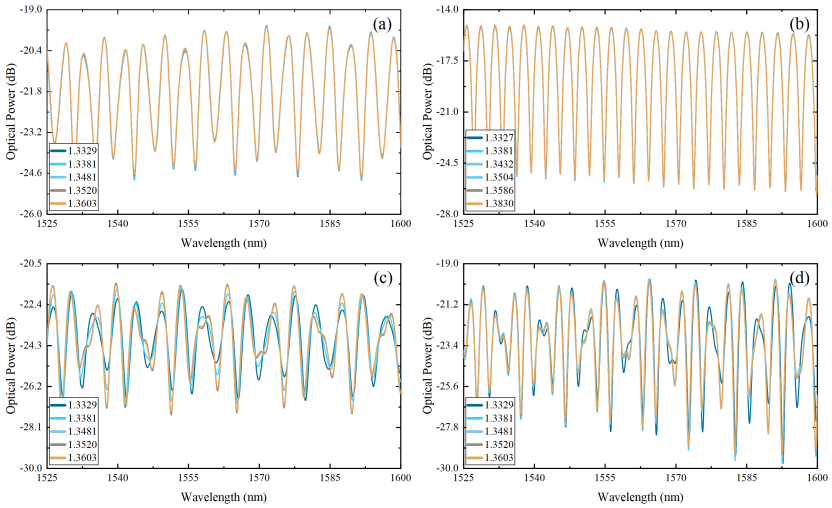

Figure 4.17: Reflected spectrum measured with the cavity immersed in liquid environments having different refractive indices ($n_{out} = 1.3327 - 1.3830$) for (a) uncoated fiber; (b) PEI coated fiber; (c) fiber coated with 10 PEI/GO layers; (d) fiber coated with 40 PEI/GO layers.

The influence of variations on the external RI can be more comprehensible by decomposing the reflected spectra in its main components. This can be achieved by calculating the fast Fourier transform (FFT) of the linear reflected spectra, as can be observed in Figure 4.18. Before converting the spectra to the respective FFT signal, the optical spectra were converted to the optical frequency domain and plotted in terms of cavity length that can be calculated using the following expression [124]:

$$FSR_\nu = \Delta\nu = \frac{c}{2nl} \tag{4.6}$$

where FSR is the free spectral range, ν is the optical frequency of light, c is the constant of the speed of light, n is the RI of the cavity, and l is the cavity length. The cavity length was calculated assuming a RI $n = 1$.

In the FFT signals, presented in Figure 4.18, it can be observed three major peaks associated with the three components of equation 4.4. The first peak is associated with the optical cavity composed of silica and the PEI/GO hybrid film, which is related to the constant Λ_2 of Equation 4.5, and can be approximated to $n_s d$. The second peak corresponds to the optical cavity composed exclusively of air, with a length given by D, that is related to Λ_1. The third peak is related to Λ_3 and is determined by the cavity composed of air, silica, and the hybrid film, with a total length of $n_s d + D$. The FFT peaks and the calculated cavity lengths of the three cavities are summarized in Table 4.1.

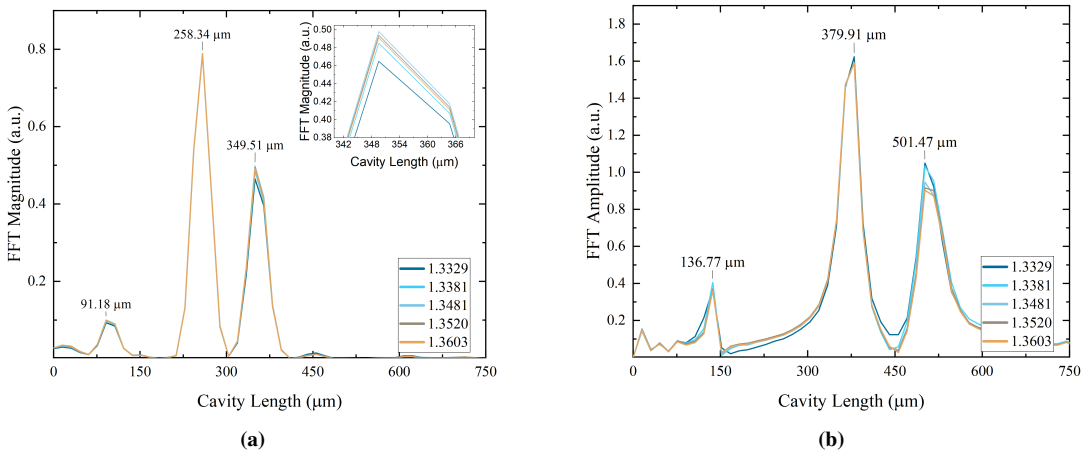

(a) **(b)**

Figure 4.18: Fast Fourier transform (FFT) of the reflected spectrum calculated for a RI equal to 1 for the different external RI for the sensor coated with (a) 10 and (b) 40 layers of PEI/GO. In Figure (a), a zoomed section of the peak corresponding to the component of the external interface is presented as an inset.

The cavity lengths attained from the FFT signals are in accordance with the values determined using microscope images. Furthermore, it can be observed that the FFT signal of both cavities suffers small variations in the first and third peaks, caused by variations in the output RI. This is consistent with the understanding that only the components corresponding to Λ_2 and Λ_3 are affected by variations in the reflection coefficient on the output coating and, therefore, can be affected by variations on the external RI.

The shape variation on the reflected spectra, presented in Figures 4.17c and d, indicates that RI variations induce an alteration on the FFT peaks that correspond to cavities sensitive to the external medium in both intensity and position. Due to the low FFT resolution, provided by the small wavelength range of the spectra, the position variation of the peaks cannot be directly observed on the FFT spectra. However, the variations in the position can be analyzed by isolating

Table 4.1: FFT peaks and corresponding calculated cavity lengths for the two sensors.

	10-layer sensor	40-layer sensor
Peak 1 ($n_s d$)	131.66 = 91.18 × 1.444	197.50 = 136.77 × 1.444
Peak 2 (D)	258.34	379.91
Peak 3 ($n_s d + D$)	390 = 258.34 + 91.18 × 1.444	577.41 = 379.91 + 197.50 × 1.444

the component corresponding to Λ_2 or Λ_3 on the original spectra, by using band-pass filters. The results, presented in Figure 4.19, show a wavelength shift of the component correspondent to Λ_2 for the 10 and 40-layer PEI/GO coated sensors.

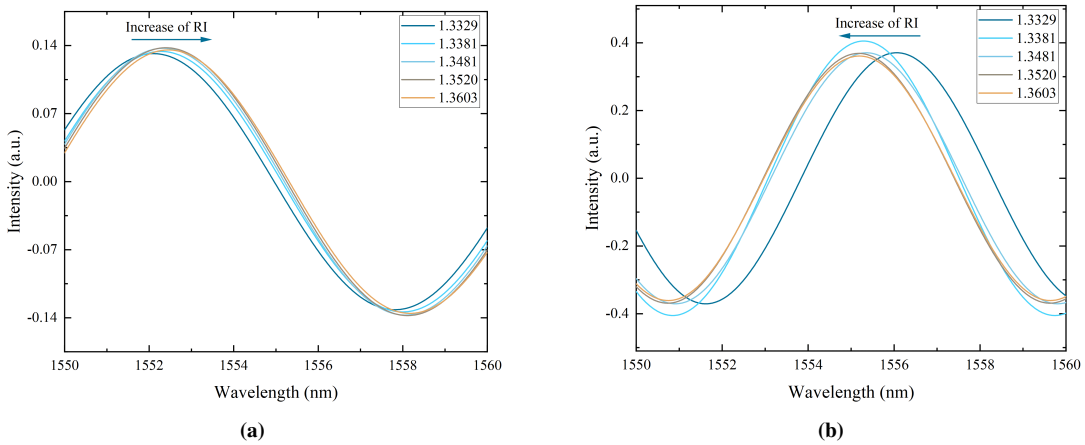

Figure 4.19: Band-pass filtered signal reconstructed by an inverse FFT for the sensor coated with (a) 10 and (b) 40 layers of PEI/GO.

The wavelength shift of the filtered signals is plotted against the theoretical predictions for the two sensors, calculated with a polymer RI equal to 1.617 [125]. The attained experimental data is in reasonably good agreement with the theoretical curves in both samples (N=10 and N=40 layers). The average distance between GO layers was calculated, attaining δ = 95.8 nm and δ = 95.6 nm for the sensor coated with 10 and 40 PEI/GO layers, respectively. The results are very similar in both cases, indicating good consistency in the production of the multilayered coating. It is noteworthy that, even though the LbL coating method produces imperfections on the PEI/GO films, the results are consistent with the downshift of a "resonant-like" behavior in the reflection phase shift at the output surface of the FP microcavity interferometer, as theoretically predicted for hybrid coatings.

4.2.4 Results and Discussion

In this section, the applicability of PEI/GO coatings for fiber sensing was studied theoretically and experimentally for RI sensing. The PEI/GO coatings, fabricated through the LbL technique, work as a hybrid coating that can be regarded as thin membranes of a two-dimensional material (GO) embedded within a dielectric matrix (PEI). The coating, which induces a reflection phase shift, enhances the sensitivity of a cascaded (or three-mirror) FP interferometer to the external medium. This reflection phase shift is attributed to the complex internal reflection, interference, and energy-loss processes that occur in the conducting surfaces within the coating. The experimental results showed a sensible agreement with the theoretical assumptions, despite inherent irregularities and imperfections provided by the thin-film fabrication method LbL.

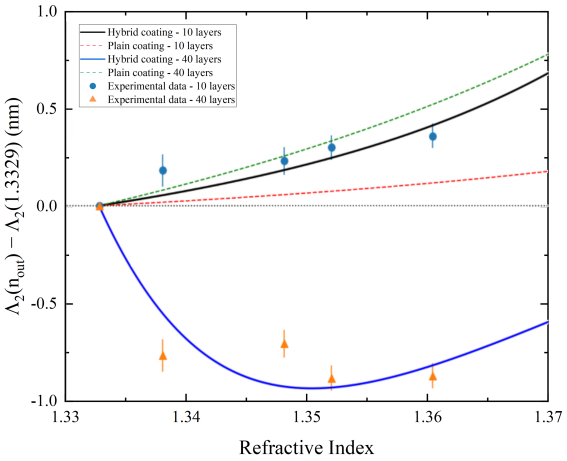

Figure 4.20: Fit of the spectral shifts in the shortest period (Λ_2) measured from the filtered FFT of the reflected spectra to the theoretical model. Two data sets are shown for identical sensors coated with 10 (blue points) and 40 GO/PEI bilayers (orange points). The solid lines represent the corresponding theoretical curves, obtained for reasonable values of the free parameters in the model — $\xi = 0.0188$, $n_{pol} = 1.617$ — and a distance between consecutive GO monolayers of $\delta = 95.8$ nm and $\delta = 95.6$ nm, respectively. For comparison, the corresponding curves in the absence of GO membranes (i.e. $\xi = 0$) are shown as dashed lines.

The interference phenomena that occur in the hybrid GO/PEI coating are very sensitive to imperfections in the layered structures, particularly surface roughness. This is a typical feature of polymeric thin films produced through LbL [126], [127] and could also be observed in the deposited thin films, as can be seen in Figure 4.21. Surface roughness can be managed by controlling deposition parameters such as solution concentration or deposition time, for example. Notwithstanding, the theoretical concepts for the principle of operation of thin films composed of dielectric/two-dimensional materials such as graphene oxide were demonstrated and showed agreement with the experimental results. In future work, the roughness of the thin films should be decreased and controlled to further study the applicability of these films as enhancers of the sensitivity of fiber sensors to external parameters such as temperature, humidity, and pH values, for example.

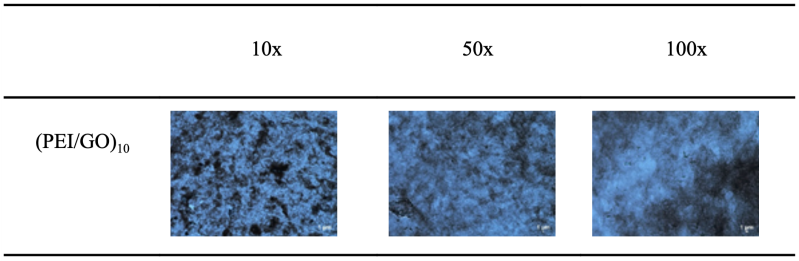

Figure 4.21: Optical microscopy images of a PEI/GO thin film, with 10 layers, deposited on glass.

4.3 Acoustic sensor based on graphene oxide membrane

Acoustic sensors can be found in many different applications from military [128], pipeline leakage [129], to biomedical [130] applications. Different configurations have been proposed for acoustic sensing using optical fibers [131], [132]. In particular, interferometry-based sensors have found many research interests due to their compact size and simple fabrication. Most interferometric acoustic sensors are composed of an FP cavity whose external mirror is composed of a diaphragm or membrane capable of deflecting when exposed to pressure variations/changes. One key aspect of FP acoustic sensors is the diaphragm material. In recent years, graphene and graphene-based materials have drawn considerable research attention due to their compelling properties. Different sensing applications have already been developed for FP interferometers using graphene and graphene-based materials [12], [108], [110]. Among these applications, acoustic fiber sensors based on graphene diaphragms have been proposed recently in literature [11], [102], [133]. Even though pristine graphene offers better mechanical properties when compared to graphene-based materials such as GO or r-GO, diaphragm fabrication relies on expensive and time-consuming techniques such as CVD and chemical etching. This limitation has been overcome by Yu Wu *et al.*[111] by developing a microphone based on a GO membrane having a controlled thickness of several hundred nanometers. The fabrication technique is initiated by dissolving GO powder in deionized water. The concentration of the GO solution can be used to control the membrane's thickness. The GO membrane is produced afterward by placing the solution on a copper foil and heating it to remove water. The copper substrate is then removed by chemical etching. The GO membrane is finally placed afloat in a deionized water container and then attached to a glass tube via Van der Waals force. The proposed sensor attained a minimum detectable pressure of 10.2 μPa/Hz$^{1/2}$, and a flat response for frequencies between 100 Hz and 20 Hz. Although the fabrication method of the proposed sensor does not rely on CVD, it still needs chemical etching, and the attained device frequency range is modest from what one can expect for such membrane thicknesses.

In this section, an acoustic sensor based on a GO membrane is presented. Contrary to acoustic sensors presented in the literature with similar configurations, in this work the membrane is fabricated using a more straightforward procedure that does not rely on chemical etching, and, therefore, reduces chemical hazards. The diaphragm is dip-coated to a 245 μm length silica capillary. The frequency response was investigated in the 20 to 100 kHz frequency range, where a maximum signal-to-noise ratio of 32.7 dB at 25 kHz was achieved. The influence of temperature on the performance of the sensor and membrane stability was also studied for temperatures between room temperature and 90 °C.

4.3.1 Working principle

4.3.1.1 Fabry-Perot interferometry

As illustrated in Figure 4.22, the sensor consists of an SMF fusion spliced to a silica capillary that serves as a spacer to the GO membrane.

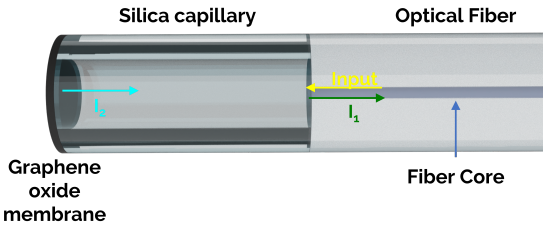

Figure 4.22: Schematic diagram of the Fabry-Perot interferometer with the GO membrane. The main reflections are annotated in the image.

The light that travels in the fiber is partially reflected in the interface between the fiber and the capillary, as annotated in Figure 4.22 as I_1. The portion of the light that is transmitted in this interface, reaches the GO membrane that, in turn, will reflect a portion of this light, annotated as I_2. Considering the low reflectivity provided by the interfaces and the small thickness of the GO membrane, the structure can be approximated to a low finesse FP interferometer in a small neighborhood from the central wavelength. The output reflected light is the result of the interference of the two light beams, I_1, and I_2, given by:

$$I_r(\lambda) = I_1 + I_2 - 2\sqrt{I_1 I_2}\cos\left(\frac{4\pi nL}{\lambda}\right) \tag{4.7}$$

where n and L are the air cavity's RI and length, respectively, and λ is the wavelength of the light. Pressure variation leads to membrane deflection, resulting in a change in cavity length. Therefore, the reflected spectrum suffers a phase shift as presented in Figure 4.23. This phase shift can be interpreted in terms of reflected power variation at a given wavelength, as shown in the inset of Figure 4.23. By setting the wavelength of the laser to a quasi-linear range around the quadrature point, as marked in Figure 4.23, the output power variation is linearly dependent on the applied pressure as can be observed in the inset of the same figure.

4.3.1.2 Acoustic Transduction Mechanism

Acoustic waves are mechanical longitudinal waves that induce pressure oscillation in the mean where it is being conducted. In the present case, the incidence of acoustic waves on the sensor will cause small oscillatory diaphragm deflections that are proportional to the applied acoustic pressure. This deflection leads to a variation in cavity length that ultimately leads to a variation in the reflected spectrum. This variation can be approximated as a wavelength shift when considering a small wavelength range.

The displacement of the membrane can be calculated assuming a circular, flat, and uniform diaphragm under small deflections (smaller than 30 % of the membrane thickness). The deformation of the membrane is given by [102]:

$$D_0\nabla^4\eta + \rho h\frac{\partial^2\eta}{\partial t^2} + \nu\frac{\partial\eta}{\partial t} = Pe^{j\omega t} \tag{4.8}$$

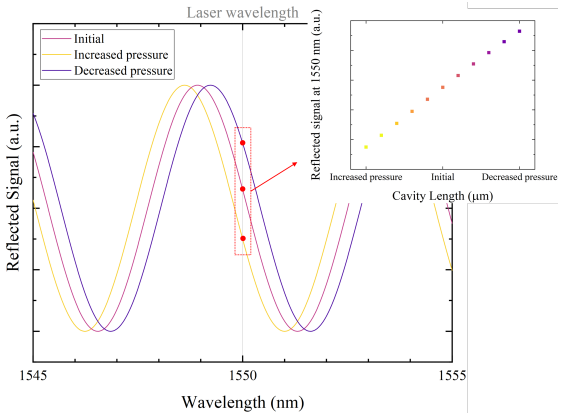

Figure 4.23: Simulated reflected spectrum for an optical cavity of approximately 250 μm, with the tunable laser wavelength set to the quasi-linear region around the quadrature point. In the inset, the variation of optical power for different applied acoustic pressure is demonstrated.

With the following physical significance:

D_0	bending stiffness of the diaphragm
η	diaphragm deformation
ρ	mass density
h	diaphragm thickness
ν	damping coefficient of forced vibration
P	amplitude of the acoustic pressure
ω	angular frequency of the acoustic wave

The bending stiffness, D_0, is given by $Eh^3/12(1-\mu^2)$, with E being the Young's modulus of the diaphragm material, and μ the Poisson's ratio. The solution of equation 4.8 for a uniformly loaded circular plate, with radius R, is given by:

$$\eta(r) = \frac{3(1-\mu^2)(R^2-r^2)^2 P}{16Eh^3} \frac{f_{mn}^2}{\sqrt{(f_{mn}^2-f^2)^2+4f^2\xi^2}} \tag{4.9}$$

where f is the frequency of the input acoustic pressure, f_{mn} is the resonant frequency of the mode order mn, and ξ is given by $\nu/(2\rho h)$. This solution is only valid when considering a clamped membrane with the boundary conditions $\eta|_{r=R} = 0$ and $\partial\eta/\partial r|_{r=R} = 0$.

The frequency range of the sensor is determined by the first resonant frequency of the membrane, as the maximum input frequency should be lower to assure linearity [134]. The resonant frequencies, f_{mn} can be calculated by:

$$f_{mn} = \frac{k_{mn}^2 h}{4\pi R^2}\sqrt{\frac{E}{3\rho(1-\mu^2)}} \tag{4.10}$$

where k_{mn} are the constant coefficient of the mn order mode. For the first vibration mode, with $m,n = 1$, the constant coefficient is given by $k_{11} = 3.196$. The first resonant frequency was calculated using the parameters from table 4.3, attaining a value of approximately 288.79 kHz. The maximum frequency range was maintained to up to 100 kHz, to ensure that all input frequencies were far from the first resonant frequency.

Table 4.3: Parameters of the properties of the sensor for the calculation of the first resonant frequency.

Parameter	Value	Reference
Radius (R)	37.5 μm	
Thickness (h)	40 nm	
Young's modulus (E)	1 TPa	[30]
Mass density (ρ)	$2.2 \times 10^3 kg/m^3$	[133]
Poisson's ratio (μ)	0.17	[105]

The first natural vibration mode was also calculated using COMSOL Multiphysics, as shown in Figure 4.24. To match the assumptions of equation 4.8, the membrane was set to a free setting, with no initial deformation or slipping ($\partial\eta/\partial r|_{r=R} = 0$), and the border of the membrane was set as a fixed constraint. The attained resonant frequency was 283.71 kHz, a difference of 5.08 kHz representing an error of approximately 1.76%.

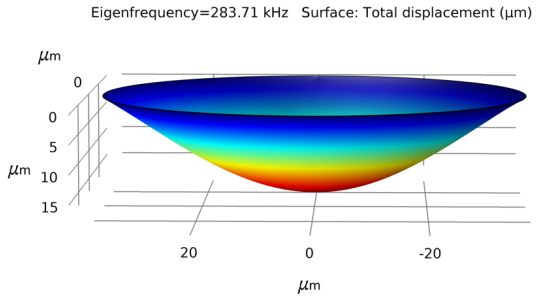

Figure 4.24: First eigenfrequency and eigenmode calculated using COMSOL Multiphysics, attaining a value of 283.71 Hz.

The total deflection with the applied static pressure was calculated both analytically and using COMSOL Multiphysics. For static pressure, the maximum deflection is given by [135]:

$$\eta(r) = \frac{3(1-\mu^2)R^4P}{16Eh^3} \tag{4.11}$$

Under these conditions, the deformation of the membrane is linearly dependent on the applied acoustic pressure. It's noteworthy that this is only valid for small deflections of the membrane, for a maximum of 30% of the membrane thickness. The results, presented in Figure 4.25, show an expected linear behavior for the maximum displacement with the applied acoustic pressure with good agreement between the two methods. For an applied pressure of 2 Pa, it is expected to attain a maximum displacement of 11.25 nm, which represents approximately 28% of the membrane's thickness. Thus, the linear behavior of the deflection with applied pressure is valid for acoustic pressure values up to 2 Pa.

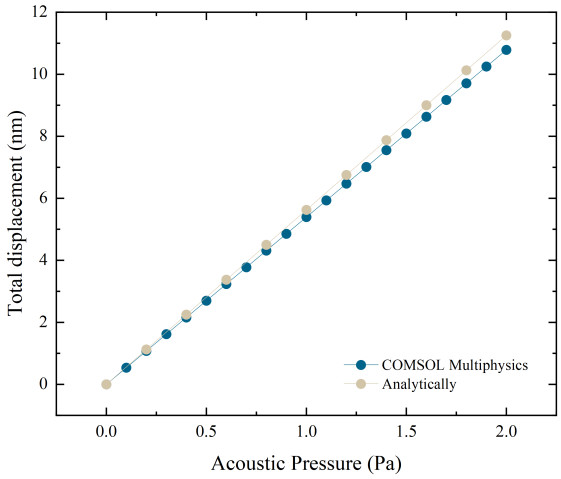

Figure 4.25: Calculated maximum displacement caused by the applied static acoustic pressure.

4.3.2 Experimental Results

4.3.2.1 Sensor Fabrication

The fabrication of the sensor has two main steps that are demonstrated in Figure 4.26a: the air cavity assembly and the deposition of the GO membrane. The fabrication of the air cavity is carried out by fusion splicing a silica capillary, with an inner diameter of approximately 75 μm and an outer diameter of 125 μm, to an SMF. The splicing was performed using the fusion splicing machine (Sumitomo Type-71C), in manual mode and setting with a lower electric arc power. The electric arc was centered far from the silica capillary to avoid its collapse, which could lead to higher losses in the interface between the SMF and the capillary [67]. Using a fiber cleaver, the capillary is subsequently cleaved to the intended length while inspecting with a stereo microscope.

The deposition of the GO membrane was achieved by dip-coating the free end face of the capillary in a water-dispersed solution of GO. The dispersion was acquired from Sigma-Aldrich (product number 777676) in water dispersion with a concentration of 4 mg/mL. The dip coating process was controlled by mounting the sensor in a translation stage with controllable velocity. The immersion of the fiber on the GO dispersion was inspected using the stereo microscope to ensure that only the tip of the capillary was immersed in the dispersion, as can be observed in Figure 4.26b. Afterward, the coated fiber was placed in an oven set at 60 °C for one hour. This allows the water to evaporate, forming the GO diaphragm at the tip of the capillary through Van der Walls interaction [12], [56]. The final sensing structure is presented in Figure 4.26c.

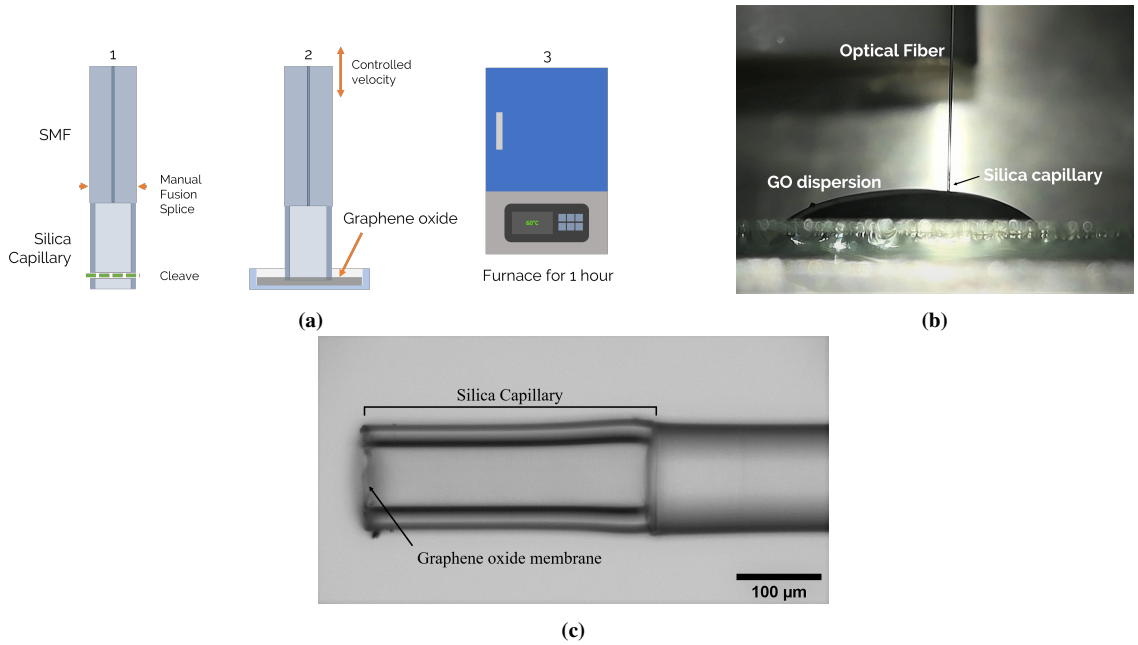

Figure 4.26: (a) Sensor fabrication process: silica capillary fusion spliced to the SMF and cleaved to the desired length; dip coating of the capillary with graphene oxide; the sensor is, then, placed on a furnace for 1 hour at 60 °C; (b) Photograph image of the dip coating process with the graphene oxide placed on a microscope slide; the fiber is placed on a motorized translation stage and is constantly monitored until the capillary reaches the GO dispersion; at this point, the fiber is pulled out at a constant speed; (c) microscope photograph of the final structure of the sensor.

4.3.2.2 Membrane characterization

To evaluate membrane thickness and homogeneity, a scanning electron microscope (SEM) image was attained in different samples. The attained membrane, shown in Figure 4.27a, is mainly homogeneous with a central region with higher density. The thickness of the membrane was estimated by bursting the GO film using an ASE light source with 100 mW power. The resultant film is demonstrated in Figure 4.27b. The thickness was determined in 12 similar samples, attaining a value of 40 nm approximately.

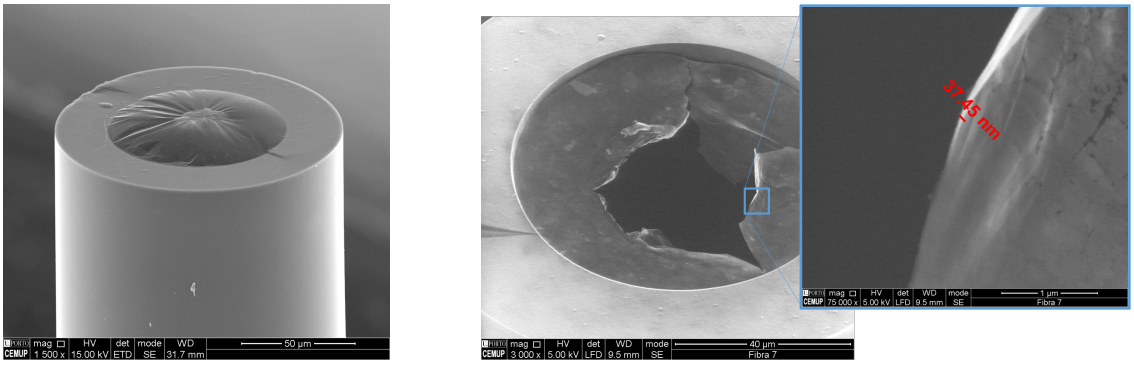

Figure 4.27: SEM image of (a) the GO membrane assembled at the top of the capillary and (b) the ruptured membrane with annotated thickness measurement of approximately 40 nm.

4.3.2.3 Fabry-Perot interferometer characterization

The optical cavity was characterized using an interrogation system composed of a broadband optical source, an optical circulator, and an OSA (Yokogawa AQ6370C) with a resolution of 0.1 nm, as presented in Figure 4.28. The broadband optical source had a central wavelength of 1550 nm and a bandwidth of approximately 100 nm. The interrogation system allows attaining the spectrum from the sensor in a reflection scheme.

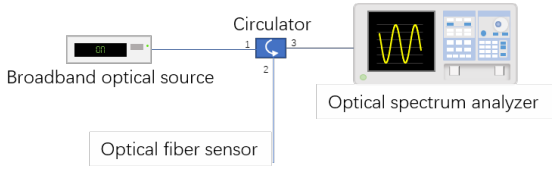

Figure 4.28: Interrogation system for the Fabry-Perot interferometer characterization.

The attained spectrum is presented in Figure 4.29a. It can be observed that it is not a pure sinusoidal signal, presenting additional components that can be the result of the interference with the small portion of the light that is coupled to the silica capillary [136]. In a smaller range, centered at the wavelength of interest, as presented in Figure 4.29b, the assumption from equation 4.7 is valid.

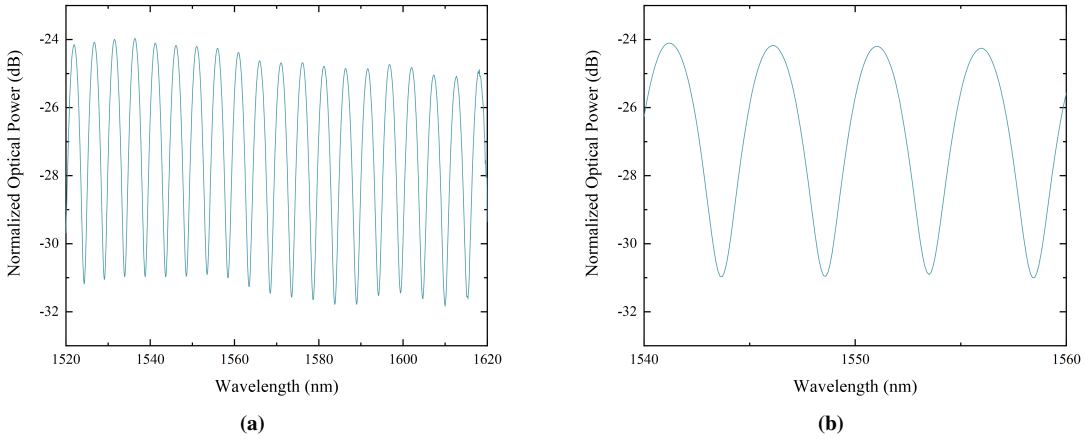

Figure 4.29: Experimental reflected spectrum for the fabricated Fabry-Perot cavity in (a) a range between 1520 and 1620 nm and (b) in the nearest region around the wavelength of interest exhibiting the pure sinusoidal behavior as expected.

The optical cavity length can be calculated from the distance between two consecutive local extreme points - two local minima or maxima. This distance, called free spectral range (FSR), is related to the cavity length by:

$$L = \frac{\lambda^2}{2n\Delta\lambda} = \frac{\lambda^2}{2nFSR} \tag{4.12}$$

where L is the cavity length, λ is the central wavelength at the extreme point, n is the RI of the cavity, and $\Delta\lambda$ is the distance between the two extreme points, i.e. the FSR. For the given FP cavity, the cavity is composed of air, with a RI of 1, and the FSR is approximately 5 nm, resulting in a cavity length of around 245 μm.

4.3.2.4 Acoustic Characterization

The acoustic characterization of the sensor was carried out using an interrogation system composed of a 11 mW tunable laser source (Thorlabs TL200C) in the C band, with a wavelength range between 1527 and 1565 nm, an optical circulator, an indium gallium arsenide (InGaAs) photodetector (Thorlabs PDA10CS-EC) with variable gain, and an oscilloscope (Tektronix TDS 1002C-EDU) with two input channels and a sample rate of 1 GS/s. The laser source and the oscilloscope were connected to the computer using a program developed in LabVIEW. The structure of the program is detailed in Appendix B. A wideband electric microphone was connected to the second input channel of the oscilloscope, to serve as a reference signal to the optical signal.

Using the OSA mode of the LabVIEW program, a linear region of the spectrum was determined, and the laser source was tuned to the central wavelength of this region. For this sensor, the selected wavelength was 1552.5 nm. This is an important step before the acoustic characterization of the sensor to ensure a linear response of the optical signal to the applied pressure as described in section 4.3.1.1. The complete experimental setup used for acoustic characterization is shown in Figure 4.30. Besides the previously described interrogation system, a function generator (Hewlett-Packard 33120A) connected to a piezoelectric actuator (Physik Instrumente P286), is placed inside an isolation box containing the fiber sensor and the electric microphone.

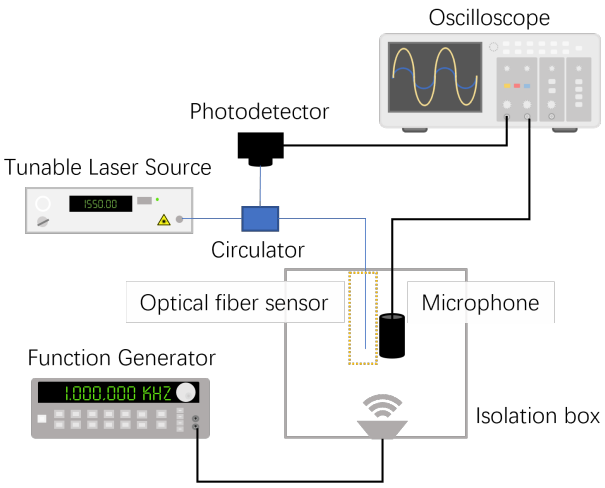

Figure 4.30: Experimental setup for the acoustic characterization of the fiber sensor.

4.3.2.4.1 Frequency response

To study the frequency response of the sensor, the amplitude of the acoustic waves was maintained fixed by fixing the output voltage of the function generator. The frequency of the acoustic waves varied between 20 and 100 kHz, a frequency range distanced from the first resonant frequency of the sensor's membrane at 288 kHz. The sound pressure level (SPL) was constant, at a value of 2.4 Pa. This SPL was calculated at a frequency equal to 20 kHz, assuming a constant sound level sensitivity of 10 mV/Pa (-40 dBV) for the electric microphone.

The signal attained by the electric microphone served as a reference to the electric signal attained by the photodetector connected to the optical fiber sensor, as presented in Figure 4.31, where the temporal signal from the electrical and optical microphones are shown for an applied acoustic frequency of 25 kHz. The electrical microphone was also used to ensure that the SPL was maintained constant during the experiment.

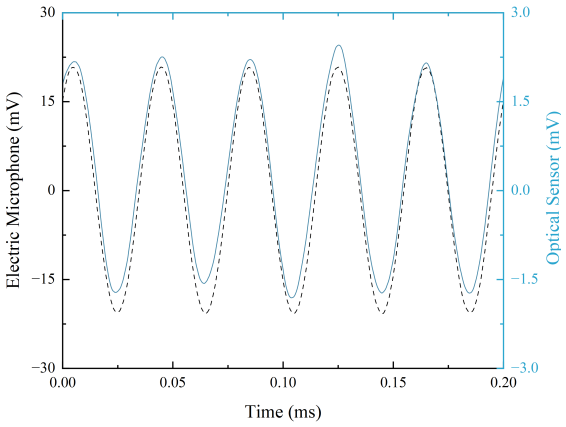

Figure 4.31: Time domain response of the electrical microphone and optical fiber sensor to an applied acoustic wave with a frequency of 25 kHz and an SPL of 2.4 Pa.

The signal-to-noise ratio (SNR) of the sensor to the applied frequency was analyzed by calculating the FFT of the temporal readout signal. The determined FFT signals to acoustic frequencies between 20 and 100 kHz are presented in Figure 4.32a. The corresponding SNR, shown in Figure 4.32b, was determined assuming a constant SPL and varied between 14.7 and 32.7 dB for frequencies of 60 and 25 kHz correspondingly.

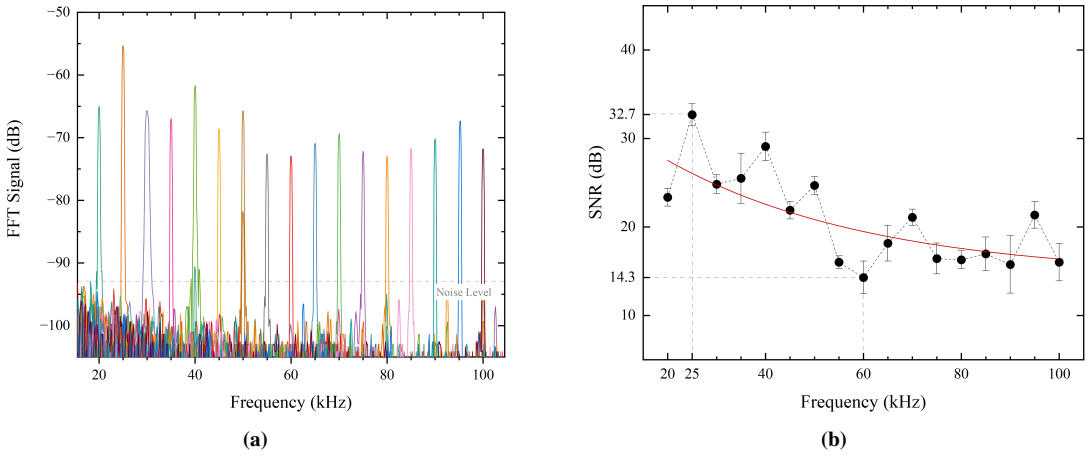

Figure 4.32: Response of the sensor for different applied acoustic frequency, with fixed SPL (a) in the frequency domain and (b) corresponding SNR.

4.3.2.4.2 Dynamic range

The dynamic range can be defined as the difference between the minimum detectable pressure level (MDP) and the maximum acoustic pressure detectable by the system with no distortion or non-linearities. The noise-limited MDP can be determined by the following expression [137]:

$$MDP = \frac{P_{in}}{10^{\,SNR/20} \times \sqrt{RBW}} \tag{4.13}$$

where RBW is the resolution bandwidth, and SNR is the signal-to-noise ratio in dB. The MDP was determined at a frequency of 25 kHz with a resolution of 50 Hz, for an applied acoustic pressure of 256 mPa, corresponding to 82.2 dB-SPL. For this applied pressure, an SNR of 37.65 dB was

attained, resulting in an MDP of 478 $\mu Pa/\sqrt{Hz}$. In Table 4.4, a comparison of membrane characteristics, MDP, and frequency range to other reported sensors with graphene and GO membranes is presented.

Table 4.4: Characteristics and performance of previously reported sensors.

Diaphragm Characteristics			MDP	Frequency Range	Reference
Material	Thickness	Diameter			
Graphene	100 nm	125 µm	59.5 µPa/Hz$^{1/2}$ @10kHz	0.2 to 22 kHz	[11]
Graphene	10 nm	1 mm	0.77 Pa/Hz$^{1/2}$@5Hz 33.97 µPa/Hz$^{1/2}$@10kHz	5 Hz to 800 kHz	[102]
Graphene-silver composite	6.36 nm	80 µm	-	0.5 to 30 kHz	[133]
Graphene	4 atomic layers	147 µm	-		
Graphene oxide	100 nm	1.8 mm	1.8 µPa/Hz$^{1/2}$ @20kHz	0.1 to 20 kHz	[111]
Graphene oxide	40 nm	75 µm	478 µPa/Hz$^{1/2}$ @25 kHz	20 to 100 kHz	This work

The MDP attained in the proposed sensor is higher than what is presented in the literature. This is due to the fact that, even though the membrane presents a thickness of the order of magnitude as presented in the literature, the membrane developed in this work its diameter is lower. The sensitivity of the sensor is given by equation 4.14 [102], and it depends on the radius of the membrane to a power of 4. This means that the sensitivity and, thus, the SNR of the sensor could be significantly improved by increasing its diameter.

$$S_a = \frac{\partial \eta}{\partial P} = \frac{3(1-\mu^2)R^4}{16Eh^3} \tag{4.14}$$

The maximum detectable pressure can be determined by evaluating the response of the sensor to the applied acoustic pressure to access the presence of non-linearities or distortion. The peak-to-peak value of the signal in the time domain for input acoustic pressures in the range between 0.07 and 1.70 Pa is presented in Figure 4.33. In this range, the response of the sensor is linearly dependent on the input pressure with an R-squared of 0.998. This means that, for this pressure range, no non-linearities were observable. However, for pressures above 1.96 Pa (99.82 dB-SPL), it was observed harmonic distortion indicating that this value is the maximum readable acoustic input. The dynamic range of this sensor is limited by the MDP (27.57 dB) and the maximum acoustic input (99.82 dB), yielding a dynamic range of 72.25 dB.

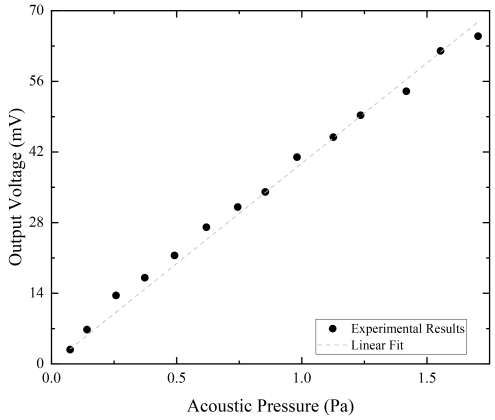

Figure 4.33: Output voltage for the applied acoustic pressure showing a linear response and, thus, no non-linearities were observed.

4.3.2.4.3 Directivity

The directional response is also an important feature of the sensor as a point-like omnidirectional receiver is a requirement in many important acoustic applications such as photoacoustic tomography and diagnostic ultrasound imaging [138], where poor directivity will lead to image artifacts and can compromise image SNR [139]. In omnidirectional receivers, a uniform acoustic sensitivity is attained for a wide angular range. This makes omnidirectional sensors suitable for mapping sound field distribution as the response of the sensor is only dependent on the distance to the target [140].

The directional characterization of the sensor was carried out by placing the sensor at a fixed distance from the piezoelectric actuator, maintaining the input acoustic wave frequency and amplitude constant, as presented in Figure 4.34a. The angle between the sensor and the actuator varied from -90° to +90°, and the SNR resultant from five different measurements of the resultant response in the frequency domain was calculated as shown in Figure 4.34b. It was expected a maximum SNR at a 0° angle, however, the maximum SNR value was attained at -10°with 33.4 dB. This may be due to small misalignments between the sensor and the actuator. The SNR value decreases monotonically to a minimum of 12 dB at an angle of 80° following a similar pattern in the symmetric direction.

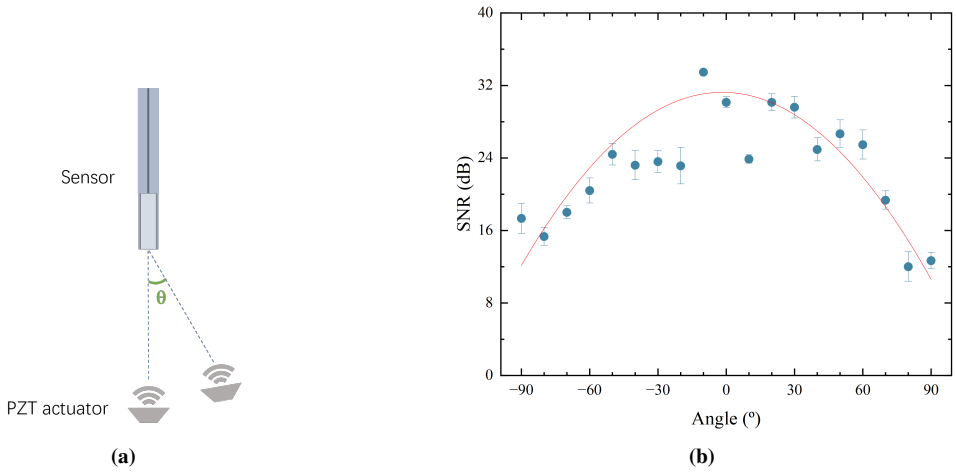

Figure 4.34: (a) Schematic diagram of the directivity characterization setup; (b) SNR directional response of the sensor for an applied frequency of 30 kHz.

4.3.2.5 Temperature Characterization

Temperature is a factor that can impact the performance of the sensor, modifying the mechanical characteristics of the GO membrane for example. To perform the temperature characterization, the sensor was placed in a low-temperature oven and was heated between room temperature and 90°C. The reflected signal was acquired using the interrogation system presented in section 4.3.2.3. The increase in temperature affected the reflected signal by inducing a wavelength shift and an amplitude decrease, as presented in Figure 4.35a. The induced wavelength shift, shown in Figure 4.35b, is linearly dependent on temperature, with a rate of 80.8 ± 0.1 pm/°C. This value is following literature [108] where a sensitivity of 87 pm/°C was reported, for the low-temperature range.

The induced decrease of signal amplitude, or fringe visibility, with the increase in temperature, was observable for temperatures up to 45 °C. For superior temperatures, the fringe contrast maintained a constant value of 4 dB. The fringe contrast did not return to the initial value when

the sensor was cooled back to room temperature, indicating a degradation of the membrane due to the high temperature.

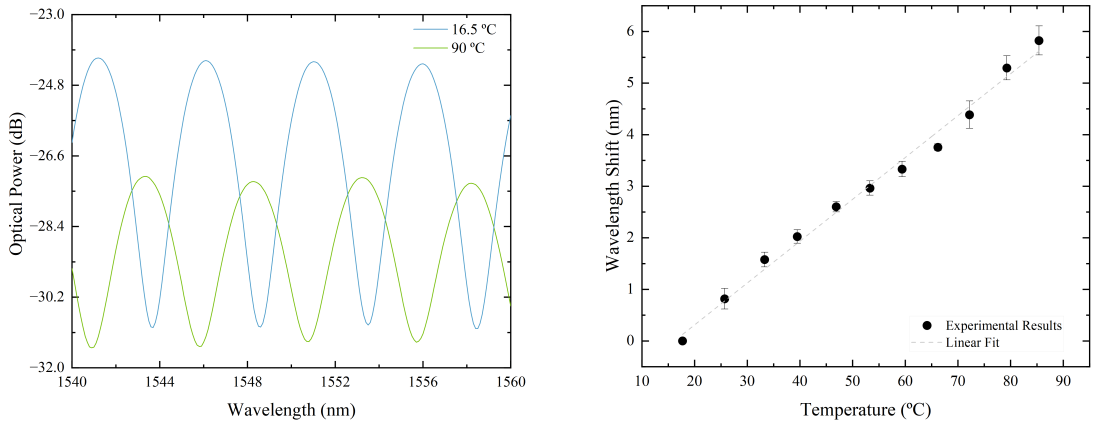

Figure 4.35: Response of the sensor to temperature for temperatures between 16 and 90 °C: (a) initial and final reflected spectrum and (b) wavelength shift with temperature.

4.3.3 Results and discussion

In this section, an acoustic sensor based on a graphene oxide membrane was presented. The fabrication method allowed to attain a sensor in a simple and fast process that did not require any hazardous chemical procedures reducing environmental impact when compared to similar graphene-based diaphragms. The sensor was characterized in terms of cavity and membrane properties, and acoustic and temperature response, by determining the frequency range of operation, the dynamic range, and the sensitivity of the sensor to temperature. The main results are summarized in Table 4.5.

Table 4.5: Review of the main results.

Parameter	Value
Cavity Length	245 μm
Membrane thickness	40 nm
Bandwidth	20 to 100 kHz
SNR	32.7 dB (at 25 kHz)
Dynamic range	72.25 dB
MDP	478 $\mu Pa/Hz^{1/2}$
Pressure dynamic range	0 to 1.96 Pa
Temperature sensitivity	80.8 pm/°C
Maximum temperature	45 °C

The application of the developed sensor in real-world problems such as its integration on complex photoacoustic imaging systems for fault detection in gas pipelines [129] or in the medical field for optical resolution photoacoustic microscopy [138], for example, is dependent on the addition of compensation mechanisms for temperature. Furthermore, the performance of the sensor should

be evaluated under dynamic temperature conditions, considering that temperature can change the mechanical properties of the GO membrane.

4.4 Concluding Remarks

This chapter presents a brief review of the main sensing mechanisms on optical fibers enabled by graphene and graphene-based materials. Afterwards, two new interferometric sensors based on GO are theoretically and experimentally studied. The first sensor showed a capacity of tunability on the sensitivity to the RI of the external medium serving as the building blocks of sensors with tailored PEI/GO coatings for different sensing applications. The second presented sensor consisted of an FP interferometer assisted by a GO membrane for acoustic sensing. The sensor was studied in a wide frequency bandwidth - between 20 and 100 kHz - and presented resistance to temperatures up to 90 °C, maintaining the spectral characteristics for temperatures up to 45 °C. The results reported in this chapter confirm the applicability of graphene-based materials and, in particular GO, in optical fiber sensing.

Chapter 5

Optical micro and nanofibers

5.1 Introduction

Optical micro and nanofibers (MNFs) can be defined as optical fibers with diameters with dimensions comparable to the wavelength of the guided light [141]. The initial investigations on the fabrication of these devices relied on bottom-up methods such as laser ablation [142], thermal evaporation [143], chemical vapor deposition (CVD) [144], among other methods [145], [146]. The irregular profile of the fabricated fibers hampered their use in optical applications. Low-loss wave guiding in microfibers was first demonstrated in 2003 by Tong and Mazur [147] using a two-step drawing process that was capable of fabricating silica wires with diameters down to 50 nm, featuring surface smoothness at the atomic level as shown in Figure 5.1.

This renewed research interest in MNFs as potential building blocks for the miniaturization of optical components [148] for application in optical communications, sensing [149], [150], spectroscopy [151], [152], nonlinear optics [153]–[155], quantum photonics [156], among other applications [157]. Optical MNFs exhibit many exciting optical and mechanical properties such as strong optical confinement, large evanescent fields, low optical losses, and full compatibility with optical systems [148], [158], [159]. In the following section, the properties of MNFs are going to be explored as well as fabrication methods and applications.

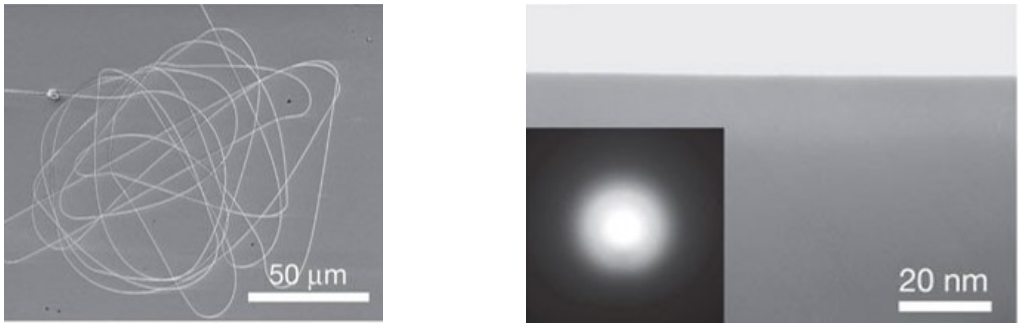

(a) (b)

Figure 5.1: (a) SEM image of a coiled fiber with a 260 nm diameter; (b) TEM image of the surface of a 330 nm silica wire, in the inset the electron diffraction pattern is shown, demonstrating that the wire is amorphous. Images adapted from [147].

5.1.1 Fabrication Techniques

Optical waveguides require geometric uniformity and surface smoothness for low-loss light propagation. Therefore, it is of utter importance to study fabrication methods that satisfy these requirements. Early research was carried out exploring fabrication methods such as CVD[144], [160], nanoimprint [161], or laser ablation [142], [162], for example. These methods yielded fibers whose surface presented high roughness resulting in fibers with high optical losses, and some of which were incapable of producing long fibers resulting in very limited transmission length. Low-loss waveguiding using nanofibers was proven possible in 2003 by Tong and Mazur [147], using a two-step taper-drawing method capable of achieving silica wires with diameters down to 50 nm. Since then, different approaches using high-temperature taper drawing were developed, reaching excellent uniformity, low surface roughness (<0.5 nm [163]), and large length (>10 cm [164]). Besides, these methods produce easily connectable fibers which are extremely important in practical applications. In the following section, the main MNF fabrication methods are going to be presented, including their main advantages and disadvantages.

5.1.1.1 High-temperature taper-drawing

High-temperature taper-drawing is a top-down method that creates thin fibers from a bulk material, typically a glass or polymer [165]. The material is heated to its softening point at which its viscosity allows taper drawing. The basic concept of the taper-drawing technique is illustrated in Figure 5.2.

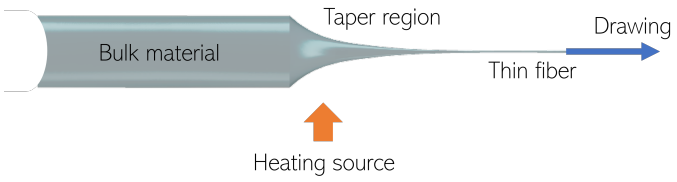

Figure 5.2: Scheme of the taper-drawing technique.

5.1.1.1.1 Flame-heated taper drawing of glass fibers

In the flame-heated taper drawing, also called the flame-brushing technique, a controlled flame scans a small region of fiber placed in axial tension. By controlling the axial tension, the fiber is elongated resulting in a reduced diameter at the heating region. The flame is commonly provided by a hydrogen (H) gas torch as it is easily controllable, clean, and reaches temperatures compatible with most glass fibers [165]. The typical flame-heated taper drawing setup is presented in Figure 5.3. The taper can be tailored in terms of length, diameter, or shape of the transition region by controlling the pulling speed and the effective hot region length by changing the velocity of the flame. This is the most commonly used technique in standard fibers and is capable of achieving MNFs with diameters down to 30 nm [166], with controllable cross-section geometries [167], and low propagation loss [168]. Besides, the fabricated MNFs are intrinsically attached to the standard fiber allowing easy connectivity to other optical components. The downsides of conventional flame-heated technique are that these systems can lead to water or OH contamination in the MNFs [158], and they can also present random gas turbulence that can decrease the quality and increase the roughness of the produced MNF [165]. Moreover, the temperature of the heating source is fixed which makes these systems incompatible with materials with different softening temperatures.

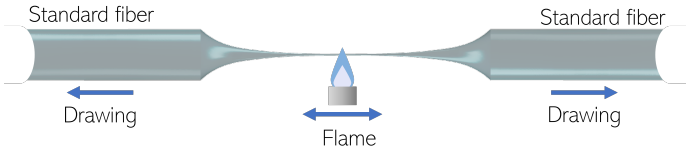

Figure 5.3: Scheme of flame-heated taper drawing setup.

5.1.1.1.2 Laser-heated taper drawing of glass fibers

In this technique, the heating source is replaced by a laser source, typically a carbon dioxide (CO_2) laser, with an emission wavelength of 10.6 μm that falls within the strong absorptive band of most glasses. The concept of this technique is essentially the same as the latter, where the continuous wave laser beam heats the fiber to its softening temperature while the fiber is being drawn. Different configurations have been proposed in the literature, making this technique very versatile. The laser beam first goes through a variable attenuator, allowing the power of the laser beam to be controlled. Then, it is focused and redirected to a scanning mirror that directs the beam to the fiber. The scanning mirror allows to control the hot zone length. In simpler setups, with no variable attenuator or scanning mirror, the laser can be focused/defocused to vary the temperature of the fiber [158].

This technique is also suitable for MNFs fabrication in vacuum or controlled atmospheres [141], reducing combustion or surrounding contamination. The main drawback of the laser-heated taper drawing is the "self-regulating" effect, which prevents the taper to reach diameters lower than 1 μm [148]. This effect is explained by the decreasing ability to absorb laser energy when the diameter is decreased, explained by the Mie effect [165], [169]. On the other hand, this effect can be regarded as an advantage as it allows the prediction of the final diameter of the fiber by controlling the power of the laser and the pulling force, making this method highly repeatable.

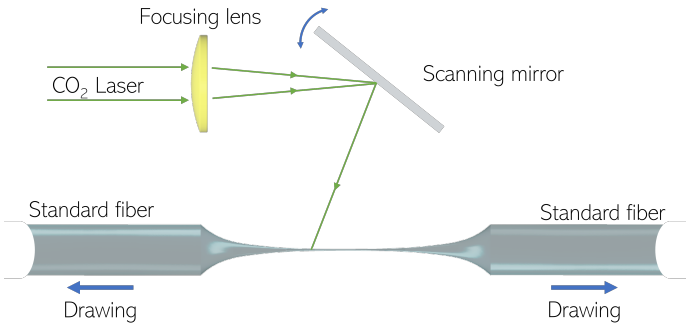

Figure 5.4: Scheme of the CO_2 laser-heated taper drawing setup.

5.1.1.1.3 Electrically-heated taper drawing of glass fibers

In the electrically-heated method, an electrical microheater is used for the taper drawing. The electrical microheater can provide controllable temperature by varying the current on the resistive element. The heaters present a simple design, are highly controllable, and do not generate disturbing gas flow [165]. Besides, this technique produces MNFs with extremely low OH content when compared to the flame-heated drawing method when used on silica optical fibers [158].

However, this method poses some disadvantages as the heaters are temperature limited, unable to reach very high temperatures, and the volatilization of the heater material at high temperatures can lead to contamination of the MNFs. The basic scheme of electrically-heated taper drawing is presented in Figure 5.5.

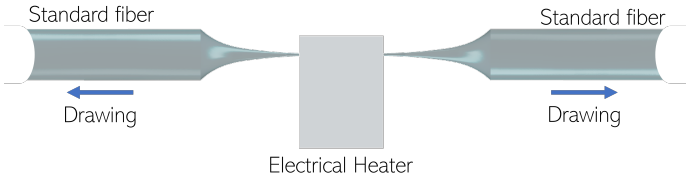

Figure 5.5: Scheme of the electrically-heated laser-heated taper drawing setup.

5.1.1.1.4 "Self-modulated" taper-drawing

The "self-modulated" taper-drawing is a two-step process that allows the attainment of MNFs with the smallest radii, reaching values as low as 10 nm [163]. In this method, a fiber is tapered to diameters in the order of a few micrometers using one of the previously described methods and then it is broken in the region with the smallest diameter. Afterwards, the tip of the tapered fiber is wrapped on the tip of a sapphire tapered rod with approximately 100 μm. Then, a drawing force perpendicular to the axis of the sapphire rod is applied, further tapering the fiber. The process is schematized in Figure 5.6.

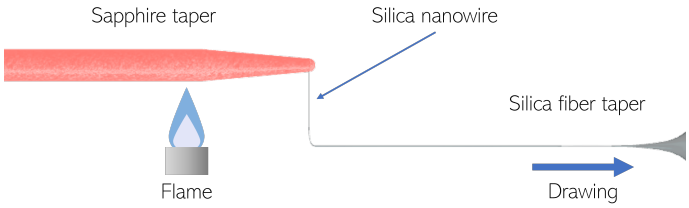

Figure 5.6: Scheme of the "self-modulated" taper drawing setup.

5.1.1.1.5 Directly drawing from bulk glasses

All the aforementioned drawing techniques require an optical fiber as a preform, restricting the available materials. When the material is not available in the fiber form, it is possible to directly draw from bulk materials. In this technique, a solid rod is heated to a temperature high enough to cause localized softening on the bulk material. By withdrawing the rod, a filament with micrometric or sub-micrometric diameter is formed [158]. In some cases, a second solid rod (usually a sapphire fiber) is used for a more controlled drawing, as schematized in Figure 5.7. In addition, the drawing can occur in a controlled atmosphere to produce MNFs from unstable materials such as fluoride glasses [170]. Moreover, this technique can be applied to pulverized glasses, tailoring the composition of the initial powder and adjusting the optical properties of the MNF. This technique

is extremely adaptable, not requiring expensive equipment when compared to the laser-heated taper drawing, for example. This technique, however, lacks controllability on the uniformity and diameter of the produced MNF.

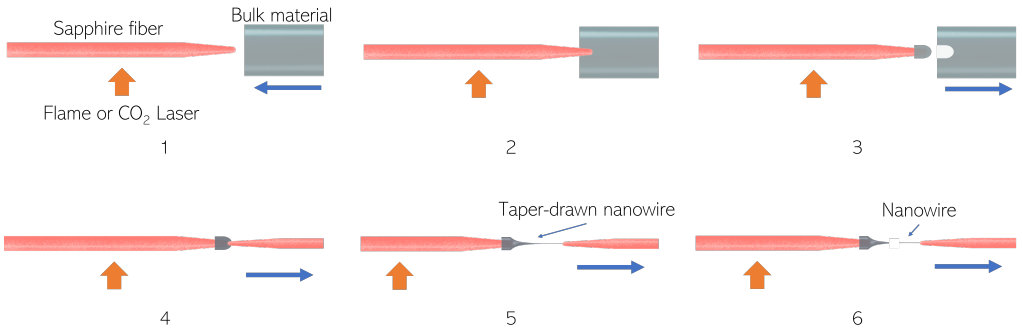

Figure 5.7: Scheme of the setup for taper drawing from bulk glasses.

5.1.2 Electrospinning

Electrospinning is a top-down nanomaterial synthesis method for the fabrication of continuous fibers in the submicron to nanometer scale [171]. This technique is mainly used for the fabrication of polymer MNFs [172] but some work has been developed for the fabrication of glass MNFs [173]. In this technique, a strong electrostatic field is used to break the balance of repulsive forces, ejecting a charged jet to a collector [174] as shown in Figure 5.8. This technique can provide MNFs from a very wide range of polymer materials, with lengths of several kilometers. However, this method is highly dependent on environmental conditions such as temperature and humidity, and also deposition conditions (polymer concentration, viscosity, work distance, electric field intensity) [171], resulting in high propagation losses [141].

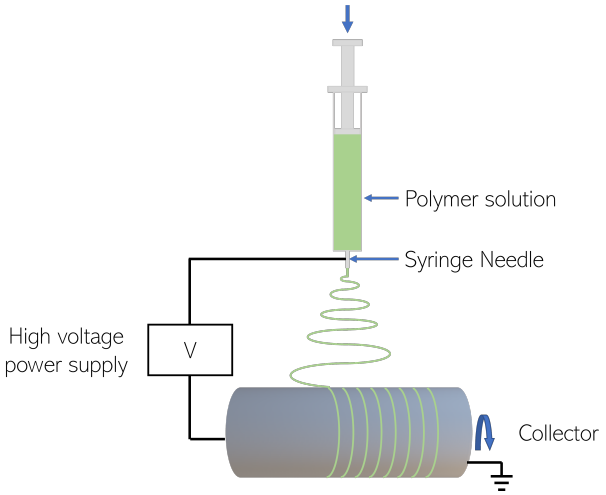

Figure 5.8: Scheme of the setup for electrospun MNFs.

5.1.3 Comparison

Table 5.1: Main advantages and disadvantages between the principal MNFs fabrication methods.

Method	Main Advantages	Main Disadvantages
Flame-heated taper drawing	Low diameters; low propagation losses; controllable geometry; pigtailed tapers.	H_2O or OH contamination; random turbulence of the flame; fixed temperature.
Laser-heated taper drawing	Simple setup; capable of working in a vacuum or controlled atmospheres; stability; high reproducibility; pigtailed tapers.	"Self-regulating" effect limiting the minimum diameter
Electrically-heated taper drawing	Simple design; controllability; do not generate disturbing gas flow; produce MNFs with extremely low OH content; pigtailed tapers.	Contamination of MNFs at high temperatures; unable to reach very high temperatures.
"Self-modulated" taper-drawing	Smallest radii; pigtailed tapers.	Time consuming; complex; high losses; only produces tip MNFs.
Directly drawing from bulk glasses	Flexible; does not require expensive equipment; can draw from multiple bulk materials; can tailor optical properties.	Lacks controllability on the uniformity and diameter of the MNF; does not produce pigtailed tapers.
Electrospinning	Wide variety of polymer materials; produces very long MNFs.	Highly dependent on the deposition conditions; high propagation losses; requires expensive equipment; does not produce pigtailed tapers.

5.1.4 Optical Properties

The mathematical model of an MNF considers a fiber with a circular cross-section, a smooth transition region and a region with uniform diameter, and an infinite air-cladding with a step-index profile [165]. This profile can be expressed as:

$$\begin{cases} n_1, & 0 < r < a \\ n_2, & a \leq r < \infty \end{cases} \tag{5.1}$$

where a is the radius of the MNF, and n_1 and n_2 are, respectively, the refractive indices of the MNF and air. Additionally, the diameter ($2a$) of the fiber cannot be too small (e.g., d > 10nm), a regime where the permittivity (ε) and permeability (μ) of the bulk material can be used to describe the response of the medium to an incident electromagnetic field, and the length must be reasonably large to establish spatial steady state [148].

The material of the fiber and the cladding medium (usually air) are typically dielectric media, in the transparent spectral range [165]. Under these conditions, the exact solution of Maxwell's equation for the hybrid modes $HE_{\nu m}$ and $EH_{\nu m}$ gives the eigenvalue equations [175]:

$$\left\{\frac{J'_\nu(U)}{UJ_\nu(U)}+\frac{K'_\nu(W)}{WK_\nu(W)}\right\}\left\{\frac{J'_\nu(U)}{UJ_\nu(U)}+\frac{n_2^2K'_\nu(W)}{n_1^2WK_\nu(W)}\right\}=\left(\frac{\nu\beta}{kn_1}\right)^2\left(\frac{V}{UW}\right)^4 \tag{5.2}$$

where J_ν is the νth-order Bessel function of the first kind, K_ν is the νth-order modified Bessel of the second kind, k is the wave number given by $k=\frac{2\pi}{\lambda}$, and β is the propagation constant given by $\beta=n_{eff}k_0$ with n_{eff} being the effective RI of the propagation medium. For the TE_{0m} and TM_{0m} modes, equation 5.2, results in:

$$TE_{0m}\ \text{mode} \qquad \frac{J_1(U)}{UJ_0(U)}+\frac{K_1(W)}{WK_0(W)}=0 \tag{5.3}$$

$$TM_{0m}\ \text{mode} \qquad \frac{n_1^2J_1(U)}{UJ_0(U)}+\frac{n_2^2K_1(W)}{WK_0(W)}=0 \tag{5.4}$$

The parameters U and W are given by:

$$U=r\sqrt{k_0^2n_1^2-\beta^2} \qquad W=r\sqrt{\beta^2-k_0^2n_2^2} \tag{5.5}$$

these parameters are related to the normalized frequency, or V number, by:

$$V=\sqrt{U^2+W^2}=\frac{2\pi}{\lambda}r\sqrt{n_1^2-n_2^2}=\frac{2\pi}{\lambda}rNA \tag{5.6}$$

where NA is the numerical aperture of the fiber and is the wavelength of the propagating light, respectively.

The guided modes supported by the MNF can be calculated by determining the propagation constants (β), that can be numerically attained from equations 5.3 and 5.4. Single mode operation, where only HE_{11} mode is guided, can also be achieved for MNF diameters lower than d_{SM}, corresponding to a V number of approximately 2.405 [165].

When the diameter of MNFs approaches the value of the wavelength of the guided light, an MNF with low-index cladding (such as air, for example) displays interesting optical properties such as strong evanescent fields, tight optical confinement, the potential for tailoring the dispersion properties, and strong nonlinearity.

5.1.4.1 Evanescent Field and Mode Confinement

Strong evanescent fields allow strong interaction between the guided light and the surroundings, in a near-field region [141]. For a cylindrical and uniform MNF, the energy flow inside and outside of the fiber can be calculated by the z-components of *Poynting* vectors given by [165]:

For $0<r<a$

$$\begin{aligned}S_{z1}=&\frac{|a^2|}{2}\left(\frac{\varepsilon_0}{\mu_0}\right)^{\frac{1}{2}}\frac{kn_1^2}{\beta J_1^2(U)}\left[a_1a_3J_0^2\left(\frac{Ur}{a}\right)+a_2a_4J_2^2\left(\frac{Ur}{a}\right)+\right.\\&\left.\frac{1-F_1F_2}{2}J_0\left(\frac{Ur}{a}\right)J_2\left(\frac{Ur}{a}\right)cos(2\phi)\right]\end{aligned} \tag{5.7}$$

For $r \geq a$:

$$S_{z2} = \frac{1}{2}\left(\frac{\varepsilon_0}{\mu_0}\right)^{\frac{1}{2}} \frac{kn_1^2}{\beta K_1^2(W)} \frac{U^2}{W^2}\left[a_1 a_5 K_0^2\left(\frac{Wr}{a}\right) + a_2 a_6 K_2^2\left(\frac{Wr}{a}\right) - \frac{1-2\Delta-F_1F_2}{2} K_0\left(\frac{Wr}{a}\right) K_2\left(\frac{Wr}{a}\right) cos(2\phi)\right] \tag{5.8}$$

where ε_0 and μ_0 are, respectively, the electric permittivity in free space and permeability in a vacuum, and Δ is the RI contrast $\left(\Delta = {}^{(n_1^2-n_2^2)}/_{2n_1^2}\right)$. The definition of the constants $a_{1,\ldots,6}$ and $F_{1,2}$ are detailed in appendix C. Using equations 5.7 and 5.8, it is possible to calculate the profile of the *Poynting* vectors as presented in Figure 5.9.

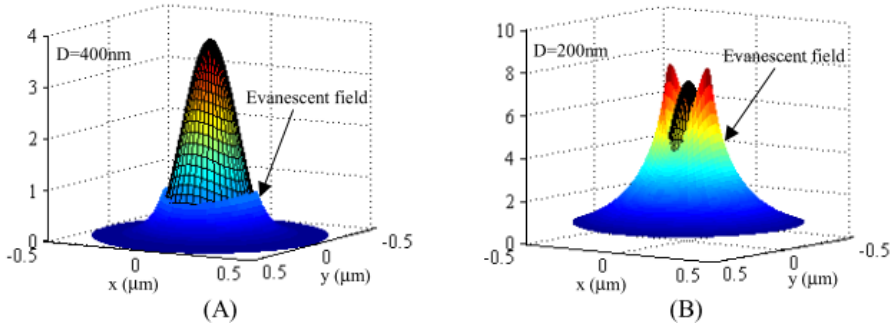

Figure 5.9: Profile of the Poynting vector in the z-direction for a fiber composed of silica at a wavelength of 633 nm with a diameter of (a) 400 and (b) 200 nm. Image adapted from [175].

The fraction of power that travels inside of the core, also called confinement factor (η), can be determined by:

$$\eta = \frac{\int_0^a S_{z1}\, dA}{\int_0^a S_{z1}\, dA + \int_a^\infty S_{z2}\, dA} \tag{5.9}$$

where $dA = rtdr \cdot d\phi$, $\int_0^a S_{z1}\, dA$ and $\int_a^\infty S_{z2}\, dA$ are the total power that travels in the core and in the cladding region, respectively.

The evanescent field can be easily tailored by controlling the radius of the MNF, the index contrast (Δ), and the wavelength of the propagating light (λ). A stronger evanescent field, a consequence of weaker confinement, results in strong near-field interaction between the guided light and the surroundings. This is beneficial for spectroscopy, sensing applications, high-Q resonators, and evanescent coupling [176]–[181], for example. Moreover, an evanescent field with a steep gradient, creating a strong gradient force, can be used for optical trapping and transport [182], [183], and for cold atom trapping [184], [185].

Conversely, by creating tighter confinement, a weaker evanescent field is achieved. This can be useful for reducing cross-talk between different optical components, increasing the density in optical circuits [165], and for the low-loss propagation in fibers with small bending radius [163], [186]. Furthermore, the tight confinement also results in enhanced nonlinearity (γ) in low-power conditions [187], and phenomena like supercontinuum generation [153], second- and third-harmonic generation have already been observed in MNFs [154], [188], for example [189].

5.1.4.2 Nonlinearity

Nonlinear effects occur when the medium responds in a nonlinear manner to the strength of an applied optical field. These effects occur when the strength of the optical field is high enough so that the polarization can no longer be described by a linear relationship with the electric field, and higher-order terms need to be considered. These higher terms are related to the second- and third-order nonlinear optical susceptibilities ($\chi^{(2)}$ and $\chi^{(3)}$) [190]. Strong electric fields can be achieved in MNFs in the tight confinement regime, where light is confined in a very small region. For example, if the radius of the fiber's core is reduced by a factor of 10, the optical power density is increased by a factor of 100. By tailoring the MNF radius, the beam spot size can be further decreased leading to an increased nonlinearity of the medium. The nonlinearity can be described by the nonlinear coefficient given by [158]:

$$\gamma = \frac{k_0 n_2}{A_{eff}} \tag{5.10}$$

where A_{eff} is the effective core area, given by $A_{eff} = \pi\omega^2/4$, with ω being the beam spot size defined as the radius at which the intensity of the electric field drops to $1/e^2$ [158]. By enhancing nonlinearity, phenomena like supercontinuum generation or second- or third-harmonic generation can occur.

Supercontinuum generation is the result of a multitude of nonlinear effects, such as four-wave mixing (FWM), self- and cross-phase modulation (SPM, XPM), stimulated Raman scattering (SRS) and other effects of dispersion [190]. When the input pulse is sufficiently intense, a broadening of the pulse extending over a frequency range exceeding 10 THz is observed. Supercontinuum has been generated in silica fibers [191], [192], and other glasses [193]–[195].

High-order harmonic generation is the conversion of a fundamental harmonic with a frequency ω into a harmonic $n\omega$ of order n that happens when an intense electric field travels in a nonlinear medium. These phenomena are particularly useful for the efficient generation of lower wavelengths without an external nonlinear crystal [189]. For the production of optical harmonics, the medium must have a nonlinear susceptibility coefficient and be lossless at the fundamental and harmonic frequencies [196]. Silica is a centrosymmetric material meaning that the second-order susceptibility ($\chi^{(2)}$) is zero, thus, it should not be possible to achieve second harmonic generation in silica fibers. However electric-quadrupole and magnetic-dipole moments can generate weak second-order nonlinear effects [197] or defects can be created by doping the glass fiber with other materials, allowing the observation of second harmonic generation in silica fibers [188], [198]–[200]. Third-harmonic generation, analogously, results in the emission of a photon with a frequency three times larger than the incident one due to the non-zero third-order susceptibility ($\chi^{(3)}$). This effect has been demonstrated in MNFs by controlling phase matching [154], [201], [202].

5.1.4.3 Dispersion

Dispersion arises from the frequency dependence of the response of a medium to a traveling electromagnetic wave. This manifests as a variation of the effective index of the guided mode with frequency [203]. Dispersion has two contributions: intrinsic material dispersion and waveguide properties. In the case of MNFs working at the single-mode regime, only chromatic dispersion of the fundamental guided mode is taken into account. In other instances, polarization mode dispersion or intermodal dispersion between transverse modes should be considered [204].

The effects of dispersion can be accounted for by expanding the mode propagation constant β in a Taylor series about the frequency of the pulse, ω_0 [203]:

$$\beta(\omega) = n(\omega)\frac{\omega}{c} = \beta_0 + \beta_1(\omega - \omega_0) + \frac{1}{2}\beta_2(\omega - \omega_0)^2 + \ldots \tag{5.11}$$

The parameters $\beta_{1,2}$ are related to the RI through:

$$\beta_1 = \frac{1}{v_g} = \frac{n_g}{c} \tag{5.12}$$

$$\beta_2 = \frac{1}{c}\left(2\frac{dn}{d\omega} + \omega\frac{d^2n}{d\omega^2}\right) \tag{5.13}$$

where n_g is the group RI and v_g is the group velocity. The dispersion of the group velocity, known as group velocity dispersion (GVD), is represented by the factor β_2 and is responsible for the broadening of the pulse. Dispersion can also be defined by $D = -(2\pi c/\lambda^2)\beta_2$. The GVD controls the broadening of ultrafast pulses, the generation of temporal optical solitons, the walk-off between pump and probe, and the phase-matching of parametric processes (e.g., FWM, high harmonic generation) [187]. Optical MNFs offer the possibility of tailoring the dispersion properties by controlling its dimensions and external medium [158].

5.1.5 Applications

The multitude of optical properties and their tailoring capability enabled the use of MNFs for a variety of applications. These applications can be divided into five different classes: waveguide and near-field optics, nonlinear optics, quantum, and atom optics, plasmonics, and optomechanics. The main applications are summarized in the diagram of Figure 5.10. In this section, the main applications of MNFs will be presented with a special focus on optical sensors, MNFs lasers, passive devices, nonlinear optics, and particle manipulation.

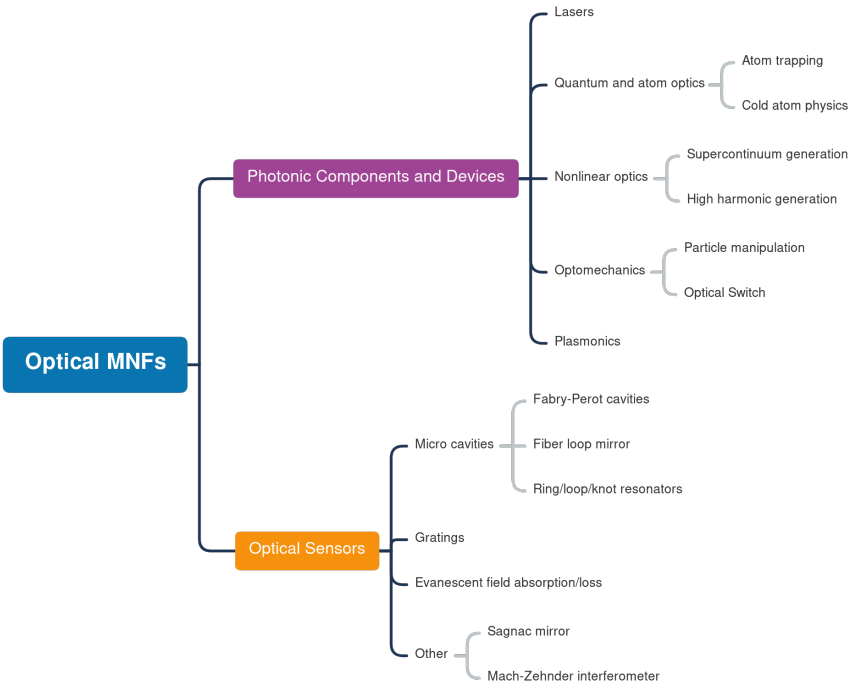

Figure 5.10: Applications of MNFs.

5.1.5.1 Optical Sensors

The optical properties described in the previous sections have been explored for the fabrication of new optical sensors based on the different physical properties of MNFs. The optical sensors proposed in the literature can be divided into five different categories: intensity detection due to evanescent field loss or absorption, resonators, microcavities, gratings, and plasmonics.

Evanescent field-based MNFs sensors take advantage of the high fractional power that travels in the vicinity of the fiber to create loss or absorption on the waveguided light to measure a property of the surrounding medium. In 2005, it was reported a hydrogen sensor based on a Pd-coated tapered fiber with a waist diameter of 1.3 μm [205]. The presence of hydrogen converted the Pd layer into a palladium hydride film, changing the attenuation of the propagating light. The sensor was capable of detecting low concentrations of hydrogen with a response time of 10 seconds. A similar working principle was used for the development of an MNF with a diameter of 900 nm embedded on a 125 μm microfluidic channel [206]. The sensor was capable of detecting methylene blue with a low detection limit. It was also tested for serum albumin measurements, where a detection limit of 10 fg mL^{-1} was attained, showing it as a promising sensor for single or few molecules detection on biological samples. More recently, Lie and Li [207] reported an abrin detection nanofiber functionalized with a rabbit-anti-abrin antibody. The developed sensor presented a limit of detection of 10 pg/mL with a response time under 10 minutes.

The strong evanescent optical fields can also be used for the fabrication of resonators, where a closed loop is created and light is evanescently coupled in the overlapping regions [208]. Typical configurations include loop, knot, or coil resonators as schematized in Figure 5.11. Loop resonators are the simplest configuration, where van der Waals and electrostatics forces sustain the position of the fiber. This configuration has been proposed for temperature [209], RI sensing [210], [211] and relative humidity [212]–[214]. Even though loop resonators offer a simple configuration and high Q-factor [165], they are not mechanically stable. In 2006, Jiang *et al.* [215] proposed a knot configuration demonstrating its mechanical stability in the air and water, and placed it on an MgF_2 substrate. Since then, similar configurations have been presented in the literature for temperature [216]–[218], humidity [219], [220], and electrical current sensing [221], among others [222]–[225]. The coil resonator is the most complex configuration of the three. It was first proposed in 2004 by Sumetsky [226] and experimentally performed in 2007 by Xu and Brambilla [227]. This structure is intrinsically more stable and has been proposed for gyroscope applications [228] and optical sensing of RI [229]–[231], current [232], salinity [233], acoustic waves [234], among other parameters [235]–[237].

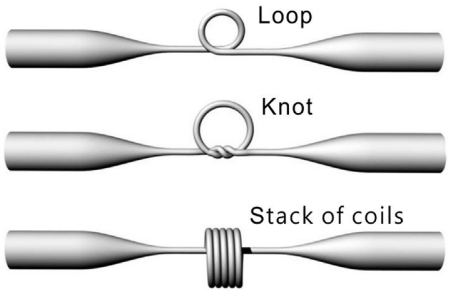

Figure 5.11: Schematic diagram of typical configurations of MNF-based optical resonators: loop, knot, and coil. Image adapted from [208].

Interferometric microcavities can be fabricated using MNFs. The main interferometric configurations are the Fabry-Perot, Sagnac, and Mach-Zehnder microcavities. Fabry-Perot microcavities can be fabricated using two FBGs separated by the tapered region resulting in a structure capable

of sensing simultaneously multiple parameters such as temperature and RI [238], [239]. The MNF can also be used as a tip for temperature sensing [240], [241]. Moreover, the MNF can be added to an FP cavity to enhance the sensitivity to different properties such as force [242]. Sagnac interferometers based on MNFs can be achieved by using a configuration similar to knot resonators [243] or by placing the tapered region inside of the cavity [244]. The two configurations have been proposed for humidity [245], RI [244], magnetic field [246], airborne contaminant sensing [247], among others [248]–[250]. Mach-Zehnder microcavities have also been reported in the literature for temperature [251], current [252], vibration [253], RI [254], and simultaneous measurements of temperature and RI [255] or pressure [256].

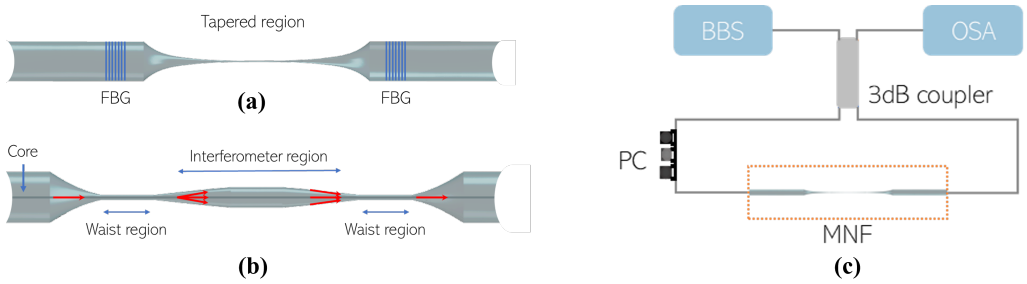

Figure 5.12: Schematic diagram of typical microcavity configurations on MNF: (a) Fabry-Perot, (b) Mach-Zehnder, and (c) Sagnac.

Due to the small size of MNFs, different writing techniques have been reported for the fabrication of FBGs including Ti:sapphire femtosecond laser direct writing [257], FIB milling [258]–[260], among others [261]. FBGs inscribed in MNFs have been proposed for temperature [257], [259], humidity [262], RI [261], and gas sensing [263]. LPGs can be inscribed in MNFs using CO_2 laser [264], by point-by-point dip coating method [265], by point-by-point laser inscription [266], or by electric arc discharge [267]. Nano LPGs have been proposed for simultaneous measurement of RI and temperature [264], [267], and strain and temperature [265]. In Figure 5.13 an example of FBG and LPG inscribed on an MNF is presented.

Plasmonic sensors have been fabricated in MNFs by coating the tapered region with gold nanoparticles that can be excited by the evanescent field from the MNF [268]. The gold nanoparticles were coated with a specific receptor material that can accept the analyte to monitor, attaining a limit of detection of 1 pg/mL. Wang et al [269] also presented a plasmonic sensor, using a gold nanorod-coated polymer MNF. The sensor was tested for humidity sensing, attaining a response time of 110 ms.

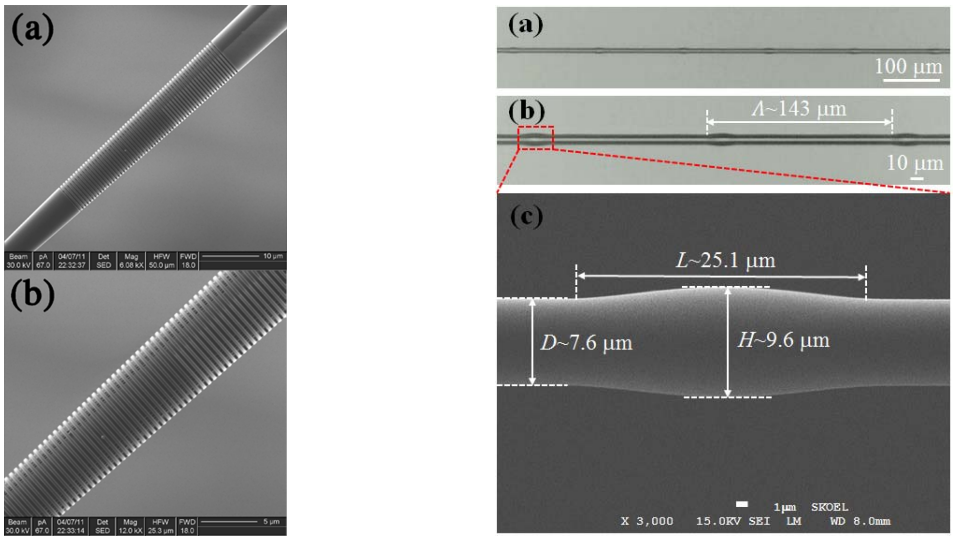

(a) (b)

Figure 5.13: Gratings inscribed on an MNF (a) an FBG inscribed by FIB milling, image adapted from [259], and (b) LPG fabricated through point-by-point dip coating method, image adapted from [265].

5.1.5.2 Lasers

Fiber lasers can be created using MNFs by incorporating an active material in an optical cavity such as a loop, knot, or on an FP cavity using FBGs [148]. The incorporation of the active material can be achieved by doping the MNF or by using the active material in the vicinity of the MNF benefiting from the strong evanescent fields. In 2006, Jiang *et al.* [270], presented a microfiber knot laser. The laser cavity had a diameter of 2 mm using a 3.8 μm microfiber drawn on an Erbium:Ytterbium (Er:Yb) doped phosphate glass. The presented laser had a maximum output power higher than 8 μW with a central wavelength of 1.5 μm. More recently, Fan *et al.* [271], proposed a microfiber laser based on a double-knot resonator in an Er:Yb co-doped phosphate glass with a diameter of 1.88 μm, shown in Figure 5.32. The presented laser attained an output power higher than 0.95 μW with a central wavelength of 1536.1 nm and a linewidth of 2 kHz. An electrically tunable laser was also reported using an Er-doped fiber on a microfiber knot resonator [272]. The peak wavelength can be tuned between 1533.3 to 1533.9 nm by applying an electrical current on the knot.

The high fractional power on evanescent fields provided by MNFs also enables the inclusion of active materials in the cladding region. The MNF is used to efficiently pump the active molecules and to collect the emission signal [273]. A laser based on this mechanism was reported by Jian *et al.* [273], where a 3.9 μm diameter nanofiber was assembled into a knot with a 350 μm diameter. The knot was immersed in ethylene glycol doped with 5 mM/L Rhodamine 6G (Rh6G) dye and was pumped with a 532 nm laser. The laser emission was observed between 570 and 580 nm with a pump energy threshold of 9.2 μJ/pulse. Similarly, doping the cavity with active materials can also be achieved by coating an MNF region inside of an optical cavity. This was reported by Ding *et al.* [274], where three different semiconductor nanowires were coated on an MNF that was pumped by a 355 nm pulsed laser afterwards. The three semiconductors - cadmium selenide (CdSe), cadmium sulfide (CdS), and zinc oxide (ZnO) - generate red-green-ultraviolet laser emission that can be attained simultaneously as demonstrated in Figure 5.14c.

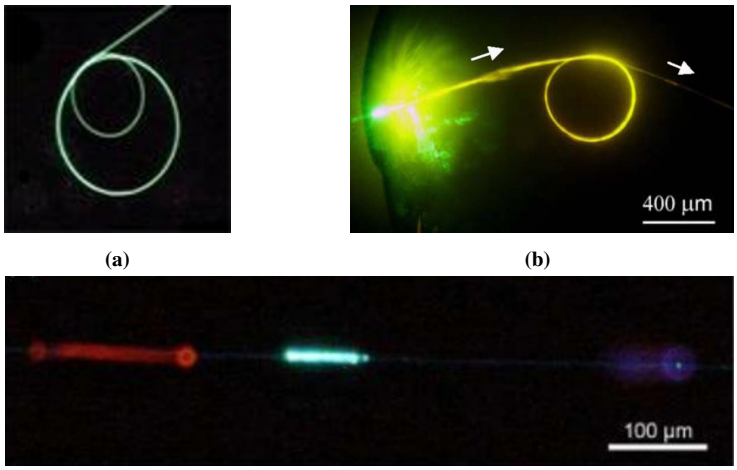

Figure 5.14: (a) Microscope photograph of the double knot laser proposed by [271]; (b) Microscope photograph of a 450 μm diameter knot immersed in a 5 mM/L rhodamine 6G dye solution, that is evanescently pumped by 532 nm wavelength light guided along the knot that exhibits yellow photoluminescence, image adapted from [273]; (c) image of the hybrid structure presented by Ding *et al.* pumped at 355 nm, image adapted from [274].

5.1.5.3 Passive Devices

5.1.5.3.1 Directional couplers

Directional couplers are photonic devices that enable power exchange between two or more waveguides. When waveguides are placed parallel and in close proximity to each other, significant interaction may occur, particularly when the guided modes propagate with the same phase velocities [275]. The strong evanescent fields and the tight optical confinement provided by MNFs offer the possibility of their use as fiber couplers. Moreover, the ultra-low propagation and bending losses make them well suited for the integration on highly compact photonic integrated circuits [276], [277]. In 2009, Jung *et al.* [278], presented an optical coupler based on a microfiber with 1.5 μm diameter for single-mode operation over a broad spectral window. The coupler was tested in a 3-dB splitting operation, for wavelengths between 400 and 1700 nm with an excess loss lower than 0.1 dB at a wavelength of 1.5 μm. More recently, a microfiber-based coupler with a variable coupling ratio was reported by Shao *et al.* [277]. The two fibers were fabricated using a parallel pulling process to ensure similar fabrication conditions and, thus, similar features. The two fibers were twisted as shown in Figure 5.15 and, by adjusting the contact length, the coupling ratio can be controlled.

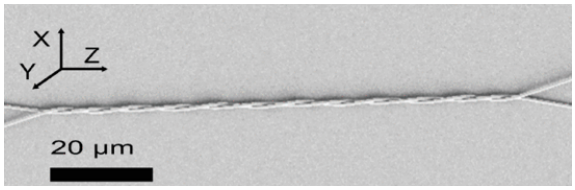

Figure 5.15: SEM image of the twisted section of the coupler proposed by Shao *et al.* [277].

5.1.5.3.2 Filters

Optical filters are an essential component in photonic devices and are capable of filtering out noise, flattening, or suppressing the gain profile after amplification [165]. One important filter

on photonic devices is the short-pass or low-pass filter. In this type of filter, the high wavelength region is rejected to reduce or suppress noise. Chen *et al.* [279] reported a compact short-pass filter with a controllable cutoff wavelength for a range of 400 nm. The filter presented an insertion loss of 0.3 dB with a working range between 600 to 1500 nm. Similarly, Jung *et al.* [280] presented a high-order mode filter to suppress higher-order modes to ensure a single-mode operation in a broad spectral window. Another relevant filtering mechanism is add-drop filtering, particularly important for wavelength division multiplexing [281]. Microfiber-based add-drop filters benefit from the high Q-factors provided by resonating cavities based on MNFs, such as knot resonators.

5.1.5.4 Other applications

5.1.5.4.1 Nonlinear optics

As a result of the small mode area and engineerable dispersion, MNFs exhibit interesting nonlinear effects such as supercontinuum generation and second- and third-harmonic generation as introduced in section 5.1.4.2. Besides these interesting effects, MNFs can also exhibit bistability [282], [283], two-photon absorption [8], [284]–[286], and the generation of solitons [287]–[289].

5.1.5.4.2 Particle manipulation

Optical manipulation of particles has found many applications, particularly in life science and biochemistry [290], due to its ability to trap and characterize biological specimens with no contact [291], [292]. MNFs can provide means for particle manipulation using two different mechanisms: using a tip configuration, the small mode area can be used for trapping and analyzing the particle; using a biconical configuration, where the strong evanescent field can be used for trapping and transport of particles. Using the tip configuration, Brambilla *et al.* [293] reported an optical tweezer based on a microfiber tip capable of trapping silica microspheres with 1 μm diameter using an input power higher than 10 mW. In the same year, the aforementioned authors [290] reported optical manipulation of polystyrene (PS) spheres taking advantage of the strong evanescent fields of MNFs with 950 nm diameter and 6-mm length. Similarly, Irawati *et al.* [294] reported the optical trapping and transport of PS spheres with two different diameters, and microfibers with variable waist diameters. More recently, Yoshino *et al.* [182] reported the optical transport of sub-micron lipid vesicles in microfiber with waist diameters between 350 and 600 nm, taking advantage of the strong evanescent fields. The concept of the trapping device is presented in Figure 5.16a. Light-induced rotation was reported by Tkachenko *et al.* [183] as presented in Figure 5.16b. The light that is guided in the single-mode microfiber induces force and torque to the 3 μm PS particles, inducing an orbital motion around the MNF.

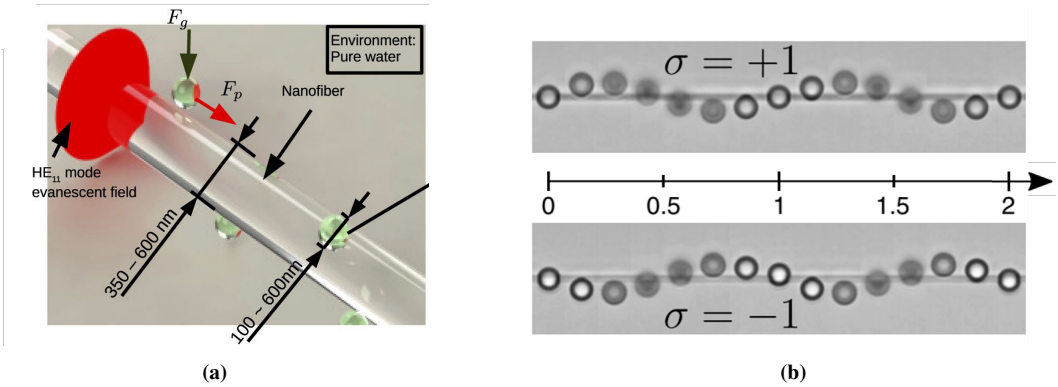

(a) (b)

Figure 5.16: (a) Concept of the particle manipulation device, trapping 100-600 nm liposomes near a nanofiber, image adapted from [182]; (b) Time-lapse image compilation of polystyrene orbiting around an optical nanofiber due to the azimuthal force caused by the guidance of an elliptically polarized field, image adapted from [183].

5.2 Experimental Results

5.2.1 Laser-heated taper drawing

The laser-heated taper drawing was the first method used in this work for fabricating microfibers. The experimental setup was composed of a continuous wave (cw) CO_2 laser with a 30 W peak power (Synrad 48-1SAM), connected to a laser controller (Synrad UC-200) that enables to control the power of the laser, duty cycle, and modulation frequency by pulse width modulation (PWM). The beam that outputs from the laser is redirected by a set of two silver-coated mirrors with a 25.4 mm diameter into a ZnSe-coated plano-convex lens with a 25.4 mm diameter and 100 mm focal length that focuses the beam on the fiber. The fiber, in turn, is clamped on two motorized linear stages (Aerotech FA130-140). The beam that passes through the fiber is, then, refocused on the fiber using a 50.8 mm diameter silver-coated concave mirror with a focal length of 150 mm. The process of taper drawing is controlled by a digital camera placed on top of the fiber. The complete experimental setup, presented in Figure 5.17, is placed inside a plexiglass box to reduce exposure to the CO_2 laser beam.

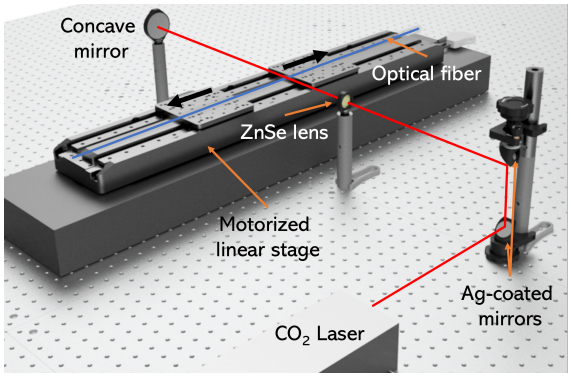

Figure 5.17: Schematic diagram of the laser-heated taper drawing setup composed of a cw CO_2 laser, a set of two silver-coated mirrors to redirect the laser beam to the fiber. The optical fiber is clamped on a motorized translation stage with two motors controlled simultaneously. A concave mirror was added to the setup to reflect the light back to the fiber, to increase the symmetry of the tapered region.

The transmission spectrum of the fiber, presented in Figure 5.18b was analyzed in real-time

during the pulling process using a broadband optical source, with a 100-nm bandwidth in the C-band region, and an optical spectrum analyzer (Yokogawa AQ6370C). The shape of the tapered region was evaluated using the digital camera, as presented in Figure 5.18a. It was observed that this technique does not allow the fabrication of tapered fibers with diameters lower than tens of micrometers. Moreover, for these dimensions, the optical losses resultant from the transition regions are exceedingly high and, therefore, make this technique impractical for the fabrication of low-loss few-micrometer fibers.

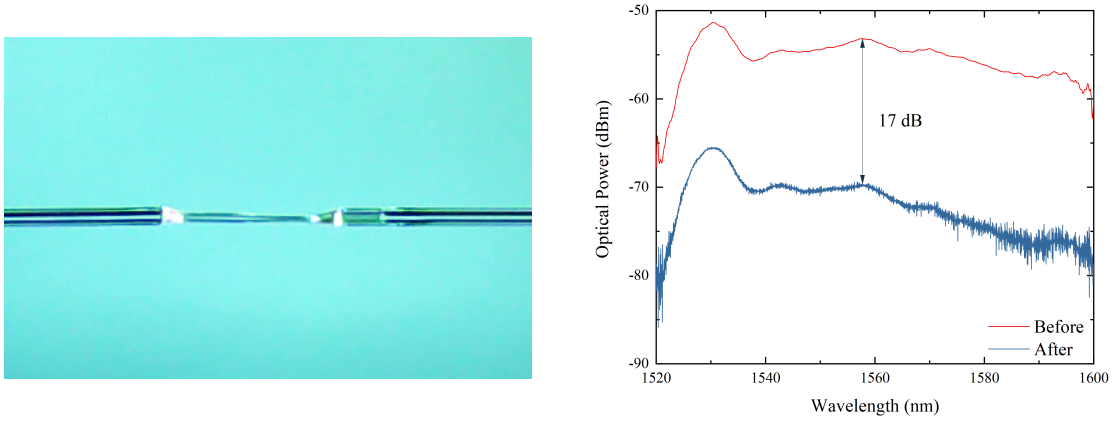

Figure 5.18: (a) Photograph of the fabricated taper using the CO_2 laser system; (b) Corresponding transmission spectra before and after taper drawing.

5.2.2 Electrically-heated taper drawing

The second method explored for the fabrication of MNFs was the electrically-heated taper drawing. The experimental setup was composed of an electric microheater (FibHeat200, Micropyretics Heaters International, USA) connected to a temperature controller (Eurotherm 2416). For the fiber pulling, two fiber clamps were attached to two independent computer-controlled motorized linear stages (LTM 120, OWIS, Germany). This setup is also capable of real-time monitoring of the transmission spectra using an optical source and a spectrometer or an OSA. To reduce turbulence from air movement, the heater and positioning stages were placed inside a plexiglass box. The complete setup is presented in Figure 5.19. In the following subsections, a more detailed overview of each system will be presented.

5.2.2.1 Experimental Setup

5.2.2.1.1 Electric microheater

The electric microheater used in this work has a heating zone of 12 mm, with a fiber slot of $2 \times 30 \times 10$ mm, and is capable of reaching temperatures up to 1800 °C. A close-up of the heating element is presented in Figure 5.20a. It is equipped with a temperature controller (Eurotherm 2416) that allows the implementation of complex temperature curves to the microheater, enabling higher flexibility when compared to other methods such as the flame brushing technique, where both the temperature and geometry of the heating source are fixed. The temperature of the heater is acquired using a B-type thermocouple. However, the position of this sensor is distanced from the heating element and from the fiber slot, meaning that the readout temperature is much lower than

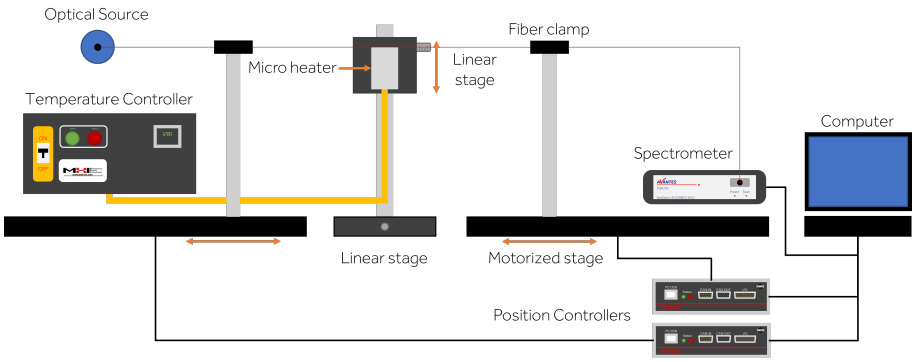

Figure 5.19: Schematic diagram of the electrically-heated taper drawing setup composed of a microheater with temperature controller, two linear stages, and the optical monitoring system composed of an optical source and a spectrometer.

at the fiber position. The real temperature can be estimated using the calibration curve provided by the supplier MHI.

5.2.2.1.2 Positioning stages

The positioning and pulling of the fiber were carried out using a system of fiber clamps, placed symmetrically from the heater, as can be observed in Figure 5.20b. The fiber clamps were fixed on two motorized linear precision stages, each of them connected to a position control unit (PS 10, OWIS, Germany). By using two position control units it is not possible to fully synchronize the movement of the two translation stages, however, considering the low velocities used in the pulling process, the delay between the two stages can be disregarded. The micro-heater was fixed on a system composed of two linear manual stages that allowed the alignment of the heater to the fiber clamps. Besides, the vertical traveling stage allowed the withdrawal of the heater once the pulling process was completed.

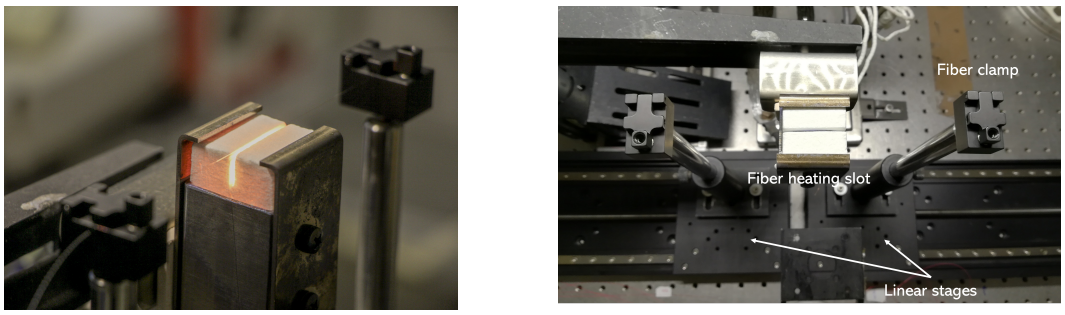

(a) **(b)**

Figure 5.20: (a) Close-up photograph of the fiber slot microheater, heated to approximately 1200° C.; (b) Fiber clamps, mounted on the motorized linear stages, placed at the same distance from the heater.

5.2.2.2 Optical monitoring system

The drawing process was monitored in real time by acquiring the transmission spectra of the tapered fiber. The simple monitoring setup was composed of a broadband light source and an OSA or a spectrometer, depending on the wavelength of interest and on the required acquisition rate. In this work, two different wavelength regions were studied in the NIR region: between 800 and 1000 nm, using a halogen light source (HL-200, Ocean Insight, USA) and a spectrometer with a high acquisition rate (ULS2048CL-EVO, Avaspec, The Netherlands) with a detection range between 200 and 1100 nm; and at 1550 nm in the C-band region, using a broadband optical source (ASE source) centered at this wavelength with a bandwidth of approximately 100 nm and an OSA (AQ6370C, Yokogawa Electric, Japan) with a wavelength range between 600 and 1700 nm and a resolution up to 0.02 nm. For the high-speed acquisition system, Python-based software was developed. This software allowed the monitoring of the total spectrum of the tapered fiber and the monitoring of the transmitted optical power at a specific wavelength. More details of this software can be found in Appendix D.

5.2.2.3 Tapering geometry

The model for the shape of optical fiber tapers was first presented by Birks *et al.* [295] in 1992, simply considerating the conservation of volume. This model is limited to cylindrical geometries and uniform temperatures in the hot zone, avoiding fluid mechanics approaches. The model is independent of temperature, but some considerations need to be made: the temperature must be high enough for the fiber to be in a soft state, but not high enough to reduce the viscosity of the fiber to the point where it starts to deform or evaporate. The final taper profile is expected to be similar to the one presented in Figure 5.21:

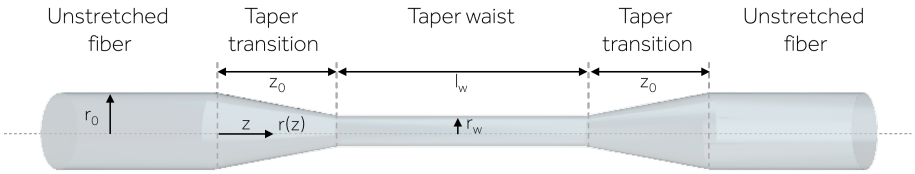

Figure 5.21: Structure of the fiber taper composed of three different regions: unstretched fiber where the diameter is r_0, taper waist where the diameter is minimum and constant, and the taper transition region.

For a constant hot-zone region, as in the present case, the final waist radius can be determined by:

$$r(z) = r_0 e^{-z/2L_0} \tag{5.14}$$

where r_0 is the radius at the unstretched region, L_0 is the length of the hot-zone region and z is the pulling distance. Using this equation it is possible to estimate the final waist diameter of the MNF.

5.2.2.3.1 Hot-zone region calibration

The effective hot-zone region was estimated using the model demonstrated by Birks *et al.* [295] by fabricating several tapered fibers with different pulling lengths (z of equation 5.14). Moreover, the influence of the vertical position of the heater concerning the fiber was also studied by fabricating tapers at three different vertical positions distanced by 500 μm. During this experiment, the pulling velocity was maintained constant at 0.1 mm/s. In Figure 5.22, the average taper waist radius for

the different traveling distances is presented. It is possible to observe that the experimental data are consistent with the theoretical model, with an r-squared of 0.996. The attained hot-zone region was 8.6±0.4 mm, which is significantly lower than the value of 12 mm provided by the supplier.

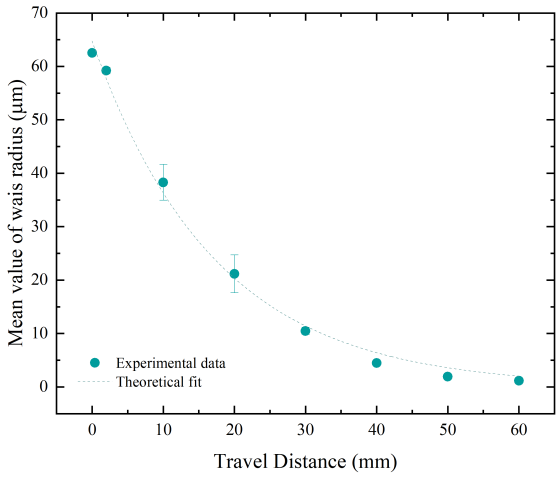

Figure 5.22: The radius of the waist of the taper with respect to the total travel distance.

The attained hot-zone dimension for the three different heater vertical positions is presented in Table 5.2. The results suggest that the effective hot-zone region can be varied by changing the vertical position of the heater regarding the fiber zone. For the following fabricated tapers, a vertical position of initial +500 µm was selected, as it presented a good fit with the theoretical model while presenting a high hot-zone dimension. Thus, the effective hot-zone dimension of the subsequently tapered fibers is 8.3 mm.

Table 5.2: Effective hot-zone dimension calculated at three different vertical positions of the heater.

Position	Fitted L_0 (mm)	R-Squared
Initial	9.3	0.985
Initial + 500 μm	8.3	0.997
Initial + 1000 μm	8.2	0.997

5.2.2.3.2 Effects of pulling velocity

The velocity of the pulling stages can affect the quality and shape of the fabricated taper. To study this influence, several fibers were tapered with a total traveling distance of 15 mm, using pulling velocities between 0.02 and 0.1 mm/s. The results, presented in Table 5.3, show that, for higher velocities, the final waist radius is larger. This suggests that, during the tapering process, the fiber slides on the fiber clamps, thus, reducing the total pulling distance. In order to reduce fiber sliding while preventing the procedure from being exceedingly time-consuming, the velocity chosen for the fabrication of subsequent tapers was 0.04 mm/s.

Table 5.3: Taper waist diameter for the different traveling velocities, for a constant traveling distance of 15 mm.

Velocity (mm/s)	Taper waist diameter (μm)
0.02	17.344
0.04	17.705
0.06	18.084
0.08	19.725
0.10	21.259

5.2.2.3.3 Taper profile

The profile of the tapered fiber is an important feature to characterize, as it gives important information concerning the adiabaticity of the taper [296]. Several methods can be used to determine the profile of the tapered region: CCD imaging [297], whispering gallery mode spectroscopy [298], or light diffraction [299], for example. Due to the simplicity of implementation and contactless nature, the light diffraction method was chosen in this work. This method uses the diffraction pattern created by the light that propagates through the optical fiber to measure its diameter with high accuracy [300], as shown in Figure 5.23.

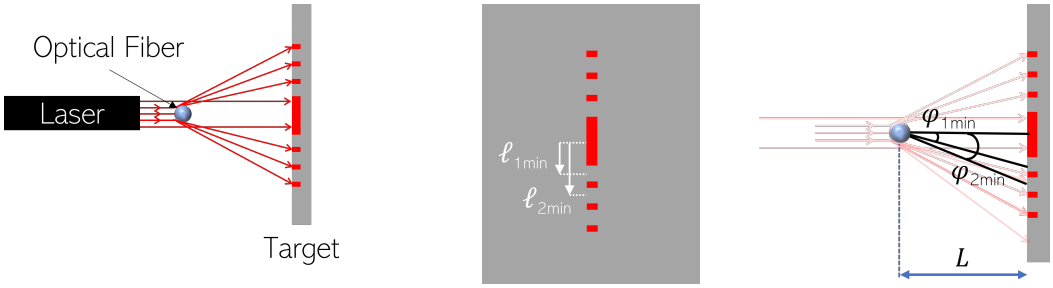

Figure 5.23: Schematic diagram of (a) the diffraction method, (b) resultant diffraction pattern, and (c) geometrical analysis.

The diameter of the fiber can be calculated by:

$$d = \frac{4\lambda}{2\varphi_{1min} + \varphi_{2min}} \tag{5.15}$$

where λ is the laser beam wavelength, and $\varphi_{1,2min}$ are the angle of the first and second minima regarding the fiber axis as shown in Figure 5.23c, which are given by:

$$\varphi_{1,2min} = arctan\left(\frac{\ell_{1,2}}{L}\right) \tag{5.16}$$

The experimental setup for the determination of the fiber profile was composed of a helium–neon (He-Ne) laser, with a central wavelength of 652.8 nm, a full-HD webcam to acquire the image of the diffraction pattern, a plano-convex lens (LA4380-YAG, Thorlabs) to focus the laser beam on the fiber, and a movable target. The experimental setup is presented in Figure 5.24. The webcam was connected to a computer through a Python script that allowed to acquire and analyze the diffraction pattern in real-time. The Python program developed is explained in more detail in Appendix E.

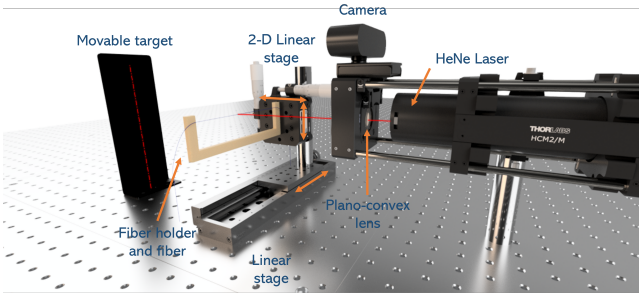

Figure 5.24: Experimental setup for the taper diameter measurement composed by a He-Ne laser that is focused on the tapered fiber, creating an interference pattern on the target.

5.2.3 Results

5.2.3.1 Real-time transmission spectra

Using the experimental setup previously described (see Section 5.2.2.1), several MNFs were drawn from standard single-mode fiber (Corning SMF-28). The transmission spectra centered at 1550 nm were analyzed in real-time for a total pulling distance of 70 mm. According to equation 5.14, and considering a hot-zone region of 8.3 mm, this traveling distance corresponds to a waist diameter of 1.84 μm. The transmission spectra, presented in Figure 5.25, indicate that no significant losses occur for traveling distances up to 30 mm. However, for higher traveling distances, transmission loss starts to increase. The origin of these losses can be caused by the increased movement of the tapered fiber induced by airflow which starts to be more relevant as the taper waist decreases. Another possible cause for the increasing losses can be due to the shape of the tapered region not allowing the adiabatic transmission of light.

Furthermore, it was observed that, for higher traveling distances, the fiber stopped being absolutely strained and started to bend between the fiber clamps possibly leading to an increased optical loss. The origin of the optical losses could not be found as the fiber broke before it was removed from the heater, even after several attempts in producing similar tapered fibers. Notwithstanding, the total optical losses added up to a maximum value of 1.9 dB.

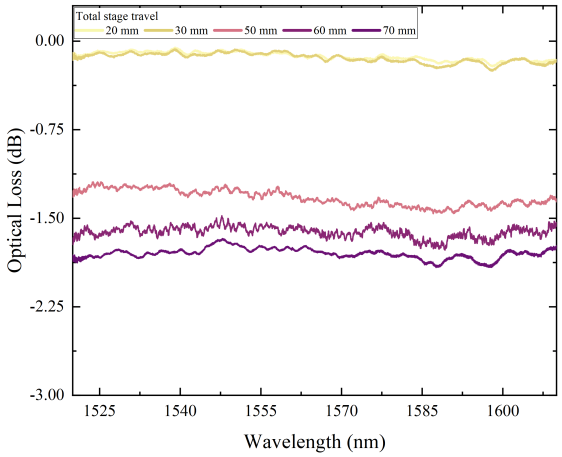

Figure 5.25: Transmission spectra of the taper during the pulling process, for wavelengths between 1520 and 1620 nm.

In order to evaluate the transmission spectrum for wavelengths between 800 and 1000 nm, several tapers were fabricated using a velocity of 0.04 mm/s. For this wavelength range, the optical monitoring system was composed of a halogen light source and a spectrometer with a

high-rate acquisition. The spectrometer was controlled by the software described in Appendix D, by setting the integration time to 50 ms, the time delay to 500 ms, and a resolution of 1.2 nm. The transmitted spectrum at 976 nm is presented in Figure 5.26a. It shows four distinct regions and the rupture of the taper, annotated on the plot. In the first region, marked as 1, no major variations in the transmitted signal are observed. Afterwards, at a pulling distance of approximately 11 mm, an oscillatory behavior starts to occur. This oscillatory behavior occurs due to the cladding modes starting to be excited and the cladding and core modes starting to beat [297]. Afterwards, a decrease in this behavior is observed, in region 3, up to a strong reduction of the transmission, where the higher propagation modes experience mode cut-off. This analysis can be extended to other wavelengths, as can be seen in Figure 5.26b. The same behavior is observed for 800 and 1000 nm wavelengths. The oscillatory behavior that is observed in the three wavelengths starts at higher taper diameters for longer wavelengths.

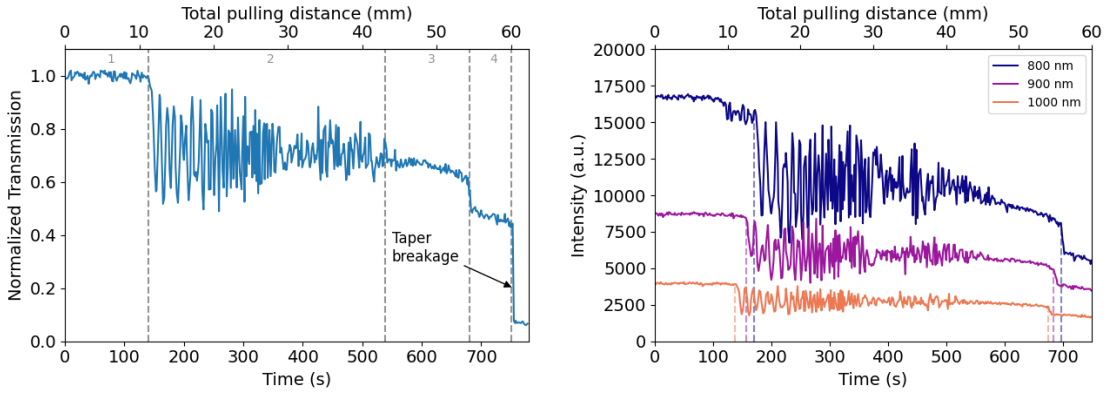

(a) (b)

Figure 5.26: Transmitted spectrum of the taper (a) at a wavelength of 976 nm, and (b) for several different wavelengths.

The microscope image of the tapered fiber allowed to determine the approximate waist diameter. In Figure 5.27, it can be seen a very constant waist region with a diameter lower than 900 nm.

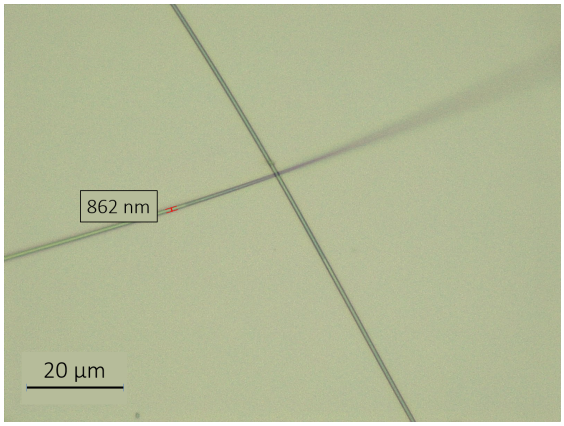

Figure 5.27: Microscope photograph of the fabricated MNF using the electrically-heated taper drawing technique, with a waist diameter lower than 900 nm.

5.2.3.2 Packaging of MNFs

The physical properties of MNFs can be affected by exposition to air and contaminants, inducing a degradation in the optical transmission [166]. To improve the stability of MNFs, it is possible to package them using materials with low refractive indices such as polydimethylsiloxane (PDMS) [301], or polytetrafluoroethylene (PTFE) [302], for example. The durability of the embedding configuration was studied by Zhang *et al.* [303], achieving one-year operation with no evident degradation. Besides protecting from environmental-induced degradation, embedded MNFs also benefit from increased robustness and portability.

It was, therefore, necessary to develop a packaging system for the MNFs as schematized in Figure 5.28. It consisted of a transparent plastic box with two fit-through openings to pass the tapered fiber. The tapered fiber was attached to a silica slab that served as a spacer to prevent the MNF from touching the plastic box walls. The packaging system increased the robustness and portability of the taper and, additionally, the operation of the MNF with air cladding.

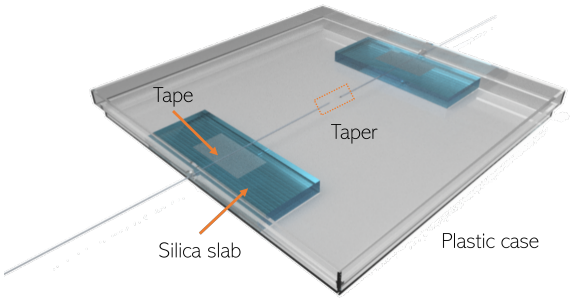

Figure 5.28: The packaging system for the MNFs was composed of a transparent plastic box and two silica slabs that prevented the MNF from touching the plastic box walls.

5.2.3.3 Deposition of GO using spray coating

The use of spray coating technology is widespread in a multitude of applications such as surface coating, humidification, combustion, and many others [304]. In this technique, a liquid sample containing the material to be deposited is accelerated through a carrier gas towards the substrate. The material particles can deform plastically and adhere to the substrate when accelerated at sufficiently high velocities [305]. In this work, an air atomizing nozzle was used for the deposition of GO on the tapered region of the fibers as schematized in Figure 5.29. The GO used in this deposition was acquired from Graphenea in water dispersion with a concentration of 4 mg/mL. In addition to its ability to be used in complex substrate geometries, this method also reduces the possibility of taper breakage during the deposition process.

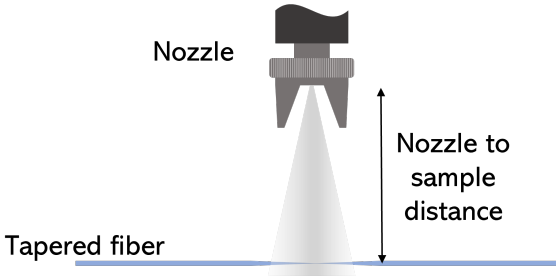

Figure 5.29: Illustration of the spray coating process, showing the basic components and vertical arrangement of the nozzle and the tapered fiber.

5.2.3.4 Optical characterization

The effects of the GO coating on the optical properties of the MNFs were studied by monitoring the transmitted spectrum during the spray coating process. The MNFs were connected to a cw diode laser with a central wavelength of 976 nm, with a maximum output power of 140 W (BWT model K976BN1RN-140.0W), while the transmitted spectra were attained with an OSA (Yokogawa AQ6370C) with a resolution of 0.02 nm. Due to the low power damage threshold of the OSA detector, the maximum peak power of the taper was maintained under 10 dBm (10 mW). The experimental setup is presented in Figure 5.30.

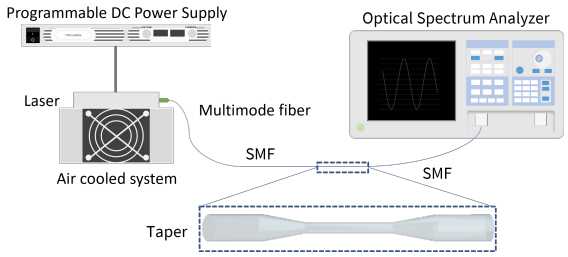

Figure 5.30: Experimental setup for the optical characterization of the GO-coated MNFs using a cw laser with a central wavelength of 976 nm.

The output power was monitored with a power meter (Coherent FieldMaxII-TO). Before connecting the taper to the laser's output fiber, the input current of the laser was calibrated using the output multimode fiber (MMF) and a standard SMF spliced to the output MMF. The two measurements allowed to determine the losses due to the fusion splice between the output MMF of the laser and the SMF. The results are presented in Figure 5.31. It is noteworthy that the MMF/SMF splice represents a loss of approximately 99.4 %, for an input laser current of 1.04 A.

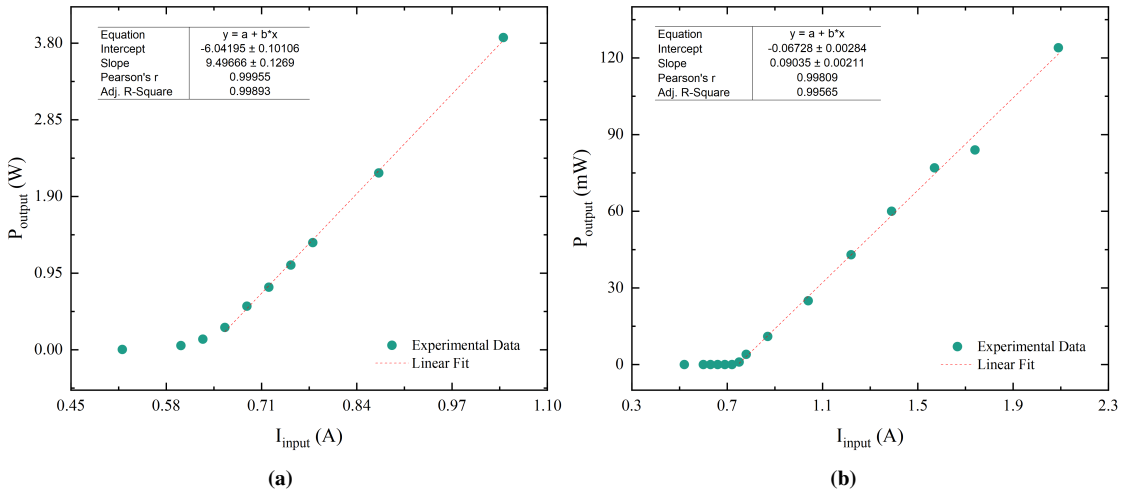

Figure 5.31: Output power with input laser current for (a) MMF and (b) MMF+SMF.

The output spectrum of a taper with a waist diameter of approximately 3 μm for different laser input currents is shown in Figure 5.32. It can be observed that laser operation starts to occur for input currents over 69 mA, corresponding to a power of approximately 540 mW at the output of the MMF, with a central wavelength of 976 nm. As input values increase, spontaneous emission lines can be observed around wavelength 968 nm, however, no other behavior could be observed.

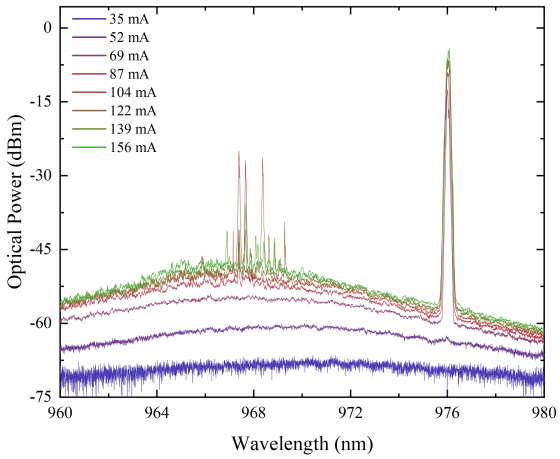

Figure 5.32: Transmission spectrum of the tapered fiber with a waist diameter of approximately $3\mu m$ using the cw laser with a central wavelength of 976 nm.

Afterwards, the taper was spray-coated with GO leading to no transmission signal being attained. All light traveling in the taper region was either absorbed or attenuated by the GO thin film.

5.2.3.5 Saturable Absorption

Graphene exhibits high carrier mobility, low non-saturable losses, fast saturable absorption, large Kerr nonlinearity, and broadband wavelength tunability making it a very suitable saturable absorber material [306]. Saturable absorption is a nonparametric nonlinear optical property of a material that translates into an intensity-dependent absorption coefficient [190]. Typically, the dependence of the absorption coefficient, α, with the intensity of the incident light I is given by:

$$\alpha = \frac{\alpha_0}{1 + I/I_s} \tag{5.17}$$

where α_0 is the low-intensity absorption coefficient, I is the intensity of the light and I_s is the saturation intensity. Saturable absorption can be used as the mechanism responsible for short and ultrashort pulse generation through passively mode-locking or Q-switching a cw laser. Short and ultrashort pulses are important tools in different applications such as precision metrology [307], [308], industrial applications [309], [310], medicine [311], [312], and nonlinear optics [313], for example. Recently, it has been shown that GO also exhibits saturable absorption, making it an interesting alternative for ultrafast pulse generation [314]. Since then, different works have been presented in the literature for ultrashort pulse generation using GO as a saturable absorber [29], [315], [316].

5.2.3.5.1 Mode-locking

Mode-locking is a process by which the longitudinal modes of a laser with comparable amplitudes are made to oscillate with a definite relation between their phases resulting in ultra-short pulses [317]. The mode-locking process can be understood when considering a laser with $2n+1$ longitudinal modes, evenly separated by $\Delta\nu$ and with the same amplitude E_0. The frequency difference of modes is given by:

$$\Delta\nu = \frac{c}{2L_0} \tag{5.18}$$

where c is the light traveling speed, and L_0 is the laser's cavity length. The total electric field $E(t)$ can be written as:

$$E(t) = \sum_{k=-n}^{n} E_0 e^{-i(\omega_k t - \phi_k)} \tag{5.19}$$

where ϕ_k and ω_k represent the phase and frequency of the k-mode, respectively. Under cw operation, these modes have random phases resulting in a random time behavior. When mode-locking occurs, the phase difference between the modes is locked at a value $\phi = \phi_k - \phi_{k-1}$. The frequency of the mode can be written as $\omega_k = \omega_0 + 2\pi k\Delta\nu$. The total intensity of the field is given by $I \propto |E(t)|^2$, that can be determined by [317]:

$$|E(t)|^2 = E_0^2 \frac{sin^2[(2n+1)\pi\Delta\nu + \phi/2]}{sin^2[\pi\Delta\nu + \phi/2]} \tag{5.20}$$

In Figure 5.33 the intensity of a mode-locked signal with five oscillating modes is demonstrated. It can be observed that mode-locking results in a train of evenly spaced light pulses, distanced by a time, τ_p given by $1/\Delta\nu$, with a pulse duration inversely proportional to the total oscillating bandwidth. For the case of a mode-locked ring-laser, the time distance τ_p can also be written in terms of the laser's cavity length as $\tau_p = L/c$ [317].

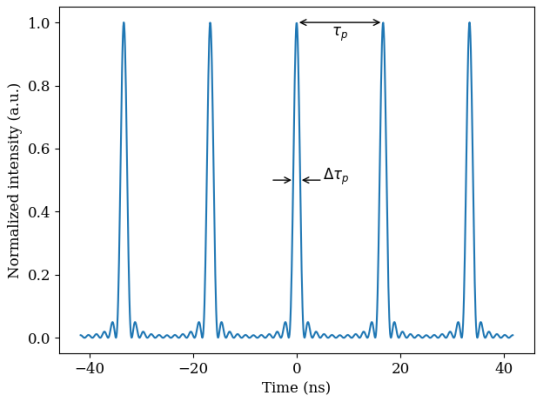

Figure 5.33: Temporal behavior of the intensity of the electric field for five oscillating modes with equal amplitude and locked phases.

Mode-locking can be achieved through active or passive methods. The active methods for mode-locking rely on an external modulator driven by an external source. In passive mode-locking, the modulation occurs due to nonlinear optical effects in the modulator element such as using a material with an intensity-dependent refractive index (Kerr effect) or by saturating a saturable absorber material.

The possibility of using a GO-coated MNF as a saturable absorber for mode-locking was studied by inserting the MNF in an Er-doped fiber laser (EDFL) ring cavity as shown in Figure 5.34a. The EDFL is composed of an Er-doped fiber amplifier (EDFA) pump laser, the tapered fiber, a polarization controller that manages the intracavity polarization state, and a coupler with a 1% output ratio allowing the monitoring of the laser's signal. The EDFA is composed of a pump diode laser at 980 nm, two wavelength division multiplexer (WDM) at 980/1550 nm, an approximately 10-m length Er-doped fiber, and an optical isolator that ensures uni-lateral light propagation. By adjusting the pump power and the intracavity polarization state, the behavior of the taper can be studied. In Figure 5.34b, the output spectrum of the EDFL ring with a taper with

3 μm waist diameter for a pump power of 300 mW is presented. The attained peak corresponds to the natural laser wavelength and no further behavior was observed.

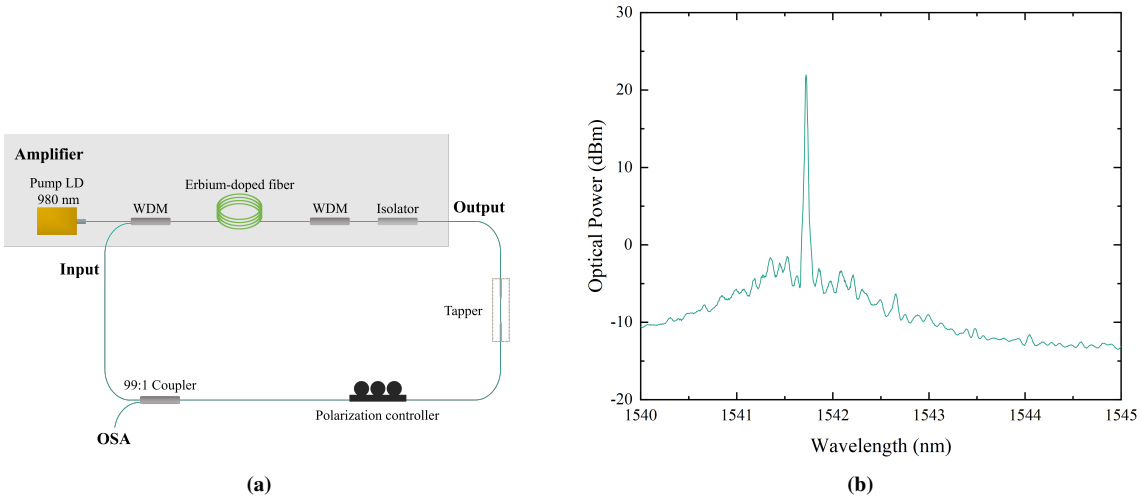

Figure 5.34: (a) Experimental setup composed of an EDFL ring laser, a polarization controller, an output 99:1 coupler connected to the OSA, and the fabricated MNF; (b) Output spectrum of the ring laser with the taper for a pump power of 300 mW.

As no effects were observed in the tapered fiber, the optical properties of the GO thin film were studied using a thin GO film deposited on the end face of a fiber with FC/PC connectors, as presented in Figure 5.35. The thin film was deposited with similar spraying time to ensure similar film thickness. Besides including the FC/PC-connected fibers with a GO coating, a 100 m SMF coil was added to control the total cavity length and the total dispersion of the cavity. In order to guarantee that the damage threshold for the OSA or the photodetector was not surpassed, a 3-dB optical attenuator was added to the laser's output.

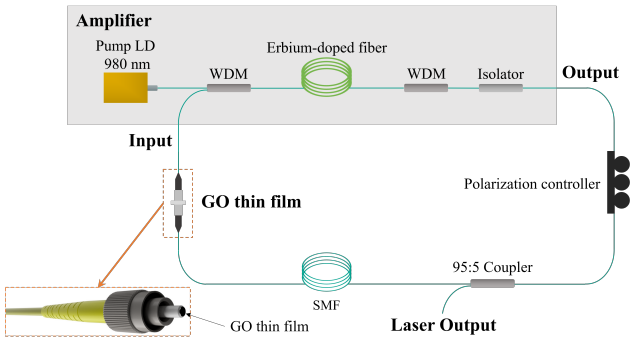

Figure 5.35: Experimental setup composed of an EDFL ring laser, a polarization controller, an output 95:5 coupler, and the GO film positioned between two connectorized fibers.

The output light of the laser was characterized with no GO thin film by changing the pump power and intracavity polarization state to assess if self-starting Q-switching or mode-locking occurs. No Q-switching or mode-locking operation induced by non-linear polarization rotation was achieved as can be observed in Figure 5.36a where only the natural wavelength of the laser's cavity is attained. Afterwards, the GO thin film was added and the optical spectrum was characterized

by changing the pump power and intracavity polarization state. In Figure 5.36a, the output spectrum exhibits sidebands for pump powers above 200 mW. These sidebands are characteristic of the soliton operation of the fiber laser resulting from periodic soliton perturbation [318].

The temporal signal, in Figure 5.36b, was acquired by using an InGaAs photodetector with switchable gain (Thorlabs PDA10CS-EC) connected to an oscilloscope with a 2-GHz sampling rate (Thorlabs PDA10CS-EC). It was observed a pulse train with a pulse interval approximately equal to 688 ns, corresponding to a repetition rate of 1.48 MHz. The attained repetition rate is in accordance with the natural frequency of the laser's cavity, with an estimated 130 m length.

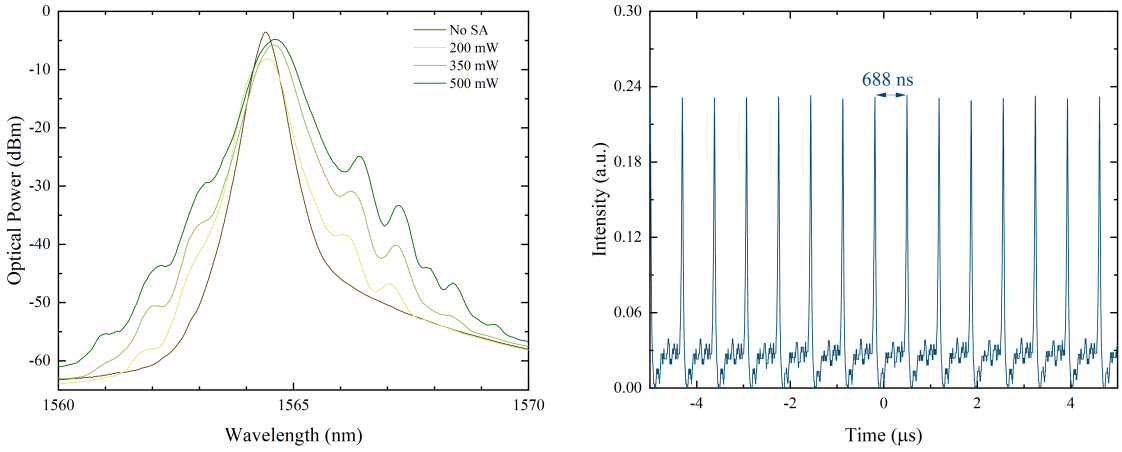

Figure 5.36: (a) Output spectrum of the ring laser without and with GO film for different pump power values; (b) Output pulse train in mode-locking operation.

5.2.3.5.2 Q-Switching

Q-swicthing is a technique used for the generation of short pulses (in the order of nanoseconds). In this technique, the lasing operation is prevented by adding an optical element that increases the optical losses to the laser's cavity and, thus, decreases the quality factor Q of the laser. By preventing lasing action, the active medium is being continuously pumped leading to a population inversion that far exceeds the threshold population under normal conditions. When the losses are suddenly reduced, thus increasing the Q factor of the cavity, the laser exhibits a gain that greatly exceeds losses, and the stored energy is released as a short and intense light pulse [317]. Similarly to mode-locking, Q-switching can be achieved using active or passive methods, and, in particular, passively induced Q-switching can be attained using saturable absorbers.

To study the Q-switching operation, the experimental setup was adjusted to decrease the fiber connectors to reduce the risk of power damage on the connectors. The experimental setup was similar to the one previously described, only changing the total length of the Er-doped fiber to 4 m, and changing the output ratio of the coupler to 10 %, as presented in Figure 5.37.

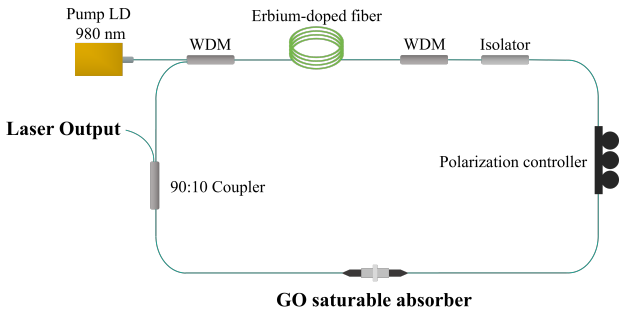

Figure 5.37: The experimental setup composed of an EDFL ring laser, a polarization controller, an output 90:10 coupler, and the GO film positioned between two connectorized fibers, for Q-switching operation.

The total cavity length was estimated to be around 15 m, determined by an OTDR. The Q-switching operation was achieved by changing the polarization state of the laser's traveling light and the pump current. Figure 5.38a shows the output pulse train for an input power of 230 mA. The resulting pulse train exhibits a 79 μs pulse interval, that corresponds to a repetition rate of 12.7 kHz. The single-pulse width was estimated using a Gaussian fitting, attaining a 12.6 $\pm$ 0.1 μs width. The evolution of the pulse repetition rate was also studied for a variable pump current resulting in a linear relationship between the two parameters, as shown in Figure 5.38b.

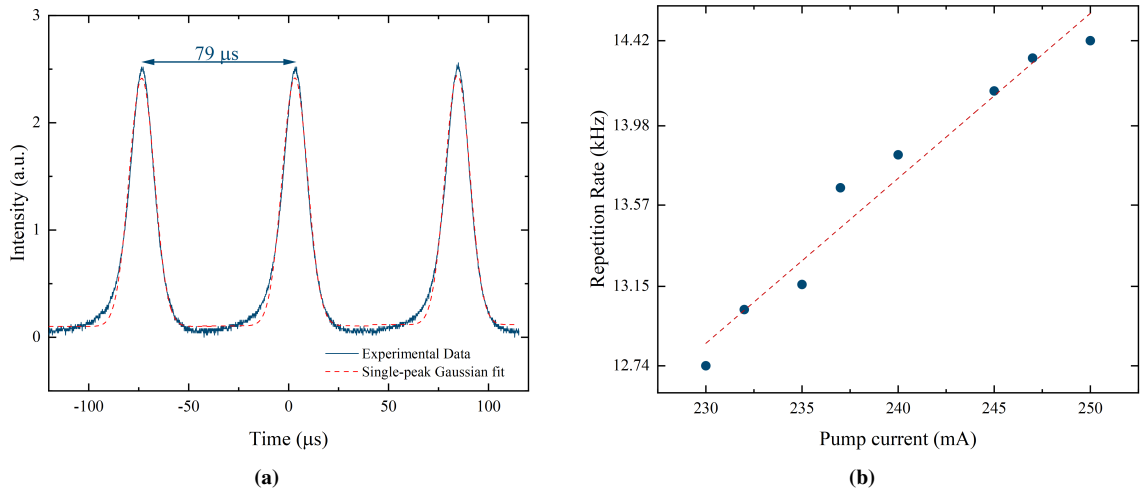

Figure 5.38: (a) Output pulse train in mode-locking operation; (b) Evolution of the repetition rate with the increase of pump current.

5.3 Concluding Remarks

In this chapter, the fundamental concept of MNFs was presented with a comprehensive introduction to their properties, fabrication methods, and applications. The experimental results followed, by presenting two MNFs fabrication methods: using a CO_2 laser and using an electric heater. The first method resulted in asymmetrical MNFs with high transmittance losses. Moreover, the minimum waist diameters attainable were in the order of several tens of micrometers, so the use of this technique was not feasible for the fabrication of MNFs. This led to the exploration of MNFs

fabricated through electrically-heated taper drawing. Using this technique tapers with waist diameters in the order of hundreds of nanometers were attained. The optical properties of the fabricated MNFs were studied before and after being GO-coated using the spray coating technique.

To further investigate the nonlinear properties of GO, a thin film was deposited on a connectorized fiber and it was added to an EDFL ring. It was observed that GO exhibited saturable absorption behavior, attaining lasing action using mode-locking and Q-switching.

Chapter 6

Conclusions and future work

The work presented in this dissertation was focused on the use of GO in photonic applications. A study has been conducted to investigate deposition methods that are compatible with the complex geometry of optical fibers, both in tapered and untapered configurations. It became apparent that two different techniques were most favorable for the GO deposition: the layer-by-layer (LbL) and the spray-coating techniques. The first technique was studied and optimized for its application in the development of new optical fiber sensing structures. The second technique was applied in tapered fibers with dimensions of the order of magnitude of the traveling light. Moreover, a study concerning the nonlinear optical properties of GO was conducted to generate ultrashort pulses.

Considering the plethora of relevant properties, synthesis, and analysis methods, an overview of the state of the art concerning graphene, GO and rGO was presented. This was followed by the study of the LbL technique, a technique compatible with the geometrical shape of optical fibers. This technique relies on intermolecular interactions to build a multilayered thin film. The LbL technique was studied in terms of its adsorption kinetics using an experimental apparatus that allows real-time measurement of the reflectance of the surface of the fiber. The experimental technique can be applied to other molecules, as an *in situ* method for real-time adsorption kinetics. The influence of the number of bilayers on the surface's reflectivity was also studied using a polycationic solution (PEI). After the optimization of the coating process, the LbL technique was applied to an interferometric structure that allows studying changes in the phase of the reflected signal induced by the PEI/GO coating. The structure was composed of a hollow microsphere at the tip of an SMF, that forms an interferometric configuration that can be approximated to a three-wave (or cascaded) Fabry-Perot interferometer. The bilayer growth was also studied in this configuration, along with the influence of the PEI on the response of the sensor, and coating stability under normal environmental conditions. It was observed that the bilayer growth leads to a phase shift of the interferometric signal, resulting from the variation of the effective RI caused by an increase of film thickness on the outer surface of the sensor. Moreover, the presence of PEI did not affect the reflected signal, meaning that the phase shift was caused entirely by the GO. Additional studies were carried out to determine the stability of the film in normal real-world conditions, for 24 hours. As a result, the reflectivity of the film decreased, decreasing the SNR of the signal.

The application of GO thin films on fiber sensors ensued, presenting an overview of the state-of-the-art fiber sensors conjugated with graphene and graphene-based materials such as GO and rGO. The overview provides an understanding of the numerous sensing configurations that benefit from the properties of graphene and GO, with applications in a wide range of scientific and industrial fields. In this context, two new sensing structures based on GO were developed. The first sensor was composed of a Fabry-Perot interferometer, that can be approximated to a three-mirror

structure. The sensor was coated with several PEI/GO layers using the LbL technique. The influence of the RI of the external medium on the reflected spectrum was studied, resulting in a phase shift attributed to the complex internal reflection, interference, and energy-loss processes that occur in the conducting surfaces within the coating. It was also observed that the phase could suffer a blue or redshift on the same structure depending on the number of PEI/GO layers. The second presented sensor was composed of a silica capillary coated with GO, forming a thin GO membrane. The GO was deposited using the dip-coating technique, an easy and fast thin-film coating technique, that allowed the production of a GO film with approximately 40 nm. The film was capable of deflecting with the applied sound pressure, for frequencies between 20 and 100 kHz, with an MDP of 478 $\mu Pa/Hz^{1/2}$. The sensor was also capable of withstanding temperatures up to 90 $^{\circ}C$ but showed a decrease of the fringe contrast, indicating that the temperature induces degradation of the membrane.

Afterwards, the integration of GO in micro and nanofibers was studied. Micro and nanofibers are optical fibers tapered to a waist diameter of the order of magnitude of the traveling light and were first experimentally demonstrated in 2003. MNFs exhibit interesting properties such as tight optical confinement and high evanescent fields, and create the opportunity for tailoring dispersion properties. As a result of the high evanescent fields, it is possible to create compact sensors with high sensitivity to the external environment. It can also be employed in passive devices and in the manipulation and trapping of particles. On the other hand, the tight confinement of the propagating modes creates electromagnetic fields with very high power densities. This can lead to the observation of nonlinear effects at low input powers, such as supercontinuum generation or high harmonic generation. The integration of GO on MNFs has already been demonstrated in the literature and its application for the generation of short and ultrashort pulses. In this work, no nonlinear effects were observed by including the GO film on MNFs. However, the deposition of a GO thin film using spray-coating on an optical fiber and its integration on an Er-doped fiber laser under CW operation allowed the observation of saturable absorption. The saturable absorption, a nonlinear effect on the material, allowed the generation of short pulses (ns) using the Q-switching technique and the generation of ultrashort pulses (ps or fs) through the mode-locking technique. The Q-switching technique allowed the attainment of highly-energetic pulses with a single-pulse width of 12.6 μs and repetition rate of 12.7 kHz (the equivalent of a period of 79 μs), dependent on the pump power. The mode-locking technique allowed for the generation of shorter pulses, with a period of 688 ns, on a laser with an approximated cavity length of 130 m.

The work developed on this PhD can serve as a starting position for further improvement and for the exploration of new ideas of application of GO on photonics as highlighted as follows.

- The stability of the PEI/GO coatings under normal environmental conditions should be further investigated. It is of paramount importance that these films have the ability to withstand this type of environment in order to be suitable for real applications.

- The LbL technique results in thin films with a high surface roughness that could lead to a lack of reproducibility in the results. Further investigation should take place to mitigate this issue by further optimizing the solution concentration of the dielectric and GO and the deposition time.

- Considering the acoustic sensor, further studies should be done to determine its performance under dynamic temperature conditions. This could allow the sensor to be employed in real-life applications such as fault detection or in photoacoustic microscopy, for example.

- The MNFs fabrication setup should be optimized to allow the fabrication of thinner fibers. This could be accomplished by adding precision tension measurement sensors or actuators

to guarantee that the tension is constant during the pulling process. This will force the fiber to stay tensioned during the process, decreasing the possibility of it breaking by getting in contact with the ceramic of the fiber heat slot.

- Considering the high evanescent fields and the possibility of expanding the interaction length by using MNFs, further study on the properties of the GO thin film on MNFs should be carried out. This would allow studying the possibility of using the saturable absorption observed on the GO films to produce ultrashort pulses in MNFs.

Appendix A

Piranha solution: experimental protocol

Piranha solutions are a mixture of concentrated sulfuric acid and hydrogen peroxide, usually in a ratio of 3:1 to 7:1. They are used to remove trace amounts of organic residues from substrates as well as hydroxylate the surface of the substrate. The reaction from the mixture is very exothermic and can reach temperatures of 100 $^{\circ}C$ or higher. Improper care during the procedure may lead to chemical and thermal burns, and increase the risk of explosion. Considering the explosion hazard and the highly irritant fumes, personal protective equipment (lab coat and gloves are a must), and the handling of the solution a fume hood is recommended.

A.1 Piranha solution preparation

1. Before starting the preparation of the piranha solution, assemble the needed ingredients inside the fume hood:

    - Concentrated sulfuric acid
    - 30% w/w hydrogen peroxide solution. The concentration should NEVER exceed 50% due to the increased explosion risk.

2. Slowly add the hydrogen peroxide to sulfuric acid while gently stirring to form a 3:1 ratio solution of three parts sulfuric acid and one part hydrogen peroxide. NEVER the other way around. Considering the exothermic reaction, an ice bath can be used for cooling the container.

3. Place the substrates in the piranha solution for a minimum of 5 to 10 minutes. The substrates must be immersed slowly and carefully to avoid injuries. In this work, the optical fibers were placed in the piranha solution for 30 minutes.

4. Carefully remove the substrates from the solution and rinse thoroughly with distilled water inside of the fume hood.

A.2 Piranha solution disposal

Piranha solution should only be collected for disposal once it has fully reacted, cooled, and the reaction gases have dissipated. The neutralization process is exothermic and an ice bath may be needed for temperature control. It should be performed in a fume hood, using personal protective equipment. The disposal should obey the following protocol:

1. Piranha solution should be diluted to a concentration of less than 10% by adding the solution to water.
2. After, a concentrated solution of sodium hydroxide or sodium carbonate can be slowly added, while vigorously stirring the solution.
3. Repeat the previous step until the pH reaches a value between 4 and 10.
4. Dispose of the solution with abundant amounts of water via a drain that leads to the sanitary sewer system.

Appendix B

Software for the acoustic characterization of the sensor based on graphene oxide membrane

The software, developed using LabVIEW, is capable of communicating with the tunable laser source and with the oscilloscope simultaneously. It is capable of three different acquisition modes: it can operate as an OSA, by acquiring the signal for a selected wavelength range; the acquisition mode, that acquires the signal for the selected wavelength; and it can recalibrate, by analyzing the acquired spectrum using the OSA mode, and searching and selecting a linear midpoint of the reflected spectrum. The main system blocks are presented in Figure B.1.

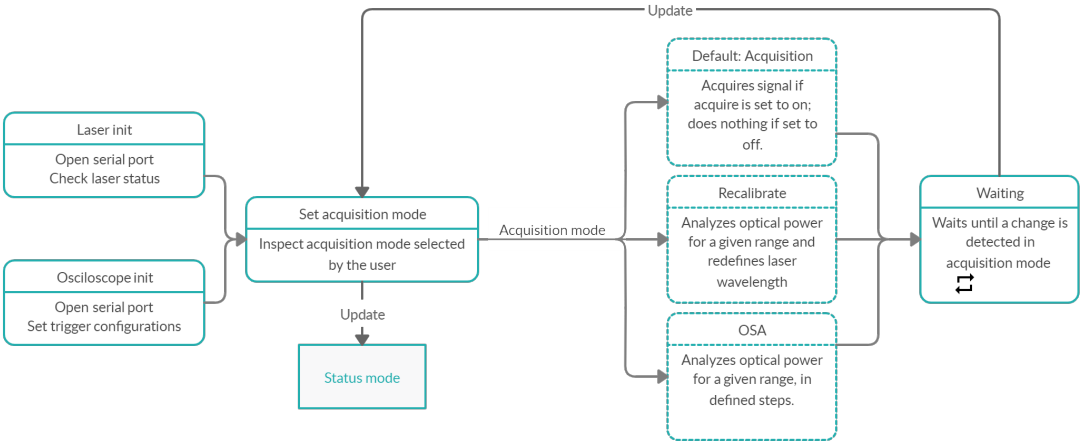

Figure B.1: Diagram of the main system blocks.

In this appendix, the different acquisition modes are going to be described in more detail, and the graphical user interface is going to be presented.

B.1 Software block diagram

B.1.1 OSA Mode

The OSA mode enables the user to inspect the reflected spectrum of the sensor, allowing it to fully characterize the optical cavity without the need to change the interrogation system to the one

presented in section 4.3.2.3. The program sweeps over the wavelength range, with a preset step, by calculating the mean signal value to the tuned laser wavelength. The mean signal value for each wavelength is, then, plotted. The spectrum can be written into a .txt file. The main code block is presented in figure B.2.

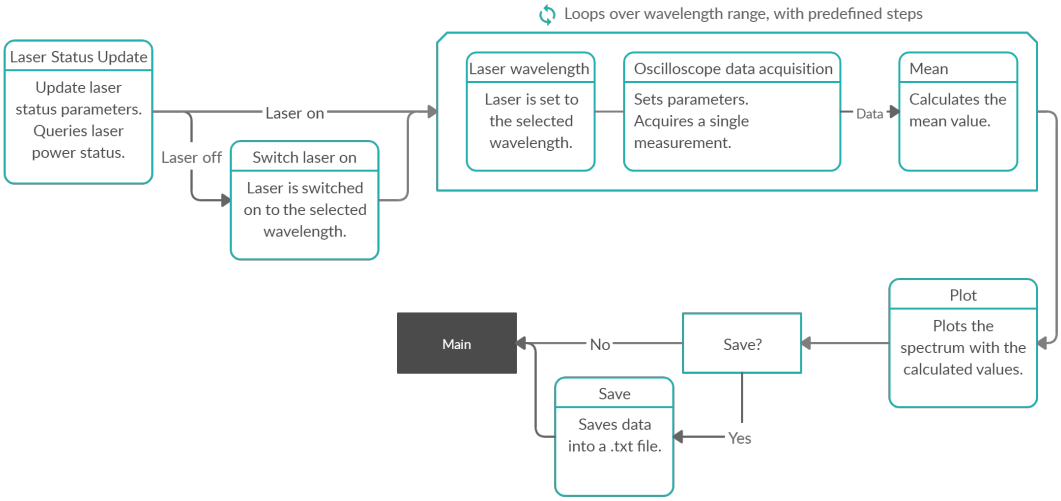

Figure B.2: Block diagram of OSA mode.

B.1.2 Acquisition Mode

The acquisition mode starts by querying the laser status and updating the parameters on the graphical user interface. If the laser is not switched on, a prompt user appears to ascertain if the user wants to switch on the laser. This prompt user serves as a security measure, to avoid the laser to be turned on accidentally. If the user selects the "Ok" button, the laser is switched on to the selected wavelength. Afterwards, the oscilloscope is set to read mode. Before reading the channel signal, the oscilloscope parameters (e.g. trigger, channel coupling) are updated. The acquired signals are translated into a physical parameter and are displayed in the plot. Subsequently, the program is set into a waiting routine until the user toggle one of the following parameters: stop button, acquire button, recalibrate button, or save button. If the user has previously set "Save" to on, the data from the oscilloscope is saved into a .txt file, in a new folder on the user's desktop. When the waiting routing is stopped, the program goes to the acquisition mode update. The main blocks of the acquisition mode are presented in figure B.3.

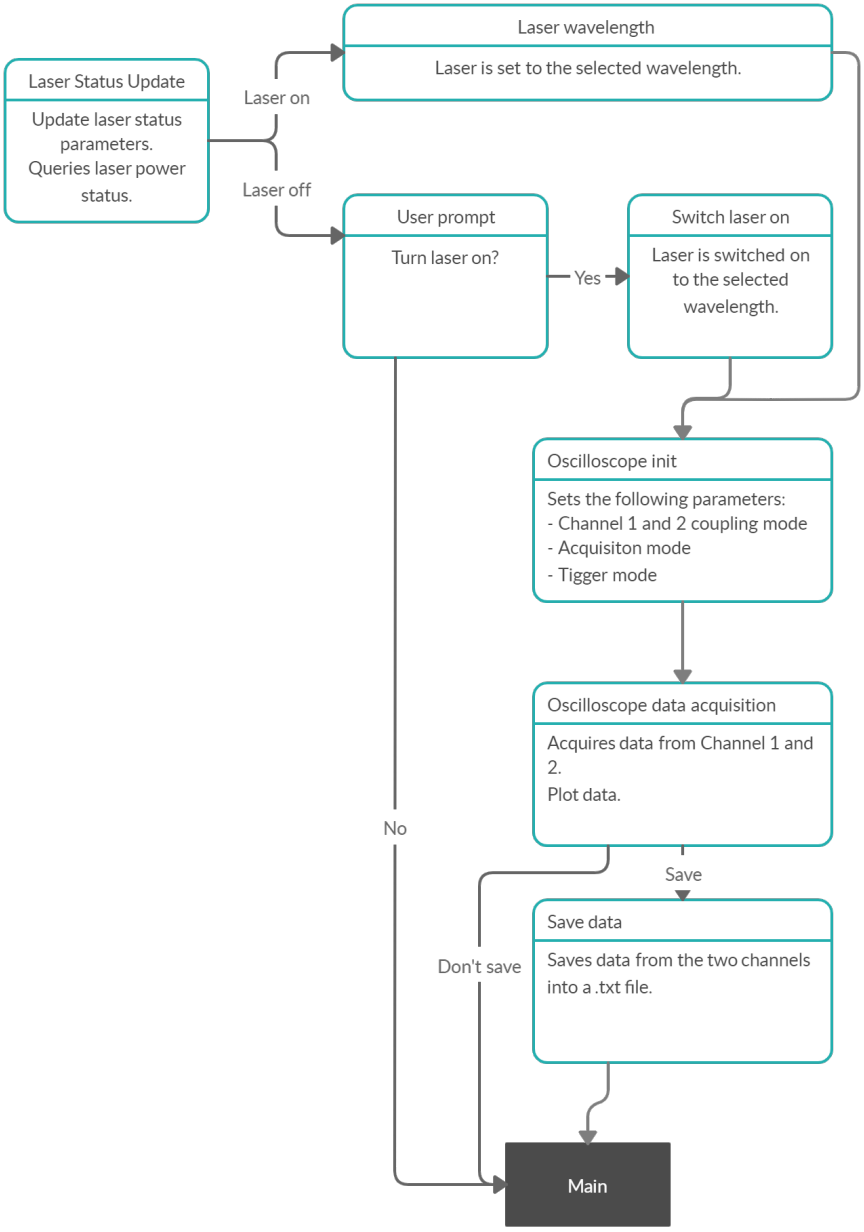

Figure B.3: Block diagram of acquisition mode.

B.1.3 Recalibration Mode

The recalibration mode is intended for the user to reset the laser wavelength, in case of changes in the position of the linear region on the reflected spectrum due to temperature variations, for example. The laser is tuned between two wavelengths selected by the user. The program calculates the linear midpoint of the reflected spectrum and sets that value as the new laser wavelength. When the recalibration process finishes, a user prompt is displayed on the screen. The main code blocks are presented in figure B.4.

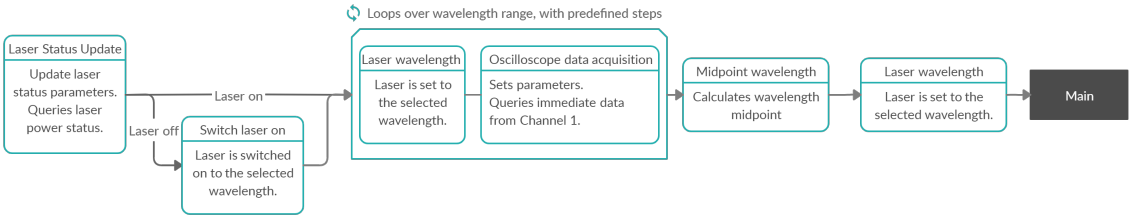

Figure B.4: Block diagram of recalibration mode.

B.2 Graphical user interface

The graphical user interface is presented in figure B.5. It is divided into three blocks: the laser display, the oscilloscope data visualization, and the acquisition control. In the laser display block, the following information from the laser is displayed: currently tuned wavelength and the corresponding frequency, a string information of laser status, LED display informing power mode (if the laser is on or off), and an LED error.

In the oscilloscope data visualization block, the data acquired by the oscilloscope on the two channels are displayed. The user has four control buttons:

1. **Recalibrate:** allows the user to reset laser wavelength to a linear region of the sensor.
2. **Acquire:** starts data acquisition.
3. **Save:** saves data in computer.
4. **Stop**: stops the program when an error occurs.

In the Acquisition control block, the user can set up the acquisition method: to OSA mode or to the sweep mode. The OSA mode can be used for full sensor characterization, allowing the user to acquire the whole reflected spectrum in the laser wavelength range, in a user-set resolution. After fully characterizing the sensor spectrum, the user can use the sweep mode to configure the wavelength range of a linear region of the spectrum. In this block, there is also a Trigger menu - that enables the user to set the trigger options -, and the port configuration of the laser and the oscilloscope.

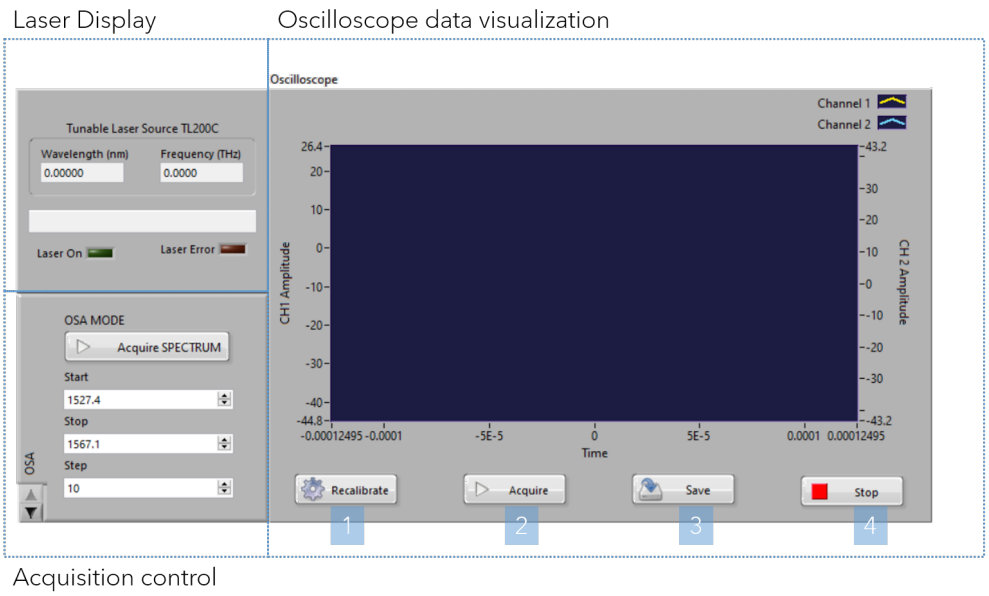

Figure B.5: Front panel of the program.

Appendix C

Constants

The fraction of power inside and outside of the fiber can be calculated by the z-components of Poynting vectors given by [165]:

For $0 < r < a$

$$S_{z1} = \frac{1}{2}\left(\frac{\varepsilon_0}{\mu_0}\right)^{\frac{1}{2}} \frac{kn_1^2}{\beta J_1^2(U)} \left[a_1 a_3 J_0^2\left(\frac{Ur}{a}\right) + a_2 a_4 J_2^2\left(\frac{Ur}{a}\right) + \frac{1 - F_1 F_2}{2} J_0\left(\frac{Ur}{a}\right) J_2\left(\frac{Ur}{a}\right) cos(2\phi) \right] \tag{C.1}$$

For $r \geq a$:

$$S_{z2} = \frac{1}{2}\left(\frac{\varepsilon_0}{\mu_0}\right)^{\frac{1}{2}} \frac{kn_1^2}{\beta K_1^2(W)} \frac{U^2}{W^2} \left[a_1 a_5 K_0^2\left(\frac{Wr}{a}\right) + a_2 a_6 K_2^2\left(\frac{Wr}{a}\right) - \frac{1 - 2\Delta - F_1 F_2}{2} K_0\left(\frac{Wr}{a}\right) K_2\left(\frac{Wr}{a}\right) cos(2\phi) \right] \tag{C.2}$$

The constants $a_{1,2,3,4,5,6}$ are given by:

$$\begin{aligned} a_1 &= \frac{F_2 - 1}{2} & a_2 &= \frac{F_2 + 1}{2} & a_3 &= \frac{F_1 - 1}{2} \\ a_4 &= \frac{F_1 + 1}{2} & a_5 &= \frac{F1 - 1 + 2\Delta}{2} & a_6 &= \frac{F_1 + 1 - 2\Delta}{2} \end{aligned} \tag{C.3}$$

The constants $F_{1,2}$ are given by:

$$F_1 = \left(\frac{UW^2}{V}\right)[b_1 + (1 - 2\Delta)b_2]; \quad F_2 = \frac{V}{UW}\frac{1}{b_1 + b_2} \tag{C.4}$$

Where b_1 and b_2 are given by:

$$b_1 = \frac{1}{2U}\left\{\frac{J_0(U)}{J_1(U)} - \frac{J_2(U)}{J_1(U)}\right\}; \quad b_2 = \frac{1}{2U}\left\{\frac{K_0(W)}{K_1(W)} - \frac{K_2(W)}{K_1(W)}\right\} \tag{C.5}$$

Appendix D

Fiber drawing monitoring software

In order to evaluate the evolution of the transmitted spectrum at a specific wavelength in real time, it was needed to develop a simple Python-based software. The graphical interface, shown in Figure D.1, displays the current full-span spectrum and the evolution of the spectrum at the wavelength selected by the user. The main parameters of the spectrometer (integration time, time delay, and wavelength) can also be changed to the best suitable values.

Figure D.1: Graphical user interface developed for the ULS2048CL-EVO spectrometer.

The main code blocks are presented in Figure D.2. Besides displaying the spectrum in real time, the software also allows the user to save all data acquired during the tapering process.

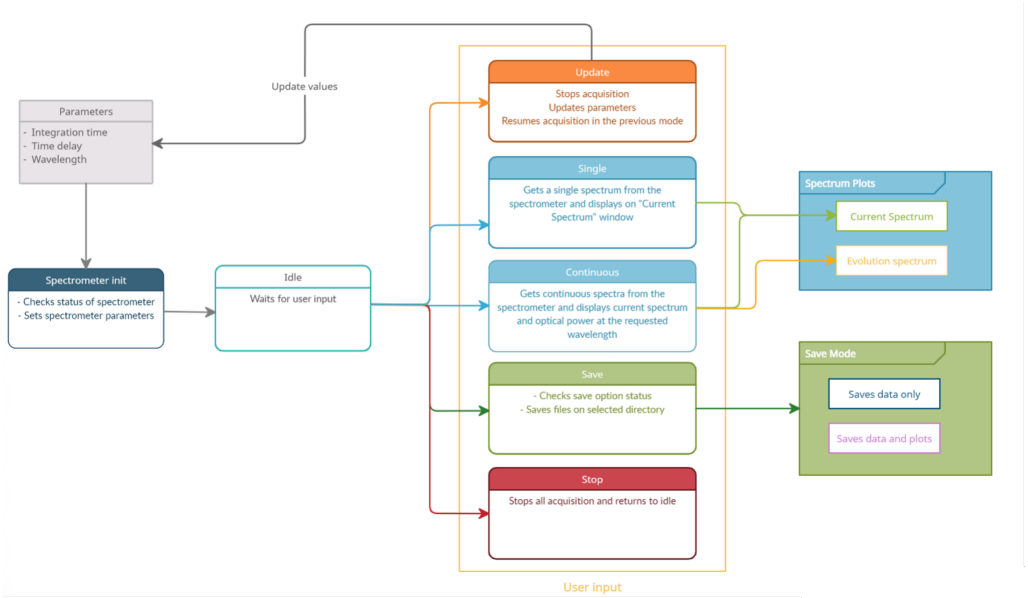

Figure D.2: Block diagram of the software developed for the ULS2048CL-EVO spectrometer.

Appendix E

Fiber profile monitoring software

The program for the fiber profile calculation was developed in Python and had a graphical interface that eases the user's interaction with the program. The graphical interface, shown in Figure E.1, can be divided into two sections: the image capture section and the diameter calculation section. In the image capture section, the user can open already captured images or capture new images with the computer's webcam. In the image, the user can select the profile line using the mouse's left button and the scale line using the mouse's right button. In this section, the user can also determine the profile line that is, afterward, plotted in the second section. The user can set the distance between the camera (that should be placed at the same distance as the laser) and the target as well as the line scale measurement. Besides the profile line, the local minima are displayed in the plot, and the two points of interest can be directly selected. Then, the diameter can be calculated and is displayed in μm units. The complete code is shown on the following page.

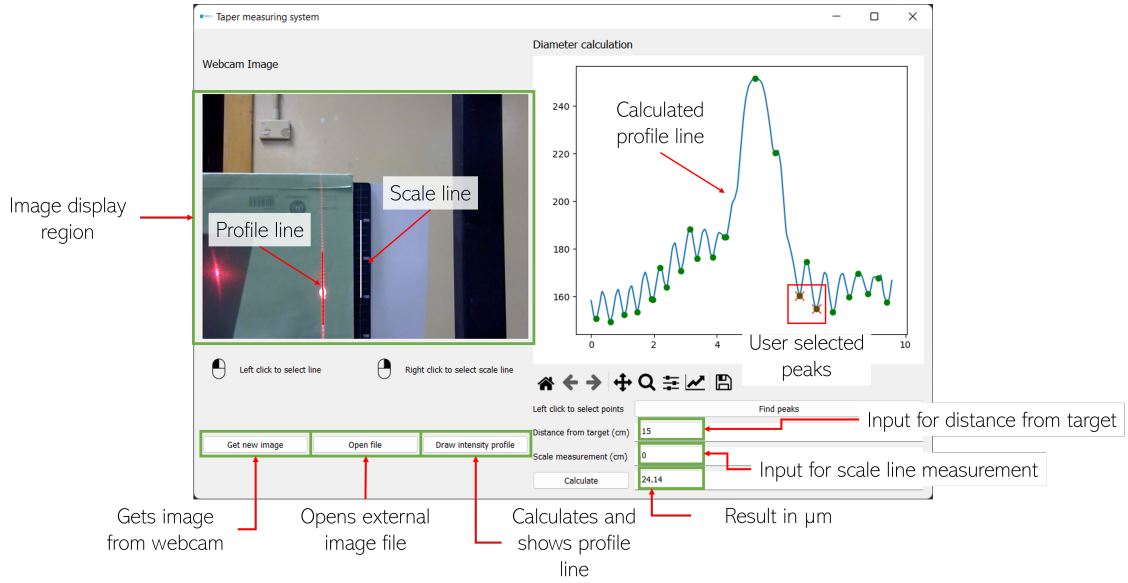

Figure E.1: Graphical interface of the program.

```
import cv2
from PyQt5.QtCore import *
from PyQt5.QtGui import *
from PyQt5.QtWidgets import *
from matplotlib.backends.backend_qt5agg import FigureCanvasQTAgg,
    NavigationToolbar2QT
from matplotlib.pyplot import *
from numpy import *
from scipy.signal import find_peaks, savgol_filter
from shapely.geometry import LineString
from skimage import measure


# Class for plotting
class Canvas(FigureCanvasQTAgg):
    def __init__(self, parent):
        self.fig = Figure(figsize=(6, 6))
        self.ax1 = self.fig.add_subplot(111)
        self.ax1.set_ylabel("Intensity")
        self.ax1.set_xlabel('Distance (pixels)')
        super(Canvas, self).__init__(self.fig)
        self.fig.tight_layout()


class widget(QWidget):

    def __init__(self):
        super().__init__()
        #Definition of window properties
        self.setWindowTitle("Taper measuring system")
        self.setWindowIcon(QIcon(r"..\inesc_logo.png"))

        self.setMinimumSize(994, 559)
        sizePolicy = QSizePolicy(QSizePolicy.Expanding, QSizePolicy.Expanding)
        sizePolicy.setHorizontalStretch(0)
        sizePolicy.setVerticalStretch(0)
        sizePolicy.setHeightForWidth(self.sizePolicy().hasHeightForWidth())
        #Global layout in grid
        self.global_layout = QGridLayout(self)

        # Acquisition region: show image, set distance, get new image
        self.acquisition = QVBoxLayout()
        self.global_layout.addLayout(self.acquisition, 0, 0, 1, 1)

        self.title1 = QLabel("Webcam Image")
        self.acquisition.addWidget(self.title1)
        self.title1.setStyleSheet(u"font: 75 10pt ;")

        self.wimage = QLabel()
        self.image_pixmap = QPixmap(r"..\Sample.png")
        self.img_scl = self.image_pixmap.scaled(500, 600, Qt.KeepAspectRatio, Qt.
    SmoothTransformation)
        self.wimage.setPixmap(self.img_scl)
        self.wimage.mousePressEvent = self.clicked_image
        self.acquisition.addWidget(self.wimage)

        self.buttons = QHBoxLayout()
        self.global_layout.addLayout(self.buttons, 1, 0, 1, 1)

        self.new_photo = QPushButton()
```

```
59          self.new_photo.setText("Get new image")
60          self.new_photo.clicked.connect(self.take_photo)
61          self.buttons.addWidget(self.new_photo)
62
63          self.openImage = QPushButton()
64          self.openImage.setText("Open file")
65          self.openImage.clicked.connect(self.openFile)
66          self.buttons.addWidget(self.openImage)
67
68          self.update_button = QPushButton()
69          self.update_button.setText("Draw intensity profile")
70          self.update_button.clicked.connect(self.Update)
71          self.buttons.addWidget(self.update_button)
72          self.update_button.setDisabled(True)  # Disables update button until line
    profile and scale line are selected
73
74          self.text = QHBoxLayout()
75          self.acquisition.addLayout(self.text)
76          self.left_image = QLabel()
77          self.left_image.setPixmap(QPixmap(r"..\left.png"))
78          self.left_image.setScaledContents(True)
79          self.left_image.setMaximumSize(QSize(50, 50))
80          self.text.addWidget(self.left_image)
81
82          self.left_text = QLabel("Left click to select line")
83          self.text.addWidget(self.left_text)
84
85          self.right_image = QLabel()
86          self.right_image.setPixmap(QPixmap(r"..\right.png"))
87          self.right_image.setScaledContents(True)
88          self.right_image.setMaximumSize(QSize(50, 50))
89          self.text.addWidget(self.right_image)
90
91          self.right_text = QLabel("Right click to select scale line")
92          self.text.addWidget(self.right_text)
93
94          self.results = QVBoxLayout(self)
95          self.title2 = QLabel("Diameter calculation")
96          self.title2.setStyleSheet(u"font: 75 10pt ;")
97          self.results.addWidget(self.title2)
98
99          self.plot = Canvas(self)
100         self.results.addWidget(self.plot)
101         self.toolbar = NavigationToolbar2QT(self.plot, self)
102         self.results.addWidget(self.toolbar)
103         self.plot.figure.canvas.mpl_connect('pick_event', self.pick)
104         self.global_layout.addLayout(self.results, 0, 1, 1, 1)
105
106         self.results = QGridLayout()
107         self.global_layout.addLayout(self.results, 1, 1, 1, 1)
108
109         self.distance_label = QLabel("Distance from target (cm)")
110         self.results.addWidget(self.distance_label, 1, 0, 1, 1)
111         self.distance_input = QPlainTextEdit()
112         self.distance_input.setPlainText("20")
113         self.results.addWidget(self.distance_input, 1, 1, 1, 1)
114         self.distance_input.setMaximumHeight(30)
115         self.scaleVal_label = QLabel("Scale measurement (cm)")
116         self.results.addWidget(self.scaleVal_label, 2, 0, 1, 1)
117         self.scaleVal = QPlainTextEdit()
```

```
118         self.scaleVal.setPlainText("5")
119         self.scaleVal.setMaximumHeight(30)
120         self.results.addWidget(self.scaleVal, 2, 1, 1, 1)
121 
122         self.text2 = QLabel("Left click to select points")
123         self.results.addWidget(self.text2, 0, 0, 1, 1)
124 
125         #Find peaks button
126         self.find_peaks = QPushButton("Find peaks")
127         self.find_peaks.clicked.connect(self.calculate)
128         self.results.addWidget(self.find_peaks, 0, 1, 1, 1)
129 
130         #Calculate button
131         self.calculate_button = QPushButton()
132         self.results.addWidget(self.calculate_button, 3, 0, 1, 1)
133         self.calculate_button.setText("Calculate")
134         self.calculate_button.clicked.connect(self.diameter)
135 
136         #Result text box
137         self.result = QTextBrowser()
138         self.result.setMaximumHeight(30)
139         self.results.addWidget(self.result, 3, 1, 1, 1)
140 
141         #Variables for the diameter calculation
142         self.position_x = []
143         self.position_y = []
144         self.scale_x = []
145         self.scale_y = []
146         self.measure_line = 0
147         self.ysmoothed = 0
148         self.xvals = 0
149         self.peaks = 0
150         self.peaks_x = []
151         self.peaks_y = []
152 
153     # Gets position of clicked point, saves position and scale positions, draws
        lines of position in red and scale in white
154     def clicked_image(self, event):
155         # Gets clicked button information
156         side = event.button()
157 
158         # Gets x and y position of the click
159         x = event.pos().x()
160         y = event.pos().y()
161 
162         # If left button is clicked
163         if side == 1:
164             self.position_x.append(x)
165             self.position_y.append(y)
166 
167         # If right button is clicked
168         elif side == 2:
169             self.scale_x.append(x)
170             self.scale_y.append(y)
171 
172         # Creates a QPixmap reference to draw lines and points
173         pixmap = QPixmap(self.img_scl)
174         line = QPainter(pixmap)
175 
176         # Creates scale point
```

```
177         if len(self.scale_x) == 1 and len(self.position_y) == 0:
178             line.setPen(QPen(Qt.white, 5))
179             line.drawPoint(self.scale_x[-1], self.scale_y[-1])
180 
181         elif len(self.position_y) == 1 and len(self.scale_x) == 0:
182             line.setPen(QPen(Qt.red, 5))
183             line.drawPoint(self.position_x[-1], self.position_y[-1])
184 
185         elif len(self.position_y) > 1 and len(self.scale_x) > 1:
186             line.setPen(QPen(Qt.red, 2))
187             line.drawLine(self.position_x[-1], self.position_y[-1], self.position_x
    [-2], self.position_y[-2])
188             self.position_x = self.position_x[-2:]
189             self.position_y = self.position_y[-2:]
190             line.setPen(QPen(Qt.white, 2))
191             line.drawLine(self.scale_x[-1], self.scale_y[-1], self.scale_x[-2],
    self.scale_y[-2])
192             self.scale_y = self.scale_y[-2:]
193             self.scale_x = self.scale_x[-2:]
194             self.update_button.setDisabled(False)  # Enables update button for line
     profile
195 
196         # Creates scale line and updates scale points info
197         elif len(self.scale_x) > 1 and len(self.position_y) == 0:
198             line.setPen(QPen(Qt.white, 2))
199             line.drawLine(self.scale_x[-1], self.scale_y[-1], self.scale_x[-2],
    self.scale_y[-2])
200             self.scale_y = self.scale_y[-2:]
201             self.scale_x = self.scale_x[-2:]
202 
203         elif len(self.position_x) > 1 and len(self.scale_x) == 0:
204             line.setPen(QPen(Qt.red, 2))
205             line.drawLine(self.position_x[-1], self.position_y[-1], self.position_x
    [-2], self.position_y[-2])
206             self.scale_y = self.scale_y[-2:]
207             self.scale_x = self.scale_x[-2:]
208 
209         elif len(self.position_x) > 1 and len(self.scale_x) == 1:
210             line.setPen(QPen(Qt.red, 2))
211             line.drawLine(self.position_x[-1], self.position_y[-1], self.position_x
    [-2], self.position_y[-2])
212             self.scale_y = self.scale_y[-2:]
213             self.scale_x = self.scale_x[-2:]
214             line.setPen(QPen(Qt.white, 2))
215             line.drawPoint(self.scale_x[-1], self.scale_y[-1])
216 
217         elif len(self.scale_x) > 1 and len(self.position_y) == 1:
218             line.setPen(QPen(Qt.white, 2))
219             line.drawLine(self.scale_x[-1], self.scale_y[-1], self.scale_x[-2],
    self.scale_y[-2])
220             self.scale_y = self.scale_y[-2:]
221             self.scale_x = self.scale_x[-2:]
222             line.setPen(QPen(Qt.red, 2))
223             line.drawPoint(self.position_x[-1], self.position_y[-1])
224 
225         line.end()
226         self.wimage.setPixmap(pixmap)
227 
228     # Function that calculates line profile
229     def Update(self):
```

```
230         # Clear up plot
231         self.plot.ax1.cla()
232 
233         # Transforms pixmap to array
234         a = self.wimage.pixmap().toImage()
235 
236         # Creats empty array with the same size as the image
237         height = a.height()
238         width = a.width()
239         array = np.zeros((height, width))
240 
241         # Writes red channel information on the array
242         for i in range(height):
243             for j in range(width):
244                 array[i, j] += QColor(a.pixel(i, j)).getRgb()[0]
245 
246         # Source and destination of line profile
247         src = (self.position_x[-2], self.position_y[-2])
248         dst = (self.position_x[-1], self.position_y[-1])
249 
250         # Measures line profile with 3 pixel width
251         self.measure_line = measure.profile_line(array, src, dst, linewidth=10)
252 
253         # Plots measure line
254         self.plot.ax1.plot(self.measure_line)
255         self.plot.ax1.set_xlabel("Distance (pixels)")
256         self.plot.ax1.set_ylabel('Intensity')
257         self.plot.draw()
258 
259     # Function take_photo captures new photo from webcam
260     def take_photo(self):
261         webcam = cv2.VideoCapture(0, cv2.CAP_DSHOW)
262         check, frame = webcam.read()
263         image = cv2.cvtColor(frame, cv2.COLOR_BGR2RGB)
264         height, width, channel = image.shape
265         bytesPerLine = 3 * width
266         qImg = QImage(image.data, width, height, bytesPerLine, QImage.Format_RGB888
    )
267         self.wimage.setPixmap(QPixmap(qImg))
268         self.image_pixmap = QPixmap(qImg)
269 
270     # Function that calculates peak values from profile line and calculates the
    diameter of the fiber
271     def calculate(self):
272         scale = (int(self.scaleVal.toPlainText()))
273         x = self.scale_x
274         y = self.scale_y
275 
276         #Calculates distance in pixels
277         dist_x = abs(x[-1] - x[-2])
278         dist_y = abs(y[-1] - y[-2])
279         distance = sqrt(dist_x ** 2 + dist_y ** 2) / scale  # Number of pixels that
     correspond to 1 cm
280 
281         # Calculate corrected x values and replots with corrected x label
282         x_val = linspace(0, len(self.measure_line), len(self.measure_line)) /
    distance
283         self.plot.ax1.cla()  # Clear axis
284         # self.plot.ax1.plot(x_val, self.measure_line, '-', picker=True, pickradius
    =5)
```

```
285         self.plot.ax1.set_xlabel('Distance (cm)')
286         self.plot.ax1.set_picker(2)
287 
288         ## Find minimum values of the profile line ##
289         # Interpolate function for better resolution
290         self.xvals = linspace(min(x_val), max(x_val), 5000)
291         yinterp = interp(self.xvals, x_val, self.measure_line)
292         self.ysmoothed = savgol_filter(yinterp, 51, 3)  # Smooth interpolated
    signal
293         self.peaks, _ = find_peaks(-self.ysmoothed)
294         self.plot.ax1.plot(self.xvals[self.peaks], self.ysmoothed[self.peaks],
    linewidth=0, color='green', marker='o',
295                            picker=True, pickradius=5)
296         self.plot.ax1.plot(self.xvals, self.ysmoothed)
297         self.plot.draw()
298 
299     # Function openFile gets new image file, opens and stores new pixmap
    information
300     def openFile(self):
301         print("Open file")
302         new_img, _ = QFileDialog.getOpenFileName()
303         self.image_pixmap = QPixmap(new_img)
304         self.img_scl = self.image_pixmap.scaled(500, 600, Qt.KeepAspectRatio, Qt.
    SmoothTransformation)
305         self.wimage.setPixmap(self.img_scl)
306 
307     # Function triggered by clicking on the graph
308     def pick(self, event):
309         if isinstance(event.artist, Line2D):
310             thisline = event.artist
311 
312             #Gets x and y data and appends to variables peaks_x and peaks_y
313             xdata = thisline.get_xdata()
314             ydata = thisline.get_ydata()
315             ind = event.ind
316             self.peaks_x.append(xdata[ind][0])
317             self.peaks_y.append(ydata[ind][0])
318 
319             #More than 2 peaks are selected
320             if len(self.peaks_x) > 2:
321                 #Resets list to only 2 points
322                 self.peaks_x = self.peaks_x[-2:]
323                 self.peaks_y = self.peaks_y[-2:]
324                 #Clears plot and replots functions
325                 self.plot.ax1.cla()
326                 self.plot.ax1.plot(self.xvals, self.ysmoothed)
327                 self.plot.ax1.plot(self.xvals[self.peaks], self.ysmoothed[self.
    peaks], linewidth=0, color='green',
328                                    marker='o', picker=True, pickradius=5)
329             #Plots selected points
330             self.plot.ax1.plot(self.peaks_x, self.peaks_y, linewidth=0, color='red'
    , marker='x', markersize=10)
331             self.plot.draw()
332 
333     # Calculates diameter
334     def diameter(self):
335         y = self.measure_line
336         x = self.xvals
337 
338         # Calculate rough FWHM of the 0-th order peak
```

```
339         fwhm = ((max(y) + 1.25 * mean(y)) / 2)  # Estimated value of FWHM of the
    peak
340 
341         #Smoothes calculated profile line
342         y_smoothed = self.ysmoothed
343 
344         # Intersection between profile line and fwhm value
345         fwhm_lst = ones(len(x)) * fwhm
346         line1 = LineString(column_stack((x, y_smoothed)))
347         line2 = LineString(column_stack((x, fwhm_lst)))
348         intersection = line1.intersection(line2)
349 
350         # Get the 0-th order peak position
351         pos_x, _ = intersection.centroid.xy
352 
353         # Determines position of nearest xval to the position of the estimated
    centroid
354         i = (abs(x - pos_x)).argmin()
355         zero = self.xvals[i]
356 
357         # Calculates distance for the first two peaks and sorts
358         dist_peaks = [abs(x - zero) for x in self.peaks_x]
359         dist_peaks.sort()
360 
361         # Calculates phi1 and phi2
362         L = float(self.distance_input.toPlainText())
363         wavelength = 632.8 * 1E-9  # in nm
364         phi1 = arctan(dist_peaks[0] / (2 * L))
365         phi2 = arctan(dist_peaks[1] / (2 * L))
366 
367         # Calculates diameter in um and sets text to result output
368         d = 1E6 * 4 * wavelength / ((2 * phi1) + phi2)
369         self.result.setPlainText(str(round(d, 2))) #Displays rounded value for
    diameter
```

Bibliography

[1] A. K. Geim and K. S. Novoselov, "The rise of graphene", *Nature Materials*, vol. 6, pp. 183–191, 2007. DOI: 10.1038/nmat1849.

[2] K. S. Novoselov, D. Jiang, F. Schedin, *et al.*, "Two-dimensional atomic crystals", *Proceedings of the National Academy of Sciences of the United States of America*, vol. 102, no. 30, pp. 10 451–10 453, 2005, ISSN: 00278424. DOI: 10.1073/pnas.0502848102.

[3] K. Kao and G. Hockham, "Dielectric-fibre surface waveguides for optical frequencies", *IEE Proceedings J Optoelectronics*, vol. 133, no. 3, p. 191, 1986, ISSN: 02673932. DOI: 10.1049/ip-j.1986.0030. [Online]. Available: https://digital-library.theiet.org/content/journals/10.1049/ip-j.1986.0030.

[4] A. Chryssis, S. Saini, S. Lee, Hyunmin Yi, W. Bentley, and M. Dagenais, "Detecting hybridization of DNA by highly sensitive evanescent field etched core fiber Bragg grating sensors", *IEEE Journal of Selected Topics in Quantum Electronics*, vol. 11, no. 4, pp. 864–872, Jul. 2005, ISSN: 1077-260X. DOI: 10.1109/JSTQE.2005.857724.

[5] C. Viphavakit, S. O. Keeffe, M. Yang, S. Andersson-Engels, and E. Lewis, "Gold Enhanced Hemoglobin Interaction in a Fabry–Pérot Based Optical Fiber Sensor for Measurement of Blood Refractive Index", *Journal of Lightwave Technology*, vol. 36, no. 4, pp. 1118–1124, Feb. 2018, ISSN: 0733-8724. DOI: 10.1109/JLT.2017.2782078.

[6] C. Davis, S. Tejedor, I. Grabovac, J. Kopczyk, and T. Nuyens, "High-strain fiber bragg gratings for structural fatigue testing of military aircraft", *Photonic Sensors*, vol. 2, no. 3, pp. 215–224, 2012, ISSN: 16749251. DOI: 10.1007/s13320-012-0066-3.

[7] J. Jiang, X. Wu, Z. Wang, C. Zhang, G. Ma, and X. Li, "Moisture Content Measurement in Transformer Oil Using Micro-nano Fiber", *IEEE Transactions on Dielectrics and Electrical Insulation*, vol. 27, no. 6, pp. 1829–1836, 2020, ISSN: 15584135. DOI: 10.1109/TDEI.2020.008885.

[8] S. M. Hendrickson, M. M. Lai, T. B. Pittman, and J. D. Franson, "Observation of two-photon absorption at low power levels using tapered optical fibers in rubidium vapor", *Physical Review Letters*, vol. 105, no. 17, pp. 1–4, 2010, ISSN: 00319007. DOI: 10.1103/PhysRevLett.105.173602. eprint: 1007.1941.

[9] A. M. Dimiev and S. Eigler, *Graphene Oxide: Fundamentals and Applications*, A. M. Dimiev and S. Eigler, Eds. Chichester, UK: John Wiley & Sons, Ltd, Oct. 2016, ISBN: 9781119069447. DOI: 10.1002/9781119069447.

[10] R. Wang, X. G. Ren, Z. Yan, L. J. Jiang, W. E. Sha, and G. C. Shan, "Graphene based functional devices: A short review", *Frontiers of Physics*, vol. 14, no. 1, pp. 9–18, 2019, ISSN: 20950470. DOI: 10.1007/s11467-018-0859-y. arXiv: 1810.07487.

[11] J. Ma, H. Xuan, H. L. Ho, W. Jin, Y. Yang, and S. Fan, "Fiber-Optic Fabry–Pérot Acoustic Sensor With Multilayer Graphene Diaphragm", *IEEE Photonics Technology Letters*, vol. 25, no. 10, pp. 932–935, May 2013, ISSN: 1041-1135. DOI: 10.1109/LPT.2013.2256343.

[12] C. Li, X. Yu, W. Zhou, Y. Cui, J. Liu, and S. Fan, "Ultrafast miniature fiber-tip Fabry–Perot humidity sensor with thin graphene oxide diaphragm", *Optics Letters*, vol. 43, no. 19, p. 4719, 2018, ISSN: 0146-9592. DOI: 10.1364/ol.43.004719.

[13] X. Yang, A. Vorobiev, A. Generalov, *et al.*, "A flexible graphene terahertz detector", *Applied Physics Letters*, vol. 111, no. 021102, pp. 2–6, 2017. DOI: 10.1063/1.4993434.

[14] X. M. Liu, H. R. Yang, Y. D. Cui, *et al.*, "Graphene-clad microfibre saturable absorber for ultrafast fibre lasers", *Scientific Reports*, vol. 6, no. May, pp. 1–8, 2016, ISSN: 20452322. DOI: 10.1038/srep26024.

[15] A. T. Smith, A. M. LaChance, S. Zeng, B. Liu, and L. Sun, "Synthesis, properties, and applications of graphene oxide/reduced graphene oxide and their nanocomposites", *Nano Materials Science*, vol. 1, no. 1, pp. 31–47, 2019, ISSN: 25899651. DOI: 10.1016/j.nanoms.2019.02.004.

[16] C. Lee, X. Wei, J. W. Kysar, and J. Hone, "Measurement of the elastic properties and intrinsic strength of monolayer graphene", *Science*, vol. 321, no. 5887, pp. 385–388, 2008, ISSN: 00368075. DOI: 10.1126/science.1157996.

[17] J. W. Suk, R. D. Piner, J. An, and R. S. Ruoff, "Mechanical properties of monolayer graphene oxide", *ACS Nano*, vol. 4, no. 11, pp. 6557–6564, 2010, ISSN: 19360851. DOI: 10.1021/nn101781v.

[18] C. Gómez-Navarro, M. Burghard, and K. Kern, "Elastic properties of chemically derived single graphene sheets", *Nano Letters*, vol. 8, no. 7, pp. 2045–2049, 2008, ISSN: 15306984. DOI: 10.1021/nl801384y.

[19] P. Zhang, L. Ma, F. Fan, *et al.*, "Fracture toughness of graphene", *Nature Communications*, vol. 5, pp. 1–7, 2014, ISSN: 20411723. DOI: 10.1038/ncomms4782.

[20] Y. Zhu, S. Murali, W. Cai, *et al.*, "Graphene and graphene oxide: Synthesis, properties, and applications", *Advanced Materials*, vol. 22, no. 35, pp. 3906–3924, 2010, ISSN: 09359648. DOI: 10.1002/adma.201001068.

[21] C. Soldano, A. Mahmood, and E. Dujardin, "Production, properties and potential of graphene", *Carbon*, vol. 48, no. 8, pp. 2127–2150, 2010, ISSN: 00086223. DOI: 10.1016/j.carbon.2010.01.058.

[22] K. I. Bolotin, K. J. Sikes, Z. Jiang, *et al.*, "Ultrahigh electron mobility in suspended graphene", *Solid State Communications*, vol. 146, no. 9-10, pp. 351–355, 2008, ISSN: 00381098. DOI: 10.1016/j.ssc.2008.02.024. arXiv: 0802.2389.

[23] G. Eda, C. Mattevi, H. Yamaguchi, H. Kim, and M. Chhowalla, "Insulator to semimetal transition in graphene oxide", *Journal of Physical Chemistry C*, vol. 113, no. 35, pp. 15 768–15 771, 2009, ISSN: 19327447. DOI: 10.1021/jp9051402. arXiv: 0905.2799.

[24] D. Voiry, J. Yang, J. Kupferberg, *et al.*, "High-quality graphene via microwave reduction of solution-exfoliated graphene oxide", *Science*, vol. 353, no. 6306, pp. 1413–1416, 2016, ISSN: 10959203. DOI: 10.1126/science.aah3398.

[25] G. Jayalakshmi, K. Saravanan, B. K. Panigrahi, B. Sundaravel, and M. Gupta, "Tunable electronic, electrical and optical properties of graphene oxide sheets by ion irradiation", *Nanotechnology*, vol. 29, no. 18, 2018, ISSN: 13616528. DOI: 10.1088/1361-6528/aab011.

[26] Z. H. Ni, H. M. Wang, J. Kasim, *et al.*, "Graphene Thickness Determination Using Reflection and Contrast Spectroscopy", *Nano Letters*, vol. 7, no. 9, pp. 2758–2763, Sep. 2007, ISSN: 1530-6984. DOI: 10.1021/nl071254m.

[27] S. A. Mikhailov, "Graphene-based voltage-tunable coherent terahertz emitter", *Physical Review B - Condensed Matter and Materials Physics*, vol. 87, no. 11, pp. 1–6, 2013, ISSN: 10980121. DOI: 10.1103/PhysRevB.87.115405. arXiv: 1203.3983.

[28] "Antenna Enhanced Graphene THz Emitter and Detector", *Nano Letters*, vol. 15, no. 8, pp. 5295–5301, 2015, ISSN: 15306992. DOI: 10.1021/acs.nanolett.5b01635.

[29] F. Bonaccorso, Z. Sun, T. Hasan, and A. C. Ferrari, "Graphene photonics and optoelectronics", *Nature Photonics*, vol. 4, no. 9, pp. 611–622, 2010, ISSN: 17494885. DOI: 10.1038/nphoton.2010.186. arXiv: 1006.4854.

[30] K. S. Novoselov, V. I. Fal'Ko, L. Colombo, P. R. Gellert, M. G. Schwab, and K. Kim, "A roadmap for graphene", *Nature*, vol. 490, no. 7419, pp. 192–200, 2012, ISSN: 00280836. DOI: 10.1038/nature11458.

[31] C. J. Docherty and M. B. Johnston, "Terahertz properties of graphene", *Journal of Infrared, Millimeter, and Terahertz Waves*, vol. 33, no. 8, pp. 797–815, 2012, ISSN: 18666892. DOI: 10.1007/s10762-012-9913-y.

[32] M. Hernaez, C. R. Zamarreño, S. Melendi-Espina, L. R. Bird, A. G. Mayes, and F. J. Arregui, "Optical fibre sensors using graphene-based materials: A review", *Sensors (Switzerland)*, vol. 17, no. 1, pp. 1–24, 2017, ISSN: 14248220. DOI: 10.3390/s17010155.

[33] P. O'Brien, "Chemical Vapor Deposition", in *Encyclopedia of Materials: Science and Technology*, Elsevier, 2001, pp. 1173–1176, ISBN: 978-0-08-043152-9. DOI: 10.1016/B0-08-043152-6/00219-9.

[34] Y. Zhang, L. Zhang, and C. Zhou, "Review of chemical vapor deposition of graphene and related applications", *Accounts of Chemical Research*, vol. 46, no. 10, pp. 2329–2339, 2013, ISSN: 00014842. DOI: 10.1021/ar300203n.

[35] X. Chen, L. Zhang, and S. Chen, "Large area CVD growth of graphene", *Synthetic Metals*, vol. 210, pp. 95–108, 2015, ISSN: 03796779. DOI: 10.1016/j.synthmet.2015.07.005.

[36] B. C. Brodie, "On the Atomic Weight of Graphite", *Philosophical Transactions of the Royal Society A: Mathematical, Physical and Engineering Sciences*, vol. 149, pp. 249–259, 1859.

[37] L. Staudenmaier, "Method for the preparation of graphitic acid", *Ber. Dtsch. Chem. Ges.*, vol. 31, pp. 1481–1487, 1898, ISSN: 0365-9496.

[38] W. S. Hummers and R. E. Offeman, "Preparation of Graphitic Oxide", *Journal of the American Chemical Society*, vol. 80, no. 6, p. 1339, 1958, ISSN: 15205126. DOI: 10.1021/ja01539a017.

[39] D. C. Marcano, D. V. Kosynkin, J. M. Berlin, *et al.*, "Improved Synthesis of Graphene Oxide", *ACS Nano*, vol. 4, no. 8, pp. 4806–4814, Aug. 2010, ISSN: 1936-0851. DOI: 10.1021/nn1006368.

[40] S. Pei and H. M. Cheng, "The reduction of graphene oxide", *Carbon*, vol. 50, no. 9, pp. 3210–3228, 2012, ISSN: 00086223. DOI: 10.1016/j.carbon.2011.11.010.

[41] J. Chen, B. Yao, C. Li, and G. Shi, "An improved Hummers method for eco-friendly synthesis of graphene oxide", *Carbon*, vol. 64, no. 1, pp. 225–229, 2013, ISSN: 00086223. DOI: 10.1016/j.carbon.2013.07.055.

[42] S. V. Morozov, K. S. Novoselov, M. I. Katsnelson, *et al.*, "Giant intrinsic carrier mobilities in graphene and its bilayer", *Physical Review Letters*, vol. 100, no. 1, pp. 11–14, 2008, ISSN: 00319007. DOI: 10.1103/PhysRevLett.100.016602.

[43] E. Pallecchi, F. Lafont, V. Cavaliere, *et al.*, "High Electron Mobility in Epitaxial Graphene on 4H-SiC(0001) via post-growth annealing under hydrogen", *Scientific Reports*, vol. 4, no. 1, p. 4558, May 2015, ISSN: 2045-2322. DOI: 10.1038/srep04558.

[44] L. Banszerus, M. Schmitz, S. Engels, *et al.*, "Ultrahigh-mobility graphene devices from chemical vapor deposition on reusable copper", *Science Advances*, vol. 1, no. 6, pp. 1–7, 2015, ISSN: 23752548. DOI: 10.1126/sciadv.1500222.

[45] F. C. Bocquet, Y. R. Lin, M. Franke, *et al.*, "Surfactant-Mediated Epitaxial Growth of Single-Layer Graphene in an Unconventional Orientation on SiC", *Physical Review Letters*, vol. 125, no. 10, p. 106 102, 2020, ISSN: 10797114. DOI: 10.1103/PhysRevLett.125.106102.

[46] P. Blake, E. W. Hill, A. H. Castro Neto, *et al.*, "Making graphene visible", *Applied Physics Letters*, vol. 91, no. 6, 2007, ISSN: 00036951. DOI: 10.1063/1.2768624. arXiv: 0705.0259.

[47] M. Hu, Z. Yao, and X. Wang, "Characterization techniques for graphene-based materials in catalysis", *AIMS Materials Science*, vol. 4, no. 3, pp. 755–788, 2017, ISSN: 23720468. DOI: 10.3934/matersci.2017.3.755.

[48] A. Sikora, M. Woszczyna, M. Friedemann, F. J. Ahlers, and M. Kalbac, "AFM diagnostics of graphene-based quantum Hall devices", *Micron*, vol. 43, no. 2-3, pp. 479–486, 2012, ISSN: 09684328. DOI: 10.1016/j.micron.2011.11.010.

[49] M. Begliarbekov, O. Sul, S. Kalliakos, E. H. Yang, and S. Strauf, "Determination of edge purity in bilayer graphene using μ-Raman spectroscopy", *Applied Physics Letters*, vol. 97, no. 3, pp. 2010–2013, 2010, ISSN: 00036951. DOI: 10.1063/1.3464972.

[50] C. Casiraghi, A. Hartschuh, E. Lidorikis, *et al.*, "Rayleigh imaging of graphene and graphene layers", *Nano Letters*, vol. 7, no. 9, pp. 2711–2717, 2007, ISSN: 15306984. DOI: 10.1021/nl071168m. arXiv: 0705.2645.

[51] L. Lu, H. Tian, J. He, and Q. Yang, "Graphene-MnO2 Hybrid Nanostructure as a New Catalyst for Formaldehyde Oxidation", *Journal of Physical Chemistry C*, vol. 120, no. 41, pp. 23 660–23 668, 2016, ISSN: 19327455. DOI: 10.1021/acs.jpcc.6b08312.

[52] B. Lee, "Review of the present status of optical fiber sensors", *Optical Fiber Technology*, vol. 9, no. 2, pp. 57–79, 2003, ISSN: 10685200. DOI: 10.1016/S1068-5200(02)00527-8.

[53] M. Zhang, X. Ma, L. Wang, *et al.*, "Progress of optical fiber sensors and its application in harsh environment", *Photonic Sensors*, vol. 1, no. 1, pp. 84–89, 2011, ISSN: 16749251. DOI: 10.1007/s13320-010-0012-1.

[54] M. Yang and J. Dai, "Review on optical fiber sensors with sensitive thin films", *Photonic Sensors*, vol. 2, no. 1, pp. 14–28, Mar. 2012, ISSN: 1674-9251. DOI: 10.1007/s13320-011-0047-y. [Online]. Available: http://link.springer.com/10.1007/s13320-011-0047-y.

[55] C. Li, W. Yang, M. Wang, *et al.*, "A review of coating materials used to improve the performance of optical fiber sensors", *Sensors (Switzerland)*, vol. 20, no. 15, pp. 1–24, 2020, ISSN: 14248220. DOI: 10.3390/s20154215.

[56] S. P. Koenig, N. G. Boddeti, M. L. Dunn, and J. S. Bunch, "Ultrastrong adhesion of graphene membranes", *Nature Nanotechnology*, vol. 6, no. 9, pp. 543–546, 2011, ISSN: 17483395. DOI: 10.1038/nnano.2011.123.

[57] S. Stankovich, D. A. Dikin, G. H. Dommett, *et al.*, "Graphene-based composite materials", *Nature*, vol. 442, no. 7100, pp. 282–286, 2006, ISSN: 00280836. DOI: 10.1038/nature04969.

[58] M. Raposo and O. N. Oliveira, "Energies of adsorption of poly(o-methoxyaniline) layer-by-layer films", *Langmuir*, vol. 16, no. 6, pp. 2839–2844, 2000, ISSN: 07437463. DOI: 10.1021/la990945y.

[59] M. Keeney, X. Y. Jiang, M. Yamane, M. Lee, S. Goodman, and F. Yang, "Nanocoating for biomolecule delivery using layer-by-layer self-assembly", *Journal of Materials Chemistry B*, vol. 3, no. 45, pp. 8757–8770, 2015, ISSN: 2050750X. DOI: 10.1039/c5tb00450k.

[60] G. William Kajjumba, S. Emik, A. Öngen, H. Kurtulus Özcan, and S. Aydın, "Modelling of Adsorption Kinetic Processes—Errors, Theory and Application", in *Advanced Sorption Process Applications*, tourism, IntechOpen, Feb. 2019, p. 13. DOI: 10.5772/intechopen.80495.

[61] Y. Liu and L. Shen, "From Langmuir kinetics to first- and second-order rate equations for adsorption", *Langmuir*, vol. 24, no. 20, pp. 11 625–11 630, 2008, ISSN: 07437463. DOI: 10.1021/la801839b.

[62] M. Raposo, R. S. Pontes, L. H. C. Mattoso, and O. N. Oliveira, "Kinetics of adsorption of poly(o-methoxyaniline) self-assembled films", *Macromolecules*, vol. 30, no. 20, pp. 6095–6101, 1997, ISSN: 00249297. DOI: 10.1021/ma970228f.

[63] Q. Ferreira, P. António Ribeiro, and M. Raposo, "Villain's fractal growth of poly[1-[4-(3-carboxy-4-hydroxyphenylazo) benzenesulfonamido]-1,2-ethanediyl, sodium salt] J-aggregates onto layer-by-layer films and its effect on film absorbance spectrum", *Journal of Applied Physics*, vol. 113, no. 24, 2013, ISSN: 00218979. DOI: 10.1063/1.4812381.

[64] S. Jaworski, M. Wierzbicki, E. Sawosz, *et al.*, "Graphene oxide-based nanocomposites decorated with silver nanoparticles as an antibacterial agent", *Nanoscale Research Letters*, vol. 13, no. 1, 2018, ISSN: 1556276X. DOI: 10.1186/s11671-018-2533-2.

[65] K. Tsirka, A. Katsiki, N. Chalmpes, D. Gournis, and A. S. Paipetis, "Mapping of graphene oxide and single layer graphene flakes—defects annealing and healing", *Frontiers in Materials*, vol. 5, no. June, pp. 1–11, 2018, ISSN: 22968016. DOI: 10.3389/fmats.2018.00037.

[66] S. Liu, K. Yang, Y. Wang, *et al.*, "High-sensitivity strain sensor based on in-fiber rectangular air bubble", *Scientific Reports*, vol. 5, no. 1, p. 7624, Jul. 2015, ISSN: 2045-2322. DOI: 10.1038/srep07624.

[67] C. Monteiro, S. Silva, and O. Frazao, "Hollow Microsphere Fabry–Perot Cavity for Sensing Applications", *IEEE Photonics Technology Letters*, vol. 29, no. 15, pp. 1229–1232, Aug. 2017, ISSN: 1041-1135. DOI: 10.1109/LPT.2017.2701000.

[68] S. Novais, M. S. Ferreira, and J. L. Pinto, "Lateral Load Sensing with an Optical Fiber Inline Microcavity", *IEEE Photonics Technology Letters*, vol. 29, no. 17, pp. 1502–1505, 2017, ISSN: 10411135. DOI: 10.1109/LPT.2017.2735021.

[69] C. Liao, S. Liu, L. Xu, *et al.*, "Sub-micron silica diaphragm-based fiber-tip Fabry–Perot interferometer for pressure measurement", *Optics Letters*, vol. 39, no. 10, p. 2827, 2014, ISSN: 0146-9592. DOI: 10.1364/OL.39.002827.

[70] R. M. André, S. C. Warren-Smith, M. Becker, *et al.*, "Simultaneous measurement of temperature and refractive index using focused ion beam milled Fabry-Perot cavities in optical fiber micro-tips", *Optics Express*, vol. 24, no. 13, p. 14 053, 2016, ISSN: 1094-4087. DOI: 10.1364/OE.24.014053.

[71] E. Hecht, *Optics*, 4th ed. Addison Wesley, 2002, ISBN: 9780805385663.

[72] A. K. Sharma and J. Gupta, "Graphene based chalcogenide fiber-optic evanescent wave sensor for detection of hemoglobin in human blood", *Optical Fiber Technology*, vol. 41, no. December 2017, pp. 125–130, 2018, ISSN: 10685200. DOI: 10.1016/j.yofte.2018.01.012.

[73] H. W. Qiu, S. C. Xu, S. Z. Jiang, *et al.*, "A novel graphene-based tapered optical fiber sensor for glucose detection", *Applied Surface Science*, vol. 329, pp. 390–395, 2015, ISSN: 01694332. DOI: 10.1016/j.apsusc.2014.12.093.

[74] Y. Zhao, S. Y. Zhang, G. F. Wen, and Z. X. Han, "Graphene-based optical fiber ammonia gas sensor", *Instrumentation Science & Technology*, vol. 46, no. 1, pp. 12–27, 2018, ISSN: 1073-9149. DOI: 10.1080/10739149.2017.1326936.

[75] B. Yao, Y. Wu, Y. Cheng, *et al.*, "All-optical Mach-Zehnder interferometric NH3 gas sensor based on graphene/microfiber hybrid waveguide", *Sensors and Actuators, B: Chemical*, vol. 194, pp. 142–148, Apr. 2014, ISSN: 09254005. DOI: 10.1016/j.snb.2013.12.085.

[76] Y. Wu, B. Yao, A. Zhang, *et al.*, "Graphene-coated microfiber Bragg grating for high-sensitivity gas sensing", *Optics Letters*, vol. 39, no. 5, p. 1235, 2014, ISSN: 0146-9592. DOI: 10.1364/ol.39.001235.

[77] Y. Xiao, J. Yu, L. Shun, *et al.*, "Reduced graphene oxide for fiber-optic toluene gas sensing", *Optics Express*, vol. 24, no. 25, p. 28 290, 2016, ISSN: 1094-4087. DOI: 10.1364/oe.24.028290.

[78] J. Zhang, G. Liao, S. Jin, *et al.*, "All-fiber-optic temperature sensor based on reduced graphene oxide", *Laser Physics Letters*, vol. 11, no. 3, p. 035 901, Mar. 2014, ISSN: 1612-2011. DOI: 10.1088/1612-2011/11/3/035901.

[79] J. Zhang, L. Zhang, and W. Xu, "Surface plasmon polaritons: Physics and applications", *Journal of Physics D: Applied Physics*, vol. 45, no. 11, 2012, ISSN: 00223727. DOI: 10.1088/0022-3727/45/11/113001.

[80] S. Roh, T. Chung, and B. Lee, "Overview of the characteristics of micro- and nano-structured surface plasmon resonance sensors", *Sensors*, vol. 11, no. 2, pp. 1565–1588, 2011, ISSN: 14248220. DOI: 10.3390/s110201565.

[81] P. K. Maharana, R. Jha, and P. Padhy, "On the electric field enhancement and performance of SPR gas sensor based on graphene for visible and near infrared", *Sensors and Actuators, B: Chemical*, vol. 207, no. Part A, pp. 117–122, 2015, ISSN: 09254005. DOI: 10.1016/j.snb.2014.10.006.

[82] A. Patnaik, K. Senthilnathan, and R. Jha, "Graphene-Based Conducting Metal Oxide Coated D-Shaped Optical Fiber SPR Sensor", *IEEE Photonics Technology Letters*, vol. 27, no. 23, pp. 2437–2440, 2015, ISSN: 10411135. DOI: 10.1109/LPT.2015.2467189.

[83] G. An, S. Li, T. Cheng, *et al.*, "Ultra-stable D-shaped Optical Fiber Refractive Index Sensor with Graphene-Gold Deposited Platform", *Plasmonics*, vol. 14, no. 1, pp. 155–163, 2019, ISSN: 15571963. DOI: 10.1007/s11468-018-0788-1.

[84] M. S. Rahman, S. S. Noor, M. S. Anower, L. F. Abdulrazak, M. M. Rahman, and K. A. Rikta, "Design and numerical analysis of a graphene-coated fiber-optic SPR biosensor using tungsten disulfide", *Photonics and Nanostructures - Fundamentals and Applications*, vol. 33, no. November 2018, pp. 29–35, 2019, ISSN: 15694429. DOI: 10.1016/j.photonics.2018.11.005.

[85] X. Xi, J. Xu, S. Li, *et al.*, "An Au Nanofilm-Graphene/D-Type Fiber Surface Plasmon Resonance Sensor for Highly Sensitive Specificity Bioanalysis", *Sensors*, vol. 20, no. 4, p. 991, Feb. 2020, ISSN: 1424-8220. DOI: 10.3390/s20040991.

[86] S. K. Mishra, S. N. Tripathi, V. Choudhary, and B. D. Gupta, "SPR based fibre optic ammonia gas sensor utilizing nanocomposite film of PMMA/reduced graphene oxide prepared by in situ polymerization", *Sensors and Actuators, B: Chemical*, vol. 199, pp. 190–200, 2014, ISSN: 09254005. DOI: 10.1016/j.snb.2014.03.109.

[87] Q. Wang and W. M. Zhao, "A comprehensive review of lossy mode resonance-based fiber optic sensors", *Optics and Lasers in Engineering*, vol. 100, no. February 2017, pp. 47–60, 2018, ISSN: 01438166. DOI: 10.1016/j.optlaseng.2017.07.009.

[88] M. Hernaez, A. G. Mayes, and S. Melendi-Espina, "Graphene oxide in lossy mode resonance-based optical fiber sensors for ethanol detection", *Sensors (Switzerland)*, vol. 18, no. 1, pp. 1–10, 2018, ISSN: 14248220. DOI: 10.3390/s18010058.

[89] M. Hernaez, A. G. Mayes, and S. Melendi-Espina, "Lossy Mode Resonance Generation by Graphene Oxide Coatings Onto Cladding-Removed Multimode Optical Fiber", *IEEE Sensors Journal*, vol. 19, no. 15, pp. 6187–6192, Aug. 2019, ISSN: 1530-437X. DOI: 10.1109/JSEN.2019.2906010.

[90] S. W. James and R. P. Tatam, "Optical fibre long-period grating sensors: Characteristics and application", *Measurement Science and Technology*, vol. 14, no. 5, 2003, ISSN: 09570233. DOI: 10.1088/0957-0233/14/5/201.

[91] V. Bhatia, "Applications of long-period gratings to single and multi-parameter sensing", *Optics Express*, vol. 4, no. 11, p. 457, 1999, ISSN: 1094-4087. DOI: 10.1364/oe.4.000457.

[92] G. D. Marshall, R. J. Williams, N. Jovanovic, M. J. Steel, and M. J. Withford, "Point-by-point written fiber-Bragg gratings and their application in complex grating designs", *Optics Express*, vol. 18, no. 19, p. 19 844, 2010, ISSN: 1094-4087. DOI: 10.1364/oe.18.019844.

[93] S. S, K. S. Vasu, S. Asokan, and A. K. Sood, "Enhanced strain and temperature sensing by reduced graphene oxide coated etched fiber Bragg gratings", *Optics Letters*, vol. 41, no. 11, p. 2604, Jun. 2016, ISSN: 0146-9592. DOI: 10.1364/OL.41.002604.

[94] Y. Wang, C. Shen, W. Lou, *et al.*, "Fiber optic relative humidity sensor based on the tilted fiber Bragg grating coated with graphene oxide", *Applied Physics Letters*, vol. 109, no. 3, pp. 1–6, 2016, ISSN: 00036951. DOI: 10.1063/1.4959092.

[95] F. H. Koppens, T. Mueller, P. Avouris, A. C. Ferrari, M. S. Vitiello, and M. Polini, "Photodetectors based on graphene, other two-dimensional materials and hybrid systems", *Nature Nanotechnology*, vol. 9, no. 10, pp. 780–793, 2014, ISSN: 17483395. DOI: 10.1038/nnano.2014.215.

[96] B. N. Shivananju, X. Bao, W. Yu, *et al.*, "Graphene Heterostructure Integrated Optical Fiber Bragg Grating for Light Motion Tracking and Ultrabroadband Photodetection from 400 nm to 10.768 μm", *Advanced Functional Materials*, vol. 29, no. 19, pp. 1–9, 2019, ISSN: 16163028. DOI: 10.1002/adfm.201807274.

[97] F. Esposito, L. Sansone, C. Taddei, S. Campopiano, M. Giordano, and A. Iadicicco, "Ultrasensitive biosensor based on long period grating coated with polycarbonate-graphene oxide multilayer", *Sensors and Actuators, B: Chemical*, vol. 274, no. August, pp. 517–526, 2018, ISSN: 09254005. DOI: 10.1016/j.snb.2018.08.002.

[98] B. Xu, J. Huang, L. Ding, and J. Cai, "Graphene oxide-functionalized long period fiber grating for ultrafast label-free glucose biosensor", *Materials Science and Engineering C*, vol. 107, no. October 2019, p. 110 329, 2020, ISSN: 18730191. DOI: 10.1016/j.msec.2019.110329.

[99] J. N. Dash and R. Jha, "Temperature Insensitive PCF Interferometer Coated with Graphene Oxide Tip Sensor", *IEEE Photonics Technology Letters*, vol. 28, no. 9, pp. 1006–1009, 2016, ISSN: 10411135. DOI: 10.1109/LPT.2016.2522979.

[100] C.-B. Yu, Y. Wu, X.-L. Liu, *et al.*, "Graphene oxide deposited microfiber knot resonator for gas sensing", *Optical Materials Express*, vol. 6, no. 3, p. 727, Mar. 2016, ISSN: 2159-3930. DOI: 10.1364/OME.6.000727.

[101] C. Yu, Y. Wu, X. Liu, *et al.*, "Miniature fiber-optic NH_3 gas sensor based on Pt nanoparticle-incorporated graphene oxide", *Sensors and Actuators B: Chemical*, vol. 244, pp. 107–113, Jun. 2017, ISSN: 09254005. DOI: 10.1016/j.snb.2016.12.126.

[102] W. Ni, P. Lu, X. Fu, *et al.*, "Ultrathin graphene diaphragm-based extrinsic Fabry-Perot interferometer for ultra-wideband fiber optic acoustic sensing", *Optics Express*, vol. 26, no. 16, p. 20 758, 2018, ISSN: 1094-4087. DOI: 10.1364/oe.26.020758.

[103] Y. O. Barmenkov, D. Zalvidea, S. Torres-Peiró, J. L. Cruz, and M. V. Andrés, "Effective length of short Fabry-Perot cavity formed by uniform fiber Bragg gratings", *Optics Express*, vol. 14, no. 14, p. 6394, 2006, ISSN: 1094-4087. DOI: 10.1364/OE.14.006394.

[104] V. R. Machavaram, R. A. Badcock, and G. F. Fernando, "Fabrication of intrinsic fibre Fabry-Perot sensors in silica fibres using hydrofluoric acid etching", *Sensors and Actuators, A: Physical*, vol. 138, no. 1, pp. 248–260, 2007, ISSN: 09244247. DOI: 10.1016/j.sna.2007.04.007.

[105] J. Ma, W. Jin, H. L. Ho, and J. Y. Dai, "High-sensitivity fiber-tip pressure sensor with graphene diaphragm", *Optics Letters*, vol. 37, no. 13, p. 2493, 2012, ISSN: 0146-9592. DOI: 10.1364/ol.37.002493.

[106] C. Li, T. Lan, X. Yu, N. Bo, J. Dong, and S. Fan, "Room-temperature pressure-induced optically-actuated Fabry-Perot nanomechanical resonator with multilayer graphene diaphragm in air", *Nanomaterials*, vol. 7, no. 11, 2017, ISSN: 20794991. DOI: 10.3390/nano7110366.

[107] Q. Cui, P. Thakur, C. Rablau, I. Avrutsky, and M. M.-C. Cheng, "Miniature Optical Fiber Pressure Sensor With Exfoliated Graphene Diaphragm", *IEEE Sensors Journal*, vol. 19, no. 14, pp. 5621–5631, Jul. 2019, ISSN: 1530-437X. DOI: 10.1109/JSEN.2019.2904020.

[108] C. Li, Q. Liu, X. Peng, and S. Fan, "Analyzing the temperature sensitivity of Fabry-Perot sensor using multilayer graphene diaphragm", *Optics Express*, vol. 23, no. 21, p. 27 494, 2015. DOI: 10.1364/oe.23.027494.

[109] L. Li, Z. Feng, X. Qiao, *et al.*, "Ultrahigh sensitive temperature sensor based on Fabry-Pérot interference assisted by a graphene diaphragm", *IEEE Sensors Journal*, vol. 15, no. 1, pp. 505–509, 2015, ISSN: 1530437X. DOI: 10.1109/JSEN.2014.2361174.

[110] J. Ma, Y. Zhou, X. Bai, K. Chen, and B. O. Guan, "High-sensitivity and fast-response fiber-tip Fabry-Pérot hydrogen sensor with suspended palladium-decorated graphene", *Nanoscale*, vol. 11, no. 34, pp. 15 821–15 827, 2019, ISSN: 20403372. DOI: 10.1039/c9nr04274a.

[111] Y. Wu, C. Yu, F. Wu, *et al.*, "A Highly Sensitive Fiber-Optic Microphone Based on Graphene Oxide Membrane", *Journal of Lightwave Technology*, vol. 35, no. 19, pp. 4344–4349, 2017, ISSN: 07338724. DOI: 10.1109/JLT.2017.2737639.

[112] J. S. Sirkis, D. D. Brennan, M. A. Putman, T. A. Berkoff, A. D. Kersey, and E. J. Friebele, "In-Line Fiber Etalon for Strain-Measurement", *Optics Letters*, vol. 18, no. 22, pp. 1973–1975, 1993, ISSN: 0146-9592. DOI: Doi10.1364/Ol.18.001973.

[113] M. S. Ferreira, P. Roriz, J. Bierlich, *et al.*, "Fabry-Perot cavity based on silica tube for strain sensing at high temperatures", *Optics Express*, vol. 23, no. 12, p. 16 063, 2015, ISSN: 1094-4087. DOI: 10.1364/OE.23.016063.

[114] C. S. Monteiro, M. S. Ferreira, S. O. Silva, *et al.*, "Fiber Fabry-Perot interferometer for curvature sensing", *Photonic Sensors*, vol. 6, no. 4, pp. 339–344, Dec. 2016, ISSN: 1674-9251. DOI: 10.1007/s13320-016-0333-9.

[115] B. Wang, J. Tian, L. Hu, and Y. Yao, "High Sensitivity Humidity Fiber-Optic Sensor Based on All-Agar Fabry-Perot Interferometer", *IEEE Sensors Journal*, vol. 18, no. 12, pp. 4879–4885, 2018, ISSN: 1530437X. DOI: 10.1109/JSEN.2018.2828134.

[116] S. Tierney, S. Volden, and B. T. Stokke, "Glucose sensors based on a responsive gel incorporated as a Fabry-Perot cavity on a fiber-optic readout platform", *Biosensors and Bioelectronics*, vol. 24, no. 7, pp. 2034–2039, 2009, ISSN: 09565663. DOI: 10.1016/j.bios.2008.10.014.

[117] X. Zou, N. Wu, Y. Tian, J. Ouyang, K. Barringhaus, and X. Wang, "Miniature Fabry–Perot Fiber Optic Sensor for Intravascular Blood Temperature Measurements", *IEEE Sensors Journal*, vol. 13, no. 6, pp. 2155–2160, 2013, ISSN: 1530-437X. DOI: 10.1109/jsen.2013.2251330.

[118] W. R. Habel and K. Krebber, "Fiber-optic sensor applications in civil and geotechnical engineering", *Photonic Sensors*, vol. 1, no. 3, pp. 268–280, Sep. 2011, ISSN: 1674-9251. DOI: 10.1007/s13320-011-0011-x.

[119] W. Zhang, P. Lu, W. Ni, W. Xiong, D. Liu, and J. Zhang, "Gold-Diaphragm Based Fabry-Perot Ultrasonic Sensor for Partial Discharge Detection and Localization", *IEEE Photonics Journal*, vol. 12, no. 3, pp. 1–12, 2020, ISSN: 19430655. DOI: 10.1109/JPHOT.2020.2982460.

[120] V. G. Kravets, F. Schedin, and A. N. Grigorenko, "Plasmonic blackbody: Almost complete absorption of light in nanostructured metallic coatings", *Physical Review B - Condensed Matter and Materials Physics*, vol. 78, no. 20, pp. 97–99, 2008, ISSN: 10980121. DOI: 10.1103/PhysRevB.78.205405.

[121] K. Jiang, A. Zakutayev, J. Stowers, *et al.*, "Low-temperature, solution processing of TiO2 thin films and fabrication of multilayer dielectric optical elements", *Solid State Sciences*, vol. 11, no. 9, pp. 1692–1699, Sep. 2009, ISSN: 12932558. DOI: 10.1016/j.solidstatesciences.2009.05.026.

[122] D. J. Choi, J. S. Maeng, K.-o. Ahn, M. J. Jung, S. H. Song, and Y.-H. Kim, "Synthesis of Cu or Cu_2O-polyimide nanocomposites using Cu powders and their optical properties", *Nanotechnology*, vol. 25, no. 37, p. 375 604, Sep. 2014, ISSN: 0957-4484. DOI: 10.1088/0957-4484/25/37/375604.

[123] R. Peixoto, J. S. Pires, C. S. Monteiro, *et al.*, "Environmental Sensitivity of Fabry-Perot Microcavities Induced by Layered Graphene-Dielectric Hybrid Coatings", *Physical Review Applied*, vol. 16, no. 4, 2021, ISSN: 23317019. DOI: 10.1103/physrevapplied.16.044041. arXiv: 2106.01287.

[124] S. C. Warren-Smith, R. M. André, C. Perrella, J. Dellith, and H. Bartelt, "Direct core structuring of microstructured optical fibers using focused ion beam milling", *Optics Express*, vol. 24, no. 1, p. 378, 2016. DOI: 10.1364/oe.24.000378.

[125] X. Zhang, J. Qiu, X. Li, J. Zhao, and L. Liu, "Complex refractive indices measurements of polymers in visible and near-infrared bands", *Appl. Opt.*, vol. 59, no. 8, pp. 2337–2344, Mar. 2020. DOI: 10.1364/AO.383831. [Online]. Available: http://opg.optica.org/ao/abstract.cfm?URI=ao-59-8-2337.

[126] Q. Ferreira, P. J. Gomes, Y. Nunes, M. J. Maneira, P. A. Ribeiro, and M. Raposo, "Atomic force microscope characterization of PAH/PAZO multilayers", *Microelectronic Engineering*, vol. 84, no. 3, pp. 506–511, 2007, ISSN: 01679317. DOI: 10.1016/j.mee.2006.10.075.

[127] A. A. Duarte, S. L. Filipe, L. M. Abegão, P. J. Gomes, P. A. Ribeiro, and M. Raposo, "Adsorption kinetics of DPPG liposome layers: A quantitative analysis of surface roughness", *Microscopy and Microanalysis*, vol. 19, no. 4, pp. 867–875, 2013, ISSN: 14319276. DOI: 10.1017/S1431927613001621.

[128] G. A. Cranch, P. J. Nash, and C. K. Kirkendall, "Large-scale remotely interrogated arrays of fiber-optic interferometric sensors for underwater acoustic applications", *IEEE Sensors Journal*, vol. 3, no. 1, pp. 19–30, 2003, ISSN: 1530437X. DOI: 10.1109/JSEN.2003.810102.

[129] J. M. Muggleton, R. Hunt, E. Rustighi, G. Lees, and A. Pearce, "Gas pipeline leak noise measurements using optical fibre distributed acoustic sensing", *Journal of Natural Gas Science and Engineering*, vol. 78, no. January, p. 103 293, 2020, ISSN: 18755100. DOI: 10.1016/j.jngse.2020.103293.

[130] D. Gallego and H. Lamela, "High-sensitivity ultrasound interferometric single-mode polymer optical fiber sensors for biomedical applications", *Optics Letters*, vol. 34, no. 12, p. 1807, 2009, ISSN: 0146-9592. DOI: 10.1364/ol.34.001807.

[131] G. Sui, H. Liu, F. Pang, J. Cheng, and T. Wang, "Broadband Acoustic Vibration Sensor Based on Cladding-Mode Resonance of Double-Cladding Fiber", *Photonic Sensors*, vol. 9, no. 3, pp. 230–238, 2019, ISSN: 21907439. DOI: 10.1007/s13320-019-0548-7.

[132] L. Zhang, P. Lu, Z. Zhou, *et al.*, "High-Efficiency Random Fiber Laser Based on Strong Random Fiber Grating for MHz Ultrasonic Sensing", *IEEE Sensors Journal*, vol. 20, no. 11, pp. 5885–5892, 2020, ISSN: 15581748. DOI: 10.1109/JSEN.2020.2972021.

[133] Q. Dong and H. Liu, "Miniature fiber optic acoustic pressure sensors with air-backed graphene diaphragms", *The Journal of the Acoustical Society of America*, vol. 145, no. 3, pp. 1863–1864, 2019, ISSN: 0001-4966. DOI: 10.1121/1.5101732.

[134] C. W. de Silva, *Sensor Systems: Fundamentals and Applications*. Boca Raton : Taylor Francis, CRC Press, 2017.: CRC Press, Dec. 2016, ISBN: 9781315371160. DOI: 10.1201/9781315371160.

[135] M. Di Giovanni, *Flat and Corrugated Diaphragm Design Handbook*, 1st ed. Routledge, Nov. 1982, ISBN: 9780203755969. DOI: 10.1201/9780203755969.

[136] M. S. Ferreira, L. Coelho, K. Schuster, J. Kobelke, J. L. Santos, and O. Frazão, "Fabry-Perot cavity based on a diaphragm-free hollow-core silica tube", *Optics letters*, vol. 36, no. 20, pp. 4029–31, 2011, ISSN: 1539-4794. DOI: 10.1364/OL.36.004029.

[137] J. Chen, C. Xue, Y. Zheng, *et al.*, "Acoustic Performance Study of Fiber-Optic Acoustic Sensors Based on Fabry–Pérot Etalons with Different Q Factors", *Micromachines*, vol. 13, no. 1, p. 118, Jan. 2022, ISSN: 2072-666X. DOI: 10.3390/mi13010118.

[138] J. A. Guggenheim, J. Li, T. J. Allen, *et al.*, "Ultrasensitive plano-concave optical microresonators for ultrasound sensing", *Nature Photonics*, vol. 11, no. 11, pp. 714–719, 2017, ISSN: 17494893. DOI: 10.1038/s41566-017-0027-x.

[139] T. J. Allen and P. C. Beard, "Optimising the detection parameters for deep-tissue photoacoustic imaging", in *Photons Plus Ultrasound: Imaging and Sensing 2012*, A. A. Oraevsky and L. V. Wang, Eds., vol. 8223, Feb. 2012, 82230P, ISBN: 9780819488664. DOI: 10.1117/12.908813.

[140] J. Wang, F. Ai, Q. Sun, *et al.*, "Diaphragm-based optical fiber sensor array for multipoint acoustic detection", *Optics Express*, vol. 26, no. 19, p. 25 293, 2018, ISSN: 1094-4087. DOI: 10.1364/oe.26.025293.

[141] L. Tong, F. Zi, X. Guo, and J. Lou, "Optical microfibers and nanofibers: A tutorial", *Optics Communications*, vol. 285, no. 23, pp. 4641–4647, 2012, ISSN: 00304018. DOI: 10.1016/j.optcom.2012.07.068.

[142] D. P. Yu, Q. L. Hang, Y. Ding, *et al.*, "Amorphous silica nanowires: Intensive blue light emitters", *Applied Physics Letters*, vol. 73, no. 21, pp. 3076–3078, 1998, ISSN: 00036951. DOI: 10.1063/1.122677.

[143] C. H. Liang, L. D. Zhang, G. W. Meng, Y. W. Wang, and Z. Q. Chu, "Preparation and characterization of amorphous SiOx nanowires", *Journal of Non-Crystalline Solids*, vol. 277, no. 1, pp. 63–67, 2000, ISSN: 00223093. DOI: 10.1016/S0022-3093(00)00296-9.

[144] Z. Q. Liu, S. S. Xie, L. F. Sun, *et al.*, "Synthesis of α–SiO 2 nanowires using Au nanoparticle catalysts on a silicon substrate", *Journal of Materials Research*, vol. 16, no. 3, pp. 683–686, Mar. 2001, ISSN: 0884-2914. DOI: 10.1557/JMR.2001.0102.

[145] M. Zhang, Y. Bando, K. Wada, and K. Kurashima, "Synthesis of nanotubes and nanowires of silicon oxide", *Journal of Materials Science Letters*, vol. 18, no. 23, pp. 1911–1913, 1999, ISSN: 02618028. DOI: 10.1023/A:1006664711344.

[146] B. Zheng, Y. Wu, P. Yang, and J. Liu, "Synthesis of ultra-long and highly oriented silicon oxide nanowires from liquid alloys", *Advanced Materials*, vol. 14, no. 2, pp. 122–124, 2002, ISSN: 09359648. DOI: 10.1002/1521-4095(20020116)14:2<122::AID-ADMA122>3.0.CO;2-V.

[147] Tong, L., Gattass, *et al.*, "Subwavelength-diameter silica wires for low-loss optical wave guiding", *Nature*, vol. 426, no. 6968, pp. 816–819, 2003.

[148] X. Wu and L. Tong, "Optical microfibers and nanofibers", *Nanophotonics*, vol. 2, no. 5-6, pp. 407–428, 2013, ISSN: 21928606. DOI: 10.1515/nanoph-2013-0033.

[149] H. Zhang, A. Kulkarni, H. Kim, *et al.*, "Detection of Acetone Vapor Using Graphene on Polymer Optical Fiber", *Journal of Nanoscience and Nanotechnology*, vol. 11, no. 7, pp. 5939–5943, 2011, ISSN: 15334880. DOI: 10.1166/jnn.2011.4408.

[150] G. Chen, D. Lancaster, and T. Monro, "Optical Microfiber Technology for Current, Temperature, Acceleration, Acoustic, Humidity and Ultraviolet Light Sensing", *Sensors*, vol. 18, no. 1, p. 72, Dec. 2017, ISSN: 1424-8220. DOI: 10.3390/s18010072.

[151] M. J. Morrissey, K. Deasy, M. Frawley, *et al.*, "Spectroscopy, manipulation and trapping of neutral atoms, molecules, and other particles using optical nanofibers: A review", *Sensors (Switzerland)*, vol. 13, no. 8, pp. 10 449–10 481, 2013, ISSN: 14248220. DOI: 10.3390/s130810449. arXiv: 1306.5821.

[152] A. Godet, A. Ndao, T. Sylvestre, *et al.*, "Brillouin spectroscopy of optical microfibers and nanofibers", *Optica*, vol. 4, no. 10, p. 1232, 2017, ISSN: 23342536. DOI: 10.1364/optica.4.001232.

[153] M. A. Foster and A. L. Gaeta, "Ultra-low threshold supercontinuum generation in subwavelength waveguides", *Optics Express*, vol. 12, no. 14, p. 3137, 2004, ISSN: 1094-4087. DOI: 10.1364/OPEX.12.003137.

[154] T. Lee, Y. Jung, C. A. Codemard, M. Ding, N. G. R. Broderick, and G. Brambilla, "Broadband third harmonic generation in tapered silica fibres", *Optics Express*, vol. 20, no. 8, p. 8503, 2012, ISSN: 1094-4087. DOI: 10.1364/oe.20.008503.

[155] G. Fanjoux, J. Chrétien, A. Godet, K. Phan-Huy, J.-C. Beugnot, and T. Sylvestre, "Demonstration of the evanescent Kerr effect in optical nanofibers", *Optics Express*, vol. 27, no. 20, p. 29 460, 2019, ISSN: 10944087. DOI: 10.1364/oe.27.029460.

[156] R. Finkelstein, G. Winer, D. Z. Koplovich, *et al.*, "Super-extended nanofiber-guided field for coherent interaction with hot atoms", *Optica*, vol. 8, no. 2, p. 208, 2021, ISSN: 23342536. DOI: 10.1364/optica.413372. arXiv: 2010.08935.

[157] X. Yu, S. Zhang, M. Olivo, and N. Li, "Micro- and nano-fiber probes for optical sensing, imaging, and stimulation in biomedical applications", *Photonics Research*, vol. 8, no. 11, p. 1703, 2020, ISSN: 2327-9125. DOI: 10.1364/prj.387076.

[158] G. Brambilla, "Optical fibre nanowires and microwires: A review", *Journal of Optics A: Pure and Applied Optics*, vol. 12, no. 4, 2010, ISSN: 14644258. DOI: 10.1088/2040-8978/12/4/043001.

[159] M. Liu, Z. W. Wei, A. P. Luo, W. C. Xu, and Z. C. Luo, *Recent progress on applications of 2D material-decorated microfiber photonic devices in pulse shaping and all-optical signal processing*. 2020, vol. 9, pp. 2641–2671, ISBN: 0000000221. DOI: 10.1515/nanoph-2019-0564.

[160] J. B. Caughman, L. R. Baylor, M. A. Guillorn, V. I. Merkulov, D. H. Lowndes, and L. F. Allard, "Growth of vertically aligned carbon nanofibers by low-pressure inductively coupled plasma-enhanced chemical vapor deposition", *Applied Physics Letters*, vol. 83, no. 6, pp. 1207–1209, 2003, ISSN: 00036951. DOI: 10.1063/1.1597981.

[161] D. Pisignano, G. Maruccio, E. Mele, L. Persano, F. Di Benedetto, and R. Cingolani, "Polymer nanofibers by soft lithography", *Applied Physics Letters*, vol. 87, no. 12, pp. 1–3, 2005, ISSN: 00036951. DOI: 10.1063/1.2046731.

[162] F. Weisbuch, V. N. Tokarev, S. Lazare, C. Belin, and J. L. Bruneel, "Millimeter long PMMA nanofibers - A new form of material removal in laser ablation", *Thin Solid Films*, vol. 453-454, pp. 394–398, 2004, ISSN: 00406090. DOI: 10.1016/j.tsf.2003.11.182.

[163] L. Tong, J. Lou, Z. Ye, G. T. Svacha, and E. Mazur, "Self-modulated taper drawing of silica nanowires", *Nanotechnology*, vol. 16, no. 9, pp. 1445–1448, 2005, ISSN: 09574484. DOI: 10.1088/0957-4484/16/9/004.

[164] Y. H. Li, Y. Y. Zhao, and L. J. Wang, "Demonstration of almost octave-spanning cascaded four-wave mixing in optical microfibers", *Optics Letters*, vol. 37, no. 16, p. 3441, 2012, ISSN: 0146-9592. DOI: 10.1364/ol.37.003441.

[165] L. Tong and M. Sumetsky, *Subwavelength and Nanometer Diameter Optical Fibers* (Advanced Topics in Science and Technology in China). Berlin, Heidelberg: Springer Berlin Heidelberg, 2011, ISBN: 978-3-642-03361-2. DOI: 10.1007/978-3-642-03362-9.

[166] G. Brambilla, F. Xu, and X. Feng, "Fabrication of optical fibre nanowires and their optical and mechanical characterisation", *Electronics Letters*, vol. 42, no. 9, p. 517, 2006, ISSN: 00135194. DOI: 10.1049/el:20060611.

[167] S. Pricking and H. Giessen, "Tapering fibers with complex shape", *Optics Express*, vol. 18, no. 4, p. 3426, 2010, ISSN: 10944087. DOI: 10.1364/oe.18.003426.

[168] G. Brambilla, V. Finazzi, and D. J. Richardson, "Ultra-low-loss optical fiber nanotapers", *Optics Express*, vol. 12, no. 10, p. 2258, 2004, ISSN: 10944087. DOI: 10.1364/opex.12.002258.

[169] C. F. Bohren and D. R. Huffman, *Absorption and Scattering of Light by Small Particles*. Wiley, Apr. 1998, ISBN: 9780471293408. DOI: 10.1002/9783527618156.

[170] L. Tong, L. Hu, J. Zhang, *et al.*, "Photonic nanowires directly drawn from bulk glasses", *Optics Express*, vol. 14, no. 1, p. 82, 2006, ISSN: 10944087. DOI: 10.1364/opex.14.000082.

[171] R. Jose Varghese, E. H. M. Sakho, S. Parani, S. Thomas, O. S. Oluwafemi, and J. Wu, *Introduction to nanomaterials: Synthesis and applications*. Elsevier Inc., 2019, pp. 75–95, ISBN: 9780128133378. DOI: 10.1016/B978-0-12-813337-8.00003-5. [Online]. Available: http://dx.doi.org/10.1016/B978-0-12-813337-8.00003-5.

[172] A. Camposeo, L. Persano, and D. Pisignano, "Light-emitting electrospun nanofibers for nanophotonics and optoelectronics", *Macromolecular Materials and Engineering*, vol. 298, no. 5, pp. 487–503, 2013, ISSN: 14387492. DOI: 10.1002/mame.201200277.

[173] M. Praeger, E. Saleh, A. Vaughan, W. J. Stewart, and W. H. Loh, "Fabrication of nanoscale glass fibers by electrospinning", *Applied Physics Letters*, vol. 100, no. 6, pp. 8–11, 2012, ISSN: 00036951. DOI: 10.1063/1.3684940.

[174] "Electrospinning", in Elsevier, 2019, pp. 21–52, ISBN: 9780323512701. DOI: 10.1016/B978-0-323-51270-1.00002-9. [Online]. Available: http://dx.doi.org/10.1016/B978-0-323-51270-1.00002-9%20https://linkinghub.elsevier.com/retrieve/pii/B9780323512701000029.

[175] L. Tong, J. Lou, and E. Mazur, "Single-mode guiding properties of subwavelength-diameter silica and silicon wire waveguides", *Optics Express*, vol. 12, no. 6, p. 1025, 2004, ISSN: 1094-4087. DOI: 10.1364/opex.12.001025.

[176] K. P. Nayak, M. Das, F. Le Kien, and K. Hakuta, "Spectroscopy of near-surface atoms using an optical nanofiber", *Optics Communications*, vol. 285, no. 23, pp. 4698–4704, 2012, ISSN: 00304018. DOI: 10.1016/j.optcom.2012.04.018. [Online]. Available: http://dx.doi.org/10.1016/j.optcom.2012.04.018.

[177] N. M. Y. Zhang, M. Qi, Z. Wang, *et al.*, "One-step synthesis of cyclodextrin-capped gold nanoparticles for ultra-sensitive and highly-integrated plasmonic biosensors", *Sensors and Actuators, B: Chemical*, vol. 286, no. February, pp. 429–436, 2019, ISSN: 09254005. DOI: 10.1016/j.snb.2019.01.166. [Online]. Available: https://doi.org/10.1016/j.snb.2019.01.166.

[178] S. K. Ruddell, K. E. Webb, M. Takahata, S. Kato, and T. Aoki, "Ultra-low-loss nanofiber Fabry–Perot cavities optimized for cavity quantum electrodynamics", *Optics Letters*, vol. 45, no. 17, p. 4875, 2020, ISSN: 0146-9592. DOI: 10.1364/ol.396725. eprint: 2008.12374.

[179] A. Godet, J. Chretien, K. P. Huy, and J.-C. Beugnot, "Micronewton nanofiber force sensor using Brillouin scattering", *Optics Express*, vol. 30, no. 2, p. 815, 2022, ISSN: 10944087. DOI: 10.1364/oe.443594.

[180] J. Hütner, T. Hoinkes, M. Becker, M. Rothhardt, A. Rauschenbeutel, and S. M. Skoff, "Nanofiber-based high-Q microresonator for cryogenic applications", *Optics Express*, vol. 28, no. 3, p. 3249, Feb. 2020, ISSN: 1094-4087. DOI: 10.1364/OE.381286. eprint: 2001.01084. [Online]. Available: https://www.osapublishing.org/abstract.cfm?URI=oe-28-3-3249.

[181] X. Yan, J. Xie, Z. Yang, D. You, K. Li, and T. Guo, "High sensitivity hydrogen sensor based on optical micro/nanofiber couplers working at the dispersion turning point", *Journal of Lightwave Technology*, vol. 8724, no. c, pp. 1–7, 2022, ISSN: 15582213. DOI: 10.1109/JLT.2022.3165218.

[182] T. Yoshino, D. Yamaura, M. Komiya, *et al.*, "Optical transport of sub-micron lipid vesicles along a nanofiber", *Optics Express*, vol. 28, no. 26, p. 38 527, 2020, ISSN: 1094-4087. DOI: 10.1364/oe.411124.

[183] G. Tkachenko, I. Toftul, C. Esporlas, *et al.*, "Light-induced rotation of dielectric microparticles around an optical nanofiber", *Optica*, vol. 7, no. 1, p. 59, Jan. 2020, ISSN: 2334-2536. DOI: 10.1364/OPTICA.374441. eprint: 1907.13363. [Online]. Available: https://opg.optica.org/abstract.cfm?URI=optica-7-1-59.

[184] T. Hennessy and T. Busch, "Detecting atoms trapped in an optical lattice using a tapered optical nanofiber", *Optics Express*, vol. 22, no. 26, p. 32 509, 2014, ISSN: 10944087. DOI: 10.1364/oe.22.032509. eprint: arXiv:1311.6860.

[185] K. S. Rajasree, T. Ray, K. Karlsson, J. L. Everett, and S. N. Chormaic, "Generation of cold Rydberg atoms at submicron distances from an optical nanofiber", *Physical Review Research*, vol. 2, no. 1, p. 012 038, Feb. 2020, ISSN: 2643-1564. DOI: 10.1103/PhysRevResearch.2.012038. eprint: 1907.10802. [Online]. Available: https://link.aps.org/doi/10.1103/PhysRevResearch.2.012038.

[186] G. Brambilla, F. Xu, P. Horak, *et al.*, "Optical fiber nanowires and microwires: fabrication and applications", *Advances in Optics and Photonics*, vol. 1, no. 1, p. 107, Jan. 2009, ISSN: 1943-8206. DOI: 10.1364/AOP.1.000107. [Online]. Available: https://opg.optica.org/abstract.cfm?URI=aop-1-1-107.

[187] M. A. Foster, A. C. Turner, M. Lipson, and A. L. Gaeta, "Nonlinear optics in photonic nanowires", *Optics Express*, vol. 16, no. 2, p. 1300, 2008, ISSN: 1094-4087. DOI: 10.1364/OE.16.001300. [Online]. Available: https://opg.optica.org/oe/abstract.cfm?uri=oe-16-2-1300.

[188] M. A. Gouveia, T. Lee, R. Ismaeel, *et al.*, "Second harmonic generation and enhancement in microfibers and loop resonators", *Applied Physics Letters*, vol. 102, no. 20, p. 201 120, May 2013, ISSN: 0003-6951. DOI: 10.1063/1.4807767. [Online]. Available: http://aip.scitation.org/doi/10.1063/1.4807767.

[189] G. Brambilla, "[INVITED] Optical microfibre devices", *Optics Laser Technology*, vol. 78, pp. 76–80, Apr. 2016, ISSN: 00303992. DOI: 10.1016/j.optlastec.2015.09.012. [Online]. Available: https://linkinghub.elsevier.com/retrieve/pii/S003039921500256X.

[190] R. W. Boyd, *Nonlinear Optics*, 3rd. Academic Press, 2008, ISBN: 9780123694706.

[191] R. R. Gattass, G. T. Svacha, L. Tong, and E. Mazur, "Supercontinuum generation in submicrometer diameter silica fibers", *Optics Express*, vol. 14, no. 20, p. 9408, 2006, ISSN: 1094-4087. DOI: 10.1364/oe.14.009408. [Online]. Available: https://www.osapublishing.org/oe/abstract.cfm?uri=oe-14-20-9408.

[192] P. Ying, G. Feng, X. Li, *et al.*, "Supercontinuum generation based on nanofiber", *Optik*, vol. 119, no. 13, pp. 648–653, 2008, ISSN: 00304026. DOI: 10.1016/j.ijleo.2007.05.001.

[193] D.-I. Yeom, E. C. Mägi, M. R. E. Lamont, M. a. F. Roelens, L. Fu, and B. J. Eggleton, "Low-threshold supercontinuum generation in highly nonlinear chalcogenide nanowires", *Optics Letters*, vol. 33, no. 7, p. 660, Apr. 2008, ISSN: 0146-9592. DOI: 10.1364/OL.33.000660. [Online]. Available: http://ol.osa.org/abstract.cfm?URI=ol-33-7-660%20https://www.osapublishing.org/abstract.cfm?URI=ol-33-7-660.

[194] J. H. Price, X. Feng, A. M. Heidt, *et al.*, "Supercontinuum generation in non-silica fibers", *Optical Fiber Technology*, vol. 18, no. 5, pp. 327–344, 2012, ISSN: 10685200. DOI: 10.1016/j.yofte.2012.07.013. [Online]. Available: http://dx.doi.org/10.1016/j.yofte.2012.07.013.

[195] F. Wang, K. Wang, C. Yao, *et al.*, "Tapered fluorotellurite microstructured fibers for broadband supercontinuum generation", *Optics Letters*, vol. 41, no. 3, p. 634, Feb. 2016, ISSN: 0146-9592. DOI: 10.1364/OL.41.000634. [Online]. Available: https://www.osapublishing.org/abstract.cfm?URI=ol-41-3-634.

[196] P. A. Franken, A. E. Hill, C. W. Peters, and G. Weinreich, "Generation of optical harmonics", *Physical Review Letters*, vol. 7, no. 4, pp. 118–119, 1961, ISSN: 00319007. DOI: 10.1103/PhysRevLett.7.118.

[197] V. Vysloukh, *Nonlinear fiber optics*. 1990, vol. 160, p. 151, ISBN: 0120451433. DOI: 10.3367/ufnr.0160.199005k.0151.

[198] U. Österberg and W. Margulis, "Dye laser pumped by Nd:YAG laser pulses frequency doubled in a glass optical fiber", *Optics Letters*, vol. 11, no. 8, p. 516, 1986, ISSN: 0146-9592. DOI: 10.1364/ol.11.000516.

[199] S. Richard, "Second-harmonic generation in tapered optical fibers", *Journal of the Optical Society of America B*, vol. 27, no. 8, p. 1504, 2010, ISSN: 0740-3224. DOI: 10.1364/josab.27.001504.

[200] Q. Ai, F. Sterl, H. Zhang, J. Wang, and H. Giessen, "Giant Second Harmonic Generation Enhancement in a High- Q Doubly Resonant Hybrid Plasmon-Fiber Cavity System", *ACS Nano*, vol. 15, no. 12, pp. 19 409–19 417, 2021, ISSN: 1936086X. DOI: 10.1021/acsnano.1c05970.

[201] X. Jiang, D. Zhang, T. Lee, and G. Brambilla, "Optimized microfiber-based third-harmonic generation with adaptive control of phase mismatch", *Optics Letters*, vol. 43, no. 12, p. 2728, 2018, ISSN: 0146-9592. DOI: 10.1364/ol.43.002728.

[202] C. K. Ha, K. H. Nam, and M. S. Kang, "Efficient harmonic generation in an adiabatic multimode submicron tapered optical fiber", *Communications Physics*, vol. 4, no. 1, pp. 1–9, 2021, ISSN: 23993650. DOI: 10.1038/s42005-021-00677-2.

[203] G. P. Agrawal, *Nonlinear Fiber Optics*, 5th Edition. Elsevier, 2013, ISBN: 9780123970237. DOI: 10.1016/C2011-0-00045-5.

[204] J. Dudley and R. Taylor, *Supercontinuum Generation in Optical Fibers*, J. M. Dudley and J. R. Taylor, Eds. Cambridge University Press, Apr. 2010, ISBN: 9780521514804. DOI: 10.1017/CBO9780511750465.

[205] J. Villatoro and D. Monzón-Hernández, "Fast detection of hydrogen with nano fiber tapers coated with ultra thin palladium layers", *Optics Express*, vol. 13, no. 13, p. 5087, 2005, ISSN: 10944087. DOI: 10.1364/opex.13.005087.

[206] L. Zhang, P. Wang, Y. Xiao, H. Yu, and L. Tong, "Ultra-sensitive microfibre absorption detection in a microfluidic chip", *Lab on a Chip*, vol. 11, no. 21, pp. 3720–3724, 2011. DOI: 10.1039/c1lc20519f.

[207] G. Liu and K. Li, "Micro/nano optical fibers for label-free detection of abrin with high sensitivity", *Sensors and Actuators, B: Chemical*, vol. 215, pp. 146–151, 2015, ISSN: 09254005. DOI: 10.1016/j.snb.2015.03.056. [Online]. Available: http://dx.doi.org/10.1016/j.snb.2015.03.056.

[208] L. Zhang, Y. Tang, and L. Tong, "Micro-/Nanofiber Optics: Merging Photonics and Material Science on Nanoscale for Advanced Sensing Technology", *iScience*, vol. 23, no. 1, p. 100 810, 2020, ISSN: 25890042. DOI: 10.1016/j.isci.2019.100810. [Online]. Available: https://doi.org/10.1016/j.isci.2019.100810.

[209] M. Sumetsky, Y. Dulashko, J. M. Fini, A. Hale, and D. J. DiGiovanni, "The microfiber loop resonator: Theory, experiment, and application", *Journal of Lightwave Technology*, vol. 24, no. 1, pp. 242–250, 2006, ISSN: 07338724. DOI: 10.1109/JLT.2005.861127.

[210] L. Shi, Y. Xu, W. Tan, and X. Chen, "Simulation of optical microfiber loop resonators for ambient refractive index sensing", *Sensors*, vol. 7, no. 5, pp. 689–696, 2007, ISSN: 14248220. DOI: 10.3390/s7050689.

[211] M. H. Jali, H. R. A. Rahim, S. S. Hamid, *et al.*, "Microfiber loop resonator for formaldehyde liquid sensing", *Optik*, vol. 196, no. July, 2019, ISSN: 00304026. DOI: 10.1016/j.ijleo.2019.163174.

[212] Y. Zheng, X. Dong, C. Zhao, Y. Li, L. Shao, and S. Jin, "Relative humidity sensor based on microfiber loop resonator", *Advances in Materials Science and Engineering*, vol. 2013, 2013, ISSN: 16878434. DOI: 10.1155/2013/815930.

[213] N. Irawati, T. N. Abdullah, H. A. Rahman, H. Ahmad, and S. W. Harun, "PMMA microfiber loop resonator for humidity sensor", *Sensors and Actuators, A: Physical*, vol. 260, pp. 112–116, 2017, ISSN: 09244247. DOI: 10.1016/j.sna.2017.04.041. [Online]. Available: http://dx.doi.org/10.1016/j.sna.2017.04.041.

[214] M. H. Jali, H. R. A. Rahim, M. A. M. Johari, *et al.*, "Optical characterization of different waist diameter on microfiber loop resonator humidity sensor", *Sensors and Actuators, A: Physical*, vol. 285, pp. 200–209, 2019, ISSN: 09244247. DOI: 10.1016/j.sna.2018.11.025. [Online]. Available: https://doi.org/10.1016/j.sna.2018.11.025.

[215] X. Jiang, L. Tong, G. Vienne, *et al.*, "Demonstration of optical microfiber knot resonators", *Applied Physics Letters*, vol. 88, no. 22, pp. 86–89, 2006, ISSN: 00036951. DOI: 10.1063/1.2207986.

[216] X. Zeng, Y. Wu, C. Hou, J. Bai, and G. Yang, "A temperature sensor based on optical microfiber knot resonator", *Optics Communications*, vol. 282, no. 18, pp. 3817–3819, 2009, ISSN: 00304018. DOI: 10.1016/j.optcom.2009.05.079. [Online]. Available: http://dx.doi.org/10.1016/j.optcom.2009.05.079.

[217] Y. Wu, L. Jia, T. Zhang, Y. Rao, and Y. Gong, "Microscopic multi-point temperature sensing based on microfiber double-knot resonators", *Optics Communications*, vol. 285, no. 8, pp. 2218–2222, 2012, ISSN: 00304018. DOI: 10.1016/j.optcom.2011.12.107.

[218] J. Li, L. Gai, H. Li, and H. Hu, "A high sensitivity temperature sensor based on packaged microfibre knot resonator", *Sensors and Actuators, A: Physical*, vol. 263, pp. 369–372, 2017, ISSN: 09244247. DOI: 10.1016/j.sna.2017.06.031. [Online]. Available: http://dx.doi.org/10.1016/j.sna.2017.06.031.

[219] Y. Wu, T. Zhang, Y. Rao, and Y. Gong, "Miniature interferometric humidity sensors based on silica/polymer microfiber knot resonators", *Sensors and Actuators, B: Chemical*, vol. 155, no. 1, pp. 258–263, 2011, ISSN: 09254005. DOI: 10.1016/j.snb.2010.12.030.

[220] J. C. Shin, M. S. Yoon, and Y. G. Han, "Relative humidity sensor based on an optical microfiber knot resonator with a polyvinyl alcohol overlay", *Journal of Lightwave Technology*, vol. 34, no. 19, pp. 4511–4515, 2016, ISSN: 07338724. DOI: 10.1109/JLT.2016.2552494.

[221] K. S. Lim, S. W. Harun, S. S. Damanhuri, A. A. Jasim, C. K. Tio, and H. Ahmad, "Current sensor based on microfiber knot resonator", *Sensors and Actuators, A: Physical*, vol. 167, no. 1, pp. 60–62, 2011, ISSN: 09244247. DOI: 10.1016/j.sna.2011.02.036.

[222] S. Dass and R. Jha, "Square Knot Resonator-Based", *IEEE Photonics Technology Letters*, vol. 30, no. 18, pp. 1649–1652, 2018.

[223] Y. Li, S. Pu, Y. Zhao, and T. Yao, "Fiber-optic magnetic field sensing based on microfiber knot resonator with magnetic fluid cladding", *Sensors (Switzerland)*, vol. 18, no. 12, pp. 4–9, 2018, ISSN: 14248220. DOI: 10.3390/s18124358.

[224] H. Yang, L. Kong, L. Li, *et al.*, "Enhanced-sensitive dual microfiber knot resonators based sensor with vernier effect for simultaneous measurement of refractive index and temperature", *Optik*, vol. 250, no. P1, p. 168 350, 2022, ISSN: 00304026. DOI: 10.1016/j.ijleo.2021.168350.

[225] Q. Wu, S. Chen, L. Guan, and H. Wu, "Highly Sensitive Photothermal Fiber Sensor Based on MXene Device and Vernier Effect", *Nanomaterials*, vol. 12, no. 5, p. 766, 2022. DOI: 10.3390/nano12050766.

[226] M. Sumetsky, "Optical fiber microcoil resonators", *Optics Express*, vol. 12, no. 10, p. 2303, 2004, ISSN: 1094-4087. DOI: 10.1364/opex.12.002303.

[227] F. Xu and G. Brambilla, "Manufacture of 3-D microfiber coil resonators", *IEEE Photonics Technology Letters*, vol. 19, no. 19, pp. 1481–1483, 2007, ISSN: 10411135. DOI: 10.1109/LPT.2007.903762.

[228] J. Scheuer, "Fiber microcoil optical gyroscope", *Optics Letters*, vol. 34, no. 11, p. 1630, 2009, ISSN: 0146-9592. DOI: 10.1364/ol.34.001630.

[229] F. Xu, P. Horak, and G. Brambilla, "Optical microfiber coil resonator refractometric sensor", *Optics Express*, vol. 15, no. 12, p. 7888, 2007, ISSN: 1094-4087. DOI: 10.1364/OE.15.007888.

[230] F. Xu and G. Brambilla, "Demonstration of a refractometric sensor based on optical microfiber coil resonator", *Applied Physics Letters*, vol. 92, no. 10, pp. 2006–2009, 2008, ISSN: 00036951. DOI: 10.1063/1.2898211.

[231] F. Xu, V. Pruneri, V. Finazzi, and G. Brambilla, "An embedded optical nanowire loop resonator refractometric sensor", *Optics Express*, vol. 16, no. 2, p. 1062, 2008, ISSN: 10944087. DOI: 10.1364/oe.16.001062.

[232] G. Y. Chen, T. Lee, R. Ismaeel, G. Brambilla, and T. P. Newson, "Resonantly enhanced Faraday rotation in an microcoil current sensor", *IEEE Photonics Technology Letters*, vol. 24, no. 10, pp. 860–862, 2012, ISSN: 10411135. DOI: 10.1109/LPT.2012.2189381.

[233] Y. Yin, S. Li, J. Ren, G. Farrell, E. Lewis, and P. Wang, "High-sensitivity salinity sensor based on optical microfiber coil resonator", *Optics Express*, vol. 26, no. 26, p. 34 633, 2018, ISSN: 10944087. DOI: 10.1364/oe.26.034633.

[234] G. Y. Chen, G. Brambilla, and T. P. Newson, "Compact acoustic sensor based on air-backed mandrel coiled with optical microfiber", *Optics Letters*, vol. 37, no. 22, p. 4720, Nov. 2012, ISSN: 0146-9592. DOI: 10.1364/OL.37.004720.

[235] H. Mei, J. Pan, Z. Zhang, L. Zhang, and L. Tong, "Coiled Optical Nanofiber for Optofluidic Absorbance Detection", *ACS Sensors*, vol. 4, no. 9, pp. 2267–2271, 2019, ISSN: 23793694. DOI: 10.1021/acssensors.9b00913.

[236] Y. Yin, S. Li, S. Wang, *et al.*, "Ultra-high-resolution detection of Pb 2+ ions using a black phosphorus functionalized microfiber coil resonator", *Photonics Research*, vol. 7, no. 6, p. 622, Jun. 2019, ISSN: 2327-9125. DOI: 10.1364/PRJ.7.000622.

[237] C. Yu, S. Ma, H. Ren, *et al.*, "AC field modulated DC magnetic field sensor based on optical whispering gallery mode microcapillary resonator", *Optics Express*, vol. 30, no. 13, p. 24 062, Jun. 2022, ISSN: 1094-4087. DOI: 10.1364/OE.459338.

[238] J. Zhang, Q. Sun, R. Liang, *et al.*, "Microfiber fabry-perot interferometer for dual-parameter sensing", *Journal of Lightwave Technology*, vol. 31, no. 10, pp. 1608–1615, 2013, ISSN: 07338724. DOI: 10.1109/JLT.2013.2252145.

[239] Y. Xiang, Y. Luo, Y. Li, *et al.*, "Quasi-Distributed Dual-Parameter Optical Fiber Sensor Based on Cascaded Microfiber Fabry-Perot Interferometers", *IEEE Photonics Journal*, vol. 10, no. 2, pp. 1–9, 2018, ISSN: 19430655. DOI: 10.1109/JPHOT.2018.2817573.

[240] Z. Chen, S. Xiong, S. Gao, *et al.*, "High-temperature sensor based on fabry-perot interferometer in microfiber tip", *Sensors (Switzerland)*, vol. 18, no. 1, pp. 11–14, 2018, ISSN: 14248220. DOI: 10.3390/s18010202.

[241] J. Li, Z. Li, J. Yang, Y. Zhang, and C. Ren, "Microfiber Fabry-Perot interferometer used as a temperature sensor and an optical modulator", *Optics and Laser Technology*, vol. 129, no. January, p. 106 296, 2020, ISSN: 00303992. DOI: 10.1016/j.optlastec.2020.106296. [Online]. Available: https://doi.org/10.1016/j.optlastec.2020.106296.

[242] Y. Gong, C.-B. Yu, T.-T. Wang, *et al.*, "Highly sensitive force sensor based on optical microfiber asymmetrical Fabry-Perot interferometer", *Optics Express*, vol. 22, no. 3, p. 3578, 2014, ISSN: 10944087. DOI: 10.1364/oe.22.003578.

[243] Y. Bai, Y. Miao, H. Zhang, and J. Yao, "Simultaneous Measurement of Temperature and Relative Humidity Based on a Microfiber Sagnac Loop and MoS2", *Journal of Lightwave Technology*, vol. 38, no. 4, pp. 840–845, 2020, ISSN: 15582213. DOI: 10.1109/JLT.2019.2947644.

[244] L.-P. Sun, Z. Yuan, T. Huang, *et al.*, "Ultrasensitive sensing in air based on Sagnac interferometer working at group birefringence turning point", *Optics Express*, vol. 27, no. 21, p. 29 501, 2019, ISSN: 10944087. DOI: 10.1364/oe.27.029501.

[245] L. P. Sun, J. Li, L. Jin, Y. Ran, and B. O. Guan, "High-birefringence microfiber Sagnac interferometer based humidity sensor", *Sensors and Actuators, B: Chemical*, vol. 231, pp. 696–700, 2016, ISSN: 09254005. DOI: 10.1016/j.snb.2016.03.102.

[246] F. Lv, C. Han, H. Ding, Z. Wu, and X. Li, "Magnetic Field Sensor Based on Microfiber Sagnac Loop Interferometer and Ferrofluid", *IEEE Photonics Technology Letters*, vol. 27, no. 22, pp. 2327–2330, 2015, ISSN: 10411135. DOI: 10.1109/LPT.2015.2462749.

[247] G. Zhou, S. Xiang, H. You, *et al.*, "A Novel Airborne Molecular Contaminants Sensor Based on Sagnac Microfiber Structure", *Sensors*, vol. 22, no. 4, 2022, ISSN: 14248220. DOI: 10.3390/s22041520.

[248] Y. Chen, Y. Semenova, G. Farrell, F. Xu, and Y. Q. Lu, "A Compact Sagnac Loop Based on a Microfiber Coupler for Twist Sensing", *IEEE Photonics Technology Letters*, vol. 27, no. 24, pp. 2579–2582, 2015, ISSN: 10411135. DOI: 10.1109/LPT.2015.2478479.

[249] S. Gao, L.-P. Sun, J. Li, *et al.*, "High-sensitivity DNA biosensor based on microfiber Sagnac interferometer", *Optics Express*, vol. 25, no. 12, p. 13 305, 2017, ISSN: 10944087. DOI: 10.1364/oe.25.013305.

[250] J. Lu, Z. Zhang, Y. Yu, *et al.*, "Simultaneous Measurement of Seawater Temperature and Pressure with Polydimethylsiloxane Packaged Optical Microfiber Coupler Combined Sagnac Loop", *Journal of Lightwave Technology*, vol. 40, no. 1, pp. 323–333, 2022, ISSN: 15582213. DOI: 10.1109/JLT.2021.3120868.

[251] A. A. Jasim, S. W. Harun, H. Arof, and H. Ahmad, "Inline microfiber Mach-Zehnder interferometer for high temperature sensing", *IEEE Sensors Journal*, vol. 13, no. 2, pp. 626–628, 2013, ISSN: 1530437X. DOI: 10.1109/JSEN.2012.2224106.

[252] A. A. Jasim, S. W. Harun, M. Z. Muhammad, H. Arof, and H. Ahmad, "Current sensor based on inline microfiber Mach-Zehnder interferometer", *Sensors and Actuators, A: Physical*, vol. 192, pp. 9–12, 2013, ISSN: 09244247. DOI: 10.1016/j.sna.2012.12.012.

[253] K. Liu, J. Fan, B. Luo, *et al.*, "Highly sensitive vibration sensor based on the dispersion turning point microfiber Mach-Zehnder interferometer", *Optics Express*, vol. 29, no. 21, p. 32 983, 2021, ISSN: 10944087. DOI: 10.1364/oe.439959.

[254] O. Yaghobi and H. Karimi-Alavijeh, "Fabrication and Characterization of Single-Step Optical Microfiber Mach-Zehnder Interferometer Refractive Index Sensors", *IEEE Sensors Journal*, vol. 19, no. 5, pp. 1788–1795, 2019, ISSN: 1530437X. DOI: 10.1109/JSEN.2018.2882561.

[255] Y. Tan, L.-P. Sun, L. Jin, J. Li, and B.-O. Guan, "Microfiber Mach-Zehnder interferometer based on long period grating for sensing applications", *Optics Express*, vol. 21, no. 1, p. 154, 2013, ISSN: 1094-4087. DOI: 10.1364/oe.21.000154.

[256] Y. F. Hou, J. Wang, X. Wang, *et al.*, "Simultaneous Measurement of Pressure and Temperature in Seawater with PDMS Sealed Microfiber Mach-Zehnder Interferometer", *Journal of Lightwave Technology*, vol. 38, no. 22, pp. 6412–6421, 2020, ISSN: 15582213. DOI: 10.1109/JLT.2020.3012716.

[257] X. Fang, C. R. Liao, and D. N. Wang, "Femtosecond laser fabricated fiber Bragg grating in microfiber for refractive index sensing", *Optics Letters*, vol. 35, no. 7, p. 1007, 2010, ISSN: 0146-9592. DOI: 10.1364/ol.35.001007.

[258] K. P. Nayak, F. Le Kien, Y. Kawai, *et al.*, "Cavity formation on an optical nanofiber using focused ion beam milling technique", *Optics Express*, vol. 19, no. 15, p. 14 040, Jul. 2011, ISSN: 1094-4087. DOI: 10.1364/OE.19.014040. arXiv: 1103.1789. [Online]. Available: https://opg.optica.org/oe/abstract.cfm?uri=oe-19-15-14040.

[259] J.-l. Kou, S.-j. Qiu, F. Xu, and Y.-q. Lu, "Demonstration of a compact temperature sensor based on first-order Bragg grating in a tapered fiber probe", *Optics Express*, vol. 19, no. 19, p. 18 452, 2011, ISSN: 10944087. DOI: 10.1364/oe.19.018452.

[260] W. Li, J. Du, V. G. Truong, and S. Nic Chormaic, "Optical nanofiber-based cavity induced by periodic air-nanohole arrays", *Applied Physics Letters*, vol. 110, no. 25, 2017, ISSN: 00036951. DOI: 10.1063/1.4986789. eprint: 1705.01025.

[261] Y. Ran, Y.-N. Tan, L.-P. Sun, *et al.*, "193nm excimer laser inscribed Bragg gratings in microfibers for refractive index sensing", *Optics Express*, vol. 19, no. 19, p. 18 577, 2011, ISSN: 10944087. DOI: 10.1364/oe.19.018577.

[262] M. Tian, Y. Huang, C. Li, and M. Lv, "High-performance humidity sensor based on a micro-nano fiber Bragg grating coated with graphene oxide", *Optics Express*, vol. 28, no. 18, p. 26 395, 2020, ISSN: 10944087. DOI: 10.1364/oe.402648.

[263] H. A. Mohammed, B. Adel Esttaifan, and M. H. Yaacob, "Highly sensitive fiber Bragg grating based gas sensor integrating polyaniline nanofiber for remote monitoring", *Optical Fiber Technology*, vol. 71, no. March, p. 102 901, 2022, ISSN: 10685200. DOI: 10.1016/j.yofte.2022.102901.

[264] H. Xuan, W. Jin, and M. Zhang, "CO_2 *laser induced long period gratings in optical microfibers*", *Optics Express*, vol. 17, no. 24, p. 21 882, 2009, ISSN: 10944087. DOI: 10.1364/oe.17.021882.

[265] X. Y. Zhang, Y. S. Yu, C. Chen, *et al.*, "Point-by-point dip coated long-period gratings in microfibers", *IEEE Photonics Technology Letters*, vol. 26, no. 24, pp. 2503–2506, 2014, ISSN: 10411135. DOI: 10.1109/LPT.2014.2359546.

[266] Z. Y. Xu, Y. H. Li, and L. J. Wang, "Long-period grating inscription on polymer functionalized optical microfibers and its applications in optical sensing", *Photonics Research*, vol. 4, no. 2, p. 45, 2016, ISSN: 23279125. DOI: 10.1364/prj.4.000045.

[267] P. Fan, L.-P. Sun, Z. Yu, J. Li, C. Wu, and B.-O. Guan, "Higher-order diffraction of long-period microfiber gratings realized by arc discharge method", *Optics Express*, vol. 24, no. 22, p. 25 380, 2016, ISSN: 10944087. DOI: 10.1364/oe.24.025380.

[268] K. Li, W. Zhou, and S. Zeng, "Optical micro/nanofiber-based localized surface plasmon resonance biosensors: Fiber diameter dependence", *Sensors (Switzerland)*, vol. 18, no. 10, 2018, ISSN: 14248220. DOI: 10.3390/s18103295.

[269] P. Wang, L. Zhang, Y. Xia, L. Tong, X. Xu, and Y. Ying, "Polymer nanofibers embedded with aligned gold nanorods: A new platform for plasmonic studies and optical sensing", *Nano Letters*, vol. 12, no. 6, pp. 3145–3150, 2012, ISSN: 15306984. DOI: 10.1021/nl301055f.

[270] X. Jiang, Q. Yang, G. Vienne, *et al.*, "Demonstration of microfiber knot laser", *Applied Physics Letters*, vol. 89, no. 14, pp. 1–4, 2006, ISSN: 00036951. DOI: 10.1063/1.2359439.

[271] W. Fan, J. Gan, Z. Zhang, X. Wei, S. Xu, and Z. Yang, "Narrow linewidth single frequency microfiber laser", *Optics Letters*, vol. 37, no. 20, p. 4323, 2012, ISSN: 0146-9592. DOI: 10.1364/ol.37.004323.

[272] A. Sulaiman, S. W. Harun, F. Ahmad, S. F. Norizan, and H. Ahmad, "Electrically Tunable Microfiber Knot Resonator Based Erbium-Doped Fiber Laser", *IEEE Journal of Quantum Electronics*, vol. 48, no. 4, pp. 443–446, Apr. 2012, ISSN: 0018-9197. DOI: 10.1109/JQE.2012.2184525.

[273] X. Jiang, Q. Song, L. Xu, J. Fu, and L. Tong, "Microfiber knot dye laser based on the evanescent-wave-coupled gain", *Applied Physics Letters*, vol. 90, no. 23, pp. 2005–2008, 2007, ISSN: 00036951. DOI: 10.1063/1.2746935.

[274] Y. Ding, Q. Yang, X. Guo, *et al.*, "Nanowires/microfiber hybrid structure multicolor laser", *Optics Express*, vol. 17, no. 24, p. 21 813, Nov. 2009, ISSN: 1094-4087. DOI: 10.1364/OE.17.021813.

[275] C.-l. Chen, *Foundations for Guided-Wave Optics*. Hoboken, NJ, USA: John Wiley Sons, Inc., Aug. 2006, ISBN: 9780470042229. DOI: 10.1002/0470042222.

[276] H. Yu, S. Wang, J. Fu, *et al.*, "Modeling bending losses of optical nanofibers or nanowires", *Applied Optics*, vol. 48, no. 22, pp. 4365–4369, 2009, ISSN: 15394522. DOI: 10.1364/AO.48.004365.

[277] L. Shao, Y. Xu, H. Wu, W. Fang, and L. Tong, "Experimental Demonstration of a Compact Variable Single-Mode Fiber Coupler Based on Microfiber", *IEEE Photonics Technology Letters*, vol. 33, no. 14, pp. 687–690, 2021, ISSN: 19410174. DOI: 10.1109/LPT.2021.3088454.

[278] Y. Jung, G. Brambilla, and D. J. Richardson, "Optical microfiber coupler for broadband single-mode operation", *Optics Express*, vol. 17, no. 7, p. 5273, 2009, ISSN: 1094-4087. DOI: 10.1364/oe.17.005273.

[279] Y. Chen, Z. Ma, Q. Yang, and L.-M. Tong, "Compact optical short-pass filters based on microfibers", *Optics Letters*, vol. 33, no. 21, p. 2565, 2008, ISSN: 0146-9592. DOI: 10.1364/ol.33.002565.

[280] Y. Jung, G. Brambilla, and D. J. Richardson, "Broadband single-mode operation of standard optical fibers by using a sub-wavelength optical wire filter", *Optics Express*, vol. 16, no. 19, p. 14 661, 2008, ISSN: 1094-4087. DOI: 10.1364/oe.16.014661.

[281] X. Jiang, Y. Chen, G. Vienne, and L. Tong, "All-fiber add-drop filters based on microfiber knot resonators", *Optics Letters*, vol. 32, no. 12, p. 1710, 2007, ISSN: 0146-9592. DOI: 10.1364/ol.32.001710.

[282] M. K. Kim, I. K. Hwang, S. H. Kim, H. J. Chang, and Y. H. Lee, "All-optical bistable switching in curved microfiber-coupled photonic crystal resonators", *Applied Physics Letters*, vol. 90, no. 16, 2007, ISSN: 00036951. DOI: 10.1063/1.2724921.

[283] G. Vienne, Y. Li, L. Tong, and P. Grelu, "Observation of a nonlinear microfiber resonator", *Optics Letters*, vol. 33, no. 13, p. 1500, 2008, ISSN: 0146-9592. DOI: 10.1364/ol.33.001500.

[284] H. You, S. M. Hendrickson, and J. D. Franson, "Analysis of enhanced two-photon absorption in tapered optical fibers", *Physical Review A - Atomic, Molecular, and Optical Physics*, vol. 78, no. 5, pp. 1–5, 2008, ISSN: 10502947. DOI: 10.1103/PhysRevA.78.053803.

[285] B. C. Jacobs and J. D. Franson, "All-optical switching using the quantum Zeno effect and two-photon absorption", *Physical Review A - Atomic, Molecular, and Optical Physics*, vol. 79, no. 6, pp. 1–10, 2009, ISSN: 10502947.

[286] S. M. Hendrickson, C. N. Weiler, R. M. Camacho, *et al.*, "All-optical-switching demonstration using two-photon absorption and the Zeno effect", *Physical Review A - Atomic, Molecular, and Optical Physics*, vol. 87, no. 2, pp. 1–5, 2013, ISSN: 10502947. DOI: 10.1103/PhysRevA.87.023808.

[287] C. Zeng, Y. D. Cui, and J. Guo, "Observation of dual-wavelength solitons and bound states in a nanotube/microfiber mode-locking fiber laser", *Optics Communications*, vol. 347, pp. 44–49, 2015, ISSN: 00304018. DOI: 10.1016/j.optcom.2015.02.054.

[288] M. Liu, A. P. Luo, X. W. Zheng, *et al.*, "Microfiber-Based Highly Nonlinear Topological Insulator Photonic Device for the Formation of Versatile Multi-Soliton Patterns in a Fiber Laser", *Journal of Lightwave Technology*, vol. 33, no. 10, pp. 2056–2061, 2015, ISSN: 07338724. DOI: 10.1109/JLT.2015.2396939.

[289] W. Ma, P. Yin, M. Li, *et al.*, "Graphdiyne-decorated microfiber based soliton and noise-like pulse generation", *Nanophotonics*, vol. 10, no. 16, pp. 3967–3977, 2021, ISSN: 21928614. DOI: 10.1515/nanoph-2021-0299.

[290] G. Brambilla, G. S. Murugan, J. S. Wilkinson, and D. J. Richardson, "Optical manipulation of microspheres along a subwavelength optical wire", *Optics Letters*, vol. 32, no. 20, p. 3041, 2007, ISSN: 0146-9592. DOI: 10.1364/ol.32.003041.

[291] P. Polimeno, A. Magazzù, M. A. Iatì, *et al.*, "Optical tweezers and their applications", *Journal of Quantitative Spectroscopy and Radiative Transfer*, vol. 218, pp. 131–150, 2018, ISSN: 00224073. DOI: 10.1016/j.jqsrt.2018.07.013.

[292] C. J. Bustamante, Y. R. Chemla, S. Liu, and M. D. Wang, "Optical tweezers in single-molecule biophysics", *Nature Reviews Methods Primers*, vol. 1, no. 1, 2021, ISSN: 26628449. DOI: 10.1038/s43586-021-00021-6.

[293] G. Brambilla and F. Xu, "Adiabatic submicrometric tapers for optical tweezers", *Electronics Letters*, vol. 43, no. 4, p. 204, 2007, ISSN: 00135194. DOI: 10.1049/el:20073709.

[294] N. Irawati, V. John, M. M. Aeinehvand, F. Ibrahim, H. Ahmad, and S. W. Harun, "Evanescent wave optical trapping and transport of polystyrene microspheres on microfibers", *Microwave and Optical Technology Letters*, vol. 56, no. 11, pp. 2630–2634, Nov. 2014, ISSN: 08952477. DOI: 10.1002/mop.28659. eprint: mop.28659.

[295] T. A. Birks and Y. W. Li, "The Shape of Fiber Tapers", *Journal of Lightwave Technology*, vol. 10, no. 4, pp. 432–438, 1992, ISSN: 15582213. DOI: 10.1109/50.134196.

[296] A. Azari, A. Bananej, and A. A. Belgabad, "Theoretical analysis of optimum adiabatic tapering length and pulse shape modulation along tapered multimode fiber", *Optik*, vol. 127, no. 14, pp. 5663–5669, 2016, ISSN: 00304026. DOI: 10.1016/j.ijleo.2016.03.086.

[297] H. L. Sørensen, "Controlling the shape of subwavelength-diameter tapered optical fibers", Ph.D. dissertation, University of Copenhagen, 2013, p. 109.

[298] V. Kavungal, G. Farrell, Q. Wu, A. Kumar Mallik, and Y. Semenova, "Studies of geometrical profiling in fabricated tapered optical fibers using whispering gallery modes spectroscopy", *Optical Fiber Technology*, vol. 41, no. November 2017, pp. 82–88, 2018, ISSN: 10685200. DOI: 10.1016/j.yofte.2018.01.007.

[299] A. Azzoune, P. Delaye, and G. Pauliat, "Optical microscopy for measuring tapered fibers beyond the diffraction limit", *Optics Express*, vol. 27, no. 17, p. 24 403, 2019, ISSN: 1094-4087. DOI: 10.1364/oe.27.024403.

[300] N. G. Kokodii and A. O. Natarova, "Optical fiber diameter measurement by the diffraction method with digital processing of the light scattering indicatrix", *Optics and Spectroscopy*, vol. 121, no. 1, pp. 103–108, Jul. 2016, ISSN: 0030-400X. DOI: 10.1134/S0030400X16070110.

[301] P. Polynkin, A. Polynkin, N. Peyghambarian, and M. Mansuripur, "Evanescent field-based optical fiber sensing device for measuring the refractive index of liquids in microfluidic channels", *Optics Letters*, vol. 30, no. 11, p. 1273, 2005, ISSN: 0146-9592. DOI: 10.1364/ol.30.001273.

[302] F. Xu and G. Brambilla, "Embedding optical microfiber coil resonators in Teflon", *Optics Letters*, vol. 32, no. 15, p. 2164, Aug. 2007, ISSN: 0146-9592. DOI: 10.1364/OL.32.002164.

[303] Z. Zhang, N. Yao, J. Pan, L. Zhang, W. Fang, and L. Tong, "A new route for fabricating polymer optical microcavities", *Nanoscale*, vol. 11, no. 12, pp. 5203–5208, 2019, ISSN: 20403372. DOI: 10.1039/c8nr10007a.

[304] A. Abdellah, B. Fabel, P. Lugli, and G. Scarpa, "Spray deposition of organic semiconducting thin-films: Towards the fabrication of arbitrary shaped organic electronic devices", *Organic Electronics*, vol. 11, no. 6, pp. 1031–1038, 2010, ISSN: 15661199. DOI: 10.1016/j.orgel.2010.02.018.

[305] B. AlMangour, "Fundamentals of cold spray processing: Evolution and future perspectives", in *Cold-Spray Coatings: Recent Trends and Future perspectives*, P. Cavaliere, Ed. Cham: Springer International Publishing, 2018, pp. 3–24, ISBN: 978-3-319-67183-3. DOI: 10.1007/978-3-319-67183-3_1.

[306] D. Steinberg, J. D. Zapata, E. A. De Souza, and L. Saito, "Mechanically exfoliated graphite onto D-shaped optical fiber for femtosecond mode-locked Erbium-doped fiber laser", *Journal of Lightwave Technology*, vol. 36, no. 10, pp. 1868–1874, 2018, ISSN: 07338724. DOI: 10.1109/JLT.2018.2793764.

[307] J. S. Oh and S.-W. Kim, "Femtosecond laser pulses for surface-profile metrology", *Optics Letters*, vol. 30, no. 19, p. 2650, 2005, ISSN: 0146-9592. DOI: 10.1364/ol.30.002650.

[308] X. Lu, S. Zhang, C.-G. Jeon, C.-S. Kang, J. Kim, and K. Shi, "Time-of-flight detection of femtosecond laser pulses for precise measurement of large microelectronic step height", *Optics Letters*, vol. 43, no. 7, p. 1447, 2018, ISSN: 0146-9592. DOI: 10.1364/ol.43.001447.

[309] A. Horn, I. Mingareev, A. Werth, M. Kachel, and U. Brenk, "Investigations on ultrafast welding of glass-glass and glass-silicon", *Applied Physics A: Materials Science and Processing*, vol. 93, no. 1, pp. 171–175, 2008, ISSN: 09478396. DOI: 10.1007/s00339-008-4654-4.

[310] S. Wang, L. Wang, S. Zhang, *et al.*, "A low-damage copper removal process by femtosecond laser for integrated circuits", *Vacuum*, vol. 203, no. June, p. 111 273, 2022, ISSN: 0042207X. DOI: 10.1016/j.vacuum.2022.111273.

[311] B. A. Rockwell, R. J. Thomas, and A. Vogel, "Ultrashort laser pulse retinal damage mechanisms and their impact on thresholds", *Medical Laser Application*, vol. 25, no. 2, pp. 84–92, 2010, ISSN: 16151615. DOI: 10.1016/j.mla.2010.02.002.

[312] C. L. Hoy, O. Ferhanoğlu, M. Yildirim, *et al.*, "Clinical ultrafast laser surgery: Recent advances and future directions", *IEEE Journal on Selected Topics in Quantum Electronics*, vol. 20, no. 2, 2014, ISSN: 1077260X. DOI: 10.1109/JSTQE.2013.2287098.

[313] M. Liu, Z. W. Wei, H. Li, *et al.*, "Visualizing the "Invisible" Soliton Pulsation in an Ultrafast Laser", *Laser and Photonics Reviews*, vol. 14, no. 4, pp. 1–8, 2020, ISSN: 18638899. DOI: 10.1002/lpor.201900317.

[314] X. Zhao, Z. B. Liu, W. B. Yan, *et al.*, "Ultrafast carrier dynamics and saturable absorption of solution-processable few-layered graphene oxide", *Applied Physics Letters*, vol. 98, no. 12, pp. 2009–2012, 2011, ISSN: 00036951. DOI: 10.1063/1.3570640.

[315] Z.-B. Liu, X. He, and D. N. Wang, "Passively mode-locked fiber laser based on a hollow-core photonic crystal fiber filled with few-layered graphene oxide solution", *Optics Letters*, vol. 36, no. 16, p. 3024, 2011, ISSN: 0146-9592. DOI: 10.1364/ol.36.003024.

[316] J. Xu, J. Liu, S. Wu, Q.-H. Yang, and P. Wang, "Graphene oxide mode-locked femtosecond erbium-doped fiber lasers", *Optics Express*, vol. 20, no. 14, p. 15 474, 2012, ISSN: 1094-4087. DOI: 10.1364/oe.20.015474.

[317] O. Svelto, *Principles of Lasers*. Boston, MA: Springer US, 2010, ISBN: 978-1-4419-1301-2. DOI: 10.1007/978-1-4419-1302-9.

[318] Q. Bao, H. Zhang, Y. Wang, *et al.*, "Atomic-layer graphene as a saturable absorber for ultrafast pulsed lasers", *Advanced Functional Materials*, vol. 19, no. 19, pp. 3077–3083, 2009, ISSN: 1616301X. DOI: 10.1002/adfm.200901007.